QUANTUM LIQUIDS AND QUANTUM CRYSTALS

Sound propagation in a porous medium filled with superfluid helium

Sh. E. Kekutiya* and N. D. Chkhaidze

Institute of Cybernetics, Georgian Academy of Sciences, yl. S. Éuli, 5, Tbilisi, 380086, Georgia
(Submitted September 10, 2001; resubmitted June 17, 2002)
Fiz. Nizk. Temp. **28**, 1115–1125 (November 2002)

A theory of the propagation of acoustic waves in a porous medium filled with superfluid helium is developed. The elastic coefficients in the system of equations are expressed in terms of physically measurable quantities. The equations obtained describe all volume modes which propagate in a porous medium saturated with superfluid helium. The propagation velocities of longitudinal and transverse waves are calculated in the limit of high and low oscillation frequencies of the thermodynamic quantities. © *2002 American Institute of Physics.*
[DOI: 10.1063/1.1528570]

Sound propagation in a porous medium filled with a liquid has been investigated theoretically and experimentally for a long time.

Porous media are bodies which contain a large number of voids which are small in size compared with any characteristic dimension of the experimental body. The distribution of these voids inside the body is ordered or disordered and the channels connecting the voids are curved. If the fluid particles traverse a path that is longer than the sample, then it is helpful to introduce the concept of sinuosity, defined as the ratio of the average trajectory length of a free particle in the sample length. The presence of voids leads to the definition of the porosity φ of a porous material as the fraction of its total volume occupied by voids. The property of a porous body that characterizes the capacity of the body to pass liquid under an applied pressure gradient is the permeability. The macroscopic characteristics, studied in the present work, of the system play an important role in describing the motion of liquids in porous media.

There are three basic approaches to studying sound propagation in the physical system under study—He II in a porous medium. In the first one the superfluid helium fills the porous solid body, which can be taken as absolutely rigid, i.e. the solid body does not participate in the vibrational motion of the liquid. This direction of investigation first appeared in 1948 in Ref. 1, where attention was first called to the fact that the character of sound propagation in superfluid helium can be strongly altered by retarding the motion of the normal component in the helium. Fourth sound propagates in this case.[2] The first experimental measurements[3,4] of the propagation velocity of fourth sound were described well by a formula derived from a two-fluid linearized system of equations of hydrodynamics in which velocity of the normal component of the fluid was set equal to zero and the equation describing the law of conservation of momentum was eliminated. These experiments were performed on a complicated system of branched capillaries; of course, it is very difficult to investigate such a system theoretically. A quite complete theory of sound propagation in a porous medium was constructed in Refs. 5 and 6, where sound propagation was studied in an isolated capillary and in a system of identical capillaries oriented parallel to one another. The experimental results, which agreed well with this theory, are published in Refs. 7 and 8.

The second direction of research is more recent and arose after the first experiments on sound propagation in an easily entrained porous medium—an aerogel.[9–11] An aerogel is of interest because of its unique acoustic, mechanical, and electrochemical properties. For example, it exhibits high acoustic insulation—the sound velocity through an aerogel is only 100 m/s.

The third direction is based on the works of Biot[12,13] for classical liquids filling a ''partially entrained'' porous medium. Our work concerns this more general direction, the first two directions being particular cases of the latter. The Biot theory predicts propagation of two different volume longitudinal waves and one shear wave. These waves are solutions of two coupled differential equations which describe the motion of a two-component system. The parameters of the Biot theory are the porosity φ, the sinuosity α, the fluid density ρ_f, and the solid body density ρ_{sol}, the bulk modulus of the fluid K_f and of the solid K_{sol}, and the bulk modulus K_b and the shear modulus N of the ''dry'' sample.[14,15] It should be noted that if the solid framework is very stiff, i.e. K_b, $N \gg K_f$, the phase velocity of the slow longitudinal wave is $C = V_f/\sqrt{\alpha_\infty}$, where $V_f = \sqrt{K_f/\rho_f}$ is the sound velocity in the liquid and α_∞ is the sinuosity at high vibrational frequencies. In this limit the slow wave is also the wave propagating in a liquid, the difference being that because of the sinuosity of the channel it becomes modified. This wave was observed first in Ref. 16 in a porous medium consisting of sintered water-filled glass beads (consolidated porous medium). The porosity of the samples ranged from 7.5 to 28.3%; the measurements were performed using the the ultrasonic load conversion technique.

Biot's theory of wave propagation in a fluid-filled porous medium has been was used[17] to study the propagation of superfluid ^{4}He in a porous medium. In Ref. 17 it was as-

sumed that at $T<1$ K, when the density of the normal component of He II can be set equal to zero, fourth sound in helium corresponds to the slow longitudinal wave arising in the Biot theory. The coefficient n, due to multiple scattering of sound in a porous medium and playing a large role in the description of the measurements of the velocity of sound, is related with the structure factor α_∞ in the Biot theory by the relation $n^2=\alpha_\infty$. The values of the velocity of the corresponding waves in He II were predicted on the basis of the results obtained from the experimental study of Biot waves in water filling a porous structure. The velocity of the slow longitudinal wave agrees well with the velocity of fourth sound.

Landau predicted the existence of second sound in free He II.[18] Peshkov was the first to observe the propagation of second sound.[19] Singer *et al.* studied experimentally in the temperature range $1.3-T_\lambda$ second sound in He II filling the channels of a porous medium. The porous medium consists of sintered 180–210 μm glass particles with porosity ranging from 16 to 33%. Capacitive transducers with a vibrating porous membrane served as emitter and detector of second sound. It was shown that the second sound velocity in a porous medium is lower than the bulk velocity, and the difference is all the greater, the smaller the porosity. The parameter n was determined in Ref. 20 from these data.

The ultrasonic properties of unconsolidated (in the ideal case a suspension) and consolidated porous media saturated with water have also been investigated.[21] Only one wave was observed in the first case; a small and a fast waves propagated in the second case. The ultrasound emission technique, based on the concept of mutual conversion and refraction at a liquid-solid interface, was used to excite volume waves in a solid layer of the material. The acoustics of He II filling a porous medium consisting of spherical glass grains with 38% porosity was analyzed. The results obtained in Ref. 21 for an superleak consisting of compressed Al_2O_3 powder with 65% porosity and filled with He II agreed with the conjectures made in Ref. 17.

Investigations of transverse waves in a porous solid-liquid system are very informative. The authors of Ref. 22 probed various ceramic materials with superfluid helium. The porosities of the samples were 44, 45, and 92%. The different pore sizes and the wide spectrum of permeabilities made it possible to perform measurements in the high- and low-frequency limits of the oscillations of the thermodynamic quantities. Ultrasonic measurements were performed using a phase-sensitive pulsed technique. The results obtained made it possible to determine the structural parameters of the porous medium: the sinuosity, the permeability, and the effective size of the pores. In Ref. 22 specific porous media filled with He II were studied, and Biot's approach must be used in order to investigate simultaneously the transverse and longitudinal waves propagating in such systems.

The experimental and theoretical works presented above indicate that the Biot theory needs to be extended to the case where superfluid helium saturates a porous medium. In a superfluid liquid, in contrast to an ordinary liquid, several waves propagate. In the present paper the propagation of waves is studied in a three-component system porous medium-superfluid liquid-normal liquid in a wide range of porosities. This made it possible to study the properties of the porous medium in greater detail.[22,23] The problem studied in this paper is to obtain the equations describing sound propagation in a consolidated porous medium filled with superfluid ^{4}He, determine the elastic coefficients, appearing in the equations, in terms of physically measurable quantities, and calculate the propagation velocities of transverse and longitudinal waves at high and low vibrational frequencies.

1. RELATIONS BETWEEN THE STRESS AND STRAIN TENSORS

Let us introduce a rectangular coordinate system and consider a cube of unit volume whose edges are parallel to the coordinate axes and which contains a large number of pores. In a state of mechanical equilibrium of the system porous body-superfluid liquid the resultant of all forces acting on this distinguished volume is zero. In the presence of a deformation the system leaves the state of equilibrium which it initially occupied. In the process, internal stresses arise in the system. The normal and tangential stresses in the system can be determined as follows:[12,13]

$$\begin{pmatrix} \sigma_x+s'+s'' & \tau_z & \tau_y \\ \tau_z & \sigma_y+s'+s'' & \tau_x \\ \tau_y & \tau_x & \sigma_z+s'+s'' \end{pmatrix}, \tag{1}$$

where $\sigma_x,\sigma_y,\sigma_z$ and τ_x,τ_y,τ_z are the normal and tangential forces acting on an element of the solid surface with the corresponding orientation; s' and s'' are the forces acting on the liquid part of a phase, which correspond to the superfluid and thermal components of the liquid, and

$$s'=-\varphi p^s, \quad s''=-\varphi p^n. \tag{2}$$

Here $p^s=\rho^s\mu$ and $p^s+p^n=p$,[15] where μ is the chemical potential and p is the pressure of the liquid. Thus, we have taken into account the fact that in contrast to an ordinary liquid the existence of a pressure gradient is insufficient to accelerate the superfluid and normal components of the liquid.

Following Biot, we shall write the deformation tensor of the solid in the form

$$\begin{pmatrix} e_x & \frac{1}{2}\gamma_z & \frac{1}{2}\gamma_y \\ \frac{1}{2}\gamma_z & e_y & \frac{1}{2}\gamma_x \\ \frac{1}{2}\gamma_y & \frac{1}{2}\gamma_x & e_z \end{pmatrix}, \tag{3}$$

where

$$e_x=\frac{\partial u_x}{\partial x}, \quad e_y=\frac{\partial u_y}{\partial y}, \quad e_z=\frac{\partial u_z}{\partial z},$$

$$\gamma_x=\frac{\partial u_y}{\partial z}+\frac{\partial u_z}{\partial y}, \gamma_y=\frac{\partial u_x}{\partial z}+\frac{\partial u_z}{\partial x}, \gamma_z=\frac{\partial u_x}{\partial y}+\frac{\partial u_y}{\partial x};$$

u_x, u_y, and u_z are the components of the displacement vector of the solid. Since the present system is a porous structure, we shall assume that the unit volume is much larger

than the pore size. We shall determine the displacement vector **u** as the displacement of the solid averaged over a volume element.

The average displacement vector **U** of the liquid part of the cube, which vector determines the fluid flow, can be determined in the same manner. Since two types of motions are possible in He II, **U** consists of a sum of two parts:

$$\mathbf{U}=\frac{\rho^s}{\rho}\mathbf{U}^s+\frac{\rho^n}{\rho}\mathbf{U}^n, \tag{4}$$

corresponding to the displacement of the superfluid and normal components; here ρ^s and ρ^n are the densities of the superfluid and normal components of the fluid, and ρ is the total volume density of the superfluid liquid. Thus, the deformation of the liquid can be determined as follows:

$$\varepsilon=\frac{\rho^s}{\rho}\nabla\mathbf{U}^s+\frac{\rho^n}{\rho}\nabla\mathbf{U}^n. \tag{5}$$

We shall now establish the relations between the components of the stress and strain tensors which were defined above. For the time being we shall neglect the dissipative forces and assume that the system is in equilibrium. Then any deformation is a deviation from the state with minimum potential energy. Therefore, to a first approximation the potential energy is a positive-definite quadratic form

$$2E_p=\sigma_x e_x+\sigma_y e_y+\sigma_z e_z+\tau_x\gamma_x+\tau_y\gamma_y+\tau_z\gamma_z+s'\varepsilon^s+s''\varepsilon^n. \tag{6}$$

Here the eight components of the stress tensor $\sigma_x,\sigma_y,\sigma_z,\tau_x,\tau_y,\tau_z,s'$, and s'' are linear combinations of the eight components of the deformation tensor $e_x,e_y,e_z,\gamma_x,\gamma_y,\gamma_z,\varepsilon^s$, and ε^n. The linear relations between the eight deformation and eight independent stresses (Hooke's law) are determined by 64 elastic moduli. Since the potential energy is a real quantity, these coefficients must be symmetric. Thus, in the most general case with the highest symmetry there remain only 36 independent elastic moduli. As a further simplification we shall consider a statically isotropic system. Indeed, let us consider, for example, the relation

$$\sigma_x=a_{11}e_x+a_{12}e_y+a_{13}e_z+a_{14}\gamma_x+a_{15}\gamma_y+a_{16}\gamma_z+a_{17}\varepsilon^s+a_{18}\varepsilon^n. \tag{7}$$

It follows from the static isotropy of the system that all directions in the system are equivalent, so that $a_{12}=a_{13}$, i.e. the same deformations of the solid along the y and z directions produce identical stresses in the x direction. It can also be assumed that $a_{14}=a_{15}=a_{16}=0$, i.e. stresses in the x direction should not give rise to displacements. As a result of similar considerations $a_{11}=a_{22}=a_{33}$ and $a_{44}=a_{55}=a_{66}$.

Then the relations between the stresses and strains have the form

$$\sigma_x=(a_{11}-a_{12})e_x+a_{12}e+a_{17}\varepsilon^s+a_{18}\varepsilon^n;$$

$$\sigma_y=(a_{11}-a_{12})e_y+a_{12}e+a_{17}\varepsilon^s+a_{18}\varepsilon^n;$$

$$\sigma_z=(a_{11}-a_{12})e_z+a_{12}e+a_{17}\varepsilon^s+a_{18}\varepsilon^n;$$

$$\tau_x=a_{44}\gamma_x,\quad \tau_y=a_{44}\gamma_y,\quad \tau_z=a_{44}\gamma_z;$$

$$s'=a_{17}e+a_{77}\varepsilon^s+a_{78}\varepsilon^n;$$

$$s''=a_{18}e+a_{78}\varepsilon^s+a_{88}\varepsilon^n, \tag{8}$$

where $e=e_x+e_y+e_z$ characterizes the volume expansion (or, correspondingly, compression) as a result of deformation and is an invariant. The construction of the remaining invariants from $\sigma_x,\sigma_y,\sigma_z,\tau_x,\tau_y$, and τ_z establishes a relation between $a_{11}-a_{22}$ and a_{44}. Indeed, we can write

$$\sigma_x^2+\sigma_y^2+\sigma_z^2+2(\tau_x^2+\tau_y^2+\tau_z^2)=\text{inv}; \tag{9}$$

$$e_x^2+e_y^2+e_z^2+2\left[\left(\frac{1}{2}\gamma_x\right)^2+\left(\frac{1}{2}\gamma_y\right)^2+\left(\frac{1}{2}\gamma_z\right)^2\right]=\text{inv}. \tag{10}$$

Equation (8) gives

$$\sigma_x^2+\sigma_y^2+\sigma_z^2=(a_{11}-a_{12})^2(e_x^2+e_y^2+e_z^2)+2(a_{11}-a_{12})\times(e_x+e_y+e_z)B+3B, \tag{11}$$

where

$$B=a_{12}e+a_{17}\varepsilon^s+a_{18}\varepsilon^n=\text{inv};$$

$$2(\tau_x^2+\tau_y^2+\tau_z^2)=2a_{44}^2(\gamma_x^2+\gamma_y^2+\gamma_z^2). \tag{12}$$

Since $e_x+e_y+e_z=\text{inv}$ and taking account of the relation (9), we can write

$$(a_{11}-a_{12})^2(e_x^2+e_y^2+e_z^2)+2a_{44}^2(\gamma_x^2+\gamma_y^2+\gamma_z^2)=\text{inv}. \tag{13}$$

Comparing the relations (10) and (13) we conclude that $a_{11}-a_{12}=2a_{44}$. Consequently, introducing the notations

$$a_{44}=N;\quad a_{12}=A;\quad a_{17}=Q^s;\quad a_{18}=Q^n;$$

$$a_{77}=R^s;\quad a_{88}=R^n;\quad a_{78}=R^{sn},$$

we replace the relation (8) with

$$\sigma_x=2Ne_x+Ae+Q^s\varepsilon^s+Q^n\varepsilon^n;$$

$$\sigma_y=2Ne_y+Ae+Q^s\varepsilon^s+Q^n\varepsilon^n;$$

$$\sigma_z=2Ne_z+Ae+Q^s\varepsilon^s+Q^n\varepsilon^n;$$

$$\tau_x=N\gamma_x,\quad \tau_y=N\gamma_y,\quad \tau_z=N\gamma_z;$$

$$s'=Q^se+R^s\varepsilon^s+R^{sn}\varepsilon^n;$$

$$s''=Q^ne+R^n\varepsilon^n+R^{sn}\varepsilon^s. \tag{14}$$

Since the superfluid and normal components cannot be physically separated in He II and it is meaningless to talk about whether individual atoms of the liquid belong to the superfluid or normal components, the following relation should be satisfied:

$$Q^s\varepsilon^s+Q^n\varepsilon^n=Q\varepsilon, \tag{15}$$

whence follows

$$Q^s=\frac{\rho^s}{\rho}Q,\quad Q^n=\frac{\rho^n}{\rho}Q,$$

$$s'+s''=(Q^s+Q^n)e+(R^s+R^{sn})\varepsilon^s+(R^n+R^{sn})\varepsilon^n=Qe+R\varepsilon. \tag{16}$$

Correspondingly, the deformations of the normal and superfluid components of He II are

$$\varepsilon^s = \operatorname{div} \mathbf{U}^s, \quad \varepsilon^n = \operatorname{div} \mathbf{U}^n. \tag{17}$$

The constants A and N correspond to the well-known Lamé coefficients in the theory of elasticity and are positive; Q and R were introduced by Biot;[12,14] $R^S(R^n)$ is a measure of the stress arising in the superfluid (normal) component when a unit volume of the system is compressed without compressing the normal (superfluid) component and the porous medium. The coefficient R^{sn} determines the stresses arising in the superfluid component when the normal component is compressed without compression of the superfluid component and the porous medium, and vice versa.

Let us consider hypothetical experiments which make it possible to determine the generalized elastic coefficients in terms of the measured coefficients K_s, K_f, K_b, and N. Such an approach was proposed in Ref. 25 for a normal liquid.

In the first experiment the porous sample was placed in a superfluid liquid to which pressure p' was applied. Under pressure liquid completely penetrates into the pores and the quantities e and ε are measured. Therefore K_s and K_f can be determined as

$$\frac{1}{K_s} = -\frac{e}{p'}, \quad \frac{1}{K_f} = -\frac{\varepsilon}{p'} \tag{18}$$

and according to Eq. (14) we can write

$$\begin{aligned} &\sigma_x = \sigma_y = \sigma_z = -(1-\varphi)p'; \\ &s' = -\varphi\frac{\rho^s}{\rho}p'; \quad s'' = -\varphi\frac{\rho^n}{\rho}p'. \end{aligned} \tag{19}$$

We shall also use the condition $\varepsilon^s = \varepsilon^n = \varepsilon$. Then the relations (19) can be put into the form

$$\begin{aligned} &\frac{2}{3}Ne + Ae + Q\varepsilon = -(1-\varphi)p'; \\ &\frac{\rho^s}{\rho}Qe + (R^s + R^{sn})\varepsilon = -\varphi\frac{\rho^s}{\rho}p'; \\ &\frac{\rho^n}{\rho}Qe + (R^n + R^{sn})\varepsilon = -\varphi\frac{\rho^n}{\rho}p'. \end{aligned} \tag{20}$$

The last two equations give

$$\begin{aligned} &R^s + R^{sn} = K_f\frac{\rho^s}{\rho}\left(\varphi - \frac{Q}{K_f}\right); \\ &R^n + R^{sn} = K_f\frac{\rho^n}{\rho}\left(\varphi - \frac{Q}{K_f}\right). \end{aligned} \tag{21}$$

In the second experiment the porous solid sample is enclosed in a thin impermeable shell and is subjected to the pressure p' of the liquid. To ensure a constant pressure inside the liquid the liquid must flow out through a tube into an external reservoir. Thus, $\varepsilon^s = \varepsilon^n = \varepsilon$ and K_b is given by the relation

$$\frac{1}{K_b} = -\frac{e}{p'}. \tag{22}$$

In this experiment

$$\begin{aligned} &\sigma_x = \sigma_y = \sigma_z = -p', \\ &s' = s'' = 0 \end{aligned} \tag{23}$$

or

$$\begin{aligned} &\left(\frac{2}{3}N + A\right)\frac{1}{K_b} - Q\frac{\varepsilon}{p'} = 1; \\ &\frac{\rho^s}{\rho K_b}Q - (R^s + R^{sn})\frac{\varepsilon}{p'} = 0; \\ &\frac{\rho^n}{\rho K_b}Q - (R^n + R^{sn})\frac{\varepsilon}{p'} = 0, \end{aligned} \tag{24}$$

whence

$$\rho^n(R^s + R^{sn}) = \rho^s(R^n + R^{sn}). \tag{25}$$

It is easy to show from Eqs. (20), (21), and (24) that[25]

$$\begin{aligned} &Q = \frac{\varphi K_s\left(1 - \varphi - \dfrac{K_b}{K_s}\right)}{1 - \varphi + \varphi\dfrac{K_s}{K_f} - \dfrac{K_b}{K_s}}; \\ &\frac{2}{3}N + A = K_s\frac{(1-\varphi)\left(1 - \varphi - \dfrac{K_b}{K_s}\right) + \varphi\dfrac{K_s}{K_f}}{1 - \varphi + \varphi\dfrac{K_s}{K_f} - \dfrac{K_b}{K_s}}. \end{aligned} \tag{26}$$

In the third experiment a superleak provides the coupling with the reservoir. This leak passes only the superfluid component, so that

$$\begin{aligned} &\sigma_x = \sigma_y = \sigma_z = -(1-\varphi)p'; \\ &s' = 0; \quad s'' = -\varphi p' \end{aligned} \tag{27}$$

or

$$\begin{aligned} &\left(\frac{2}{3}N + A\right)e + \frac{\rho^s}{\rho}Q\varepsilon^s + \frac{\rho^n}{\rho}Q\varepsilon^n = -(1-\varphi)p'; \\ &\frac{\rho^s}{\rho}Qe + R^s\varepsilon^s + R^{sn}\varepsilon^n = 0; \\ &\frac{\rho^n}{\rho}Qe + R^n\varepsilon^n + R^{sn}\varepsilon^s = -\varphi p'. \end{aligned} \tag{28}$$

In this case the relation between ε^s and ε^n can be obtained using the laws of conservation of mass and entropy. Then

$$\varepsilon^s - \varepsilon^n = \frac{C_{\mathrm{He}}p'}{\rho^s\sigma^2T}, \tag{29}$$

where C_{He} and σ are the specific heat and entropy per unit mass of He II. Finally, after some laborious calculations we find the desirable relations

$$\begin{aligned} &R^{sn} = \frac{\rho^s\rho^n}{\rho^2}R - \frac{\varphi(\rho^s)^2T\sigma^2}{\rho C_{\mathrm{He}}}; \\ &R^s = \frac{(\rho^s)^2}{\rho^2}R + \frac{\varphi(\rho^s)^2T\sigma^2}{\rho C_{\mathrm{He}}}; \\ &R^n = \frac{(\rho^n)^2}{\rho^2}R + \frac{\varphi(\rho^s)^2T\sigma^2}{\rho C_{\mathrm{He}}}, \end{aligned} \tag{30}$$

where the Biot–Willis coefficient R is[25]

$$R=\frac{\varphi^2 K_s}{1-\varphi+\varphi\dfrac{K_s}{K_f}-\dfrac{K_b}{K_s}}. \tag{31}$$

We note once again that the coefficients K_f, K_s, K_b, and N are experimentally measurable quantities.

2. EQUATIONS OF MOTION

We shall use Lagrange's formalism to find the equations of motion of the system porous solid-superfluid liquid. To construct the desired equations the kinetic energy of the system must be determined after the generalized coordinates are chosen. We assume that the physical point is a region of size much greater than the pore size but much smaller than the characteristic lengths in the problem (for example, the wavelength when considering wave processes). For the generalized coordinates of the system we choose the nine components of the displacement vectors of the liquid and solid, averaged over the volume of the physical point: $u_x, u_y, u_z, U_x^s, U_y^s, U_z^s, U_x^n, U_y^n, U_z^n$. Then the kinetic energy T per unit volume can be represented as

$$\begin{aligned}2T=&\rho_{11}\left[\left(\frac{\partial u_x}{\partial t}\right)^2+\left(\frac{\partial u_y}{\partial t}\right)^2+\left(\frac{\partial u_z}{\partial t}\right)^2\right]+2\rho_{12}^s\left[\frac{\partial u_x}{\partial t}\frac{\partial U_x^s}{\partial t}\right.\\&\left.+\frac{\partial u_y}{\partial t}\frac{\partial U_y^s}{\partial t}+\frac{\partial u_z}{\partial t}\frac{\partial U_z^s}{\partial t}\right]+2\rho_{12}^n\left[\frac{\partial u_x}{\partial t}\frac{\partial U_x^n}{\partial t}\right.\\&\left.+\frac{\partial u_y}{\partial t}\frac{\partial U_y^n}{\partial t}+\frac{\partial u_z}{\partial t}\frac{\partial U_z^n}{\partial t}\right]+2\rho_{22}^s\left[\left(\frac{\partial U_x^s}{\partial t}\right)^2+\left(\frac{\partial U_y^s}{\partial t}\right)^2\right.\\&\left.+\left(\frac{\partial U_z^s}{\partial t}\right)^2\right]+2\rho_{22}^n\left[\left(\frac{\partial U_x^n}{\partial t}\right)^2+\left(\frac{\partial U_y^n}{\partial t}\right)^2+\left(\frac{\partial U_z^n}{\partial t}\right)^2\right].\end{aligned} \tag{32}$$

The form (32) presupposes that the system is statistically isotropic. The mass coefficients $\rho_{11}, \rho_{12}^{s(n)}$, and $\rho_{22}^{s(n)}$ take account of the additional motion which the solid and liquid acquire.[12,26] Therefore by analogy to Ref. 12 it is easily found that

$$\begin{aligned}&\varphi\rho^s=\rho_{22}^s+\rho_{12}^s, \quad \varphi\rho^n=\rho_{22}^n+\rho_{12}^n,\\&(1-\varphi)\rho_{\mathrm{sol}}=\rho_{11}+\rho_{12}^s+\rho_{12}^n.\end{aligned} \tag{33}$$

Here

$$\rho_{12}^s<0, \quad \rho_{12}^n<0 \tag{34}$$

are mass parameters characterizing the increase in the inertial mass and, as usual, this increment to the inertial mass is called the associated mass. Accorrding to Berryman[27] the associated mass tensor is given by

$$\rho_{12}^{s(n)}=-(\alpha_\infty-1)\varphi\rho^{s(n)}, \tag{35}$$

where $\alpha_\infty \geqslant 1$ is a geometric quantity, independent of the density of the solid and the density of the liquid, and can vary from 1 (for plane-parallel capillaries) to ∞ (for isolated pores or pores oriented perpendicular to the motion).

Let q_x be the total force acting on the solid part of a unit volume and Q_x^s and Q_x^n the total forces acting on the superfluid and normal components per unit volume. Then the Lagrangian equations become

$$\begin{aligned}&\frac{\partial}{\partial t}\left(\frac{\partial T}{\partial \dot u_x}\right)=\frac{\partial^2}{\partial t^2}(\rho_{11}u_x+\rho_{12}^sU_x^s+\rho_{12}^nU_x^n)=q_x;\\&\frac{\partial}{\partial t}\left(\frac{\partial T}{\partial \dot U_x^s}\right)=\frac{\partial^2}{\partial t^2}(\rho_{12}^su_x+\rho_{22}^sU_x^s)=Q_x^s;\\&\frac{\partial}{\partial t}\left(\frac{\partial T}{\partial \dot U_x^n}\right)=\frac{\partial^2}{\partial t^2}(\rho_{12}^nn_x+\rho_{22}^nU_x^n)=Q_x^n.\end{aligned} \tag{36}$$

With no loss of generality we shall write the equations for the motion only along the x direction. Expressing these forces in terms of the stress tensor

$$q_x=\frac{\partial\sigma_x}{\partial x}+\frac{\partial\tau_z}{\partial y}+\frac{\partial\tau_y}{\partial z}, \quad Q_x^s=\frac{\partial s'}{\partial x}, \quad Q_x^n=\frac{\partial s''}{\partial x}, \tag{37}$$

we obtain the dynamical equations

$$\begin{aligned}&\frac{\partial\sigma_x}{\partial x}+\frac{\partial\tau_z}{\partial y}+\frac{\partial\tau_y}{\partial z}=\frac{\partial^2}{\partial t^2}(\rho_{11}u_x+\rho_{12}^sU_x^s+\rho_{12}^nU_x^n);\\&\frac{\partial s'}{\partial x}=\frac{\partial^2}{\partial t^2}(\rho_{22}^sU_x^s+\rho_{12}^su_x);\\&\frac{\partial s''}{\partial x}=\frac{\partial^2}{\partial t^2}(\rho_{22}^nU_x^n+\rho_{12}^nu_x).\end{aligned} \tag{38}$$

Similar equations can be obtained for motion along the y and z directions.

Substituting the expression (14) into Eq. (38) we easily obtain the equation in vector form:

$$\begin{aligned}&N\nabla^2\mathbf{u}+(A+N)\ \mathrm{grad}\ e+\frac{\rho^s}{\rho}Q\ \mathrm{grad}\,\varepsilon^s+\frac{\rho^n}{\rho}Q\ \mathrm{grad}\ \varepsilon^n\\&\quad=\frac{\partial^2}{\partial t^2}(\rho_{11}\mathbf{u}+\rho_{12}^s\mathbf{U}^s+\rho_{12}^n\mathbf{U}^n);\\&\frac{\rho^s}{\rho}Q\ \mathrm{grad}\ e+R^s\ \varepsilon^s+R^{sn}\ \mathrm{grad}\ \varepsilon^n=\frac{\partial^2}{\partial t^2}(\rho_{12}^s\mathbf{u}+\rho_{22}^s\mathbf{U}^s);\\&\frac{\rho^n}{\rho}Q\ \mathrm{grad}\ e+R^n\ \mathrm{grad}\ \varepsilon^n+R^{sn}\ \mathrm{grad}\ \varepsilon^s=\frac{\partial^2}{\partial t^2}(\rho_{12}^n\mathbf{u}+\rho_{22}^n\mathbf{U}^n).\end{aligned} \tag{39}$$

In Eqs. (39) we neglected dissipative processes. To take such processes into account we shall assume that the main mechanism of dissipation in the system porous body-superfluid liquid is deceleration of the normal component of the superfluid liquid by the walls of the pores. Since all deformations are assumed to be small, the macroscopic motions studied in the theory are small elastic oscillations or waves. Consequently, as in most physical systems, the friction forces are proportional to the velocities of the moving physical points and can be described using a dissipative function. The dissipative function is, by definition, a homogeneous quadratic function of generalized velocities. Then, similarly to the Biot procedure, we obtain for the dissipative terms in the equations of motion of the solid and normal component of the superfluid liquid

$$\begin{aligned}&\frac{\partial^2}{\partial t^2}(\rho_{11}\mathbf{u}+\rho_{12}^s\mathbf{U}^s+\rho_{12}^n\mathbf{U}^n)+bF(w)\frac{\partial}{\partial t}(\mathbf{u}-\mathbf{U}^n)\\&\quad=N\nabla^2\mathbf{u}+(A+N)\,\mathrm{grad}\,e+\frac{\rho^s}{\rho}Q\ \mathrm{grad}\,\varepsilon^s+\frac{\rho^n}{\rho}Q\ \mathrm{grad}\,\varepsilon^n;\end{aligned}$$

$$\frac{\partial^2}{\partial t^2}(\rho_{22}^n \mathbf{U}^n + \rho_{12}^n \mathbf{u}) - bF(w)\frac{\partial}{\partial t}(\mathbf{u}-\mathbf{U}^n) = \frac{\rho^n}{\rho} Q \operatorname{grad} e + R^n \operatorname{grad} \varepsilon^n + R^{sn} \operatorname{grad} \varepsilon^s. \quad (40)$$

The complex function $F(w)$ reflects the deviation from a Poiseuille flow taking account of the geometric features of the porous material;[23] the coefficient $b=\eta\varphi^2/k_0$ is the ratio of the total friction force to the average (relative to the solid) velocity of the normal component, where η is the viscosity of the fluid and k_0 is the permeability.[13] The possibilities of using the acoustics of a superfluid liquid to study various parameters of porous materials was analyzed theoretically in Ref. 23. To this end the function $F(w)$ was expressed in terms of the key parameters: the sinuosity, the permeability, a dynamical parameter with the dimension of length, and the porosity. Some of them were obtained from the solution of the problem of the electric conductivity of a porous medium consisting of an insulating porous material filled with a conducting liquid. The response of the rigid porous medium was calculated. The results obtained make it possible to investigate the characteristic features of two-fluid hydrodynamics of He II in a rigid porous medium and to determine the parameters of the medium from experimental data for the velocities of first, second, and fourth sounds.

3. WAVE PROPAGATION IN THE HIGH-FREQUENCY LIMIT

Solids, in contrast to liquids, are characterized by, in addition to ordinary elasticity, elasticity with respect to shear deformations. Not only longitudinal but also transverse waves can exist even in an infinite solid medium.[14] Consequently, the picture of wave propagation in our system is much richer than in a solid and in a superfluid liquid considered separately. On the other hand two important limiting cases are possible. The penetration depth of a viscous wave can be large or small compared with the pore sizes. The first case corresponds to low oscillatory frequencies of the thermodynamic quantities and the second case corresponds to high frequencies.

In the high-frequency limit the dissipative terms can be neglected, and the system of equations (39) can be used to investigate propagating waves. Taking the curl of both sides of these equations gives

$$N\nabla^2\Omega^2 = \rho_{11}\frac{\partial^2\Omega}{\partial t^2} + \rho_{12}^s\frac{\partial^2\omega_s}{\partial t^2} + \rho_{12}^n\frac{\partial^2\omega_n}{\partial t^2};$$
$$\rho_{12}^n\Omega + \rho_{12}^n\omega_n = 0; \quad \rho_{12}^{ns}\Omega + \rho_{22}^s\omega_n = 0, \quad (41)$$

where $\mathbf{\Omega} = \operatorname{curl}\mathbf{u}$, $\omega_n = \operatorname{curl}\mathbf{U}^n$, and $\omega_s = \operatorname{curl}\mathbf{U}^s$.

The equations (41) show that the vorticity of the solid and the superfluid liquid are intercoupled. The following expression for the velocity of transverse sound can be easily obtained from the system of equations (41) using the expressions (33) and (35):[10]

$$C_t^2 = \frac{N}{\rho_{sc} + \left(1 - \frac{1}{\alpha_\infty}\right)\varphi\rho}. \quad (42)$$

Here $\rho_{sc} = (1-\varphi)\rho_{\mathrm{sol}}$. In the expression (42) the velocity becomes lower than for a ''dry'' material as a result of entrainment of a portion $(1-\alpha_\infty^{-1})$ of the liquid by the ''framework'' of the porous body because of the sinuosity and the associated increase in the effective density. In this wave the superfluid and normal components move as a single entity:

$$\omega_n = \omega_s = \frac{\alpha_\infty - 1}{\alpha_\infty}\Omega, \quad (43)$$

and the liquid and solid rotate in the same directions.

Landau always supplemented the hydrodynamic equations of motion of a superfluid liquid by the requirement that the superfluid motion be potential: curl $\mathbf{V}^s = 0$. That is, the superfluid component cannot rotate as a rigid body. If in our theory the displacement (deformation vector) $\mathbf{U}^s$ of the superfluid component occurred in a region greater in size than the size of atoms but much smaller than the distance between pores, then Landau's condition would be satisfied in this case. However, in the theory which we are proposing $\mathbf{U}^s$ is the displacement of the superfluid component averaged over an element much greater in size than the pore size. Consequently, there is no need for the motion to be irrotational. For this reason, the displacements $\mathbf{U}^s$ and $\mathbf{U}^n$ appear in the equations as equivalent quantities. The only difference between them is that the superfluid motion occurs without entropy transport. We note that in this work the vortex motion (43) of the superfluid liquid is not a complex rotation around vortex singularities, but rather it is due to the fact that the solid gives rise to partial entrainment of the liquid in the vortex motion.

To study longitudinal waves we shall consider all displacements as a gradient of some scalar function. Then, the following dispersion equation follows from the system of equations (39):

$$\left(\alpha_\infty\varphi\rho^s C^2 + \frac{\rho^s}{\rho^n}R^{sn} - R^s\right)\{[(\rho_{sc}+\varphi\rho)\alpha_\infty - \varphi\rho]\varphi\rho^n C^4 - \rho^n C^2[(\rho_{sc}/\rho+\varphi)R - 2\varphi(\Omega+R) + \alpha_\infty\varphi(A+2N+2Q+R)] + R(A+2N) - Q^2\} = 0. \quad (44)$$

One solution of this dispersion equation is second sound (temperature wave) in a porous medium:[8]

$$C^2 = \frac{C_2^2}{\alpha_\infty}, \quad (45)$$

where C_2 is the velocity of second sound in unbounded helium. In addition to this solution Eq. (44) possesses two other solutions which are similar to the fast and weak waves in a porous medium filled with an ordinary classical liquid.

For an unconsolidated porous medium ($K_b = N = 0$) the velocity of the slow wave, just as the velocity of the shear wave, is identically equal to zero even in the limit of high oscillation frequencies:[21]

$$C_{\mathrm{slow}}^2(K_b = N = 0) = 0. \quad (46)$$

Finally, the velocity of a fast compressible wave has the form[21]

$$C_{\text{fast}}^2(K_b=N=0)=\frac{\alpha_\infty+\varphi\left(\dfrac{\rho_{sc}}{\rho}+\varphi-2\right)}{[(\rho_{sc}+\varphi\rho)\alpha_\infty-\varphi\rho]\left(\dfrac{1-\varphi}{K_s}+\dfrac{\varphi}{K_f}\right)}. \tag{47}$$

For a rigid porous medium $K_f \ll K_b$, $N \ll K_s$. In this case, for the fast and slow modes we obtain from Eq. (44) the well-known expressions[21]

$$C_{\text{fast}}^2=\frac{K_b+\dfrac{4}{3}N}{\rho_{sc}+\varphi\rho(1-\alpha_\infty^{-1})}; \tag{48}$$

$$C_{\text{slow}}^2=\frac{C_1^2}{\alpha_\infty}, \tag{49}$$

where $C_1=(\partial p/\partial\rho)^{1/2}$ is the volume propagation velocity of first sound in He II.

4. WAVE PROPAGATION IN THE LOW-FREQUENCY LIMIT

Since the penetration depth of the viscous wave becomes large in the limit of low oscillation frequencies, the normal component of the superfluid liquid completely sticks to the matrix of the porous medium, as a result of which the ''framework'' of the solid body and the normal liquid move with the same velocity $\mathbf{V}^n \neq 0$. Obviously, to examine this situation the friction force must be eliminated in Eqs. (40) and $\mathbf{U}^n=\mathbf{u}$ must be set in the two equations obtained. This yields

$$\begin{aligned}
&N\nabla^2\mathbf{u}^n+\left(A+N+2\frac{\rho^n}{\rho}Q+R^n\right)\text{grad div}\,\mathbf{u}^n\\
&\quad+\left(\frac{\rho^s}{\rho}Q+R^{sn}\right)\text{grad div}\,\mathbf{u}^s=\frac{\partial^2}{\partial t^2}[(\rho_{11}+2\rho_{12}^n\\
&\quad+\rho_{22}^n)\mathbf{u}^n+\rho_{12}^s\mathbf{u}^s],\\
&\left(\frac{\rho^s}{\rho}Q+R^{sn}\right)\text{grad div}\,\mathbf{u}^n+R^s\,\text{grad div}\,\mathbf{u}^s\\
&\quad=\frac{\partial^2}{\partial t^2}(\rho_{12}^s\mathbf{u}^s+\rho_{22}^s\mathbf{u}^s).
\end{aligned} \tag{50}$$

Just as in the preceding section, from Eq. (50) we can calculate the velocity of a transverse wave in the limit of low oscillation frequencies:[22]

$$C_t^2=\frac{N}{(\rho_{sc}+\varphi\rho^n)+(1-\alpha_\infty^{-1})\varphi\rho^s}. \tag{51}$$

For low oscillation frequencies the velocity of a transverse wave is lower than for the ''dry'' material by an even larger amount than at high frequencies. This is because the normal component of He II now completely sticks to the ''framework'' of the porous body on account of viscosity, while the superfluid component is entrained only partially because of sinuosity, just as at high frequencies. The formula (51) makes it possible to determine the parameter α_∞ directly.[22] In this case we have for the transverse wave

$$\omega^s=\frac{\alpha_\infty-1}{\alpha_\infty}\omega^n. \tag{52}$$

For longitudinal waves we obtain the equation

$$\begin{aligned}
&\varphi\rho^s[\alpha_\infty\rho_{sc}+\varphi(\alpha_\infty\rho-\rho^s)]C^4-C^2\\
&\quad\times\left[R^s(\rho_{sc}+\varphi\rho)+\varphi\rho^s\alpha_\infty(A+2N+2Q+R)\right.\\
&\quad\left.-2\varphi\rho^s\left(\frac{\rho^s}{\rho}Q+R^s+R^{sn}\right)\right]+R^s(A+2N+2Q+R)\\
&\quad-\left(\frac{\rho^s}{\rho}Q+R^s+R^{sn}\right)^2=0.
\end{aligned} \tag{53}$$

The two solutions of this equation in the low-frequency limit are the velocities of fast and slow waves. For an aerogel or, equivalently, for an open geometry $\varphi \simeq 1$ and $K_b \gg K_s$. Under these conditions, taking account of the fact that in a ''framework'' which is not filled with liquid the velocity of the transverse wave $C_{sc}^2=(K_b+(4/3)N)/\rho_{sc}$, the dispersion equation (53) is identical to the dispersion equation obtained in Refs. 9 and 10.

The theory developed in this paper makes it possible to find relations between quantities which oscillate in the waves. Specifically, the temperature and pressure oscillations are related with the displacement vector as

$$\begin{aligned}
T'&=\frac{\sigma\rho^s T}{\rho C_{\text{He}}}\text{div}(\mathbf{U}^s-\mathbf{U}^n);\\
p'&=-\frac{K_f}{\rho}\text{div}(\rho^n\mathbf{U}^n+\rho^s\mathbf{U}^s).
\end{aligned} \tag{54}$$

Using these expressions, we obtain for aerogels at low frequencies

$$\frac{p'}{T'}=\frac{K_f C_{\text{He}}}{\sigma T}\frac{\rho^n(C^2-C_2^2)}{\rho^s(C^2-C_1^2)}. \tag{55}$$

According to these formulas the pressure and temperature oscillate in fast and slow waves.[11] However, it should be noted that the main oscillatory quantity is the pressure in fast sound and the temperature in slow sound. Therefore, for identical temperature oscillations we have

$$\frac{p'_{\text{fast}}}{p'_{\text{slow}}}=\frac{C_{\text{fast}}^2-C_2^2}{C_{\text{fast}}^2-C_1^2}\frac{C_{\text{slow}}^2-C_1^2}{C_{\text{slow}}^2-C_2^2}\approx\frac{C_1^2}{C_{\text{slow}}^2}\gg 1, \tag{56}$$

and for identical pressure oscillations in the waves $(T'_{\text{slow}}/p'_{\text{slow}})\gg 1$ for the ratio of the oscillatory values of the temperature. Likewise, the ratios $(p'/T')_{\text{slow}}$ and $(T'/p')_{\text{fast}}$ in aerogels are much larger than the corresponding ratios in pure helium. This shows that the temperature oscillations in first sound and pressure oscillations in second sound are much stronger in an aerogel filled with superfluid helium than in pure helium. It is well known that a similar phenomenon is observed in weak solutions of ^{3}He in ^{4}He; this is due to the finite value of $\partial\rho/\partial c$ (c is the concentration). This results in peculiarities in the method used for their excitation. This phenomenon was studied first, theoretically and experimentally, in Ref. 8 and in greater detail in Ref. 11.

One solution for a rigid body, corresponding to a wave propagating in the ''framework,'' is modified because the

normal component sticks to the ''framework'' and because a nonviscous superfluid component is present. It is expressed as follows:

$$C_{\text{fast}}^2=\frac{K_b+\frac{4}{3}N}{\rho_{sc}+\varphi\rho-\varphi\alpha_\infty^{-1}\rho^s}. \tag{57}$$

The second solution is fourth sound in a porous medium:[28]

$$C_{\text{slow}}^2=\frac{C_4^2}{\alpha_\infty}. \tag{58}$$

In Ref. 28 a correction factor n, equal to the ratio of the true to the measured value of the velocity of fourth sound, was introduced to determine the velocity of fourth sound and a filter consisting of tightly compressed Fe_2O_3 powder was used to observe the sound.

In summary, we have obtained the hydrodynamic equations for the three-component system porous body-superfluid liquid ^{4}He, using which enabled us to analyze the propagation of longitudinal and transverse waves in the low- and high-frequency limits for any values of the porosity and elasticity coefficients. The elasticity coefficients appearing in the equations were expressed in terms of physically measurable quantities.

*E-Mail: kekuka@yahoo.com

[1] J. Pellam, Phys. Rev. **73**, 608 (1948).
[2] K. R. Atkins, Phys. Rev. **113**, 962 (1959).
[3] I. Rudnick and K. Shapiro, Phys. Rev. Lett. **9**, 191 (1962).
[4] G. Pollack and J. Pellam, Phys. Rev. A **137**, 1676 (1965).
[5] D. Sanikidze, I. Adamenko, and M. Kaganov, Zh. Éksp. Teor. Fiz. **52**, 584 (1967) [Sov. Phys. JETP **25**, 383 (1967)].
[6] I. Adamenko and M. Kaganov, Zh. Éksp. Teor. Fiz. **53**, 615 (1967) [Sov. Phys. JETP **26**, 394 (1968)].
[7] N. Dyumin, B. Esel'son, É. Rudavskiĭ, and I. Serbin, Zh. Éksp. Teor. Fiz. **59**, 88 (1970) [Sov. Phys. JETP **32**, 50 (1970)].
[8] L. Dikina, É. Rudavskiĭ, and I. Serbin, Zh. Éksp. Teor. Fiz. **58**, 843 (1970) [Sov. Phys. JETP **31**, 452 (1970)].
[9] M. J. Mackenna, T. Slawecki, and J. D. Maynard, Phys. Rev. Lett. **66**, 1878 (1991).
[10] D. A. Geller, A. Golov, N. Mulders, M. H. W. Chan, and J. M. Parpia, J. Low Temp. Phys. **113**, 339 (1998).
[11] Peter Brusov, J. M. Parpia, Paul Brusov, and G. Lawes, Phys. Rev. B **63**, 140507 (2001).
[12] M. A. Biot, J. Acoust. Soc. Am. **28**, 168 (1956).
[13] M. A. Biot, J. Acoust. Soc. Am. **28**, 179 (1956).
[14] L. D. Landau and E. M. Lifshitz, *Theory of Elasticity*, Nauka, Moscow (1965).
[15] D. L. Johnson, T. J. Plona, and C. Scala, Phys. Rev. Lett. **49**, 1840 (1982).
[16] T. J. Plona, Appl. Phys. **36**, 259 (1980).
[17] D. L. Johnson, Appl. Phys. Lett. **37**, 1065 (1980).
[18] L. D. Landau, Zh. Éksp. Teor. Fiz. **11**, 592 (1941).
[19] V. P. Peshkov, Zh. Éksp. Teor. Fiz. **16**, 1000 (1946).
[20] D. Singer, F. Pasierb, R. Ruel, and H. Kojima, Phys. Rev. B **30**, 2909 (1984).
[21] D. L. Johnson and T. J. Plona, J. Acoust. Soc. Am. **72**, 556 (1982).
[22] K. Werner and J. R. Beamish, Phys. Rev. B **50**, 15896 (1994).
[23] D. L. Johnson, J. Koplik, and R. Dashen, J. Fluid Mech. **176**, 379 (1987).
[24] S. Patterman, *Hydrodynamics of Superfluid Liquids*, [Mir, Moscow (1978)].
[25] M. A. Biot and D. G. Willis, J. Appl. Mech. **24**, 594 (1957).
[26] L. D. Landau and E. M. Lifshitz, *Hydrodynamics*, Nauka, Moscow (1986).
[27] J. G. Berryman, Appl. Phys. Lett. **37**, 382 (1980).
[28] I. E. Dyumin and E. Ya. Rudavskiĭ, Fiz. Nizk. Temp. **1**, 521 (1975) [Sov. J. Low Temp. Phys. **1**, 255 (1975)].

Translated by M. E. Alferieff

SUPERCONDUCTIVITY, INCLUDING HIGH-TEMPERATURE SUPERCONDUCTIVITY

Heat capacity of mesoscopically disordered superconductors: implications for MgB_2

A. M. Gabovich* and A. I. Voitenko*

Crystal Physics Department, Institute of Physics of the National Academy of Sciences, 46 Nauki Ave., Kiev 03028, Ukraine

Mai Suan Li and H. Szymczak

Institute of Physics of the Polish Academy of Sciences, Al. Lotnikow 32/46, 02-668 Warsaw, Poland
(Submitted March 11, 2002)
Fiz. Nizk. Temp. **28**, 1126–1137 (November 2002)

The electronic specific heat C as a function of temperature T is calculated for a mesoscopically disordered s-wave superconductor treated as a spatial ensemble of domains with continuously varying superconducting properties. Each domain is characterized by a certain critical temperature T_{c0} in the range $[0,T_c]$ and is supposed to have a size $L>\xi$, where ξ is the coherence length. Specific calculations are performed for exponential and Gaussian distributions of T_{c0}. For low T, the spatially averaged $\langle C(T)\rangle$ is proportional to T^2, whereas the anomaly at T_c is substantially smeared even for small dispersions. For narrow gap distributions there exists an intermediate T range, where the curve $\langle C(T)\rangle$ can be well approximated by an exponential Bardeen–Cooper–Schrieffer-like dependence with an effective gap smaller than the weak-coupling value. The results obtained successfully reproduce the salient features of the $C(T)$ data for MgB_2, where a wide superconducting gap distribution has been observed previously in the tunneling, point-contact, photoemission and Raman spectra. The conclusion is reached that the multiple-gap behavior of superconducting MgB_2 is due to the spatial distribution of dissimilar domains. Intrinsic nonstoichiometry of the compound or possible electronic phase separation may be the origin of the mesoscopic inhomogeneities. The same model describes the low-T heat capacity of cuprates, although the sources of inhomogeneity are different from those in MgB_2. © *2002 American Institute of Physics.* [DOI: 10.1063/1.1528571]

1. INTRODUCTION

After the discovery of the superconducting compound MgB_2 with a critical temperature $T_c \approx 40$ K[1] it became clear that high T_c's may be brought about not only by various exotic mechanisms such as spin-fluctuation-driven Cooper pairing.[2] Indeed, in MgB_2 the electron-phonon origin of superconductivity seems highly plausible,[3–10] phonon anharmonicity probably playing a decisive role.[11] As for the symmetry of the superconducting order parameter, the available data are rather controversial, although the main body of the data correlate better with the isotropic s-wave behavior. In any case, the Cooper pairing *per se* as the background of superconductivity in MgB_2 is beyond question, as stems from the existence of the Josephson effect in break junctions.[12] Moreover, coherent peaks in the optical conductivity[13] and spin-lattice relaxation[14] (the latter results were disputed in Ref. 15) are indicative of conventional Bardeen-Cooper-Schrieffer (BCS) s-wave pairing in MgB_2. Nevertheless, the low-temperature (low-T) properties of MgB_2 deserve further attention, since genuine BCS-like asymptotics of various quantities are never observed. The situation resembles that for high-T_c oxides, where a predominantly $d_{x^2-y^2}$-wave symmetry of the superconducting order parameter is inferred both from phase-sensitive experiments and phase-insensitive ones, including measurements of low-T asymptotics.[16] However, it was shown earlier that the power-law behavior of the electronic contribution to the heat capacity $C(T)$, thermal conductivity, NMR spin-lattice relaxation, ultrasound attenuation, or magnetic field penetration depth may be equally well explained by the spatial averaging of these quantities over a random spatial distribution of superconducting domains with different T_c's and energy gaps.[17–19] This analysis was qualitative, and to describe the diverse experimental data for MgB_2 a more rigorous quantitative approach has been developed and is given below.

Before proceeding further to the model, it is necessary to give a short summary of the measurements of different properties appropriate to MgB_2 with a special emphasis on the inferred electron spectrum gapping in the superconducting state.

The low-T asymptotics of the magnetic field penetration depth $\lambda(T)$ was shown by muon spin-rotation,[20] microwave surface resistance,[21] and optical[13] measurements to be a power-law one. This was interpreted as either unconventional superconductivity or at least as a highly anisotropic s-wave pairing. On the other hand, resonant technique investigations of MgB_2 wires[22] and c-axis oriented films[23] revealed the exponential decrease of the T-dependent term

$\Delta\lambda(T)$ in $\lambda(T)$, with the pertinent superconducting energy gap $\Delta(T)$ much smaller than is required by the weak-coupling BCS theory in view of the large resistively determined T_c of the substance. Actually, similar results were obtained by muon spin-rotation,[24] mutual inductance,[25] and resonance[26–28] techniques. Nevertheless, those authors ascribed the apparent deviations from the BCS theory to a two-gap character of superconductivity in MgB_2. We should stress that those experiments, giving averaged quantities, can not justify *precisely* this scenario, although clearly indicating that a simple conventional description is not adequate. As for the improvement of fitting on the basis of the two-gap approximation, its merits should be considered with caution too, since in this case at least two extra free parameters are added. On the other hand, $\lambda(T)$ measurements are particularly sample-dependent,[29,30] which is very important for the interpretation. Namely, a single-coil mutual inductance technique showed[29,30] that for sintered pellets $\Delta\lambda(T)\propto T^2$, whereas for thin films $\Delta\lambda(T)\propto\exp(-\Delta_L/T)$, with Δ_L reduced in comparison with the BCS-inferred value (the Boltzmann constant $k_B=1$). Alternatively, the data for bulk samples of MgB_2 can be fitted well by the superposition of two *s*-wave-gap contributions, previously used to describe properties of $YBa_2Cu_3O_{7-y}$ (Ref. 31). The authors of Refs. 29 and 30 also make the important point that the magnitudes of $\lambda(0)$ and the $\lambda(T)$ curves near T_c differ substantially for samples made in the same batch.

The results of thermoelectric power $S(T)$ studies reveal the complexity of the electronic properties of MgB_2. In Ref. 32 measurements of $S(T)$ and the resistivity $\rho(T)$ of $Mg_{1-x}Al_xB_2$ above T_c were carried out, and a predominately hole character of the current carriers was found, the deviations from linearity at higher temperatures being attributed to the electron-like sheets of the Fermi surface (FS). The existence of both holes and electrons in MgB_2 with a considerable change of transport properties above 150 K also follows from the $S(T)$ measurements carried out in Refs. 33–35. The thermal conductivity $\kappa(T)$ in polycrystalline samples of MgB_2 shows a superconducting gapping below T_c (Ref. 33), apparently with smaller Δ than is consistent with the weak-coupling BCS value. On the other hand, experiments on single crystals,[36] followed by the subsequent subtraction of the lattice term $\kappa_{ph}(T)$ from the overall $\kappa(T)$, led those authors to the conclusion that the electronic part $\kappa_{el}(T)$ of the thermal conductivity is fitted well by a combination of two BCS-like terms with smaller and larger gaps, $\Delta_S(0)=1.65$ meV and $\Delta_L(0)=5.3$ meV.

The optical data are more ambiguous than their transport counterparts. Specifically, in the infrared reflectance,[37,38] transmission,[39,40] and Raman[41] spectra only one *s*-wave-like superconducting gap manifests itself. It also turns out that the quasiparticle scattering rates τ^{-1} strongly exceed the relevant Δ amplitudes, so that the dirty limit is achieved (the Planck's constant $\hbar=1$). This is at variance with estimates of the mean free path l from transport phenomena,[42–44] according to which MgB_2 is a well-defined clean superconductor. High-resolution photoemission studies[45] also found one isotropic gap with $\Delta(T=15\text{ K})\approx 4.5$ meV and a T dependence of the BCS type.

Other Raman,[46] optical transmission[47] and reflectance[47,48] measurements, as well as photoemission studies,[49] testify that a two-gap description in this case is more adequate than a conventional one, involving a single gap. In Ref. 38 it is concluded that the single gap $\Delta\approx 1.5-2$ meV found there is a minimal value of the anisotropic gap covering the multi-sheet FS of MgB_2.

Thermodynamic measurements might be decisive in determining the low-T symmetry-based superconducting properties of MgB_2 because the minority phases or grain boundaries do not affect the results substantially, in contrast to transport phenomena, for example. The behavior of the electronic heat capacity $C(T)$ near T_c is also of great importance for elucidating the nature of superconductivity here. And, indeed, there have been many specific heat investigations for MgB_2 performed by various groups.[50] Unfortunately, the isolation of the current-carrier contribution to the overall heat capacity is obscured by (i) phonon anharmonicity, (ii) the involvement of low-T Einstein optical modes, especially for compounds containing light elements, (iii) the Schottky term due to paramagnetic impurities, and (iv) the complex electronic band structure of MgB_2, leading to at least two important electron-DOS-driven terms.[51] In this connection, it should be stressed that although the *two-band* approximation involving two Sommerfeld constants γ_S[51] turns out to be a satisfactory fitting procedure, it cannot be true from a fundamental point of view because an almost continuous set of energy gaps is observed in different point-contact spectra of the *same* polycrystalline MgB_2 pellet for varying locations of the Pt needle.[52] Such apparently random distribution of gaps has been observed, e.g., in the tunneling spectra of Nb_3Sn.[17,53]

The main features of the data for $C(T)$ are (i) small values of the phase transition anomaly $\Delta C=C_s-C_n$ at T_c[50,54–56] in comparison to the BCS case,[57] when the ratio

$$\mu=\frac{\Delta C}{\gamma_S(T_c)T_c} \tag{1}$$

is equal to

$$\mu_{BCS}=\frac{12}{7\zeta(3)}\approx 1.43; \tag{2}$$

and (ii) deviations from the asymptotic BCS behavior at $T\ll T_c$,

$$C_s^{\text{asympt}}(T)=N(0)\left(\frac{2\pi\Delta_0^5}{T^3}\right)^{1/2}\exp\left(-\frac{\Delta_0}{T}\right). \tag{3}$$

Here the subscripts *s* and *n* correspond to the superconducting and normal states, respectively, $N(0)$ is the electron DOS at the Fermi level, and Δ_0 is the energy gap value at $T=0$. As indicated above, for MgB_2 it is necessary to take into account a possible T dependence of the Sommerfeld ''constant''. The deviations from Eq. (3) may be twofold: power-law-like $\propto T^2$ (Ref. 54) and of the form $\propto\exp(-A/T)$,[56,58,59] where the constant A is much less than $(\pi/\gamma)T_c\approx 1.76T_c$, the value inherent to the weak-coupling superconductor,[57] and $\gamma=1.7810...$ is the Euler constant. Thus, the raw specific heat data do not give definite answers to the problems of the order parameter symmetry and the underlying mechanisms of superconductivity.

In this article, on the basis of the experimentally proved *distribution* of energy gaps we show that *both* main features of the bulk property $C_s(T)$ can be explained by the conventional *s*-wave superconductivity, so that these data can be easily reconciled with other observations.[13,14] The adopted approach, being an outgrowth of the earlier one,[17–19] is phenomenological because the origin of the gap distribution is not known precisely. However, in accordance with the tunneling data,[60] the gap distribution is considered to occur *in real space* rather than in **k** space, as was suggested, e.g., in Refs. 50 and 54. The theoretical description of such spatially disordered superconductors depends on the ratio between the characteristic superconducting domain size L and the coherence length ξ.[61] If $L>\xi$, the superconducting properties are determined by local values of the order parameter Δ. Our approach corresponds to these so-called large-scale inhomogeneities, whereas the small-scale inhomogeneities correspond to the reverse inequality $L<\xi$ (Refs. 62 and 63). The quantity ξ is T-dependent and tends to infinity at T_c. Hence, in the close vicinity of T_c, strictly speaking, all inhomogeneities become small-scale ones, and a divergent correction proportional to $(T_c/T-1)^{-1/2}$ appears in the expression for $C_s(T)$.[62] Nevertheless, it can be easily shown that for conventional superconductors including MgB_2 the relevant T range is very small, so that its influence on the phase transition smearing is negligible. Moreover, it has been disclosed recently that the correction for three-dimensional superconductors is actually finite.[63] Therefore we can identify ξ with the T-independent coherence length, dependent on the Pippard coherence length $\xi_0 \approx v_F/\pi\Delta$ and the mean free path l (Ref. 57). Here v_F is the Fermi velocity. For MgB_2, which can be considered a clean superconductor,[42,44] the quantities of interest are $\xi \approx \xi_0 \ll l \approx 600$ Å, although there is a significant scatter of the values of ξ_0 inferred from different experiments and for *different kinds* of samples,[6,64] so that we may estimate this quantity as lying in the range from 25 to 120 Å. This dispersion of ξ_0 qualitatively correlates with the broad spectra of gaps in tunnel and point-contact spectra.[6,50,52,60]

A competitive theory[65–72] was put forward to reconcile the numerous transport, optical, microwave, and thermodynamic experimental data and the almost obvious *s*-wave and phonon-driven character of superconductivity in MgB_2. It is based on the idea of multi-gap superconductivity with the gap diversity on the different sheets of the Fermi surface, i.e., in momentum **k** space. This is an extension of the well-known two-band superconductivity concept,[73] which, in turn, approximates the complex anisotropy of the electron spectrum in MgB_2.[6,74–77] A more direct version of the anisotropic *s*-wave superconductivity in MgB_2 has also been considered.[78,79]

The expected observable results of our theory and the two-band model differ in the sense that in the latter case there should be two different gap parameters connected by interband scattering matrix elements or gaps clustered into two groups.[68] On the other hand, we suggest that the gap distribution should be quasi-continuous due to the proximity effect. Since our theory is phenomenological, it may be also directly applied to other substances, including cuprates. This will be done in subsequent publications.

2. THEORY

Let us examine a T-independent configuration of mesoscopic domains, with each domain having the following properties:

(A) at $T=0$ it is described by a certain superconducting order parameter $\Delta_0 \leqslant \Delta_0^{\max}$;

(B) up to a relevant critical temperature $T_{c0}(\Delta_0) = (\gamma/\pi)\Delta_0$, it behaves like an isotropic BCS superconductor, i.e., the superconducting order parameter $\Delta(T)$ is the Mühlschlegel function $\Delta(T)=\Delta_{BCS}(\Delta_0,T)$;[57] and the electronic specific heat is characterized in this interval by the function $C_s(\Delta T)$;

(C) at $T>T_{c0}$ it transforms into the normal state, and the relevant property is $C_n(T)$.

At the same time, the values of Δ_0 scatter for different domains. The current carriers move freely across domains and acquire appropriate properties inside each domain. The adopted picture is especially suitable for superconductors with small coherence lengths ξ_0 (Ref. 50), where even nanoscale intrinsic inhomogeneities may comprise domains of the sort discussed above.

In other words, each domain above its T_{c0} is in the normal phase, and its specific heat is[57]

$$C_n(T)=\frac{\pi^2}{3}N(0)T. \tag{4}$$

For simplicity we restrict ourselves to the situation when the whole sample above T_c is electronically homogeneous, i.e., is characterized by a common, approximately constant $N(0)$ value. Below T_{c0} for a given mesoscopic domain, a corresponding isotropic gap appears on the Fermi surface. The microscopic background of the assumed scatter in T_{c0} may be diverse but ultimately manifests itself as a variation either of the magnitude of the electron-phonon interaction or of the local values of the Coulomb pseudopotential.

In the framework of our phenomenological approach, superconductivity (if any) inside a chosen domain is described by the relevant parameters Δ_0 and T_{c0}. They are bounded from above by $\Delta_0^{\max}$ and T_c, respectively. These Δ_0 may or may not group around a certain crowding value Δ_0^*, depending on the sample texture. The existence of such two possibilities is in accordance with the varied data for MgB_2.[6,50–52,60] The specific gap distribution is described by the function $f_0(\Delta_0)$.

Thus, for all T in the interval $[0,T_c]$, where $T_c = \max T_{c0}$, the superconducting sample consists of superconducting (s) and nonsuperconducting (n) grains more or less homogeneously distributed over the sample volume. The critical temperature T_c defined in such a manner may not necessarily coincide with the resistively determined $T_c^{\rm res}$ governed by percolation networks in the disordered samples.[80,81]

The measured $C_s(T)$ is an averaged sum of contributions from both phases,

$$\langle C(T)\rangle = \langle C_n(T)\rangle + \langle C_s(T)\rangle, \tag{5}$$

which depends on the distribution function $f(\Delta,T)$ of superconducting domains and on the normal-phase fraction $\rho_n(T)$:[17–19]

$$\langle C_n(T)\rangle = C_n(T)\rho_n(T), \tag{6}$$

$$\langle C_s(T)\rangle = \int_0^{\Delta^{\max}(T)} C_s(\Delta,T) f(\Delta,T) d\Delta. \quad (7)$$

Here $\Delta^{\max}(T)=\Delta_{BCS}(\Delta_0^{\max},T)$, and $f(\Delta,T)$ is a result of the thermal evolution of the initial (at $T=0$) distribution function $f_0(\Delta_0)$.

It is convenient to normalize all temperatures by T_c and all energy parameters by $\Delta_0^{\max}$:

$$t=T/T_c, \quad \delta=\Delta/\Delta_0^{\max}, \quad (8)$$

with relevant indices retained, and to consider $C_s(T)$ and $C_n(T)$ together with their averaged counterparts, normalized by the $C_n(T_c)$ value, i.e., for example,

$$c_{s,n}(t)=\frac{C_{s,n}(T)}{C_n(T_c)}. \quad (9)$$

Then one can easily find that for each domain, characterized by the parameter δ_0 at $t=0$, the dimensionless heat capacity is either

$$c_n(t)=t \quad \text{for} \quad t>\delta_0 \quad (10)$$

or

$$c_s(t)=\delta_0 c_{BCS}\left(\frac{t}{\delta_0}\right) \quad \text{for} \quad t<\delta_0, \quad (11)$$

where $c_{BCS}(x)$ is a well-known normalized heat-capacity function for a standard BCS superconductor.[57] The parameter $N(0)$, due to the assumption $N(0)=\text{const}$, disappears from the normalized dependences (10) and (11).

For a surmised domain ensemble a distribution function $f(\Delta,T)$ for finite T is defined by the formula

$$f(\Delta,T)d\Delta = f_0(\Delta_0)d\Delta_0. \quad (12)$$

Then Eq. (7) can be rewritten as

$$\langle c_s(t)\rangle = \int_t^1 c_{BCS}\left(\frac{t}{\delta_0}\right) f_0(\delta_0)\,\delta_0 d\delta_0. \quad (13)$$

To obtain the low-T asymptotics, we introduce a new integration variable $z=t/\delta_0$. Then,

$$\langle c_s(t)\rangle = t^2 \int_t^1 \frac{dz}{z^3} f_0\left(\frac{t}{z}\right) c_{BCS}(z). \quad (14)$$

Expanding the function $f_0(t/z)$ into a series

$$f_0\left(\frac{t}{z}\right) = f_0(0) + \sum_{k=1}^{\infty} B_k \left(\frac{t}{z}\right)^k, \quad (15)$$

we arrive at

$$\langle c_s(t)\rangle = t^2 f_0(0) \int_0^1 \frac{dz}{z^3} c_{BCS}(z) + t^2 \times \left[-f_0(0) \int_0^t \frac{dz}{z^3} c_{BCS}(z) + \sum_{k=1}^{\infty} B_k t^k \int_t^1 \frac{dz}{z^{k+3}} c_{BCS}(z) \right]. \quad (16)$$

The first term in the right-hand side is the sought asymptotics

$$\langle c_s(t\to 0)\rangle = t^2 f_0(0) \int_0^1 \frac{dz}{z^3} c_{BCS}(z) \approx 2.45 f_0(0) t^2. \quad (17)$$

Note that in our previous works,[17–19] to estimate the numerical coefficient in the asymptotic term we used the dependence $C_s^{\text{asympt}}(T)$ instead of $C_{BCS}(T)$, which led to the result $\langle c_s(t\to 0)\rangle \approx 0.54 f_0(0) t^2$.

The dependence of the next term in the expansion for $\langle c_s(t)\rangle$ can be estimated in the limit $t\to 0$ by substitution of the normalized expression (3) for $c_{BCS}(z)$. Then

$$\int_0^t \frac{dz}{z^3} c_{BCS}(z) \approx \frac{3\sqrt{2}\,\gamma}{\pi^2\sqrt{\pi}} \Gamma\left(\frac{7}{2}, \frac{\pi}{\gamma t}\right). \quad (18)$$

For small t this expression decreases as $O[t^{5/2} \times \exp(-\pi/\gamma t)]$. At the same time, the convergence of the series in Eq. (16) for $t\to 0$ is $O(t^4)$ if the function $f_0(\delta_0)$ has an extremum at $\delta_0=0$ (then the coefficient $B_1=0$), or $O(t^3)$ otherwise.

Now, in the same low-T region let us take a look at the contribution $\langle c_n(t)\rangle$ of the continuously expanding normal phase. At any T, all domains with $\Delta_0<(\pi/\gamma)T$ (i.e., $\delta_0<t$) are nonsuperconducting, with the total normal-phase fraction being

$$\rho_n(t)=\rho_n(0)+\int_0^t f_0(\delta_0)\,d\delta_0. \quad (19)$$

For simplicity, below we restrict ourselves to the case when all domains at $t=0$ are superconducting, i.e., $\rho_n(0)=0$. The generalization to the case $\rho_n(0)\neq 0$ is obvious: at each temperature there exists an additional contribution from the normal phase. Then the function $f_0(\delta_0)$ should be normalized by $1-\rho_n(0)$, and all averaging-driven effects would accordingly decrease. Moreover, if $\rho_n(0)\neq 0$, the observed heat capacity $\langle c(t)\rangle$ must include an extra linear contribution $\rho_n(0)t$ in the true superconducting state exhibiting the Meissner effect. On the other hand, the observation of the resistive macroscopic superconductivity depends on the crossing of the percolation threshold by the superconducting domain fraction.

As to the second term in Eq. (19), the approximation of $f_0(\delta_0)$ by its limiting value $f_0(0)$ demonstrates that the main temperature-dependent contribution to $\rho_n(t)$ is *linear* in t. Since $c_n(t)$ is also a linear function of t, the apparent contribution $\langle c_n(t)\rangle$ of the normal phase to the total specific heat $\langle c(t)\rangle$ is quadratic in t for small t, similarly to $\langle c_s(t)\rangle$. Thus, in the proposed model of a disordered superconductor with a broad continuous spatial distribution of domains possessing different T_{c0}'s, the normal and superconducting contributions to thermodynamic quantities are *functionally indistinguishable* from each other.

3. NUMERICAL RESULTS

In addition to the low-T asymptotics the overall T dependence of the heat capacity C up to T_c is also of considerable interest. It is especially important to trace the smearing of the anomaly ΔC by the *same* disorder effect that leads to the transformation of the intrinsic exponential low-T behavior of $C_s(T)$ into power-law behavior. These objectives were met by numerical calculations.

For this purpose, two model distribution functions $f_0(\delta_0)$, namely, exponential

$$f_0^E(\delta_0) \propto \exp\left[-\frac{|\delta_0-\delta_0^*|}{d}\right] \tag{20}$$

and Gaussian

$$f_0^G(\delta_0) \propto \exp\left[-\frac{(\delta_0-\delta_0^*)^2}{2d^2}\right] \tag{21}$$

were used. The parameter δ_0^* designates the peak position, which may vary from 0 to 1. By changing the parameter d we control the dispersion of the domain superconducting properties: the sharper the function $f_0(\delta_0)$, the more homogeneous the ensemble. Nevertheless, for any d both functions are nonvanishing in the limit $\delta_0=0$ and their Taylor series (15) begin with the relevant constants as the main terms. Only for highly improbable distribution functions such that $f_0(\delta_0)$ extends to $\delta_0=0$ and also satisfies the condition $f_0(\delta_0=0)=0$ can the Taylor series begin with the next term, resulting in the asymptotics $C_s(T)\propto T^3$.

Figure 1 shows the influence of the choice of distribution function on $\langle c_s(t)\rangle$ for $\delta_0^*=1$ (a) and $\delta_0^*=0$ (b). In all cases, for larger d the curves converge towards a common limit which corresponds to the uniform distribution $f_0^U(\delta_0)$

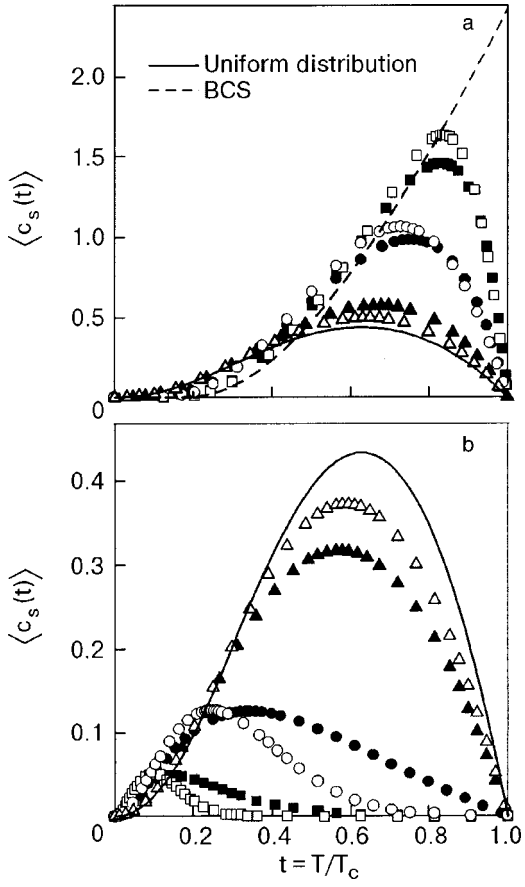

FIG. 1. Temperature dependences of normalized (see the text) electronic heat capacity $\langle c_s(t)\rangle$ of superconducting phase fraction for exponential and Gaussian distributions of the parameter δ_0 over the inhomogeneous ensemble of domains. The panels correspond to the maximum position at $\delta_0^*=1$ (a) and $\delta_0^*=0$ (b). For $d=0.1-$exponential (■), Gaussian (□); $d=0.25-$exponential (●), Gaussian (○); $d=1-$exponential (▲), Gaussian (△).

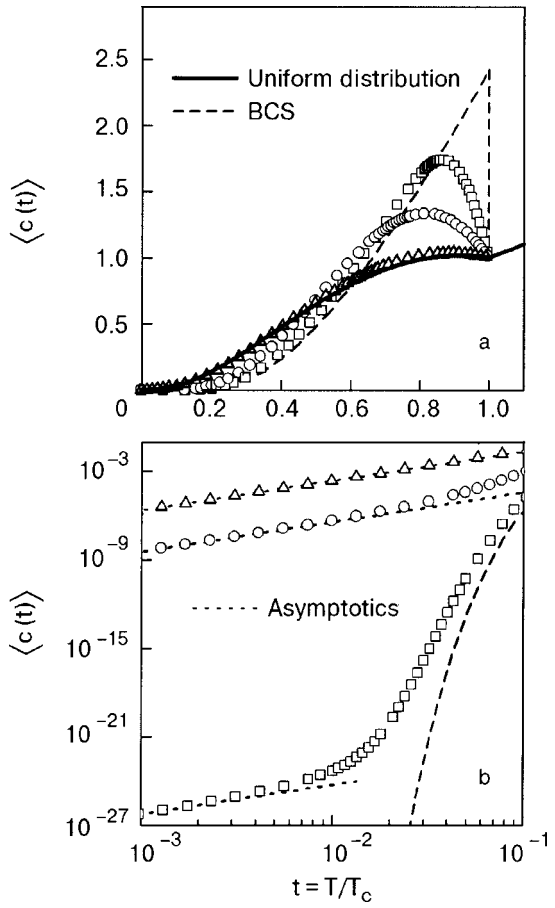

FIG. 2. Temperature dependences of normalized total electronic heat capacity $\langle c(t)\rangle$ in comparison with the BCS dependence of the superconducting-phase fraction. Gaussian distributions with $\delta_0^*=1$ (a). Low-temperature portions of the relevant curves on a log-log scale together with their t^2 asymptotics (b). For $d=0.1$ (□), $d=0.25$ (○), $d=1$ (△).

$=$const. For smaller d the curves approach opposite homogeneous bounds: the discontinuous curve for a clean BCS superconductor (Fig. 1a) and the straight line, coinciding with the abscissa, for a normal metal (Fig. 1b). Thus, on Fig. 1b the curves become more and more flat. As to Fig. 1a even for $d=0.1$ [i.e., when $f_0(0)/f_0(1)\approx 4.5\times 10^{-6}$ for the exponential distribution and $\approx 1.9\times 10^{-22}$ for the Gaussian] the resulting curves are no longer discontinuous: the jump transforms into a hump. In addition, with variation of the parameter d the peak positions on the two panels shift in opposite directions.

Thus, the substantial spreading of the anomaly ΔC readily seen in Fig. 1 seems quite natural in view of the results for MgB_2.[50,54–56] However, the concomitant superposition of various domain contributions causes distortion of the overall curves $C_s(T)$ and $C(T)$, which is much less trivial. This very superposition may lead for low T to the power-law behavior whose the asymptotics was analyzed above.

Figure 1 also evidences that different distributions lead to similar results for each set of parameters, and it would be the more so if we plotted the relevant $\langle c(t)\rangle$ curves. Hence, hereafter we confine ourselves to the Gaussian distribution.

The dependences $\langle c(t)\rangle$ are depicted in the Fig. 2a for $\delta_0^*=1$ and different dispersion values d. The low-T parts of

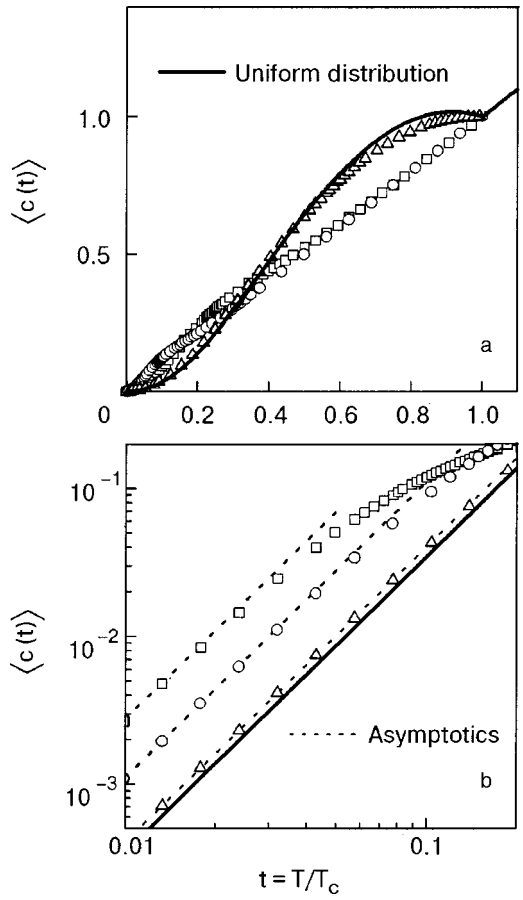

FIG. 3. Temperature dependences of normalized total electronic heat capacity $\langle c(t)\rangle$ for Gaussian distributions with $\delta_0^*=0$ (a). Low-temperature portions of the relevant curves on a log-log scale together with their t^2 asymptotics (b). For $d=0.1$ (□), $d=0.25$ (○), $d=1$ (△).

the $\langle c(t)\rangle$ curves are displayed on a log-log scale in Fig. 2b. The dotted straight lines correspond to the pertinent T^2 asymptotics for each curve. It is clear that the validity range of the asymptotics extends with the increase of d. Although intervals where the T^2 approximation holds good exist for any d, for small d this is merely of academic interest, because both temperatures and heat capacities become too tiny to be experimentally significant. On the other hand, for higher T in this case the averaged curves $\langle c(t)\rangle$ lie rather close to the exponential curve inherent to the BCS theory (the dashed curve). Such transitional parts of the dependences $\langle c(t)\rangle$ describe well the exponential low-T behavior for some samples of MgB_2 (Refs. 56 and 58) with smaller exponents than in the BCS case.

For large d, when the Gaussian distribution function $f_0^G(\delta_0)$ becomes almost uniform (such a random dense, although quasi-discrete, distribution of gaps was found in point-contact spectra),[52] the quadratic asymptotics are valid at least up to $t=0.1$ (for the uniform distribution $f_0^U(\delta_0)$ the relative error of the t^2 asymptotics is $\approx 0.6\%$ at $t=0.1$ and $\approx 5\%$ at $t=0.2$), which agrees with the measurements.[54] For intermediate d the experimental data in the relevant T range may be satisfactorily represented by power-law curves $C(T)\propto T^n$ with $n\geqslant 2$.

Figure 3 demonstrates the dependences $\langle c(t)\rangle$ for $\delta_0^*=0$. The overall behavior remains the same as for $\delta_0^*=1$, but the validity range of the asymptotics extends because now $f_0(\delta_0)$ has a maximum at $\delta_0=0$, in full agreement with the analysis given above (see Sec. 2).

One can make another important conclusion from the numerical data shown in Figs. 2 and 3. Specifically, a one-parameter fitting explains *both* the smearing of the heat-capacity anomaly at T_c and the appearance of the power-law asymptotics. The latter reproduces the results appropriate to superconductors with order parameters of $d_{x^2-y^2}$-wave[82] or extended s-wave with uniaxial anisotropy[50,54] symmetry. The patterns displayed in these figures explain well the experimental heat capacity dependences $C(T)$ for MgB_2, which demonstrate power-law behavior for lowest attainable T[50,54] or above the exponential low-T tail.[58] At the same time, the reduction of the anomaly ΔC at T_c with the increase of d, traced in Fig. 2a, adequately describes the ΔC magnitudes inferred from the analysis of the observed total heat capacity of MgB_2, with allowance made for the crystal-lattice and impurity components. Namely, $\mu\approx 1.13$,[56] 0.82,[50,54] 0.7,[55] so that the experimental specific heat jump is substantially smaller than the BCS value μ_{BCS} [see Eq. (2)].

A comparison of Figs. 2a and 3a shows that for wide enough distribution functions the resulting $\langle c(t)\rangle$ curves are almost identical. They lie very close to the corresponding curve for the uniform distribution. The latter has a gentle maximum at about $t=0.9$, so that the actual t dependence in the interval $0.8\leqslant t\leqslant 1$ may be readily overlooked. It is clear that the peak position δ_0^* has no meaning in this case. At the same time, for small d, if the parameter δ_0^* changes from 1 to 0, the curves transform from ones possessing well-pronounced maxima to almost monotonic ones. Such a transformation "process" is depicted in Fig. 4. In particular, the results show an interesting feature: if the distribution over Δ_0 is characterized by a small dispersion and a maximum position at about $\Delta_0^{\max}/2$, the apparent dependence $\langle C(T)\rangle$ should demonstrate "oscillating" behavior in the superconducting temperature region. For example, for $d=0.1$ it would happen above $t\approx 0.4$, according to Fig. 4a. These departures from the BCS electronic specific heat describe qualitatively the deviations of the experimental $C(T)$ from their counterparts measured in strong magnetic fields, when superconductivity is suppressed.[51,54,55]

4. DISCUSSION AND CONCLUSIONS

The results obtained here are of a quite general nature and fit well the observed heat capacity dependencies both for cuprates and magnesium diboride. Our main assumptions are the s-wave symmetry of the superconducting order parameter and the proposed large scale ($L>\xi_0$) spatial inhomogeneities of Δ (and T_c). As for cuprates, the origin of those heterogeneities was discussed in our previous publications.[17,18] On the other hand, in MgB_2 large enough inclusions (they influence the heat capacity!) of different phases or planar defects may be the most probable cause of the Δ spread. One can mention, e.g., observed MgB_4 grains and stacking faults[83] or nonstoichiometry modeled by $Mg_{1+\delta}B_2$ phases.[84] Mg vacancies or B interstitials as well as some degree of oxidation may be the inhomogeneities leading to conspicuous scatter of T_c.[85] X-ray analysis shows that MgB_2 can be microscopically nonstoichiometric up to 5–10%.[86] Nonstoichiometry is most likely an intrinsic phenomenon, since pressure depen-

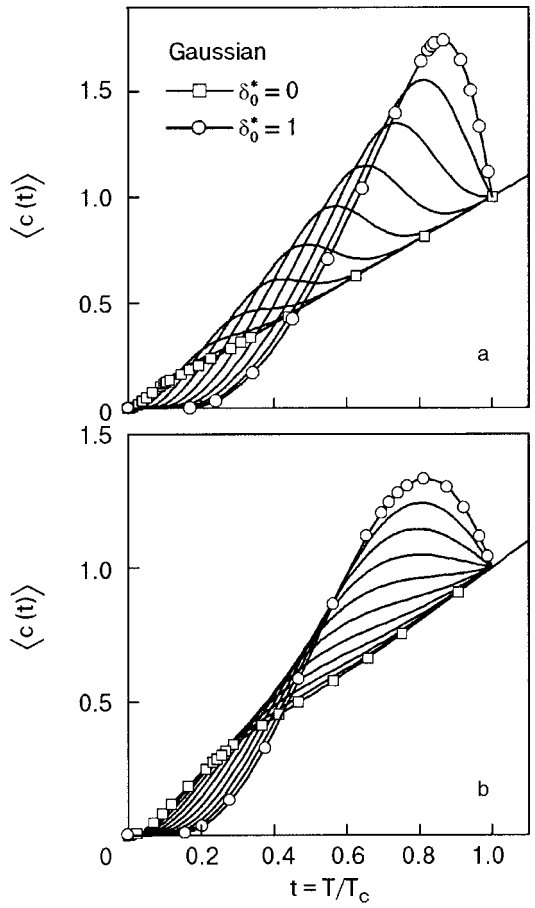

FIG. 4. Influence of the peak position δ_0^* in the Gaussian distribution function on the behavior of $\langle c(t)\rangle$. Dispersion $d=0.1$ (a) and $d=0.25$ (b). δ_0^* varies from 0 to 1 in steps of 0.1.

dences of T_c are substantially different for various specimens.[10,87] However, we cannot also exclude a purely electronic phase separation,[81,88–94] because the substance concerned is on the verge of an electronic topological transition[74,77,95] or a structural one.[87,96]

Bearing in mind these inhomogeneities of sintered, single-crystal, and thin-film MgB_2 samples, we applied our theory to calculate the spatially averaged electronic heat capacity $\langle C(T)\rangle$. The low-T asymptotics was shown to be a power-law one $\propto T^2$, the anomaly ΔC at T_c being simultaneously smeared. These very features are appropriate to the heat capacity of MgB_2. The existence of regions (domains) with varying T_c undoubtedly manifests itself in the photoemission, Raman, point-contact, and tunneling spectra.[6,46,49,52,60,97–104] Usually the two-gap description is sufficient to fit the observations, but we should stress that it may be only a crude approximation of the actual really *multiple-gap* picture. For example, a three-gap structure was also seen in the same tunneling spectrum.[105]

We suggest that the observed multiple-gap superconductivity in MgB_2 originates from some kind of a phase separation or an intrinsic nonstoichiometry rather than from the existence of several groups of current carriers in the same volume.[65–68,70,72] The proposed theory may be also invoked to explain the low-T properties of cuprates,[17–19] although the microscopic background of the multi-gapness may be quite different in both cases.

One more circumstance should be highlighted to distinguish between various scenarios of apparent two-gap (or, better to say, multiple-gap) manifestations. It is often claimed[49,98] that for MgB_2 both gaps close at a *common* T_c. But even a cursory examination of the relevant data shows that the instrumental errors in the neighborhood of T_c and the obvious uncertainties of applied fittings are too large to ensure the validity of such a conclusion. Indeed, some point-contact spectra could be explained on the basis of two gaps, one vanishing at the bulk T_c while the other closing at $\approx 0.7\,T_c$.[52] Also the differential conductivities of MgB_2/Ag and MgB_2/In junctions have been interpreted in terms of two gaps with energies 4 and 2.6 meV, which close at 20 and 38 K, respectively.[99] This alleged anticorrelation between the Δ's and T_c's seems doubtful and apparently is a consequence of the two-gap prescription. On the other hand, the experimental results[49,98,99] can be naturally described in the framework of the scheme adopted here with a continuous set of gaps and critical temperatures rigidly bound to them. Hence, the two-gap fitting procedure is only a first approximation to the actual multiple gap superposition. Aside from the formal aspect of the problem consisting in the selection of a proper fitting procedure, our point of view is favored by the direct simultaneous experimental observations of more than two gaps for a number of samples.[52,60]

A. M. G. is grateful to the Mianowski Foundation for support of his visit to Warsaw University. M. S. L. was supported by the Polish agency KBN (Grant No. 2P03B-146-18).

*E-mail: collphen@iop.kiev.ua

[1] J. Nagamatsu, N. Nakagawa, T. Muranaka, Y. Zenitani, and J. Akimitsu, Nature (London) **410**, 63 (2001).
[2] Yu. A. Izyumov, Usp. Fiz. Nauk **169**, 225 (1999) [Phys. Usp. **42**, 215 (1999)].
[3] S. L. Bud'ko, G. Lapertot, C. Petrovic, C. E. Cunningham, N. Anderson, and P. C. Canfield, Phys. Rev. Lett. **86**, 1877 (2001).
[4] K.-P. Bohnen, R. Heid, and B. Renker, Phys. Rev. Lett. **86**, 5771 (2001).
[5] R. Osborn, E. A. Goremychkin, A. I. Kolesnikov, and D. G. Hinks, Phys. Rev. Lett. **87**, 017005 (2001).
[6] C. Buzea and T. Yamashita, Supercond. Sci. Technol. **14**, R115 (2001).
[7] J. Kortus, I. I. Mazin, K. D. Belashchenko, V. P. Antropov, and L. L. Boyer, Phys. Rev. Lett. **86**, 4656 (2001).
[8] T. Muranaka, S. Margadonna, I. Maurin, K. Brigatti, D. Colognesi, K. Prassides, Y. Iwasa, M. Arai, M. Takata, and J. Akimitsu, J. Phys. Soc. Jpn. **70**, 1480 (2001).
[9] D. G. Hinks, H. Claus, and J. D. Jorgensen, Nature (London) **411**, 457 (2001).
[10] B. Lorenz, R. L. Meng, and C. W. Chu, Phys. Rev. B **64**, 012507 (2001).
[11] L. Boeri, G. B. Bachelet, E. Cappelluti, and L. Pietronero, Phys. Rev. B **65**, 214501 (2002).
[12] R. S. Gonnelli, A. Calzolari, D. Daghero, G. A. Ummarino, V. A. Stepanov, G. Giunchi, S. Ceresara, and G. Ripamonti, Phys. Rev. Lett. **87**, 097001 (2001).
[13] A. V. Pronin, A. Pimenov, A. Loidl, and S. I. Krasnosvobodtsev, Phys. Rev. Lett. **87**, 097003 (2001).
[14] H. Kotegawa, K. Ishida, Y. Kitaoka, T. Muranaka, and J. Akimitsu, Phys. Rev. Lett. **87**, 127001 (2001).
[15] J. K. Jung, S. H. Baek, F. Borsa, S. L. Bud'ko, G. Lapertot, and P. C. Canfield, Phys. Rev. B **64**, 012514 (2001).
[16] C. C. Tsuei and J. R. Kirtley, Rev. Mod. Phys. **72**, 969 (2000).
[17] A. M. Gabovich and A. I. Voitenko, in *Supermaterials*, R. Cloots, M. Ausloos, M. Pekata, A. J. Hurd, and G. Vacquier (Eds.), Kluwer Academic, Dordrecht (2000), p. 193.
[18] A. M. Gabovich and A. I. Voitenko, Phys. Rev. B **60**, 7465 (1999).

[19]A. M. Gabovich and A. I. Voitenko, Fiz. Nizk. Temp. **25**, 677 (1999) [Low Temp. Phys. **25**, 503 (1999)].
[20]C. Panagopoulos, B. D. Rainford, T. Xiang, C. A. Scott, M. Kambara, and I. H. Inoue, Phys. Rev. B **64**, 094514 (2001).
[21]A. A. Zhukov, L. F. Cohen, K. Yates, G. K. Perkins, Y. Bugoslavsky, M. Polichetti, A. Berenov, J. L. M. Driscoll, A. D. Caplin, L. Hao, and J. Gallop, Supercond. Sci. Technol. **14**, L13 (2001).
[22]R. Prozorov, R. W. Giannetta, S. L. Bud'ko, and P. C. Canfield, Phys. Rev. B **64**, 180501 (2001).
[23]B. B. Jin, N. Klein, W. N. Kang, H.-J. Kim, E.-M. Choi, and S.-I. Lee, *cond-mat/0112350*.
[24]Ch. Niedermayer, C. Bernhard, T. Holden, R. K. Kremer, and K. Ahn, Phys. Rev. B **65**, 094512 (2002).
[25]M.-S. Kim, J. A. Skinta, T. R. Lemberger, W. N. Kang, H.-J. Kim, E.-M. Choi, and S.-I. Lee, cond-mat/0201550.
[26]F. Manzano, A. Carrington, N. E. Hussey, S. Lee, A. Yamamoto, and S. Tajima, Phys. Rev. Lett. **88**, 047002 (2002).
[27]F. Manzano and A. Carrington, cond-mat/0106166.
[28]A. Dulcic, D. Paar, M. Po ek, G. V. M. Williams, S. Krämer, C. U. Jung, M.-S. Park, and S-I. Lee, cond-mat/0108071.
[29]G. Lamura, E. Di Gennaro, M. Salluzzo, A. Andreone, J. Le Cochec, A. Gauzzi, C. Cantoni, M. Paranthaman, D. K. Christen, H. M. Christen, G. Giunchi, and S. Ceresara, Phys. Rev. B **65**, 020506 (2002).
[30]A. Andreone, G. Ausanio, E. Di Gennaro, G. Lamura, M. Salluzzo, J. Le Cochec, A. Gauzzi, C. Cantoni, M. Paranthaman, G. Giunchi, and S. Ceresarain, in *Studies of High Temperature Superconductors* **41**, A. V. Narlikar (Ed.), Nova Science, New York (2001), ch. 6.
[31]N. Klein, N. Tellmann, H. Schulz, K. Urban, S. A. Wolf, and V. Z. Kresin, Phys. Rev. Lett. **71**, 3355 (1993).
[32]B. Lorenz, R. L. Meng, Y. Y. Xue, and C. W. Chu, Phys. Rev. B **64**, 052513 (2001).
[33]T. Muranaka, J. Akimitsu, and M. Sera, Phys. Rev. B **64**, 020505 (2001).
[34]W. Liu, J. Huang, Y. Wang, X. Wang, Q. Feng, and S. Yan, Solid State Commun. **118**, 575 (2001).
[35]M. Schneider, D. Lipp, A. Gladun, P. Zahn, A. Handstein, G. Fuchs, S.-L. Drechsler, M. Richter, K.-H. Müller, and H. Rosner, Physica C **363**, 6 (2001).
[36]A. V. Sologubenko, J. Jun, S. M. Kazakov, J. Karpinski, and H. R. Ott, Phys. Rev. B **66**, 014504 (2002).
[37]A. Pimenov, A. Loidl, and S. I. Krasnosvobodtsev, Phys. Rev. B **65**, 172502 (2002).
[38]B. Gorshunov, C. A. Kuntscher, P. Haas, M. Dressel, F. P. Mena, A. B. Kuz'menko, D. van der Marel, T. Muranaka, and J. Akimitsu, Eur. Phys. J. B **21**, 159 (2001).
[39]R. A. Kaindl, M. A. Carnahan, J. Orenstein, D. S. Chemla, H. M. Christen, H.-Y. Zhai, M. Paranthaman, and D. H. Lowndes, Phys. Rev. Lett. **88**, 027003 (2002).
[40]J. H. Jung, K. W. Kim, H. J. Lee, M. W. Kim, T. W. Noh, W. N. Kang, H.-J. Kim, E.-M. Choi, C. U. Jung, and S.-I. Lee, Phys. Rev. B **65**, 052413 (2002).
[41]J. W. Quilty, S. Lee, A. Yamamoto, and S. Tajima, Phys. Rev. Lett. **88**, 087001 (2002).
[42]P. C. Canfield, D. K. Finnemore, S. L. Bud'ko, J. E. Ostenson, G. Lapertot, C. E. Cunningham, and C. Petrovic, Phys. Rev. Lett. **86**, 2423 (2001).
[43]A. K. Pradhan, Z. X. Shi, M. Tokunaga, T. Tamegai, Y. Takano, K. Togano, H. Kito, and H. Ihara, Phys. Rev. B **64**, 212509 (2001).
[44]D. K. Finnemore, J. E. Ostenson, S. L. Bud'ko, G. Lapertot, and P. C. Canfield, Phys. Rev. Lett. **86**, 2420 (2001).
[45]T. Takahashi, T. Sato, S. Souma, T. Muranaka, and J. Akimitsu, Phys. Rev. Lett. **86**, 4915 (2001).
[46]X. K. Chen, M. J. Konstantinoviæ, J. C. Irwin, D. D. Lawrie, and J. P. Franck, Phys. Rev. Lett. **87**, 157002 (2001).
[47]H. J. Lee, J. H. Jung, K. W. Kim, M. W. Kim, T. W. Noh, Y. J. Wang, W. N. Kang, E.-M. Choi, H.-J. Kim, and S.-I. Lee, Phys. Rev. B **65**, 224519 (2002).
[48]J. J. Tu, G. L. Carr, V. Perebeinos, C. C. H. M. Strongin, P. B. Allen, W. N. Kang, E.-M. Choi, H.-J. Kim, and S.-I. Lee, Phys. Rev. Lett. **88**, 277001 (2001).
[49]S. Tsuda, T. Yokoya, T. Kiss, Y. Takano, K. Togano, H. Kito, H. Ihara, and S. Shin, Phys. Rev. Lett. **87**, 177006 (2001).
[50]A. Junod, Y. Wang, F. Bouquet, and P. Toulemonde, in *Studies of High Temperature Superconductors* **38**, A. V. Narlikar (Ed.), Nova Science, New York (2001), p. 179.
[51]F. Bouquet, Y. Wang, R. A. Fisher, D. G. Hinks, J. D. Jorgensen, A. Junod, and N. E. Phillips, Europhys. Lett. **56**, 856 (2001).
[52]F. Laube, G. Goll, H. V. Löhneysen, D. Ernst, and T. Wolf, Europhys. Lett. **56**, 296 (2001).
[53]A. I. Golovashkin and A. N. Lykov, Trudy Fiz. Inst. Akad. Nauk SSSR **190**, 144 (1988).
[54]Y. Wang, T. Plackowski, and A. Junod, Physica C **355**, 179 (2001).
[55]R. K. Kremer, B. J. Gibson, and K. Ahn, cond-mat/0102432.
[56]H. D. Yang, J.-Y. Lin, H. H. Li, F. H. Hsu, C. J. Liu, and C. Jin, Phys. Rev. Lett. **87**, 167003 (2001).
[57]A. A. Abrikosov, *Fundamentals of the Theory of Metals*, North-Holland, Amsterdam (1987).
[58]F. Bouquet, R. A. Fisher, N. E. Phillips, D. G. Hinks, and J. D. Jorgensen, Phys. Rev. Lett. **87**, 047001 (2001).
[59]E. Bauer, Ch. Paul, St. Berger, S. Majumdar, H. Michor, M. Giovannini, A. Saccone, and A. Bianconi, J. Phys.: Condens. Matter **13**, L487 (2001).
[60]A. Sharoni, O. Millo, G. Leitus, and S. Reich, J. Phys.: Condens. Matter **13**, L503 (2001).
[61]A. I. Larkin and Yu. N. Ovchinnikov, Zh. Éksp. Teor. Fiz. **61**, 2147 (1971) [Sov. Phys. JETP **34**, 1144 (1971)].
[62]A. I. Larkin and Yu. N. Ovchinnikov, Zh. Éksp. Teor. Fiz. **61**, 1221 (1971) [Sov. Phys. JETP **34**, 651 (1971)].
[63]I. A. Fomin, JETP Lett. **72**, 66 (2000).
[64]A. V. Sologubenko, J. Jun, S. M. Kazakov, J. Karpinski, and H. R. Ott, Phys. Rev. B **65**, 180505 (2002).
[65]S. V. Shulga, S.-L. Drechsler, H. Eschrig, H. Rosner, and W. Pickett, cond-mat/0103154.
[66]A. Y. Liu, I. I. Mazin, and J. Kortus, Phys. Rev. Lett. **87**, 087005 (2001).
[67]A. A. Golubov, J. Kortus, O. V. Dolgov, O. Jepsen, Y. Kong, O. K. Andersen, B. J. Gibson, K. Ahn, and R. K. Kremer, J. Phys.: Condens. Matter **14**, 1353 (2002).
[68]H. J. Choi, D. Roundy, H. Sun, M. L. Cohen, and S. G. Louie, cond-mat/0111183.
[69]K. Yamaji, J. Phip. Soc. Jpn. **70**, 1476 (2001).
[70]A. Brinkman, A. A. Golubov, H. Rogalla, O. V. Dolgov, and J. Kortus, Phys. Rev. B **65**, 180517 (2002).
[71]E. Bascones and F. Guinea, Phys. Rev. B **64**, 214508 (2001).
[72]A. B. Kuz'menko, F. P. Mena, H. J. A. Molegraaf, D. van der Marel, B. Gorshunov, M. Dressel, I. I. Mazin, J. Kortus, O. V. Dolgov, T. Muranaka, and J. Akimitsu, Solid State Commun. **121**, 479 (2002).
[73]V. A. Moskalenko, M. E. Palistrant, and V. M. Vakalyuk, Usp. Fiz. Nauk **161**, 155 (1991).
[74]V. P. Antropov, K. D. Belashchenko, M. van Schilfgaarde, and S. N. Rashkeev, in *Studies of High Temperature Superconductors* **38**, A. V. Narlikar (Ed.), Nova Science, New York (2001), ch. 5.
[75]H. Rosner, J. M. An, W. Ku, M. D. Johannes, R. T. Scalettar, W. E. Pickett, S. V. Shulga, S.-L. Drechsler, H. Eschrig, W. Weber, and A. G. Eguiluz, in *Studies of High Temperature Superconductors* **38**, A. V. Narlikar (Ed.), Nova Science, New York (2001), ch. 2.
[76]K. D. Belashchenko, M. van Schilfgaarde, and V. P. Antropov, Phys. Rev. B **64**, 092503 (2001).
[77]J. M. An and W. E. Pickett, Phys. Rev. Lett. **86**, 4366 (2001).
[78]P. Seneor, C.-T. Chen, N.-C. Yeh, R. P. Vasquez, L. D. Bell, C. U. Jung, M.-S. Park, H.-J. Kim, W. N. Kang, and S.-I. Lee, Phys. Rev. B **65**, 012505 (2002).
[79]S. Haas and K. Maki, Phys. Rev. B **65**, 020502 (2002).
[80]L. B. Ioffe and A. I. Larkin, Zh. Éksp. Teor. Fiz. **81**, 707 (1981) [Sov. Phys. JETP **54**, 378 (1981)].
[81]Yu. N. Ovchinnikov, S. A. Wolf, and V. Z. Kresin, Phys. Rev. B **63**, 064524 (2001).
[82]H. Won, K. Maki, and E. Puchkaryov, in *High-T_c Superconductors and Related Materials. Material Science, Fundamental Properties, and Some Future Electronic Applications*, S. L. Drechsler and T. Mishonov (Eds.), Kluwer Academic, Dordrecht (2001), p. 375.
[83]J. Q. Li, L. Li, Y. Q. Zhou, Z. A. Ren, G. C. Che, and Z. X. Zhao, cond-mat/0104350.
[84]S. Margadonna, T. Muranaka, K. Prassides, I. Maurin, K. Brigatti, R. M. Ibberson, M. Arai, and M. T. J. Akimitsu, J. Phys.: Condens. Matter **13**, L795 (2001).
[85]Y. G. Zhao, X. P. Zhang, P. T. Qiao, H. T. Zhang, S. L. Jia, B. S. Cao, M. H. Zhu, Z. H. Han, X. L. Wang, and B. L. Gu, Physica C **366**, 1 (2001).
[86]Y. Y. Xue, R. L. Meng, B. Lorenz, J. K. Meen, Y. Y. Sun, and C. W. Chu, Physica C **377**, 7 (2002).
[87]P. Bordet, M. Mezouar, M. Núñez-Regueiro, M. Monteverde, M. D. Núñez-Regueiro, N. Rogado, K. A. Regan, M. A. Hayward, T. He, S. M. Loureiro, and R. J. Cava, Phys. Rev. B **64**, 172502 (2001).
[88]M. A. Krivoglaz, *Diffuse Scattering of X-rays and Neutrons by Fluctua-*

tion Inhomogeneities in Non-ideal Crystals [in Russian], Naukova Dumka, Kiev (1984).
[89]E. L. Nagaev, *Physics of Magnetic Semiconductors* [in Russian], Nauka, Moscow (1979).
[90]J. C. Phillips, Philos. Mag. B **81**, 35 (2001).
[91]L. P. Gor'kov and A. V. Sokol, JETP Lett. **46**, 420 (1987).
[92]S. D. Conradson, J. Mustre De Leon, and A. R. Bishop, J. Supercond. **10**, 329 (1997).
[93]L. P. Gor'kov, J. Supercond. **13**, 765 (2000).
[94]Yu. N. Ovchinnikov, S. A. Wolf, and V. Z. Kresin, J. Supercond. **12**, 125 (1999).
[95]V. V. Struzhkin, A. F. Goncharov, R. J. Hemley, H.-K. Mao, G. Lapertot, S. L. Bud'ko, and P. C. Canfield, cond-mat/0106576.
[96]J. S. Slusky, N. Rogado, K. A. Regan, M. A. Hayward, P. Khalifah, T. He, K. Inumaru, S. Loureiro, M. K. Haas, H. W. Zandbergen, and R. J. Cava, Nature (London) **410**, 343 (2001).
[97]F. Giubileo, D. Roditchev, W. Sacks, R. Lamy, and J. Klein, Europhys. Lett. **58**, 764 (2002).
[98]F. Giubileo, D. Roditchev, W. Sacks, R. Lamy, D. X. Thanh, and J. Klein, Phys. Rev. Lett. **87**, 177008 (2001).
[99]A. Plecenik, S. Benacka, P. K'us, and M. Grajcar, Physica C **368**, 251 (2002).
[100]Yu. G. Naidyuk, I. K. Yanson, L. V. Tyutrina, N. L. Bobrov, P. N. Chubov, W. N. Kang, H.-J. Kim, E.-M. Choi, and S.-I. Lee, cond-mat/0112452.
[101]P. Szabó, P. Samuely, J. Kaèmarcik, T. Klein, J. Marcus, D. Fruchart, S. Miraglia, C. Marcenat, and A. G. M. Jansen, Phys. Rev. Lett. **87**, 137005 (2001).
[102]H. Schmidt, J. F. Zasadzinski, K. E. Gray, and D. G. Hinks, Phys. Rev. Lett. **88**, 127002 (2002).
[103]Y. Bugoslavsky, Y. Miyoshi, G. K. Perkins, A. V. Berenov, Z. Lockman, J. L. MacManus-Driscoll, L. F. Cohen, A. D. Caplin, H. Y. Zhai, M. P. Paranthaman, H. M. Christen, and M. Blamire, Supercond. Sci. Technol. **15**, 526 (2002).
[104]G. Carapella, N. Martucciello, G. Costabile, C. Ferdeghini, V. Ferrando, and G. Grassano, cond-mat/0108212.
[105]A. Sharoni, I. Felner, and O. Millo, Phys. Rev. B **63**, 220509 (2001).

This article was published in English in the original Russian journal. Reproduced here with stylistic changes by AIP.

Fluctuation conductivity in Y–Ba–Cu–O films with artificially produced defects

A. L. Solovjov*

B. Verkin Institute for Low Temperature Physics and Engineering, National Academy of Sciences of Ukraine, 47 Lenin Ave., 61103 Kharkov, Ukraine
Fiz. Nizk. Temp. **28**, 1138–1149 (November 2002)

The fluctuation-induced conductivity (paraconductivity) measured in $YBa_2Cu_3O_{7-\delta}$ (YBCO) films grown on 10° miscut $SrTiO_3$ (001) substrates is analyzed using various theoretical models describing weak fluctuations in high-T_c superconductors and considering both Aslamazov-Larkin and Maki-Thompson fluctuation contributions in the clean limit approach. The analysis reveals a highly anisotropic pair-breaking caused by structural defects produced. This result is in favor of an idea that pseudogap in high-T_c oxydes is mainly governed by the fluctuating pairing. © *2002 American Institute of Physics.* [DOI: 10.1063/1.1528572]

1. INTRODUCTION

The pseudogap (PG) phenomenon in high-T_c superconductors (HTSC) is widely debated at present.[1] Measurements taken with a wide variety of techniques demonstrate that the pseudogap is present in both the spin and charge channel but theoretical views of the problem are still rather controversial. One point of view which stands out in the context of experimental evidence is the idea of preformed pairs[1] considered to be the fluctuating Cooper pairs which are believed to be present in HTSC well above T_c (Refs. 2 and 3). As structural defects are known to deeply affect the pair-breaking mechanism in high-T_c oxides,[2] investigation of the influence of systematically produced structural defects on the fluctuation conductivity is to clarify the issue.

Measurement of the fluctuation conductivity (FC) is known to be a powerful method of getting reliable information about the normal charge scattering and superconducting coupling mechanisms in HTSC just in the PG temperature region.[4–11] Using FC analysis, such microscopic parameters as the coherence length along the c axis, $\xi_c(0)$, and the phase relaxation time of fluctuating pairs, $\tau_\varphi(100\ \mathrm{K})$, can be determined. It also gives the possibility to address more fundamental issues, such as the contribution from or absence of Maki-Thompson (MT) type fluctuations.[12] The question is of remarkable importance, since the MT fluctuation process is strongly dependent on the pairing mechanism.[12,13]

Fluctuation conductivity, $\sigma' = \sigma(T) - \sigma_N(T)$, arises from excess current carried by fluctuation-created Cooper pairs above the superconducting transition temperature T_c, as has been shown by Aslamazov and Larkin (AL).[14] The additional contribution to FC, introduced by Maki and Thompson[12] to extend the AL theory, is treated as arising from interaction of the fluctuating Cooper pairs with normal electrons resulting in the pair-breaking process. Finally, the fluctuation conductivity is taken to be

$$\sigma'(T) = [\rho_N(T) - \rho(T)]/[\rho_N(T)\rho(T)], \tag{1}$$

where $\rho(T) = \rho_{xx}(T)$ is the actually measured longitudinal resistivity and $\rho_N(T) = \alpha T + b$ is the extrapolated normal-state resistivity. According to the nearly antiferromagnetic Fermi liquid (NAFL) model,[15] the linear-in-T $\rho_{xx}(T)$ dependence at high temperatures can be considered as a true sign of the normal state of the system, a state which is characterized by stability of the Fermi surface and, hence, by stability of the normal-carrier scattering rate. As T is lowered, $\rho_{xx}(T)$ deviates downward from the T-linear dependence at some representative temperature $T_{*0} \gg T_c$, giving rise to the excess conductivity which is usually considered as a pseudogap.[1,15] However, in the temperature interval $T_c < T < T_{c0}$, the excess conductivity is well described by the conventional fluctuating theories[12–14] and is usually treated as $\sigma'(T)$.[4–10,16] $T_{c0} = (100 \pm 5)$ K is the temperature which determines the pair-breaking parameter $\delta_{\mathrm{th}} = (T_{c0} - T_c)/T_c$ (Refs. 12 and 13). The possibility of the fluctuating pairing in HTSC at $T_{c0} < T < T_{*0}$ is widely debated at present.[1–3]

As we have recently shown,[16] the $\sigma'(T)$ dependence of well-structured optimally doped (OD) and strongly underdoped (UD) YBCO films always consists of two temperature regions with different FC behavior, separated by the dimensional crossover at T_0. Accordingly, above T_0 this is the two-dimensional (2D) fluctuation region commonly described by the MT term of the Hikami-Larkin theory (HL),[13] and at $T_c < T < T_0$ it is the region of three-dimensional (3D) fluctuations always described by the 3D term of the AL theory.[14] The Lawrence-Doniach (LD) model,[17] proposed to describe FC in any layered superconducting system, was found to fail in fitting experiment in this case. Really, the LD model predicts a smooth, gradual transition from 2D AL fluctuation behavior to 3D AL behavior as the temperature approaches T_c, and it considers the MT contribution to be vanishing. This kind of FC behavior has been shown to be typical for badly structured high-T_c oxides.[2] However, in most of the previous papers devoted to the problem, FC fitted by the LD model alone is reported,[4–9] suggesting the presence of different structural defects in the samples studied. The conclusion is corroborated by measurements of the critical current densities j_c of thin epitaxial YBCO films, which are known to be at least an order of magnitude larger than that for high-quality YBCO single crystals.[18] The main reason for that is strong flux pinning in the films caused by specific defects such as point defects in the CuO_2 planes,[19] screw dislocations,[20] and twin boundaries,[21] expected to be also responsible for observed $\sigma'(T)$ dependence of the LD type. However, the properties of high-quality modern thin

TABLE I. The sample parameters.

Sample	d_0, Å	T_c, K	ΔT, K	T_c^{mf}, K	ρ(100K), $\mu\Omega\cdot$cm	ρ(300K), $\mu\Omega\cdot$cm	$d\rho/dT$, $\mu\Omega\cdot\text{cm}\cdot\text{K}^{-1}$	T_{*0}, K
M23-**L**	1975	90.0	1.0	90.14	88	287	0.93	130
M23-**T**	1900	89.9	1.2	90.19	278	628	1.6	108
M35-**L**	900	89.7	2.0	90.60	204	600	1.86	150
M35-**T**	900	89.5	2.2	90.85	1948	3325	6.06	105

epitaxial HTSC films prepared by pulsed laser deposition[22] are believed to be mostly determined by some slight degree of miscut growth of the films, resulting in the appearance of specific growth-related defects.[23,24] These defects have been identified as effective pinning centers[23] and have been found to produce an appreciable anisotropy of the resistivity, magnetic flux penetration, and critical current densities in miscut-grown YBCO films.[24] However, a systematic study of the effect of specific growth-related defects on the fluctuating pairing in HTSC is still lacking.

In this paper we presented measurements of the fluctuation conductivity in the *c*-axis-oriented $YBa_2Cu_3O_{7-\delta}$ (YBCO 123) films grown on 10° miscut $SrTiO_3$ (001) substrates. The expected strong anisotropy of the scattering of the fluctuating pairs due to growth-related defects influence is revealed. The results are treated using a recently developed approach to FC analysis in YBCO films.[2,16]

2. EXPERIMENTAL TECHNIQUES

YBCO films with a thickness of 240 to 2400 Å were grown on vicinal $SrTiO_3$ (001) substrates by pulsed laser deposition (PLD) as described in detail in Ref. 24. The $SrTiO_3$ substrates were cut and polished 10° off the (001) plane towards [010], as confirmed by Laue diffraction. After the PLD process the deposition chamber was pumped to a pressure of less than 10^{-7} mbar and the samples were transferred to the scanning tunneling microscopy (STM) stage without exposure to air. To provide measurements of expected resistivity anisotropy the samples were patterned in two different directions. These two directions are denoted in the text by **L** and **T**, respectively, since they coincide with the directions longitudinal to and transverse to the film step edges. To get the resistivity data, standard 4-probe dc measurements were performed using a fully computerized setup. It should be emphasized that a certain care in the sample preparation process enables to obtain highly reliable and systematic data despite the evident complexity of the samples' structure.

Combined STM and cross-sectional transmission electron microscopy (TEM) measurements established a close relationship between the film morphology and defect microstructure.[24] It has been shown that almost periodic surface and defect structure is generated for YBCO films grown on 10° miscut $SrTiO_3$ substrates. The TEM image has revealed a significantly disturbed YBCO lattice. The step structure persists on the YBCO surface due to the step flow growth mechanism. This generates a multitude of translational boundaries (TB), extending throughout the entire film thickness. The crystal lattice is slightly tilted across the defects. Numerous stacking faults (SF) are also created, resulting in a general waviness of the unit-cell-high layers as observed in the TEM image. A strong strain field is associated with this specific defect structure. Some extended defects (ED) with a structural width of 20–30 Å, penetrating most of the film thickness, are also present. All defects, and especially TB, are found to contribute to the strong flux pinning in the films. It has also been shown[24] that the close correspondence between the STM and TEM results suggests that most defects are aligned along the direction **L** of the regular film step edges. This one-dimensional nature of the defects is found to be responsible for observed anisotropy of the resistivity, magnetic flux penetration, and critical current densities.[24] Naturally, one can expect to reveal an anisotropy of the pair-breaking mechanism in the films, resulting in the anisotropy of the fluctuation conductivity. If pseudogap in high-T_c oxides is really governed by the fluctuating pairing different temperature regions of the PG behavior have to be observed, depending on whether measurements are performed in the **L** or in **T** direction.

3. RESULTS AND DISCUSSION

3.1. Transport properties

To obtain more information, two films with different thicknesses commonly used in experiment, $d_0 = 1900$ Å (sample M23) and $d_0 = 900$ Å (sample M35), were chosen for analysis. Both films exhibit a sharp resistive transition at $T_c \approx 90$ K in both directions (see Table I), i.e., can be considered as apparent representatives of OD YBCO systems. Figure 1 shows ρ_{xx} as a function of temperature for sample M23 measured in the **L** and **T** directions, respectively. As can be readily seen, $\rho_{\mathbf{T}}(100\text{ K})/\rho_{\mathbf{L}}(100\text{ K}) \approx 3.2$ in this case. Moreover, a value $\rho_{\mathbf{T}}(100\text{ K})/\rho_{\mathbf{L}}(100\text{ K}) \approx 9.5$ is measured for sample M35, suggesting the strong influence of the growth-related defects on the normal charges scattering. However, despite the considerable increase of the resistivity, the width of the resistive transition $\Delta T \approx 1.2$ K is estimated for M23 in both directions (Table I), a value typical for well-characterized OD systems. The representative temperature $T_{*0\mathbf{L}}$, marked by the arrow on the graphs, is also found to be in good agreement with the prediction of the NAFL model for OD films. According to the NAFL model, the **T**-linear resistivity above T_{*0}, extrapolated towards T_c (as shown by the dashed lines in the figure), is treated as the sample normal-state resistivity $\rho_N(T)$ used to determine $\sigma'(T)$ from Eq. (1). However, resistivity buckling, which is uncharacteristic of OD systems, is distinctly observed for both samples at higher temperatures (Fig. 1). The result suggests the presence of a somewhat enhanced electron-electron interaction in the films,[15] likely caused by the defect structure.

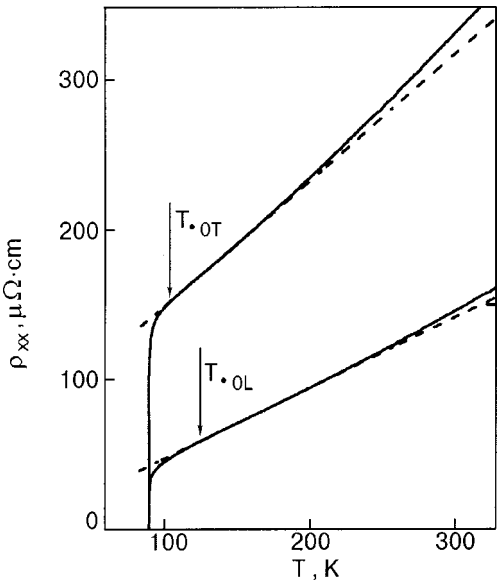

FIG. 1. Resistivity as a function of temperature for sample M23 measured in the **L** and **T** direction; the dashed lines in the extrapolated normal-state resistivity.

But the most striking result is the fact that measured for both films representative temperatures $T_{*0\mathbf{L}}$ and $T_{*0\mathbf{T}}$ appear to be noticeably different (Fig. 1 and Table I). As it is clearly seen from the figure, the larger resistivity, the shorter is the **T**-linear resistivity region but the shorter becomes the PG temperature range too, what is difficult to explain in terms of the normal charges scattering only. To account for the finding, measurements of FC, sheding light on the fluctuating pairing, are evidently required.

3.2. Fluctuation conductivity

3.2.1. Theoretical overview

The fluctuation conductivity $\sigma'(T)$ is computed from the resistivity measurements (Fig. 1) using Eq. (1), as discussed above. The experimental FC data are analyzed using the HL theory,[13] considering both the AL and MT fluctuation contributions. In the absence of magnetic field **H** the AL theory yields

$$\sigma'_{AL}=[e^2/(16\hbar d)](1+2\alpha)^{-1/2}\varepsilon^{-1} \tag{2}$$

and

$$\sigma'_{MT}=\frac{e^2}{8\hbar d(1-\alpha/\delta)} \times\ln\left\{\frac{(\delta/\alpha)[1+\alpha+(1+2\alpha)^{1/2}]}{[1+\delta+(1+2\delta)^{1/2}]}\right\}\varepsilon^{-1}, \tag{3}$$

where $d\approx 11.7$ Å is the distance between conducting CuO_2 planes, $\alpha=2\xi_c^2(T)/d^2=2[\xi_c(0)/d]^2\varepsilon^{-1}$ is a coupling parameter,

$$\delta=1.203(l/\xi_{ab}(0))(16/\pi\hbar)[\xi_c(0)/d]^2k_BT\tau_\varphi \tag{4}$$

is a pair-breaking parameter, and $\varepsilon=\ln(T/T_c^{mf})\approx(T-T_c^{mf})/T_c^{mf}$ is a reduced temperature. Here $T_c^{mf}>T_c$ is the critical temperature in the mean-field approximation actually separating the FC region from the critical fluctuation region. The factor $1.203(l/\xi_{ab}(0))$ [Eq. (4)] is introduced by Bieri, Maki, and Thompson (BMT),[25] who have extended the HL theory to incorporate the clean limit approximation. This seems to be reasonable, as the mean free path $l>\xi_{ab}(0)$ for YBCO systems, where $\xi_{ab}>\xi_c$ is the intraplane coherence length. But when $\mathbf{H}=0$ the only difference with the HL theory is that $\delta_{BMT}=1.203(l/\xi_{ab}(0))\delta_{HL}$, assuming that nonlocal effects can be ignored.[25]

Actually, Eq. (2) reproduces the result of the LD model,[17] with allowance for the presence of Josephson-like pair tunneling between conducting layers,[26] which is mainly pertinent to the 3D region, as $\xi_c(T)>d$ near T_c. Accordingly, the MT contribution gains importance at $k(T-T_c^{mf})\gg\hbar/\tau_\varphi$ (Ref. 13), where no intraplane tunneling is expected, as $\xi_c(T)<d$ (2D region).[10,26] Thus the HL theory predicts both 2D-3D and MT-LD crossovers as the temperature approaches T_c. The 2D-3D crossover should occur at the temperature

$$T_0=T_c\{1+2[\xi_c(0)/d]^2\} \tag{5}$$

at which $\alpha=1/2$, i.e., $\xi_c(0)=(d/2)\varepsilon_0^{1/2}$. The MT-LD crossover should occur at the temperature

$$\varepsilon_0=(\pi\hbar)/[1.203(l/\xi_{ab}(0))(8k_BT\tau_\varphi)], \tag{6}$$

where $\delta\approx\alpha$, and this gives an opportunity to estimate τ_φ. No significant difference between the two crossover temperatures is considered.[13] In contrast to the HL theory, the 3D fluctuation region in well-structured YBCO films[16] has been found to be described by the 3D term of the AL theory,[14]

$$\sigma'_{AL}=\{e^2/[32h\xi_c(0)]\}\varepsilon^{-1/2}. \tag{7}$$

No LD fluctuation mechanism is observed in this case, as was mentioned above. It is clear on physical grounds that with increasing temperature the 3D fluctuation regime will persist until $\xi_c(T)\geqslant d$.[16] Hence, in this case the 2D-3D crossover should occur at $\xi_c(T)\approx d$ or at

$$\xi_c(0)\approx d\varepsilon_0^{1/2}, \tag{8}$$

which is twice as large as predicted by the LD and HL theories [Eq. (5)]. Besides, the crossover at T_0 proves to be of the MT-AL type.[16]

Actually, Eq. (7) depends only on $\xi_c(0)$, which is independently determined by the measured value of ε_0 [Eq. (8)], thus noticeably reducing the number of fitting parameters. However, τ_φ [Eq. (6)] still remains uncertain, since neither l nor $\xi_{ab}(0)$ is directly measured in the FC experiment. To circumvent this problem we have designated $1.203(l/\xi_{ab}(0))=\beta$.[16] As before, to further evaluate $\tau_\varphi(100\text{ K})$ it is assumed that $\tau_\varphi(T)\sim 1/T$ and $\tau_\varphi T=\text{const}$.[7,15,16,27] Hence, Eq. (6) can be rewritten as follows:

$$\tau_\varphi\beta T=\pi\hbar/(8k_B\varepsilon_0)=A\varepsilon_0^{-1}, \tag{9}$$

where $A=\pi\hbar/(8k_B)=2.988\times10^{-12}$ s. Now the parameter $\tau_\varphi(100\text{ K})\beta$ is strictly determined by the measured value of ε_0 and can be used in the fitting procedure together with $\xi_c(0)$. Besides $\delta_{\text{th}}(\varepsilon_0)=2$ (Eq. (4)). Thus, the only fitting parameter now remains a *C*-factor introduced to take into account the structural imperfection of the sample.[5] But in contrast to Oh *et al.*,[5] we introduce *C* as a factor by which Eqs. (2), (3) and (7) must be multiplied to fit the experimen-

tal data. It is clear that the farther C is from 1, the more influence of defects is expected.[2] However, independently of the measured values of the C factors, the ratio $C^* = C_{3D}/C_{2D} = (1.82 \pm 0.2)$ was found for all well-structured YBCO films with different oxygen concentration,[2,16] as a result of the layered nature of HTSC.

Compared to OD YBCO films, the MT fluctuation mechanism in films with $T_c \leqslant 82$ K (so-called 80-kelvin samples) is somewhat suppressed and partly substituted by the LD one because of the appearance of structural defects mostly produced by oxygen vacancies in the CuO chains, as described in detail in Ref. 2. The more defects, the more pronounced is the LD part of the $\sigma'(T)$ dependence and the greater is the suppression of the MT contribution. Nevertheless, the $\sigma'(T)$ dependence near T_c is still described by the 3D term of the AL theory [Eq. (7)]. Naturally, $\sigma'(T)$ exhibits two dimensional crossovers in this case but just the second LD-AL (3D) crossover at ε_0 has been shown to determine $\xi_c(0)$ and $\tau_\varphi(100\text{ K})\beta$ in 80-kelvin samples.[2]

3.2.2. Fluctuation conductivity analysis

Outside the critical region $\sigma'(T)$ is a function of $\varepsilon \approx (T - T_c^{mf})/T_c^{mf}$ only. Thus the determination of T_c^{mf} is of primary importance to the determination of $\sigma'(T)$. As before,[2,16] T_c^{mf} is defined by extrapolating the linear 3D region of the σ'^{-2} vs T plot down to the **T** axis, since $\sigma'(T)$ should diverge as $(T - T_c^{mf})^{-1/2}$ [Eq. (7)] as T approaches T_c^{mf}. Figure 2 shows $\sigma'^{-2}(T)$ for samples M23 and M35 measured in the **L** and **T** directions. As expected, the each plot is characterized by a pronounced 3D region fitted by the straight line to determine T_c^{mf}. Above T_0 the data measured for M23-**L** (Fig. 2a dots) and the data measured for both samples in the **T** direction (Fig. 2a and 2b, circles) deviate to the left from the line. The fact means the absence of any MT fluctuation mechanism in this case.[16] On the other hand, the data measured for M35-**L** (Fig. 2b, dots) demonstrate an evident rightward deviation from the line at T_0, thus suggesting the presence of the MT fluctuation mechanism in the sample in the latter case. But, strictly speaking, the deviation is relatively small in comparison with the well-structured OD films.[16] But the more striking result is the fact that the 3D region measured for M23-**T** turns out to be extremely short (Fig. 2a, circles), resulting in $T_{0\mathbf{L}} - T_{0\mathbf{T}} \approx 0.9$ K (Fig. 2a). Possible reasons for this finding will be discussed below.

Figure 3a shows a plot of the $\ln\sigma'$ vs $\ln\varepsilon$ (dots) for sample M23-**L** in comparison with the LD term of the HL theory [Eq. (2)] (curve *2*) and the 3D term of the AL theory (Eq. (7)) (curve *3*), as no MT fluctuation contribution is expected (Fig. 2a). The LD-AL (3D) crossover, marked by the arrow on the figure, is distinctly seen on the plot at $\ln\varepsilon_0 \approx -3.98$ ($T_0 \approx 91.83$ K). Now the values $\xi_c(0) \approx (1.6 \pm 0.01)$ Å and $\tau_\varphi(100\text{ K})\beta \approx 16.03 \times 10^{-13}$ s can easily be determined using the measured ε_0 and Eqs. (8) and (9), respectively. The two parameters found enable us to reasonably fit the data in the whole temperature region of interest (Fig. 3a). Besides, the value $\delta_{\text{th}}(\varepsilon_0) \approx 2$ is computed using Eq. (4), in good agreement with the above theoretical consideration. It has been established[16] that $\delta_{\text{th}}(\varepsilon_0) = 2$ only when ε_0, which determines both $\xi_c(0)$ and $\tau_\varphi(100\text{ K})\beta$, is properly chosen. This criterion plays a significant role in the fitting procedure, especially when no MT contribution is observed.

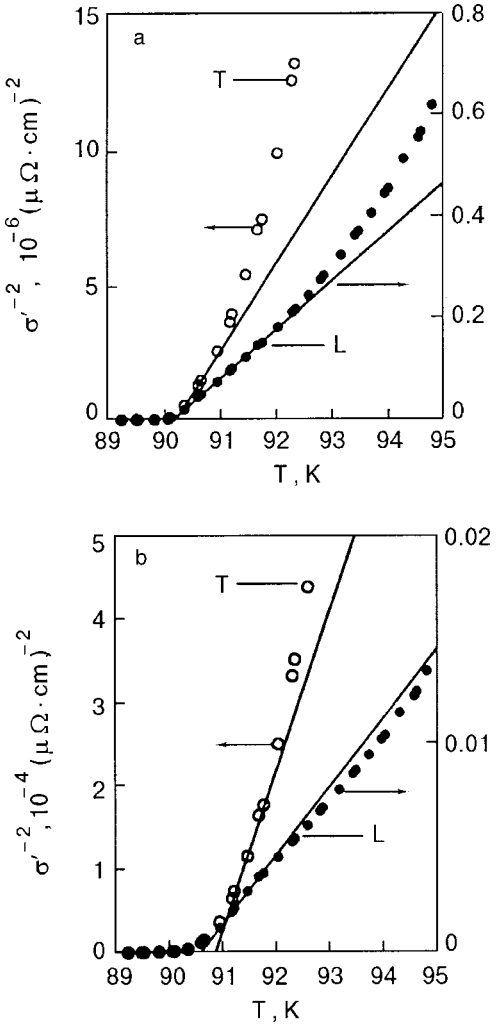

FIG. 2. σ'^{-2} vs T for samples M23 (a) and M35 (b) measured in the **L** (dots) and **T** (circles) direction, respectively; the solid lines is extrapolated 3D fluctuation regions.

Above T_0 the LD term with $C_{\text{LD}} = 0.82$ perfectly fits the data up to $\ln\varepsilon_{c0} \approx -2.98$ ($T_{c0} \approx 94.72$ K) (Fig. 3a, curve *2*). In accordance with the analysis for the 80-kelvin samples,[2] observation of a fluctuation mechanism of the LD type can be considered as an evident sign of structural imperfection of a sample. Thus there should be a scatter of the intraplane distances in the sample even in the **L** direction as a result of the influence of defects throughout the relatively thick film. This conclusion is in good agreement with the results of the defect microstructure study discussed above. Simple algebra yields $d^* = \xi_c(0)/\varepsilon_{c0}^{1/2} \approx 7.2$ Å, and, as before, $d = 11.7$ Å at ε_0 is assumed.[2] Thus, the scatter appears to be just the same as had been found for 80-kelvin films.[2] Whether this is a coincidence or not has yet to be settled.

Below T_0 the LD model fails to fit the data because there is a rather pronounced linear 3D fluctuation region here, perfectly described by the 3D term of the AL theory with $C_{3D} = 0.73$ (Fig. 3a, curve *3*). Thus, the observed crossover at T_0 is just of the LD-AL(3D) type expected to be responsible for the parameters of fluctuation analysis in the presence of

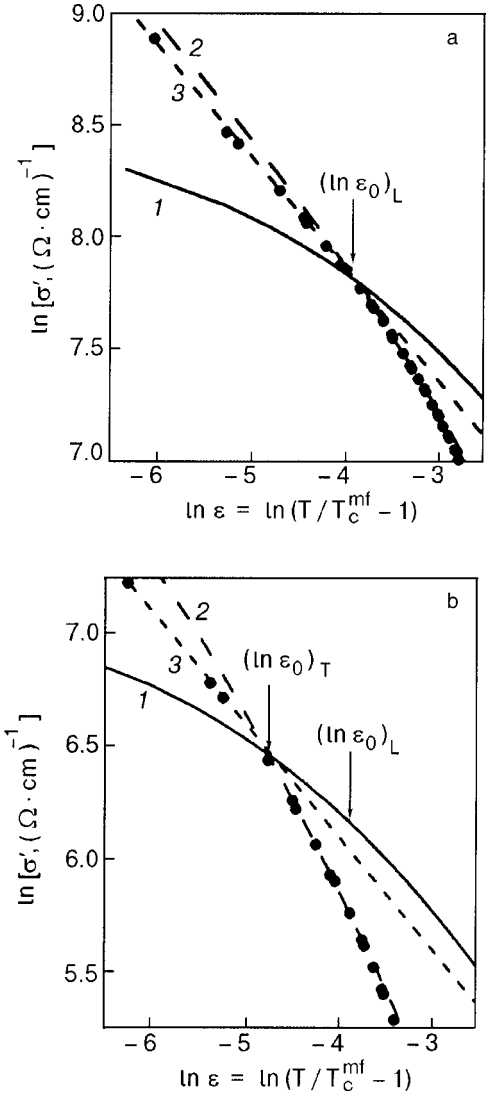

FIG. 3. a—ln σ' vs ln ε (dots) for sample M23-**L** ($T_c^{mf}=90.14$ K) compared with fluctuation theories: curve *1*—MT term ($C_{2D}=0.401$, $d=11.7$ Å), *2*—LD term ($C_{LD}=0.82$, $d=11.7$ Å), *3*—AL(3D) term ($C_{3D}=0.73$). b—ln σ' vs ln ε (dots) for sample M23-**T** ($T_c^{mf}=90.19$ K) compared with fluctuation theories: curve *1*—MT term ($C_{2D}=0.07$, $d=17.34$ Å), *2*—LD term ($C_{LD}=0.178$, $d=35$ Å), *3*—AL(3D) term ($C_{3D}=0.127$).

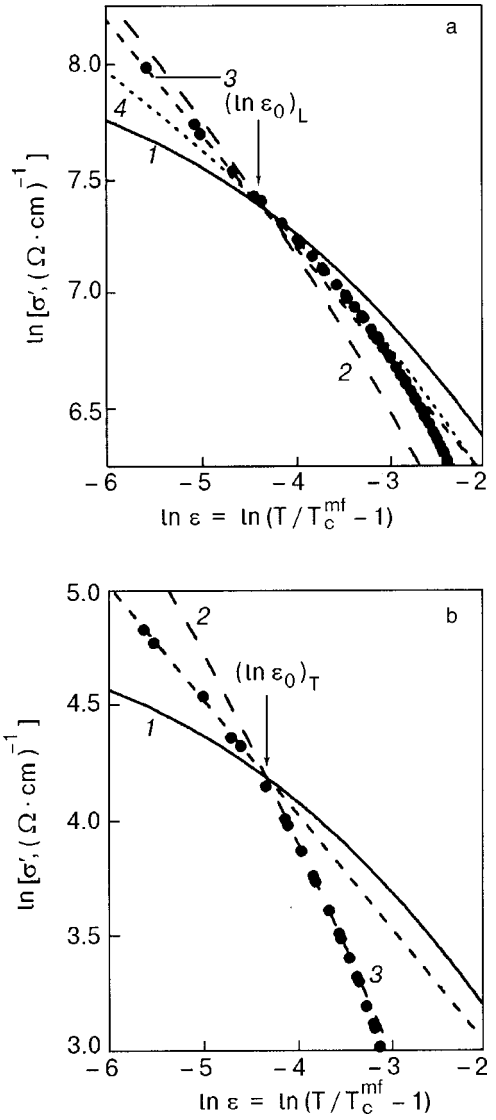

FIG. 4. a—ln σ' vs ln ε (dots) for sample M35-**L** ($T_c^{mf}=90.60$ K) compared with fluctuation theories: curve *1*—MT term ($C_{2D}=0.172$, $d=11.7$ Å), *2*—LD term ($C_{LD}=0.353$, $d=11.7$ Å), *3*—AL(3D) term ($C_{3D}=0.31$), *4*—MT+LD term ($C=0.116$, $d=11.7$ Å). b—ln σ' vs ln ε (dots) for sample M35-**T** ($T_c^{mf}=90.85$ K) compared with fluctuation theories: curve *1*—MT term ($C_{2D}=0.00714$, $d=11.7$ Å), *2*—LD term ($C_{LD}=0.0238$, $d=35$ Å), *3*—AL(3D) term ($C_{3D}=0.013$).

defects.[2] For more assurance the MT term calculated using the found values for $\xi_c(0)$ and $\tau_\varphi(100\text{ K})\beta$ is also plotted (Fig. 3a, curve *1*). As expected,[2] when drawn with $C_{2D}=C_{3D}/1.82\approx0.401$, it intersects the data just at the crossover point, accordingly marked as $\ln\varepsilon_0$ on the graph. This result once again confirms the universality of the $C^*=1.82\pm0.2$ ratio for the high-T_c oxides.[2] Nevertheless, the real MT fluctuation mechanism is completely suppressed here, being replaced by the LD one because of the presence of growth-related defects. The result of the structural imperfection is the observed diminution of the C_{3D} factor, expected to be close to 1 for well-structured OD YBCO systems.[16] We think that the $\sigma'(T)$ dependence found without any MT contribution but with clear LD-AL(3D) crossover appears to be typical for YBCO films with highly ordered defects. When defects are randomly distributed in the sample the crossover is never observed. In the latter case the data are traditionally fitted using the LD model alone,[4–9] as was mentioned above.

Despite the fact that the set of defects in sample M35 was found to be the same,[24] the FC behavior measured for sample M35-**L** appears to be rather different. Figure 4a shows a ln σ' vs ln ε plot (dots) for sample M35-**L** compared with the theory in the established manner. Here the 3D region is somewhat shorter and the crossover at $\ln\varepsilon_0\approx-4.39$ $\times(T_0\approx91.72$ K) becomes clear only when the corresponding theoretical curves are properly drawn. Using the measured ε_0, the values $\xi_c(0)=(1.3\pm0.01)$ Å, $\tau_\varphi(100\text{ K})\beta\approx24.24\times10^{-13}$ s, and $\delta_{th}(\varepsilon_0)\approx2$ can easily be derived from the experiment. The parameters found enable one to reasonably fit the data in the whole temperature region of interest (Fig. 4a). As before, the 3D fluctuation region near T_c is well described by the 3D AL term (Fig. 4a, curve *3*) with $C_{3D}\approx0.31$. However, above T_0 the fitting process turns out to be more complicated than before. As can be easily seen from the figure, the LD term (curve *2*), reduced to the crossover temperature, does not fit the data in any tempera-

ture region. To complete the analysis the MT term, calculated using the values for found $\xi_c(0)$ and $\tau_\varphi(100\,\mathrm{K})\beta$, is traditionally plotted (Fig. 4a, curve *1*). As before, when drawn with $C_{2D}=C_{3D}/1.82\approx 0.172$, it also intersects the data just at the crossover point. But in spite of the fact that the presence of the MT fluctuation contribution is evident from Fig. 2b, the MT term also does not meet the case. Actually, all three theoretical mechanisms evidently fail to fit the data in the 2D fluctuation region. In the end, all the way up to $\ln\varepsilon_{c0}\approx -3.15$ ($T_{c0}\approx 94.48$ K), the data are found to be well fitted by the summary curve MT+LD (Fig. 4a, curve *4*).

Fluctuation behavior of the MT+LD type but without crossover, likely overlooked by the authors, is reported for single crystals[7] and some YBCO films.[9] Thus a certain amount of the growth-related defects, likely produced by twins[7] or a slight degree of substrate miscut,[9] has to be present in the samples. In our case the structural imperfection is apparently much stronger because of using the specific 10° miscut substrates, as is confirmed by the very small values of the C factors measured in the experiment. Besides, ΔT and $\rho(100\ \mathrm{K})$ are about 2.2 times the value found for M23-**L**, whereas the ratio $\rho_{\mathbf{T}}(100\,\mathrm{K})/\rho_{\mathbf{L}}(100\,\mathrm{K})$ is 3 times larger, respectively (Table I). All these facts evidently indicate the enhanced role of the defects in the sample. That is why even the partial observation of the MT fluctuation contribution here turns out to be somewhat controversial.

At first sight the observed $\sigma'(T)$ dependence of the MT+LD type is difficult to explain in terms of the FC approach discussed here. Indeed, as is well established now,[2] the MT fluctuation mechanism gains importance in the distinct 2D fluctuation region and requires CuO_2 planes to be intact and regularly situated with an intraplane distance $d\approx 11.7\ \text{Å} > \xi_c(T)$, whereas the LD mechanism is found to be typical for samples with a noticeable spread of the intraplane distances and somewhat deteriorated planes. Thus, one would have to assume that the growth-related defects result in some very specific sample structure, in which both the MT and LD fluctuation mechanisms are able to exist in parallel when measurements are performed in the **L** direction. As follows from a structural analysis,[24] the sample surface looks like a remarkably regular, row-like terrace structure. The observed FC behavior makes it sure that between the rows the planes are presumably fully intact, giving rise to the MT fluctuation contribution. On the other hand, the planes are expected to be badly deteriorated on the tops of the rows. These parts of the sample are to be responsible for the appearance of the LD fluctuation mechanism. Despite the fact that the measurements are carried out in the **L** direction, the measuring current should evidently pass through both sample regions discussed, giving rise to the observed MT+LD combined fluctuation behavior (Fig. 4a, curve *4*). Thus, influence of the defects appears to be rather specific in this case. With increasing sample thickness (e.g., for the sample M23-**L**) the regions with mixed planes are likely to overlap. Naturally, no MT fluctuation mechanism will be observed in this case (Fig. 3a). Whether or not the difference in the FC behavior found for the miscut-grown films is really due solely to the more than twofold difference in the samples thickness has yet to be settled.

Unfortunately, miscut-grown films for Hall effect measurements have not been prepared. As a result, the absolute value of $\beta\sim l/\xi_{ab}(0)$ remains unknown, giving us no possibility of directly deriving the explicit value of $\tau_\varphi(100\,\mathrm{K})$ from experiment. However, for sample M23-**L** there is an evident correlation between the ratio $T_c(\text{M23-}\mathbf{L})/T_c(\text{F1})=1.03$ and $\xi_c(0)(\text{F1})/\xi_c(0)(\text{M23-}\mathbf{L})=1.031$, respectively, suggesting that the value found for $\xi_c(0)$ is in good agreement with the conventional superconducting theory[28] as to the relationship between ξ and T_c:

$$\xi_0\sim\hbar v_F/[\pi\Delta(0)], \tag{10}$$

where v_F is the Fermi velocity and $\Delta(0)$ is the order parameter at $T=0$ K (F1 is the well-structured YBCO film with $T_c=87.8$ K (Ref. 16), considered to be the principal sample). Assuming $\xi_0=\xi_c(0)$ and taking into account that $2\Delta(0)\approx 5k_BT_c$ for YBCO systems,[29] one can rewrite Eq. (10) as $\xi_c(0)=G/T_c$, where $G=2K\hbar v_F/(5\pi k_B)$ and $K\approx 0{,}12$ is the coefficient of proportionality. A plot of $\xi_c(0)$ as a function of T_c is shown in Fig. 5 (solid line) for the value $G=1.46\times 10^{-6}$ Å·K computed for F1 (Ref. 2). The dots are the experimentaly measured $\xi_c(0)$ values for samples M23, M35, and four YBCO films with different oxygen concentrations (samples F1-F6 from Refs. 2 and 16). With increasing T_c the value $\xi_c(0)$ gradually decreases in accordance with the theory (Fig. 5, dots), thus clearly suggesting the conclusion that the coupling mechanism of high-T_c superconductivity to a certain degree follows the conventional superconducting theory. At the same time the parameter $\tau_\varphi(100\,\mathrm{K})\beta$, computed for the same samples, is found to be a linear function of T_c (Fig. 5, circles). All the data are normalized to the value $\tau_\varphi(100\,\mathrm{K})\beta\approx 5.9\times 10^{-13}$ s for sample F6 (Ref. 16) in this case in order to make scales coinside. Since both $\xi_c(0)$ and $\tau_\varphi(100\,\mathrm{K})\beta$ are determined solely by ε_0, which is strictly determined by the crossover, the dependences found appear to be an inherent property of YBCO high-T_c oxides. As is clearly seen from the figure, sample M23-**L** perfectly matches both dependences shown at the highest temperature, in this way playing the role of the real OD system.

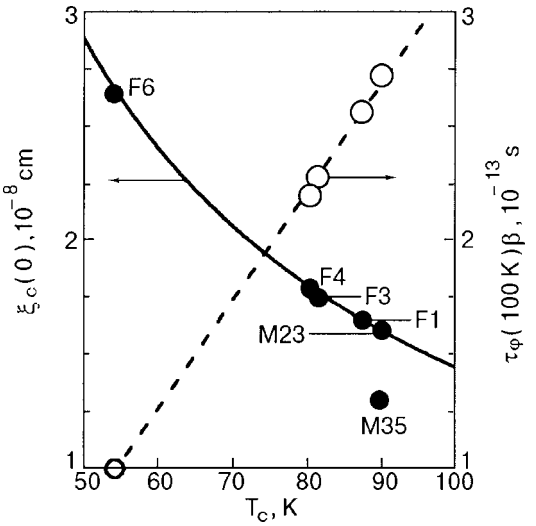

FIG. 5. $\xi_c(0)$ as a function of T_c (dots); the solid line represents the theory. Circles—$\tau_\varphi(100\,\mathrm{K})\beta$ vs T_c; the dashed line is a guide for the eye.

Summarizing the facts, it seems to be rather reasonable to ascribe to M23-**L** the same $\tau_\varphi(100\,\mathrm{K})\approx 3.35\times 10^{-13}$ s as

was found for all other films.[16] The assumption could explain the fact that no significant diminution of the PG region is observed in this case (Fig. 1). Taking found τ_φ into account one can easily derive the value $\beta \approx 4.785$ from the measured $\tau_\varphi(100\ \mathrm{K})\beta$. Since $\xi_{ab}(0) = 13$ Å for F1,[16] the values $\xi_{ab}(0) = 13/1.03 = 12.62$ Å and $l = \xi_{ab}(0)\beta/1.203 = 51.7$ Å can easily be obtained for M23-**L**. Both calculated β and l are in good agreement with the FC analysis,[16] for which evident increase of β and l with increasing T_c is observed. The result evidently confirms the assumption and suggests the conclusion that the fluctuating coupling mechanism in HTSC, leading to the appearance of fluctuation conductivity, has the same physics for all samples studied. But, on the other hand, the result looks somewhat surprising in view of the expected influence of the defects on the sample structure, and the estimated $l \approx 51.7$ Å looks suspiciously large for the same reason. To avoid this problem one would have to assume that influence of the growth-related defects on the scattering of the normal charge carriers (which is responsible for the resistivity) and on the fluctuating pairing (which determines T_c) is not very considerable here, at least when measurements are performed in the **L** direction. This conclusion seems reasonable since sample M23-**L** has the lowest resistivity, the highest T_c, and relatively large values of the C factors as compared to the samples F1-F6.[2,16] Besides, the resistive transition is very narrow (Table I) and, additionally, found $T_{*0} \approx 130$ K is very close to that predicted by the NAFL theory for OD YBCO systems.[15] The only exception is the absence of a clear MT fluctuation mechanism, which unexpectedly turns out to be the only evidence of the presence of defects in this case.

Strictly speaking, both $\xi_c(0)$ and $\tau_\varphi(100\ \mathrm{K})\beta$ found for M35 are not inconsistent with the dependences shown in Fig. 5. However, as it is easily seen from the figure, the absolute values of the parameters evidently do not match any of the plots shown. Especially $\tau_\varphi(100\ \mathrm{K})\beta \approx 24.24 \times 10^{-13}$ s proves to be extremely large. As a result, there are no reasonable assumptions as to how to get credible values of β and $\tau_\varphi(100\ \mathrm{K})$ in this case. Nevertheless, $\tau_\varphi(100\ \mathrm{K})$ is expected to be rather high. As a result, the PG temperature region determined by the measured $T_{*0\mathbf{L}} \approx 150$ K is the same as usually observed for OD YBCO films.[3,9]

As expected, results of the FC measurements, obtained from the **T**-direction experiment, appear to be noticeably different. Figure 4b shows a plot of $\ln\sigma'$ vs $\ln\varepsilon$ (dots) for the sample M35-**T** compared with the fluctuation theories. As it is easily seen, the absolute value of σ' is deeply suppressed, and, as expected, the C factors are extremely small, evidently reflecting the enhanced role of the defects in this case. It is easy to compute that $S^* = \sigma'_{\mathbf{L}}(92\ \mathrm{K})/\sigma'_{\mathbf{T}}(92\ \mathrm{K}) = 28.8$, whereas $\rho^* = \rho_{\mathbf{T}}(92\ \mathrm{K})/\rho_{\mathbf{L}}(92\ \mathrm{K}) = 10.48$ only. The corresponding values of S^* and ρ^*, found for sample M23, are 8.48 and 3.44, respectively. Here $T = 92$ K is chosen as a representative temperature which is close to the measured T_0 for each sample. Despite the fact that the absolute values of the parameters are noticeably different, the ratio S^*/ρ^* is approximately the same for both samples, namely 2.75 and 2.47, respectively. The finding apparently means that the relative diminution of the paraconductivity is approximately the same for both of the films discussed suggesting that the same mechanism of FC suppression occurs in each sample. It should be noted that $[\rho_N(T) - \rho(T)]$ [Eq. (2)], measured for both films in both directions, is of the same order. Hence, the observed diminution of σ' is actually the consequence of the corresponding increase of the **T** resistivity, as $\sigma' \sim 1/[\rho_N \rho(T)]$ [Eq. (2)]. Besides, $\sigma'(T)$ drops to zero at $T_{*0} \approx 105$ K (Table I), which is much lower than that measured in the **L** direction. Thus, the PG temperature range turns out to be rather limited in this case, as was mentioned above.

Nevertheless, despite the strong influence of defects, the standard linear $\sigma'(T)$ dependence, well described by the 3D AL term, but with $C_{3\mathrm{D}} = 0.013$ only, is observed near T_c (Fig. 4b, curve *3*). As before, the LD-AL (3D) crossover is distinctly seen on the plot at the same $\ln\varepsilon \approx -4.393$ as was measured for M35-**L**. Thus, the same values $\xi_c(0) \approx (1.3 \pm 0.01)$ Å, $\tau_\varphi(100\ \mathrm{K})\beta \approx 24.24 \times 10^{-13}$ s, and $\delta_{\mathrm{th}} \approx 2$ are derived from the analysis, which seems reasonable. To check the type of crossover, the MT term calculated using the values found for $\xi_c(0)$ and $\tau_\varphi(100\ \mathrm{K})\beta$ is also plotted (Fig. 4b, curve *1*). As before, when drawn with $C_{2\mathrm{D}} = C_{3\mathrm{D}}/1.82 \approx \approx 0.0072$, it intersects the data just at the crossover point, accordingly marked as $\ln\varepsilon_0$ on the graph. This finding indicates that the crossover is of just the type that has to determine the parameters of the fluctuation analysis,[2] and it once again confirms the universality of the ratio $C^* \approx 1.82$ found for YBCO oxides.[16] Nevertheless, the MT curve runs far away from the experimental data, which is not surprising since the CuO_2 planes are expected to be badly mixed in the **T** direction. But, surprisingly, the LD term (not shown to prevent obscuring the graph) when drawn with $\xi_c(0) \approx (1.3 \pm 0.01)$ Å and the value $d = 11.7$ Å commonly used in the FC analysis does not fit the data in any temperature region below or above T_0. After many trials it was eventually found that above T_0, all the way up to $\ln\varepsilon_{c0} \approx -3.3$ ($T_{c0} \approx 94.2$ K), the data can be perfectly extrapolated by the LD term with $\xi_c(0) \approx (1.3 \pm 0.01)$ Å but $d = (35 \pm 1)$ Å (Fig. 4b, curve *2*). At first sight the result looks somewhat puzzling, but sample M23-**T** demonstrates exactly the same FC behavior above T_0 (Fig. 3b, curve *2*). Moreover, the similar $\sigma'(T)$ dependence above T_0, fitted by the LD term with $d \approx 35$ Å, was recently found for YBCO films which structure was artificially deteriorated to increase the critical currents.[30] Thus, the specific temperature dependence found for the fluctuation conductivity above T_0 appears to be universal for the YBCO oxides with defected structure. As the CuO_2 planes are expected to be badly mixed in the **T** direction, it seems reasonable to consider this temperature region as a pseudo-two-dimensional one.

To account for this finding one would have to assume that any new structure with the intraplane distance $d \approx 35$ Å is realized in the films as a result of the growth-related defects presence. However, this most simple explanation proves to be somewhat contradictory since the **L**-direction measurements indicate that $d = 11.7$ Å, and just this value of d is used in computing $\xi_c(0)$ and $\tau_\varphi(100\ \mathrm{K})\beta$ from the **T**-direction experiment. Unfortunately, the 3D AL term [Eq. (7)] does not depend on d and cannot help solve the problem.

Finally, before proceeding with assumptions it seems rather reasonable to find out the features of the FC behavior common to both of these films above T_0. Such a feature is the faster diminution of σ' with T in this temperature interval as compared with the **L**-direction experiment. As a result, $\sigma'(T)$ steepens, suggesting enhanced pair-breaking in the pseudo-two-dimensional region. In accordance with the discussion of the 80-kelvin films,[2] this $\sigma'(T)$ dependence is to be described solely by the LD model, as a large spread of the intraplane distances in the **T** direction is expected. Strictly speaking, it is difficult to distinguish any predominant distance in this case. Taking all of the above remarks into account, the value $d=35$ Å is obviously not to be considered as the distance between the conducting layers but has only to reflect the fact that the scattering rate of the fluctuating pairs, measured in the **T** direction above T_0, is at least 3 times that measured in the **L** direction [see Eq. (2)]. As a result, the pseudogap temperature range measured in the **T** direction for both films turns out to be rather limited (Fig. 1), with $T_{*0\mathbf{L}} - T_{*0\mathbf{T}} \approx 20-45$ K (Table I). The finding permits to conclude that the PG phenomenon, at least in OD YBCO oxides, is mainly governed by the fluctuating pairing.

At first sight sample M23-**T** exhibits just the same FC behavior (Fig. 3b, dots). Above T_0, all the way up to $\ln\varepsilon_0 \approx -3.7$ ($T_{c0}\approx 92.41$ K), the $\sigma'(T)$ curve is well described by the LD model with $d=35$ Å (Fig. 3b, curve *2*), as mentioned above. But the LD-AL(3D) crossover unexpectedly occurs at $T_{0\mathbf{T}} < T_{0\mathbf{L}}$, resulting in the extremely short 3D region in this case. Really, only the leftmost few data points can be fitted by the 3D AL term with $C_{3D}=0.127$ (Fig. 3b, curve *3*) now. It looks as if all the data are shifted towards low temperatures compared with the **L**-direction experiment. The shift is distinctly seen on the graph as the difference between $\ln\varepsilon_{0\mathbf{T}}$ and $\ln\varepsilon_{0\mathbf{L}}$, also shown in the figure. The matter of whether we could again ascribe the shift to twice the difference in the samples thickness or whether it is an intrinsic feature of sample M23 has yet to be settled, leaving this an open question. Since the FC parameters are strictly determined by the ε_0, the shift evidently suggests the change of both $\xi_c(0)$ and $\tau_\varphi(100\text{ K})\beta$ compare with those measured for M23-**L**. Using the value found for $\ln\varepsilon_0 \approx -4.766$ ($T_0 \approx 90.95$ K), one can easily compute the values $\xi_c(0) \approx (1.08\pm 0.01)$ Å and $\tau_\varphi(100\text{ K})\beta \approx 35.21\times 10^{-13}$ s, suggesting the anisotropy of the parameters. But the anisotropy of $\xi_c(0)$ and the enlargement of τ_φ, appear to be rather unusual.

There are two possible approaches to estimation of $\xi_c(0)$ in the given case. The value $\xi_c(0)\approx(1.08\pm 0.01)$ Å is computed from Eq. (7) taking $d=11.7$ Å. The other possibility is the likely modification of d as a result of the influence of defects, considering $\xi_c(0)$ to be stable. Simple algebra [Eq. (8)] yields $d\approx 17.34$ Å in the latter case. Analysis of the defect microstructure[24] evidently shows that the crystal lattice is slightly tilted across the defects, and numerous stacking faults could result in a general change of the unit-cell height. That is why the second approach seems to be better, as it is difficult to see any physics behind the possible anisotropy of $\xi_c(0)$ depending on the measuring current direction in the *ab* plane. Finally, the AL and MT terms in the figure are drawn using $d=17.34$ Å, and accordingly $\xi_c(0) = 1.6$ Å and $\tau_\varphi(100\text{ K})\beta \approx 35.21\times 10^{-13}$ s. The only exception is $d=35$ Å used for the LD fit. As expected, the AL and LD fits prove to be rather good in this case. And, as before, the MT term, drawn with $C_{2D}=C_{3D}/1.82\approx 0.07$, intersects the data just at the crossover point (Fig. 4b, curve *1*). Thus, it appears that, despite the strong influence of defects, the FC approach developed in Ref. 16 enables the reasonable description of the data in all of the temperature region of interest. As far as the noticeable enhancement of $\tau_\varphi(100\text{ K})\beta$ is concerned, we think the τ_φ should be the same as calculated for M23-**L**, since the same T_c is measured in both directions (Table I), suggesting the fluctuating pairing in the 3D region to be independent of the presence of defects. The conclusion is confirmed by the fact that the temperature range of the 3D fluctuations observed for M35-**T** is the same as measured in the **L** direction (Fig. 4b). Thus, the influence of defects is evidently much more stronger for the thicker sample. Therefore, to account for the enhancement of $\tau_\varphi(100\text{ K})\beta$ one can assume the enlargement of $\beta \sim l/\xi_{ab}(0)$. Naturally, some speculations as to the likely anisotropy of l, ξ_{ab}, and, finally, of the Fermi surface due to defect structure seem to be rather possible, but more experiments are evidently required to shed light on the problem.

4. CONCLUSION

As expected, the structural defects produced by 10° miscut growth of YBCO films[24] appear to deeply affect the fluctuation conductivity of the films, ultimately resulting in a rather complicated and somewhat contradictory picture of the FC behavior (Figs. 3 and 4). Nevertheless, the results are shown to be reasonably described within the framework of the FC analysis developed for the well-structured YBCO films.[2,16]

Noticeable anisotropy of the FC behavior is found for both films studied, depending on whether measurements are performed in the **L** or in **T** direction. The FC measured in the **T** direction appears to be deeply suppressed. Moreover, above T_0 the scattering rate of the fluctuating pairs is estimated to be three times as large as measured in the **L** direction, suggesting enhanced pair-breaking in this case. As a result, the pseudogap temperature range measured in the **T** direction for both films (Fig. 1) turns out to be rather limited with $T_{*0\mathbf{L}} - T_{*0\mathbf{T}} \approx 20-45$ K (Table I). The finding permits to conclude that the PG phenomenon, at least in OD YBCO oxides, is mainly governed by the fluctuating pairing.

In the fluctuation region below T_0, where the 3D volume FC is realized, the pair-breaking mechanism appears to be the same for all samples studied, resulting in the same and very high T_c's. As a result, independently of the direction of measurements, the FC in the 3D fluctuation region near T_c is always fitted by the 3D term of the Al theory[14] and in all cases the ratio $C^* = C_{3D}/C_{2D} \approx (1.82\pm 0.2)$ is held, as a result of the layered structure of HTSC. We think that both findings suggest the same fluctuating pairing mechanism near T_c for all YBCO oxides, independently of the presence of defect structure.

However, despite the fact that the same set of growth-related defects was found for both films studied,[24] the FC

behavior, especially that measured in the **L** direction, turns out to be rather different. Most likely the result can be attributed to the noticeable difference in the sample thickness d_0, as the difference in T_c is negligible (Table I). Indeed, in the relatively thin film (sample M35) the influence of the defects on FC is not so pronounced. As a result, the fine structure of the $\sigma'(T)$ dependence, including all three AL, MT, and LD fluctuation contributions, is distinctly revealed on the plot (Fig. 4a). In contrast with the FC results an enhanced scattering rate of the normal carriers, leading to a very high resistivity measured in the **T** direction, is observed in this case (Fig. 1). As a result, $d\rho/dT(\mathrm{M35}) \approx 2d\rho/dT(\mathrm{M23})$ is found, and, besides, the wider is ΔT, the larger is ρ(T) and the ratio $\rho_{\mathbf{T}}/\rho_{\mathbf{L}}$ (Table I).

With increasing film thickness (sample M23) the sample regions responsible for the different fluctuation contributions have to overlap (see the text), apparently leading to the averaging of the influence of defects on $\sigma'(T)$. As a result, the smooth $\sigma'(T)$ dependence described by the LD model alone is observed in this case (Fig. 3a). At the same time, all resistivity parameters, including $d\rho/dT$ (Table I), measured in the **L** direction turn out to be practically the same as those usually reported for the OD YBCO oxides.[2,4–9] Accordingly, $\rho_{\mathbf{T}}$ (100 K) is about 6 times as less as measured for M35-**T**. We think all the findings have to corroborate this assumption.

Summarizing the facts, one may conclude that investigation of fluctuation conductivity additionally provides a useful method of getting reliable information on the inhomogeneity of the sample structure. Depending on what kind of $\sigma'(T)$ dependence is observed, additional information as to the type of defects and intensity of their influence on the resistivity and FC can easily be obtained. The method appears to be especially useful when no thorough structural analysis is unavailable.

The author acknowledges the staff of MPI-Stuttgart, where the experimental part of this work was done, for their hospitality. He is also grateful to Prof. H.-U. Habermeier for stimulation of the study and fruitful suggestions, to T. Haage for films preparation and to Prof. V. M. Dmitriev for valuable comments in a discussion of the results of this study.

*E-mail: solovjov@ilt.kharkov.ua

[1] T. Timusk and B. Statt, Rep. Prog. Phys. **62**, 61 (1999).
[2] A. L. Solovjov, H.-U. Habermeier, and T. Haage, Fiz. Nizk. Temp. **28**, 144 (2002) [Low Temp. Phys. **28**, 99 (2002)].
[3] C. Carballeira, S. R. Curras, J. Vina, and J. A. Veira, Phys. Rev. B **63**, 144515 (2001).
[4] P. P. Freitas, C. C. Tsuei, and T. S. Plaskett, Phys. Rev. B **36**, 833 (1987).
[5] B. Oh, K. Char, A. D. Kent, M. Naito, M. R. Beasley, T. H. Geballe, R. H. Hammond, A. Kapitulnik, and J. M. Graybeal, Phys. Rev. B **37**, 7861 (1988).
[6] T. A. Friedmann, J. P. Rice, John Giapintzakis, and D. M. Ginsberg, Phys. Rev. B **39**, 4258 (1989).
[7] K. Winzer and G. Kumm, Z. Phys. B: Condens. Matter **82**, 317 (1991).
[8] A. Gauzzi and D. Pavuna, Phys. Rev. B **51**, 15420 (1995).
[9] W. Lang, G. Heine, P. Schwab, X. Z. Wang, and D. Bauerle, Phys. Rev. B **49**, 4209 (1995).
[10] A. L. Solovjov, V. M. Dmitriev, H.-U. Habermeier, and I. E. Trofimov, Phys. Rev. B **55**, 8551 (1997) and references therein.
[11] J. Axnas, B. Lundqvist, and O. Rapp, Phys. Rev. B **58**, 6628 (1998).
[12] K. Maki, Prog. Theor. Phys. **39**, 897 (1968); R. S. Tompson, Phys. Rev. B **1**, 327 (1970).
[13] S. Hikami and A. I. Larkin, Mod. Phys. Lett. B **2**, 693 (1998).
[14] L. G. Aslamazov and A. I. Larkin, Phys. Lett. A **26**, 238 (1968).
[15] B. P. Stojkovic and D. Pines, Phys. Rev. B **55**, 8576 (1997) and references therein.
[16] A. L. Solovjov, H.-U. Habermeier, and T. Haage, Fiz. Nizk. Temp. **28**, 24 (2002) [Low Temp. Phys. **28**, 17 (2002)].
[17] W. E. Lawrence and S. Doniach, in *Proceedings of the Twelfth International Conference on Low Temperature Physics, Kioto (1971)*, p. 361.
[18] R. Knorpp, A. Forkl, H.-U. Habermeier, and H. Kronmuller, Physica C **230**, 128 (1994).
[19] T. L. Hylton and M. R. Beasley, Phys. Rev. B **41**, 11669 (1990).
[20] J. Mannhart, D. Anselmetti, J. G. Bednorz, A. Catana, Ch. Gerber, K. A. Muller, and D. G. Schlom, Z. Phys. B: Condens. Matter **86**, 177 (1992).
[21] M. Oussena, P. A. J. de Groot, and S. J. Porter, Phys. Rev. B **51**, 1389 (1995).
[22] H.-U. Habermeier, Appl. Surf. Sci. **69**, 204 (1993).
[23] D. H. Lowndes, D. K. Christen, C. E. Klabunde, Z. L. Wang, D. M. Kroeger, J. D. Budai, Shen Zhu, and P. D. Norton, Phys. Rev. Lett. **74**, 2355 (1995).
[24] T. Haage, J. Q. Li, B. Leibold, M. Cardona, J. Zegenhagen, and H.-U. Habermeier, Solid State Commun. **99**, 553 (1996).
[25] J. B. Bieri, K. Maki, and R. S. Thompson, Phys. Rev. B **44**, 4709 (1991).
[26] Y. B. Xie, Phys. Rev. B **46**, 13997 (1992).
[27] Y. Matsuda, T. Hirai, and S. Komiyama, Solid State Commun. **68**, 103 (1988).
[28] P. G. De Gennes, *Superconductivity of Metals and Alloys*, W. A. Benjamin, Inc., New York-Amsterdam (1966).
[29] V. M. Dmitriev, A. L. Solovjov, and A. I. Dmitrenko, Fiz. Nizk. Temp. **15**, 356 (1989) [Sov. J. Low Temp. Phys. **15**, 200 (1989)].
[30] V. M. Dmitriev, V. I. Stepanov, V. N. Svetlov, and A. L. Solovjov, to be published.

This article was published in English in the original Russian journal. Reproduced here with stylistic changes by AIP.

Key role of intramolecular Jahn–Teller vibrations and multivalley nature of the band spectrum in the mechanism of superconductivity in doped C_{60} fullerites

V. M. Loktev[a)]

N. N. Bogolyubov Institute of Theoretical Physics, Ukrainian National Academy of Sciences, yl. Metrologicheskaya, 14-b, Kiev, 03143, Ukraine

É. A. Pashitskiĭ[b)]

Institute of Physics, Ukrainian National Academy of Sciences, pr. Nauki, 46, Kiev, 03650, Ukraine

R. Shekhter[c)] and M. Jonson

Chalmers Technological University, Götheborg, 412-96, Sweden

(Submitted April 1, 2002; resubmitted September 17, 2002)
Fiz. Nizk. Temp. **28**, 1150–1162 (November 2002)

The possible mechanisms of superconductivity and of the increase in the critical temperature T_c of the phase transition into the superconducting state in doped cubic and hexagonal C_{60} fullerine crystals are analyzed. It is shown that the intramolecular Jahn–Teller vibrations (which are due to the high symmetry of C_{60} molecules and fullerene crystals and arise as a result of a change in the charge state of fullerene in an electron-phonon interaction), the degeneracy (multivalley nature) of the structure of narrow bands with a high density of states, and multiparticle Coulomb correlations such as local field effects (which increase the coupling constant in Cooper pariing of current carriers) all play a key role in the mechanism of superconductivity in this molecular metal. © *2002 American Institute of Physics.* [DOI: 10.1063/1.1528573]

1. INTRODUCTION

The discovery of a new allotropic form of carbon—fullerene[1]—and the subsequent discovery of superconductivity in C_{60} fullerite crystals doped with alkali metals (K, Rb, Cs)[2,3] have opened up a new direction of research in solid-state physics, specifically, the study of a new class of molecular crystals (see the reviews Refs. 4–6).

Electron (or hole) doped fullerite crystals (fullerides) are a fundamentally new type of conductor with anomalously narrow bands—a molecular metal with a high density of states (DS) at the Fermi level (FL).

The question of the mechanism of superconductivity (SC) in C_{60} fullerite and the absence of superconductivity in doped C_{70} fullerite crystals or mixed $A_3(C_{60})_{1-x}(C_{70})_x$ crystals is of special interest.[7]

The fact that the critical temperature of electron-doped face-centered cubic A_3C_{60} crystals increases monotonically as the ionic radius of the doping metal increases—from $T_c = 19.3$ K for K_3C_{60} to $T_c \approx 31.3$ K for Rb_2CsC_{60}[3] up to $T_c \approx 40$ K for Cs_3C_{60}[8] and $T_c = 48$ K for $RbTl_2C_{60}$[9]—has led to the conjecture[10] that the standard mechanism of Cooper pairing of electrons due to their interaction with phonons (BCS model[11]) is the basis for the SC observed in A_3C_{60}. Indeed, since fullerite is a molecular crystal with slightly overlapping π orbitals of neighboring C_{60} molecules (which form an intermolecular σ-type bond), doping the crystal with atoms with increasing radius increases the stretching (expansion) of the lattice and decreases the degree of overlapping of the π orbitals, i.e. it actually results in narrowing of the conduction band. In turn, this increases the density of states $N(E_F)$ at the FL and increases the dimensionless electron-phonon interaction (EPI) constant $\lambda_{ph} = N(E_F)\tilde{g}_{ph}^2$ (where $\tilde{g}_{ph}$ is the EPI matrix element averaged over the Fermi surface), which, ultimately, increases T_c in accordance with the exponential BCS relation[11]

$$T_c = \tilde{\omega}_{ph} \exp(-1/\lambda_{ph}), \tag{1}$$

where $\tilde{\omega}_{ph}$ is the average (close to the Debye) phonon frequency. It should be underscored that the relation (1) holds only in the weak coupling approximation, where $\lambda_{ph} \ll 1$, and neglects the Coulomb interaction.

According to the experimental data[3] T_c increases in A_3C_{60} compounds almost linearly with the lattice constant a, so that T_c increases by 12 K when a increases by 0.24 Å from $a = 14.25$ Å for K_3C_{60} to $a = 14.49$ Å for Rb_2CsC_{60}, which corresponds to the derivative $\partial T_c/\partial a \approx 50$ K/Å. On the other hand an experiment measuring T_c as a function of the pressure P in A_3C_{60} crystals[12,13] showed that T_c increases under hydrostatic compression and is characterized by an anomalously large (in absolute magnitude) negative derivative $\partial T_c/\partial P \approx -(6.3-7.8)$ K/GPa, which is 3 to 4 times greater than the corresponding value of $\partial T_c/\partial P_i$ with anisotropic (uniaxial) compression or stretching of layered and layer-chain HTCS crystals with $T_c \geqslant 100$ K based on cuprate metal-oxide compounds (MOC) of the type Y–Ba–Cu–O and Bi–Sr–Ca–Cu–O[14–16] and 6 to 8 times greater than in Hg–Ba–Ca-Cu-O.[17] We note that the corresponding values of $\partial T_c/\partial P$ for ordinary low-temperature superconductors (metals with $T_c < 10$ K) are 2 to 3 orders of magnitude smaller.

In the present paper we discuss the various possible effects which could give rise to superconductivity with high T_c

in C_{60} crystals and the possible reasons for the absence or suppression of superconductivity in C_{70} crystals. Specifically, we discuss the role of symmetry and degeneracy of states, the Jahn–Teller deformations of highly symmetric C_{60} molecules (bucky balls) in doped cubic and hexagonal fulleride crystals, the influence of the multivalley structure of the band spectrum, the nonadiabaticity of the EPI, and the Coulomb effects due to the ''local field'' on the value of T_c. We shall proceed from the ''molecular metal'' model, first studied in Refs. 18 and 19 in application to fullerite, with anomalously narrow degenerate bands and, which is important, the electron-phonon (electron-vibrational) interaction at a site taking account of the dynamic Jahn–Teller effect[20] accompanying a change in the charge states of the molecules in C_{60} fullerite.

2. DEGENERACY OF THE ELECTRONIC STATES AND THE MULTIVALLEY NATURE OF THE BAND SPECTRUM IN FULLERENE CRYSTALS

2.1. Electron-doped A_3C_{60} fullerides

According to the point of view previously stated in Refs. 18 and 19 the existence of SC in alkali-metal-doped A_3C_{60} crystals[2,3] and the absence of SC in A_3C_{70} crystals[7] are due to the much higher symmetry of the almost spherical C_{60} molecules and the face-centered cubic A_3C_{60} lattices as compared with the axisymmetric (ellipsoidal) C_{70} molecules and the low-symmetry A_3C_{70} crystals. As recently shown in Ref. 21 the lattice of even pure C_{70} fullerite has a low-temperature phase with a monoclinic system where the crystal field completely splits (lifts the degeneracy) of all electronic states.

At the same time only partial lifting of the degeneracy of the excited electronic terms of fullerene molecules, which possess icosahedral symmetry (point group Y_h), occurs in the crystal field of pure face-centered cubic C_{60} fullerite or the stoichiometric compound A_3C_{60}, which possesses the same lattice symmetry, where the dopant atoms A fill all three energetically favorable positions in the interstices between each C_{60} molecule. For example, the triply degenerate first excited state t_{1u} remains degenerate in the singly- and doubly-charged states, while the ground triply-charged ground state (according to Hund's rule) is nondegenerate. The ''ground'' fivefold degenerate term h_u, completely filled with 10 electrons, of the neutral C_{60} molecule remains unsplit.

The simplest electronic Hamiltonian describing the structure of an empty conduction band with one extra electron has the following form in the site approximation in the second-quantization representation:[19]

$$\mathcal{H}^{(t_{1u})}=\varepsilon\sum_{\mathbf{n},\nu,\sigma} a^{+}_{\mathbf{n}\nu\sigma}a_{\mathbf{n}\nu\sigma}\sum_{\mathbf{n},\mathbf{m},\sigma}\sum_{\nu,\mu} t^{\nu\mu}_{\mathbf{nm}}a^{+}_{\mathbf{n}\nu\sigma}a_{\mathbf{m}\mu\sigma}. \qquad (2)$$

Here $\varepsilon=E(h_{1u})-E(h_u)$ is the intramolecular electronic transition energy from the ground state into the first excited state t_{1u} of an individual C_{60} molecule. This state forms a conduction band as a result of a finite probability of electron tunneling between different crystal lattice sites **n** and **m** with matrix element (overlap integral) $t^{\nu\mu}_{\mathbf{nm}}$, where the indices ν and μ enumerate the levels (bands), and $a^{+}_{\mathbf{n}\nu\sigma}$ and $a_{\mathbf{m}\mu\sigma}$ are operators creating and annihilating an electron with spin σ in the corresponding state at the corresponding site.

In the tight-binding approximation taking account of only the nearest neighbors, which is justified for weak π-orbital overlapping, so that $t^{\nu\mu}\equiv t$, the band spectrum along the diagonals of the first Brillouin zone (BZ) assumes the form[19]

$$\varepsilon_{1,2}(k)=\varepsilon-tz\gamma(\mathbf{k});\quad \varepsilon_3(\mathbf{k})=\varepsilon+2tz\gamma(\mathbf{k}), \qquad (3)$$

where z is the coordination number and $\gamma(\mathbf{k})$ is the lattice structure factor. Hence it follows that for $t>0$ eight doubly-degenerate equivalent minima of the energy (valleys) with high a DS exist at the L points on the diagonals of the BZ, in complete agreement with numerical calculations of the band spectrum.[22,23] It should also be kept in mind that in a cubic C_{60} crystal six deeper nondegenerate equivalent valleys exist at the X points of the BZ.[23]

The high degree of degeneracy of the states (multivalue nature) of the band spectrum in C_{60} fulleride actually eliminates the problem, discussed in Ref. 24 (see also Ref. 6), of the Mott–Hubbard metal-insulator transition in A_xC_{60} with a half-filled conduction band ($x=3$), since, as shown in Ref. 25, for N-fold orbital degeneracy of the electronic states the criterion for the Mott–Hubbard transition is

$$U/W\geqslant(N+1). \qquad (4)$$

Here U is the Hubbard constant describing the Coulomb repulsion of two electrons at a single site. For fullerene $U=e^2/2R_0\approx 2$ eV, where R_0 is the radius of a C_{60} molecule ($R_0\approx 3.5$ Å) and W is the width of the conduction band, which is 0.5 eV in order of magnitude (see the review Ref. 60 for a more detailed discussion). Consequently, even if the nondegenerate valleys $l=6$ at the X points of the BZ, when $N=6$, and especially the doubly degenerate valleys $l=8$, when $N=16$, are taken into account, according to the criterion (4) there is a large ''store of strength'' for the metallic state, even taking account of the narrowing of the bands (3) accompanying splitting of the t_{1u} level.

Moreover, because of the presence of a large number of equivalent valleys ($l=6$ or 8) the electrons are uniformly distributed over all valleys. As a result, only a relatively small fraction of all electrons $n=n_e/6$ or (taking account of the double degeneracy) $\tilde{n}_e=n_e/16$, where n_e is the total electron density in a doped A_xC_{60} crystal, equal to $3/a^3$ for $x=3$ (here, once again, $a\approx 10$ Å is the average distance between the nearest C_{60} molecules), occupies each valley.

It should be noted that if the $\varepsilon_{12}(\mathbf{k})$ and $\varepsilon_3(\mathbf{k})$ bands do not overlap, then because the width of the lower doubly degenerate band $\varepsilon_{12}(\mathbf{k})$ is two times smaller [see Eq. (3)] and, correspondingly, the DS is two times higher than in the upper nondegenerate band $\varepsilon_3(\mathbf{k})$, almost all doped electrons fill the lower band. After the deeper and lighter valleys at the X points of the BZ ($l=6$) are filled the doubly degenerate valleys at the L points of the BZ ($l=8$), where the DS is much higher, are filled. If it is assumed that it is these ''heavy'' valleys that largely determine the position of the FL in the conduction band, then, estimating the electron density in each such valley as $\tilde{n}_e\approx 3/16a^3\approx 2\times 10^{20}$ cm^{-3}, we obtain the Fermi momentum $\tilde{k}_F=(3\pi^2\tilde{n}_e)^{1/3}\approx 1.8\times 10^7$ cm^{-1} and Fermi energy $E_F\approx\tilde{k}_F^2/2m_e^*\leqslant 0.12$ eV with the effective mass

of conduction electrons m_e^* of the order of or greater than the free-electron mass m_e, which is justified for a band of width $W \leqslant 0.5$ eV. The latter means that even for the stoichiometric composition A_3C_{60} the conduction band $\varepsilon_{12}(\mathbf{k})$ is half empty, which automatically eliminates the possibility of a Mott–Hubbard metal-insulator transition. In other words the multivalley structure of the band spectrum is, in a certain sense, s equivalent to deviation from stoichiometry of the compound A_xC_{60}.[26]

At the same time the sharp peak in T_c observed experimentally in electron-doped A_xC_{60} crystals precisely at $x=3$[2,3] could be due to restoration of high symmetry and ordering of the A_3C_{60} crystal. The elastic Coulomb scattering of doped conduction electrons by regularly arranged impurity ions of alkali metals (donors), forming a characteristic regular sublattice, does not result in mixing of states from different valleys, in contrast to unordered A_xC_{60} crystals with $x \neq 3$ where this does happen. Consequently, it can be assumed that the structure of the band spectrum of an A_3C_{60} crystal is essentially identical, to a high degree of accuracy, to that of pure fullerite C_{60}, while their phonon spectra differ substantially[27] because of the contribution of additional optical modes associated with the vibrations of the A^+ ions.[6]

2.2. C_{60} thin films

In contrast to C_{60} fullerite crystals, C_{60} thin films grown by evaporation in a hydrogen stream and intercallated with $CHCl_3$ and $CHBr_3$ molecules in solution[28] possess not cubic but rather hexagonal crystal structure.[29]

For a hexagonal lattice with symmetry axis $C_6 \| Z$ the crystal field is uniaxial,[30] so that all electronic states of the fullerene molecules retain the projection L_Z of the orbital angular momentum $\mathbf{L}$ on this axis and are divided into $\pm L_Z$ doublets (except for the state $L_Z=0$).

As a result, the electronic Hamiltonian of a C_{60} fullerene molecule in the hexagonal lattice of C_{60} fulleride films can be written as

$$\mathcal{H}_{\mathrm{mol}} = B_2^0 \sum_{\mathbf{n}} (L_{\mathbf{n}}^Z)^2 + B_4^0 \sum_{\mathbf{n}} (L_{\mathbf{n}}^Z)^4, \tag{5}$$

where B_2^0 and B_4^0 are crystal-field parameters, and the ligands for each C_{60} molecule consist of the identically charged (with doping) C_{60} molecules.[31]

The first excited state is the doublet $L_Z = \pm 1$, which begins to be filled when the doped hole concentration n_h corresponds to two holes per C_{60} molecule ($x_h = 2$).

It should be noted that the hexagonal crystal symmetry also results in additional degeneracy of the band spectrum relative to the C_6 axis and to the appearance in the conduction band and the valence band of six equivalent valleys at the boundary of the first BZ. This degeneracy with $N=6$ makes the metallic state of doped C_{60} fullerene films stable with respect to the Mott–Hubbard metal-insulator transition [see Ref. 25 and the criterion (4)].

The question of the spatial distribution of the charge carriers (electrons or holes) injected into a C_{60} film, taking account of the long-range Coulomb interaction and nonlinear screening of the electrostatic potential by free doped carriers (see Ref. 32 and the literature cited there), is of special interest.

In principle, such a one-dimensional problem can be solved by the Thomas–Fermi method, which reduces to solving the nonlinear Poisson equation[33]

$$\frac{d^2\varphi}{dz^2} = \frac{4e}{3\pi}\left[\frac{2m^*e}{\hbar^2}(\varphi - \varphi_0)\right]^{3/2}. \tag{6}$$

Introducing the dimensionless variables $\tilde{z} = z/a_0$ and $y = e(\varphi - \varphi_0)/E_0$, where $a_0 = \hbar^2/m^*e^2$ is the Bohr radius of the electron (hole) with effective mass m^*, and $E_0 = (3\pi/8)^2 e^2/2a_0$ is the characteristic energy of the problem, we write Eq. (6) in the form

$$\frac{d^2y(\tilde{z})}{d\tilde{z}^2} = y^{3/2}(\tilde{z}). \tag{7}$$

The equation (7) is a particular case of a nonlinear Emden–Fowler equation

$$y^a + b\tilde{z}^\nu y^m = 0 \tag{8}$$

with $b=-1$, $\nu=0$, and $m=3/2$. It is well known[34] that this equation has the exact particular solution

$$y = \alpha \tilde{z}^\beta, \tag{9}$$

where

$$\alpha^{m-1} = -\frac{(\nu+2)(\nu+m+1)}{b(m-1)^2}; \quad \beta = \frac{2+\nu}{1-m}. \tag{10}$$

In our present case $\alpha = 400$ and $\beta = -4$, i.e.

$$y = 400/\tilde{z}^4. \tag{11}$$

In the spherically symmetric case the corresponding solution has the form $y(\tilde{z}) = 144/\tilde{z}^3$.[33] Ordinarily, solutions of this type are discarded on the basis of physical considerations because they diverge as $\tilde{z} \to 0$.

However, doped C_{60} fullerite is an unusual molecular metal with spherically symmetric cavities, which are inaccessible to current carriers, with radius R_0 equal to the radius of a C_{60} molecule.[35] As a result, the particular solution (11) of Eq. (7) is actually applicable in the region $\tilde{z} \geqslant 2R_0/a_0$, where it is finite and consequently can be used to describe the nonlinear screening of the electrostatic field by doped carriers in C_{60} films. The power law

$$n(z) = \frac{1}{3\pi^2}\left\{\frac{2me}{h^2}[\varphi(z) - \varphi_0]\right\}^{3/2} - (a_0/z)^6, \tag{12}$$

i.e. $n(z)$ in the region $\tilde{z} > 2R_0 \approx 7$ Å decreases very rapidly away from the first monomolecular C_{60} layer with characteristic scale $a_0 \sim 1$ Å, describes the spatial density distribution of free charge carriers. However, this still does not give a basis for believing that the electron or hole spectrum in this layer is two-dimensional because the carrier motion taking account of carrier scattering by almost spherical C_{60} molecules is very complicated. In addition, because of the excluded volume of the impenetrable spherical cavities with radius R_0, in momentum space the electrons (holes) cannot fill states with momenta $p > p_0 = \pi/R_0 \approx 9 \times 10^7$ cm^{-1}, i.e. the Fermi momentum $k_F = (\pi^2 n_e)^{1/3}$ cannot exceed the value P_0 and the electron (hole) density n_0 cannot exceed $\pi/3R_0^3 \approx 2.4 \times 10^{22}$ cm^{-1}.

3. ELECTRON–PHONON AND COULOMB INTERACTIONS IN FULLERITES

3.1. Critical temperature

The experimental data on the dependence of T_c on the lattice parameter a of doped C_{60} fullerite crystals[2,3] and on the pressure[12,13] are generally consistent with the conjecture[10] that SC in these crystals is due to a phonon mechanism.[6] The positive isotopic effect[36] observed in A_3C_{60} with complete or partial substitution of ^{13}C for ^{12}C atoms in fullerene[36] also indicates this, though there are a number of anomalies in the measured values of the isotopic shift of T_c.[6]

The main feature of the phonon spectrum in fullerite crystals (just as in other molecular crystals) is the clear separation of the vibrational phonon modes into intermolecular low-frequency (LF) acoustic and optical (primarily, libronic) modes associated with the relative C_{60}-C_{60} translational and orientational vibrations of the molecules, and intramolecular high-frequency (HF) optical modes due to the relative vibrations of carbon atoms directly in the C_{60} molecules.[37] The frequencies of the former are $10-10^2$ cm^{-2} and those of the latter are 10^2-10^3 cm^{-1}. Addional modes due to the relative vibrations of the A^+ ions and C_{60} molecules also arise in doped A_xC_{60} crystals.

It is the ''hard'' intramolecular vibrations, which include the strongest ''breathing'' modes with A_g symmetry, that are responsible for the facts that the phonon spectrum of fullerite crystals is very wide and, just as in the C_{60} molecule, extends right up to energy $\omega_{ph}\approx 0.2$ eV.[27] There are a large number of works on computer calculations and experimental measurements of the phonon frequencies and the EPI constants (see, for example, Refs. 38–43). However, as noted in the review Ref. 6, there is a large discrepancy between the experimental data obtained by different methods (for example, neutron and Raman scattering or photoemission spectroscopy) and between theoretical results obtained by various groups using different computational methods.

Moreover, the standard theory of SC due to the EPI,[44,45] taking account of all phonon modes, cannot explain why the SC transition exists in doped C_{60} fullerite crystals and is absent (or, in any case, strongly suppressed) in C_{70} crystals, where the phonon spectrum is even more developed on account of the large number of intramolecular vibrational modes.

In this connection we shall proceed from the model proposed in Ref. 18 and 19 for a molecular metal on the basis of the tight-binding approximation with local interaction of doped current carriers (electrons, holes) with intramolecular vibrations of highly symmetric (almost spherical) C_{60} molecules whose degenerate charge states are unstable with respect to the Jahn–Teller deformation.

In contrast, the C_{70} molecules, which are shaped like elongated ellipsoids, do not undergo a Jahn–Teller instability in the charged state of C_{70} fullerite. In our opinion it is this fundamental difference in the structure and symmetry of C_{60} and C_{70} molecules (and other types of C_N fullerenes with $N>70$ or $N<60$) that explains the difference in the SC properties of doped C_{60} and C_N with $N\neq 60$ crystals.

According to quantum-chemical calculations[46] of the electronic and electron-vibrational (vibronic) states of C_{60} molecules and their negatively charged states—the molecular cations C_{60}^{n-} with $n=1-6$, with maximum relative distortion of the order of 12%, which is due to the flattening of the initial spherical shape of C_{60}, the cation C_{60}^{2-} possesses in the singlet spin state two excess electrons. At the same time, the cation C_{60}^{3-} in an energetically favorable (according to Hund's rule) state of a spin quartet with spin 3/2[46] is characterized by zero distortion, since it corresponds to an orbital singlet and has the same icosahedral symmetry as the neutral C_{60} molecule. This serves as additional confirmation of the fact that a doped fullerite crystal with stoichiometric composition A_3C_{60} in which all C_{60} molecules (on average) are in the charge state C_{60}^{3-} (with spin $S=3/2$) possesses the same symmetry as undoped C_{60} fullerite.

However, it should be kept in mind that as a result of charge-carrier migration C_{60} molecules in the conducting metallic phase, which form a narrow-band molecular crystal with a partially filled conduction band (or valence band) and are immersed in a ''sea'' of degenerate electrons (holes), are in indefinite (intermediate) valence and spin states. In addition, it is known[46] that the charge states of C_{60}^- and the singlet C_{60}^{2-} (with $S=0$) possess almost identical energy gains $\Delta E \approx -2.7$ eV, which are associated with the Jahn–Teller deformation. Consequently, it has not been ruled out that the C_{60} molecules in electron-doped crystals A_3C_{60} are in not only the state C_{60}^- but also the states C_{60}^- or C_{60}^{2-}. Transitions from one charge (anionic) state into another with (or without) a change in the total spin of the C_{60} molecule give rise to a change in the Jahn–Teller deformation (distortion) and the corresponding deformational and Coulomb energies of the fullerene molecule.

The electron (hole) interaction Hamiltonian in a narrow-band molecular metal with intramolecular vibrations of C_{60} molecules at the nth lattice site has the form[18,19]

$$\mathcal{H}_{\text{el-vib}}=\sum_{\mathbf{n},\sigma}\sum_{\nu,\mu}\chi_{\mathbf{n}}^{\nu\mu}a_{\mathbf{n}\nu\sigma}^{+}a_{\mathbf{n}\mu\sigma}Q_{\mathbf{n}}^{\nu\mu}, \tag{13}$$

where $\chi_{\mathbf{n}}^{\upsilon\mu}$ is the matrix element of the electron–vibrational (more accurately, electron–vibronic) interaction and $Q_{\mathbf{n}}^{\nu\mu}$ is the normal coordinate (operator) of the corresponding transition of an electron (hole) from the νth into the μth state (including, from one valley of the conduction band or valence band into another valley).

In electron-doped cubic fullerides A_3C_{60}[2,3] the Jahn–Teller deformations of the C_{60}^{n-} cations are determined primarily by the intramolecular quadrupole vibrations with H_g symmetry. Indeed, as shown in Ref. 46 the distortion of all charge states of C_{60}^{n-} with $n=1-5$ is almost completely determined by the displacements of carbon atoms, which correspond to five H_g modes. In addition, two of the lowest frequency modes with frequencies $\omega_1=214$ cm^{-1} (≈ 308 K) and $\omega_2=387$ cm^{-1} (≈ 557 K) determine a large part (from 60 to 80%) of the distortion. We note that in Ref. 6 somewhat higher values are given for these frequencies: $\omega_1=273$ cm^{-1} (≈ 393 K) and $\omega_2=437$ cm^{-1} (≈ 629 K).

In C_{60} thin films with hexagonal lattice symmetry transitions between electronic doublets $\pm L_Z$ conserving the projection of the orbital angular momentum $\mathbf{L}$ on the $C_6\|Z$ axis (specifically, a transition into a state with $L_Z=\pm 1$) are directly related with the quadrupole molecular vibration, which

gives rise to orthorhombic Jahn–Teller deformation of the C_{60} molecule and, correspondingly, removes the doublet degeneracy. In this case the electron-phonon interaction Hamiltonian has the form [compare with Eq. (13)]

$$\mathcal{H}_{\text{el-vib}}=B_2^2\sum_{\mathbf{n}}\,[(L_{\mathbf{n}}^X)^2-(L_{\mathbf{n}}^Y)^2]Q_{\mathbf{n}}^{\text{rh}}, \tag{14}$$

where B_2^2 is a crystal-field parameters [compare Eq. (5)] which in the present case determines the EPI constant; $L_{\mathbf{n}}^X$ and $L_{\mathbf{n}}^Y$ are projections of the orbital angular momentum $\mathbf{L}$ on the X and Y axes; and, $Q_{\mathbf{n}}^{\text{rh}}$ is the normal component of the ''shear'' orthorhombic vibration with D_{2h} symmetry. The Hamiltonian of teh crystal in the nearest-neighbors approximation of the transition in Eq. (13) or (14) to collective lattice vibrations (phonons) can be written the form[47]

$$\mathcal{H}=\mathcal{H}_{\text{mol}}+\mathcal{H}_{\text{tun}}+\mathcal{H}_{\text{el-vib}}, \tag{15}$$

where

$$\mathcal{H}_{\text{mol}}=\sum_{\mathbf{n},\sigma,\nu}\,\varepsilon_\nu a_{\mathbf{n}\nu\sigma}^+a_{\mathbf{n}\nu\sigma}+\sum_{\mathbf{n}}\,\omega_{JT}b_{\mathbf{n}}^+b_{\mathbf{n}}; \tag{16}$$

$$\mathcal{H}_{\text{tun}}=\sum_{\mathbf{n},\rho,\sigma}\,\sum_{\nu,\mu=12}\,t^{\nu\mu}a_{\mathbf{n}\nu\sigma}^+a_{\mathbf{n}+\rho,\mu\sigma}; \tag{17}$$

$$\mathcal{H}_{\text{el-vib}}=\frac{1}{\sqrt{N}}\sum_{\mathbf{n},\mathbf{q},\sigma}\,\sum_{\nu,\mu}\,\chi_{\mathbf{n}}^{\nu\mu}(\mathbf{q})a_{\mathbf{n}\nu\sigma}^+a_{\mathbf{n}\mu\sigma}[b(\mathbf{q})+b^+(\mathbf{q})], \tag{18}$$

where ε_ν is the energy of the molecular terms; ρ is the radius vector of the sites closest to the site $\mathbf{n}$ of the neighboring C_{60} molecule; $\chi_{\mathbf{n}}^{\nu\mu}(\mathbf{q})$ is the EPI matrix element with Jahn–Teller intramolecular modes; ω_{JT} is the average frequency of the deformational vibrations of C_{60} molecules with a transition into different charge states; $b_{\mathbf{n}}^+$ and $b_{\mathbf{n}}$ are Bose operators creating and annihilating, respectively, phonons for such vibrations; N is the number of C_{60} molecules in the crystal; $b^+(\mathbf{q})$ and $b(\mathbf{q})$ are operators creating and annihilating, respectively, phonons corresponding to these Jahn–Teller vibrations.

It is known[47] that the Hamiltonian (15) with the EPI in the form (18) can be exactly diagonalized by means of a unitary transformation $\exp\hat{S}$ where the antihermetian operator $\hat{S}$ is determined from the condition that the reconstructed Hamiltonian $\tilde{\mathcal{H}}$ have no terms which are linear in the Bose phonon operators, i.e. actually the operator (18). Using standard calculations[47,48] we obtain the following renormalized Hamiltonian for fullerite:

$$\begin{aligned}\tilde{\mathcal{H}}=&\sum_{\mathbf{n},\nu,\sigma}\,\varepsilon_\nu a_{\mathbf{n}\sigma}^+a_{\mathbf{n}\sigma}+\sum_{\mathbf{q}}\,\omega_{JT}(\mathbf{q})b^+(\mathbf{q})b(\mathbf{q})\\&+\sum_{\mathbf{n},\rho,\sigma}\,\sum_{\nu,\mu}\,\tilde{t}^{\nu\mu}a_{\mathbf{n}\nu\sigma}^+a_{\mathbf{n}+\rho,\mu\sigma}\\&-\sum_{\mathbf{n},\mathbf{m}}\,\tilde{V}_{\mathbf{nm}}^{\nu\mu}a_{\mathbf{n}\nu\uparrow}^+a_{\mathbf{n}\nu\uparrow}a_{\mathbf{m}\mu\downarrow}^+a_{\mathbf{m}\mu\downarrow},\end{aligned} \tag{19}$$

where $\omega_{JT}(\mathbf{q})$ is the phonon frequency corresponding to intramolecular Jahn–Teller modes; $\tilde{t}^{\nu\mu}$ is the renormalized (owing to the polaron effects) probability amplitude of electron (hole) hops between neighboring C_{60} molecules:

$$\tilde{t}^{\nu\mu}=t^{\nu\mu}\exp\left\{-\frac{1}{N}\sum_{\mathbf{q}}\,\left|\chi_{\mathbf{n}}^{\nu\mu}(\mathbf{q})\right|^2/\omega_{JT}^2(\mathbf{q})\right\}, \tag{20}$$

where $\tilde{V}_{\mathbf{nm}}^{\nu\mu}$ is the matrix element of the effective interaction of electrons at the sites $\mathbf{n}$ and $\mathbf{m}$, including the effective miniband interelectron attraction as a result of exchange of virtual phonons with frequency $\omega_{JT}(\mathbf{q})$:

$$V_{\mathbf{nm}}^{\nu\mu}=-\frac{1}{N}\sum_{\mathbf{q}}\,\chi_{\mathbf{n}}^{\nu\mu}(\mathbf{q})\chi_{\mathbf{m}}^{\nu\mu}(\mathbf{q})/\omega_{JT}(\mathbf{q}), \tag{21}$$

and screening of the Coulomb repulsion $\tilde{V}_C(|\mathbf{n}-\mathbf{m}|)>0$ which is greatest for electrons located on the same molecule ($\mathbf{n}=\mathbf{m}$) and in this case is, in order of magnitude, $\tilde{V}_C=e^2/2R_0\approx 2$ eV (neglecting polarization of the molecule). For relatively weak dispersion of the vibronic Jahn–Teller modes $\omega_{JT}(\mathbf{q})$ the interaction $V_{\mathbf{nm}}^{\nu\mu}$ is likewise different from zero only for $\mathbf{n}=\mathbf{m}$, which attests to the tendency for Cooper pairs to form with size equal to (or of the order of) the diameter of a C_{60} molecule).[1)]

The interelectron interaction Hamiltonian in Eq. (19), similar to the interaction Hamiltonian in the multiband BCS theory[11] in the site representation, can be written as

$$\tilde{\mathcal{H}}_{ee}=-\sum_{\mathbf{n},\mathbf{m}}\,\left[\sum_{\nu\mu}\,\left|V_{\mathbf{nm}}^{\nu\mu}\right|-\tilde{V}_C(|\mathbf{n}-\mathbf{m}|)\right]B_{\mathbf{nm}}^{+\,\nu\mu}B_{\mathbf{mn}}^{\mu\nu}, \tag{22}$$

where

$$B_{\mathbf{nm}}^{+\,\nu\mu}=a_{\mathbf{n}\nu\uparrow}^+a_{\mathbf{m}\mu\downarrow}^+;B_{\mathbf{mn}}^{\mu\nu}=(B_{\mathbf{nm}}^{+\,\nu\mu})^+. \tag{23}$$

The operators $B_{\mathbf{nm}}^{+\,\nu\mu}$ and $B_{\mathbf{mn}}^{\mu\nu}$ are analogs of the operators creating and annihilating spin-singlet Cooper pairs.[11] It follows from Eq. (22) that the effective attraction and the associated Cooper pairing of electrons located at the sites $\mathbf{n}$ and $\mathbf{m}$ are possible only if

$$\sum_{\nu,\mu}\,|V_{\mathbf{nm}}^{\nu\mu}|>\tilde{V}_C(\mathbf{n}-\mathbf{m}). \tag{24}$$

As follows from Eqs. (20) and (21), the lowest-frequency (''soft'') Jahn–Teller modes $\omega_{JT}(\mathbf{q})$ make the main contribution to the polaron band narrowing and to the interelectronic attraction as a result of the EPI. On the other hand it is evident from Eqs. (22)–(24) that from the standpoint of the Coulomb energy Cooper pairing of electrons (holes) on different and quite distant sites of the crystal lattice ($\mathbf{n}\neq\mathbf{m}$) is favorable when repulsion is weakened by screening effects. Consequently, when studying SC in fullerite crystals it is convenient to switch to the band (quasimomentum) representation and use the standard equations of the BCS theory.[11,44] according to which the critical temperature of the SC transition in the so-called tight-binding approximation[49] is determined, to a high degree of accuracy, by the expression[50–52]

$$T_c=\tilde{\omega}_{\text{ph}}\exp\left[-\frac{1+\lambda_{\text{ph}}}{\lambda_{\text{ph}}-\mu_C^*(1+\beta\lambda_{\text{ph}})}\right]. \tag{25}$$

Here $\tilde{\omega}_{\text{ph}}$ is the phonon frequency (energy) averaged over the phonon spectrum; in the present case it corresponds to the average value of the LF Jahn–Teller modes $\tilde{\omega}_{JT}$; the quan-

tity β is a dimensionless renormalization coefficient which depends on the form of the phonon spectrum;[51,52]

$$\lambda_{\rm ph}=\frac{1}{E_F}\sum_{\mathbf{n},\mathbf{m}}\sum_{\nu,\mu}|V^{\nu\mu}_{\mathbf{nm}}| \tag{26}$$

is the EPI constant per molecule; and, μ_C^* is the Coulomb pseudopotential,[11,53] which for $\tilde{\omega}_{JT_F}<E_F$ is

$$\mu_C^*=\mu_C[1+\mu_C\ln(E_F/\tilde{\omega}_{JT})]^{-1}, \tag{27}$$

where $\mu_C=\tilde{V}_C/E_F$ is the dimensionless Coulomb constant per molecule, which can be quite large in a narrow-band metal.

3.2. Isotopic effect

It is well known[53] that the additional dependence of μ_C^* on the phonon frequency $\tilde{\omega}_{\rm ph}\simeq\omega_{JT}\sim M^{-1/2}$ (where M is the atom mass) suppresses (weakens) the isotopic effect, which, according to Eq. (25), is determined by the index

$$\alpha_{\rm isot}\equiv\frac{\partial\ln T_c}{\partial\ln M}=\frac{1}{2}\left\{1-(1+\lambda_{\rm ph})(1+\beta\lambda_{ph})\times\left[\frac{\mu_C^*}{\lambda_{\rm ph}-\mu_C^*(1+\beta\lambda_{\rm ph})}\right]^2\right\}. \tag{28}$$

Considering the anomalously low Fermi energy in the multivalley narrow band "molecular" metal A_3C_{60} ($E_F\leqslant 2$ eV) and the characteristic value $\tilde{\omega}_{JT}\approx 500$ cm^{-1} (≈ 720 K) for the LF Jahn–Teller modes with transition from the high-symmetry state C_{60}^{3-} (orbital singlet with spin $S=3/2$) into the state C_{60}^{2-} (orbital triplet with spin $S=0$) with the maximum distortion,[46] we obtain $E_F/\tilde{\omega}_{JT}\approx 3$, $\mu_C^*\geqslant\mu_C(1+\mu_C)^{-1}\approx 1$, since $\mu_C\gg 1$. In turn, this means that for such st rong Coulomb repulsion very large values of the EPI constants $\lambda_{\rm ph}\gg 1$ are required to obtain quite high values of T_c.

One factor capable of increasing $\lambda_{\rm ph}$ substantially in A_3C_{60} crystals with the stoichiometric composition $x=3$ is the above-noted multivalley structure of the band spectrum.[22,23] This structure makes the metallic state stable [see criterion (4)] and must be taken into account in Eqs. (19) and (22) when summing over different electronic states ν and μ. The result of the latter is that in the high-symmetry A_3C_{60} cubic crystal or in the hexagonal lattice of C_{60} thin films the EPI constant (26) must be multiplied by a quite large factor $l(l-1)$, where l is the number of equivalent valleys (see Ref. 19).

On the other hand, according to Eq. (28), the large Coulomb pseudopotential should strongly suppress the isotopic effect. According to the experimental data obtained in Ref. 36 for K_3C_{60} and Rb_3C_{60} crystals with virtually complete substitution (99%) of the heavy isotope ^{13}C for ^{12}C atoms in the fullerene C_{60} molecule, the index of the isotopic shift of T_c lies in the range $\alpha_{\rm isot}=0.30\pm 0.06$, which indeed indicates strong suppression of the isotopic effect by the Coulomb interaction in accordance with Eq. (28). A somewhat larger value $\alpha_{\rm isot}=0.37\pm 0.05$ was obtained in Ref. 42 for partial substitution of ^{13}C for ^{12}C: the crystal contained 15% $^{12}C_{60}$ molecules and 85% partially substituted molecules $(^{12}C_{0.9}\,^{13}C_{0.1})_{60}$.

In Ref. 36, however, an unexpected and intriguing result was also obtained: for a mixed Rb_3C_{60} crystal containing 50% $^{12}C_{60}$ and $^{13}C_{60}$ the isotopic shift index $\alpha_{\rm isot}$ was anomalously large, $\alpha_{\rm isot}\approx 0.8$, i.e. substantially greater than the maximum possible value (on the basis of the harmonic approximation for phonons, when $\lambda_{\rm ph}$ is independent of M) $\alpha_{\rm isot}=0.5$. Even larger values of $\alpha_{\rm isot}$ ($\alpha_{\rm isot}\approx 1.0-2.5$) were obtained in Refs. 54–56 for different types of mixed crystals consisting of $^{12}C_{60}$ and $^{13}C_{60}$ molecules or partially substituted fullerene molecules $(^{12}C_{1-x}\,^{13}C_x)_{60}$ with different percentages of the ^{13}C isotope (33, 60, and 82%).

These anomalies of the isotopic effect have not yet been explained (see the review Ref. 6). However, in the concept presented above (Sec. 2) according to which the high symmetry of C_{60} molecules and stoichiometric A_3C_{60} crystals plays a key role the reason for the anomalously strong shift (decrease) of the critical temperature $|\Delta T_c|\geqslant 0.05T_c$ in mixed crystals $A_3(^{12}C_{60})_{1-x}(^{13}C_{60})_x$ or $A_3(^{12}C_{1-x}\,^{13}C_x)_{60}$ becomes understandable.[57]

In the solid solution $A_3(^{12}C_{60})_{1-x}(^{13}C_{60})_x$ with randomly distributed "light" $^{12}C_{60}$ and "heavy" $^{13}C_{60}$ fullerene molecules in lattice sites, incoherent elastic scattering of conduction electrons by "impurities" with partial (or complete) mixing of the states at the FL from different equivalent valleys in the BZ occurs (just as in crystals with nonstoichiometric composition A_xC_{60} with $x\neq 3$[19]). As a result, partial suppression of the factor $l(l-1)$ occurs in the EPI constant of a multivalley crystal $\tilde{\lambda}=l(l-1)\lambda_{\rm ph}$; this decreases T_c.

In $A_3(^{12}C_{1-x}\,^{13}C_x)_{60}$ crystals with partially substituted carbon isotopes in fullerene molecules, for x not very close to 0 or 1 a static distortion of the ideal shape of the C_{60} molecule occurs. This removes the degeneracy (additional splitting) of the electronic terms and eliminates from the EPI the relatively "soft" vibronic Jahn–Teller modes that increase T_c.[18,19]

In summary, it can be conjectured that the anomalous decrease of T_c in $A_3(^{12}C_{60})_{1-x}(^{13}C_{60})_x$ or $A_3(^{12}C_{1-x}\,^{13}C_x)_{60}$ crystals is not directly related with the suppression of the isotopic effect (25) with a strong EPI, but rather it is due to disorder or loss of icosahedral symmetry of the mixed fullerene molecules.

4. ROLE OF LOCAL-FIELD EFFECTS

Higher values of T_c can be achieved as a result of not only a higher DS in an additionally narrowed, as a result of polaron effects [see Eq. (20)], valence band but also the important role of the so-called "local-field effects," which the phonon $\Gamma_{\rm ph}$ and Coulomb Γ_C vertex parts (three-terminal diagrams) describe.

According to Migdal's theory[58] the nonadiabatic correction to the zero phonon vertex $\Gamma^0_{\rm ph}=1$ in metals is small to the extent that the ratio $\tilde{\omega}/E_F=\sqrt{m_e/M}$ is small. However, in the electron-doped narrow-band molecular metal A_3C_{60} the Fermi energy E_F of the electrons is comparable to the maximum energy of the phonons $\omega_{\rm ph}^{\max}\approx 0.2$ eV.

In this connection the nonadiabatic correction of first-order in the parameter $\lambda_{\rm ph}\tilde{\omega}_{\rm ph}/E_F$ to the equation for the SC gap was calculated as a function of the transferred momentum $\mathbf{q}$ and energy ω was calculated in a series of works for the simple model of an Einstein phonon spectrum with one

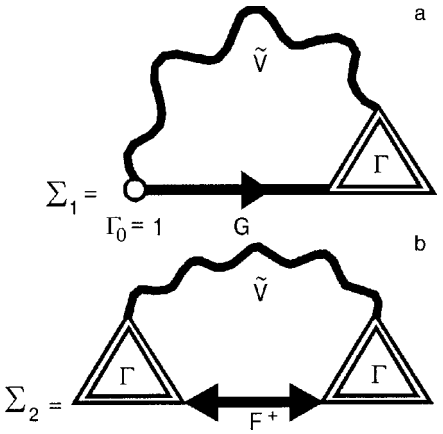

FIG. 1. Diagrammatic representations of the integral equations for the normal (a) and anomalous (b) self-energy parts. G and F^+ are the normal and anomalous one-electron Green's functions.

dispersion-free mode with energy $\omega_0 = E_F$.[59–63] As shown in Ref. 60, the leading correction of first order, actually corresponding to taking account of the first correction to the vertex function $\Gamma_{\rm ph}$, is determined by a function $P(\mathbf{q},\omega)$, which can be both positive and negative as a function of ω and $\mathbf{q}$. This means that the nonadiabatic effects in the EPI with $\tilde{\omega}_{\rm ph} \sim E_F$ can increase or decrease T_c and strengthen ($\alpha_{\rm isot} > 0.5$) or weaken ($\alpha_{\rm isot} > 0.5$) the isotopic effect (see Ref. 61).

However, it should be noted that the function $P(\mathbf{q},\omega)$ calculated in Ref. 60 in the limit $\omega \to 0$ reaches quite large values in absolute magnitude ($2P = 1$ for $q = 0$ and $2P = -1$ for $q > 0.5k_F$). This shows that higher-order terms must be taken into account, which was not done in Refs. 59–62.

At the same time, complete summation of all diagrams making the main contribution to the anomalous self-energy part $\Sigma_2(\mathbf{k},\omega)$ in a superconductor near T_c was performed in a previous work[63] taking account of the normal phonon or Coulomb vortices and the anomalous vertices containing the anomalous electron Green's functions.[64] It was found that the equation for $\Sigma_2(\mathbf{k},\omega)$ as $\omega \to 0$, in contrast to the equation for the normal self-energy part $\Sigma_1(\mathbf{k},\omega)$, contains not one vertex Γ but rather a product of two normal vertices (see Fig. 1). Hence follows directly that the EPI constant changes (increases or decreases) by the factor $\Gamma^2_{\rm ph}$. For small values of the parameter $\lambda_{\rm ph}\tilde{\omega}_{\rm ph}/E_F$, up to terms of first order this corresponds to the factor $(1+2P)$ obtained in Refs. 59–62. However, for $|P| \sim 1$ this approximation is inapplicable and results in large quantitative and possibly qualitative errors. Consequently, if the phonon vertex is defined as $\Gamma_{\rm ph} = 1 + P$, then according to Ref. 63 the factor which renormalizes the EPI constant and is due to local-field effects is $\Gamma^2_{\rm ph} = (1+P)^2$, which differs appreciably from the nonadiabatic correction $(1+2P)$ used in Refs. 59–62. In a more rigorous approach more accurate methods must be used to calculate $\Gamma_{\rm ph}$, for example, the Nambu approximation,[65] which satisfies the Ward identities[66] and is a good interpolation for $\Gamma_{\rm ph}$ in the region $\lambda_{\rm ph}\tilde{\omega}_{\rm ph}/E_F \sim 1$[67] between the two limiting cases $\lambda_{\rm ph}\tilde{\omega}_{\rm ph}/E_F \ll 1$[58] and $\lambda_{\rm ph}\tilde{\omega}_{\rm ph}/E_F \gg 1$, where Migdal's theorem is once again applicable.[67]

In this approximation the expression (see Refs. 65 and 67)

$$\Gamma(\mathbf{k},\omega;\mathbf{k}',\omega') = \frac{1}{2}[Z(\mathbf{k}+\mathbf{k}',\omega+\omega') + Z(\mathbf{k},\omega)], \quad (29)$$

where $Z(\mathbf{k},\omega)$ is the renormalization factor associated with the antisymmetric (odd in $\mathbf{k}$ and ω) part of the normal self-energy of the electrons $\Sigma^a_1(\mathbf{k},\omega) = 1/2[\Sigma_1(\mathbf{k},\omega) - \Sigma_1(-\mathbf{k},\omega)]$ following from the relation[49,58]

$$Z(\mathbf{k},\omega) = 1 - \frac{\Sigma^a_1(\mathbf{k},\omega)}{\omega} \quad (30)$$

determines the vertex part Γ for any nonlocal (retarded) interaction in the limit $T \to T_c$.

On the other hand an estimate of Γ which takes account of only the first renormalized correction Γ_1, containing the complete fermion (electron) and boson (specifically, phonon) lines (Fig. 2), also serves as a completely satisfactory approximation for two reasons. In the first place this "truncated" expression for Γ satisfies, to a high degree of accuracy, the Ward identities[66] in the static ($\omega/q \to 0, q \to 0$) and dynamic ($q/\omega \to 0, \omega \to 0$) limits. In the second place its use is fully justified by the fact that the higher-order diagrams starting with the second (with respect to the number of boson lines) are either numerically small because of the small volume of integration in momentum-energy space, as, for example, diagrams with intersecting boson lines (see Fig. 2), or largely compensate one another in each order of the renormalized perturbation theory because of opposite signs, as, for example, "ladder" diagrams containing an odd number of fermion loops (Furry's theorem).[68]

This result was recently confirmed in Ref. 69 by means of self-consistent numerical calculations of the Coulomb interaction in quasi-two-dimensional (layered) cuprate MOC with a strongly anisotropic electronic spectrum. It was found that the static Coulomb vertex $\Gamma_C(\mathbf{k}_\parallel, 0; \mathbf{q}_\parallel, 0)$ as a function of the transferred $2D$ momentum $\mathbf{q}_\parallel$ with electronic $2D$ momentum lying on a cylindrical Fermi surface ($\mathbf{k}_\parallel = \mathbf{k}_F$), differs very little in the first BZ with respect to absolute values

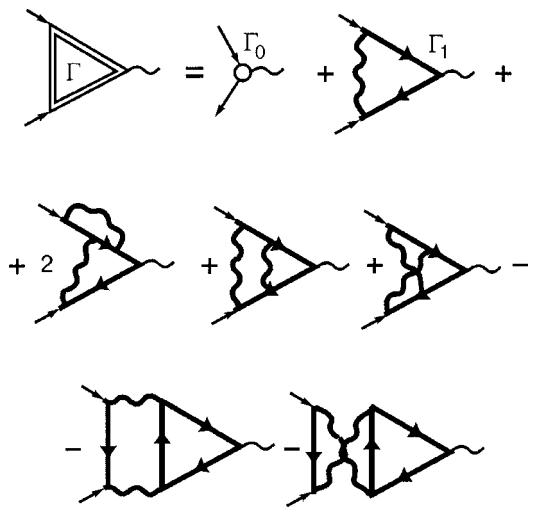

FIG. 2. First- and second-order diagrams in the renormalized perturbation theory for the normal vertex Γ. The diagrams containing one fermion loop have the opposite (negative) sign from diagrams without such loops.

and the fine structure and symmetry of the momentum dependence in calculations based on the Nambu approximation[55] or taking account of the first renormalized correction.

The question of the effect of the first correction to the Coulomb vertex Γ_C on the coupling constant and T_c for the ''plasma'' mechanism of superconductivity[70,71] in the so-called ''jellium'' model[44] was previously examined in Ref. 72. In this case the screening of the Coulomb repulsion and the retarded electron–plasmon interaction (or EPI) are described, as is well known, by a single Coulomb four-terminal diagram which depends on $\mathbf{q}$ and ω:

$$\tilde{V}_C(\mathbf{q},\omega)=\frac{4\pi e^2}{q^2\varepsilon(\mathbf{q},\omega)}, \tag{31}$$

where $\varepsilon(\mathbf{q},\omega)$ is the longitudinal permittivity (LP) of a two-component electron–hole (or electron-ion) system

$$\varepsilon(\mathbf{q},\omega)=1+\frac{\kappa^2}{q^2}-\frac{\Omega^2}{\omega^2}. \tag{32}$$

Here κ is the inverse screening radius due to ''light'' degenerate current carriers (s and p conduction electrons), and Ω is the plasma frequency of ''heavy'' charge carriers (d or f electrons, holes, ions). The summed interaction (31) corresponds to all renormalized (''dressed'') boson lines in the Feynman diagrams (Figs. 1 and 2). Thus even if the plasmon (or phonon) contribution to the vertex part Γ is small (in accordance with Migdal's theorem),[58] the ''nonadiabatic'' Coulomb contribution always remains because the Coulomb interaction exists at all energies and momenta so that $\Gamma\approx\Gamma_C\approx 1+\mu_C$.[73,74]

In addition, if a distinguished phonon mode with frequency $\omega(\mathbf{q})$, which makes the main contribution to the EPI (as, for example, the above-discussed softest Jahn–Teller mode in doped C_{60} fullerite crystals or the oxygen optical mode in cuprate crystals MOC, associated with vibrations of O^{2-} ions in CuO_2 layers, or the HF optical vibrational mode of light boron atoms in the SC compound MgB_2 with $T_c\approx 40$ K[75]), exists in the crystal, then the so-called ''plasma'' model of a metal[11] or the generalized ''jellium'' model[44] with the effective four-terminal diagram

$$\overline{V}_{\text{eff}}(\mathbf{q},\omega)=\frac{4\pi e^2}{q^2\varepsilon_{\text{eff}}(\mathbf{q},\omega)}, \tag{33}$$

where

$$\varepsilon_{\text{eff}}(\mathbf{q},\omega)=\varepsilon_e(\mathbf{q},\omega)-\frac{g_{\text{ph}}^2(\mathbf{q})}{V_C(\mathbf{q})}\frac{\omega^2(\mathbf{q})}{[1-g_{\text{ph}}^2(\mathbf{q})/V_C(\mathbf{q})]} \tag{34}$$

can be used to describe simultaneously a strong EPI and the Coulomb interaction (neglecting the weak EPI with other phonon modes). Here, ε_e is the longitudinal electronic LP, and $g_{\text{ph}}(\mathbf{q})$ and $V_C(\mathbf{q})$ are the matrix elements of the EPI and the unscreened Coulomb repulsion.

In this case, just as for the simple ''jellium'' model,[31] even for $\omega(\mathbf{q})\ll E_F$, when Migdal's theorem is applicable,[58] the Coulomb effects of the local field, which the factor $\Gamma_C^2\approx(1+\mu_C)^2$ determines, substantially strengthen the EPI.

As a result, for doped C_{60} fullerite, taking account of the multivalley structure of the band spectrum, the critical temperature of the SC transition for $\tilde{\omega}_{JT}\ll E_F$ can be estimated from the formula [compare with Eq. (25)]

$$T_c\approx\tilde{\omega}_{JT}\exp\left\{-\frac{1+\tilde{\lambda}_{JT}(1+\mu_C)}{\tilde{\lambda}(1+\mu_C)^2}\right\}; \tag{35}$$

$$\tilde{\Lambda}=\tilde{\lambda}_{\text{ph}}-\tilde{\mu}_C^*[1+\beta\tilde{\lambda}_{\text{ph}}(1+\mu_C)]; \tag{36}$$

$$\tilde{\lambda}_{\text{ph}}=\lambda_{\text{ph}}(l-1);$$

$$\tilde{\mu}_C^*=\frac{\mu_C}{1+\mu_C(1+\mu_C)^2\ln(E_F/\tilde{\omega}_{JT})}. \tag{37}$$

Equation (35) takes account of the fact that the normal self-energy part $\Sigma_1(\mathbf{k},\omega)$, determining the nonadiabatic renormalization of the coupling constant in the tight-binding approximation,[49] contains only one vertex $\Gamma\approx 1+\mu_C$.

It follows from Eqs. (35) and (36) that the multivalley structure of the electronic spectrum for $l>1$ increases the EPI constant substantially [almost by the factor l^2 (!)], while the Coulomb effects due to the local field weaken the Coulomb repulsion (decrease $\tilde{\mu}_C^*$) but increase the general renormalized coupling constant in the exponential function.

5. CONCLUSIONS

Insummary, the high initial symmetry of C_{60} fullerene molecules and the face-centered cubic crystals A_3C_{60} and the hexagonal lattice of intercallated films C_{60}/CHG_3 result, on the one hand, in a dynamic Jahn–Teller effect, which is manifested in the existence of comparatively soft electron–vibrational (vibronic) modes in the phonon spectrum of C_{60} fullerite and, on the other, in the multivalley structure of the degenerate band spectrum in a molecular narrow-band metal. The Coulomb and, possibly, phonon effects due to the local field, which can be described by the vertex parts $\Gamma_C>1$ and $\Gamma_{\text{ph}}>1$, together with the high DS, can give quite high values of T_c. We note, finally, that the Coulomb effects due to the local field, together with the strong anisotropy of the quasi-two-dimensional band spectrum, can play an important role in the mechanism of HTSC in cuprates.[74]

V. M. L. is partially supported by a SCOPES grant (Project 7UKP062150.00(1)) from the Swiss Science Foundation and E. A. P. is partially supported by a grant from the Swedish Royal Academy of Sciences.

[a)]E-Mail: vloktev@gluk.org
[b)]E-Mail: pashitsk@iop.kiev.ua
[c)]E-Mail: shekhter@fy. chalmers.se

[1)]We recall that the doubly charged cation C_{60}^{2-} is stable with a quite high binding energy due to the Jahn–Teller deformation.

[1] H. W. Kroto, J. T. Heath, S. C. O'Brien, R. F. Curl, and R. E. Smolley, Nature (London) **318**, 162 (1985).
[2] A. F. Hebard, M. J. Rosseisky, R. C. Haddon, D. W. Murphy, S. H. Glarum, T. T. M. Palstra, A. P. Ramirez, and A. R. Kortan, Nature (London) **350**, 600 (1991).
[3] R. M. Fleming, A. P. Ramirez, M. J. Rosseisky, D. W. Murphy, R. C. Haddon, S. M. Zahyrak, and A. Y. Makhija, Nature (London) **353**, 787 (1991).

[4] V. M. Loktev, Fiz. Nizk. Temp. **18**, 217 (1992) [Sov. J. Low Temp. Phys. **18**, 149 (1992)].
[5] A. P. Ramirez, Supercond. Res. **7**, 1 (1994).
[6] O. Gunnarssen, Rev. Mod. Phys. **69**, 575 (1997).
[7] A. A. Zakhidov, A. Ugawa, K. Imaeda, K. Yakushi, and H. Inokochi, Solid State Commun. **79**, 939 (1991).
[8] T. T. M. Palstra, O. Zhou, Y. Iwasa, P. E. Sulewski, R. M. Fleming, and B. R. Zagarshi, Solid State Commun. **93**, 327 (1995).
[9] Z. Igbal, R. H. Baughman, B. L. Ramakrishna, S. Khare, N. S. Murthy, H. J. Bornemann, and D. E. Morris, Science **254**, 826 (1991).
[10] M. J. Rosseinsky, A. P. Ramirez, S. H. Glarum, D. W. Murphy, B. C. Haddon, A. F. Habard, T. T. M. Palstra, A. R. Kortan, S. M. Zaburah, and A. V. Makhija, Phys. Rev. Lett. **66**, 2830 (1991).
[11] J. Schrieffer, *The Theory of Superconductivity*, Nauka, Moscow (1970).
[12] S. J. Duclos, K. Brister, R. C. Haddon, A. R. Kortan, and F. A. Thiel, Nature (London) **351**, 380 (1991).
[13] G. Sparn, J. D. Thompson, S.-M. Huang, R. B. Kaner, F. Diederich, B. J. Wetten, G. Grüner, and K. Holczer, Science **252**, 1829 (1991).
[14] C. Meigast, O. Kraut, T. Wolf, H. Wühl, A. Erb, and G. Müller-Volf, Phys. Rev. Lett. **67**, 1634 (1991).
[15] U. Welp, M. Grimsditch, S. Fisher, W. Nessler, B. Veal, and G. W. Crabtree, J. Supercond. **7**, 159 (1994).
[16] G. Meingast, A. Junod, and E. Walker, Physica C **C272**, 106 (1996).
[17] C. W. Chu, L. Gao, F. Chen, Z. J. Huang, R. L. Meng, and Y. Y. Xue, Nature (London) **365**, 323 (1993).
[18] V. M. Loktev and É. A. Pashitskiĭ, JETP Lett. **55**, 478 (1992).
[19] V. M. Loktev and É. A. Pashitskiĭ, Zh. Éksp. Teor. Fiz. **103**, 594 (1993) [JETP **76**, 297 (1993)].
[20] H. A. Jahn and E. Teller, Proc. R. Soc. London, Ser. A **161**, 220 (1937).
[21] A. P. Isakina, A. I. Prokhvatilov, M. A. Strezhemechnyĭ, and K. A. Yakotintsev, Fiz. Nizk. Temp. **27**, 1406 (2001) [Low Temp. Phys. **27**, 1037 (2001)].
[22] Y. Huang, D. F. R. Gilson, and I. S. Butler, J. Phys. Chem. **95**, 5723 (1991).
[23] S. Saito and A. Oshiyama, Phys. Rev. Lett. **66**, 2637 (1991).
[24] A. Georges, G. Kotliar, W. Krauth, and M. J. Rozenberg, Rev. Mod. Phys. **68**, 13 (1996).
[25] J. P. Lu, Phys. Rev. B **49**, 5687 (1994).
[26] C. L. Lof, M. A. van Veenendaal, B. Koopmans, H. T. Jonkman, and G. A. Sawatsky, Phys. Rev. Lett. **68**, 3924 (1992).
[27] K. Prassides, J. Tomkinson, Ch. Christides, M. J. Rosseinsky, D. W. Murphy, and R. C. Haddon, Nature (London) **354**, 462 (1991).
[28] Ch. Kloc, P. G. Simpkins, T. Siegrist, and R. A. Landise, J. Cryst. Growth **182**, 416 (1997).
[29] J. G. Hou, J. Yang, H. Wang, Q. Li, C. Zeng, I. Yuan, B. Wang, D. Chen, and Q. Zhu, Nature (London) **409**, 304 (2001).
[30] C. A. Al'tshuler and B. N. Kozyrev, *Electron Paramagnetic Resonance*, Nauka, Moscow (1972).
[31] V. M. Loktev, Fiz. Nizk. Temp. **27**, 561 (2001) [Low Temp. Phys. **27**, 414 (2001)].
[32] V. A. Kuprievich, O. L. Kapitanchuk, and O. V. Shramko, Preprint cond-mat/0206290 (2002).
[33] L. D. Landau and E. M. Lifshitz, *Quantum Mechanics*, Nauka, Moscow (1963).
[34] É. Kamke, *Handbook of Ordinary Differential Equations*, Nauka, Moscow (1976).
[35] P. E. Lammert, D. S. Rokhsar, S. Chakravarty, S. Kivelson, and M. I. Salkola, Phys. Rev. Lett. **74**, 996 (1995).
[36] C.-C. Chen and C. M. Lieber, J. Am. Chem. Soc. **111**, 3141 (1992); Science **259**, 655 (1993).
[37] A. F. Hebbard, Phys. Today **45**, No. 11, 26 (1992).
[38] C. M. Vaa, J. Zaanen, and K. Raghavachari, Science **254**, 989 (1991).
[39] M. Schluter, M. Lannoo, M. Needels, G. A. Baraff, and D. Tomanek, J. Phys. Chem. Solids **53**, 1473 (1992).
[40] J. C. R. Faulhabor, D. Y. K. Ko, and P. R. Briddon, Phys. Rev. B **48**, 661 (1993).
[41] V. P. Antropov, O. Gunnarsson, and A. I. Liechtenstein, Phys. Rev. B **48**, 7651 (1993).
[42] A. P. Ramirez, A. R. Kortan, M. J. Rosseinsky, S. J. Duclos, A. M. Mujsce, R. C. Haddon, D. W. Murphy, A. V. Makhija, S. M. Zahurak, and K. B. Lyons, Phys. Rev. Lett. **68**, 1058 (1992).
[43] A. P. Ramirez, M. J. Rosseinsky, D. W. Murphy, and R. C. Haddon, Phys. Rev. Lett. **69**, 1687 (1992).
[44] V. L. Ginzburg and D. A. Kirzhnits [Eds.], *The Problem of High-Temperature Superconductivity*, Nauka, Moscow (1977).
[45] D. Rainer, Prog. Low Temp. Phys. **10**, 371 (1986).
[46] W. H. Green Jr., S. M. Gorin, G. Fitzgerald, P. W. Fowler, A. Ceulemans, and B. C. Titeca, J. Phys. Chem. **100**, 14892 (1996).
[47] A. S. Davydov, *The Theory of Molecular Excitons*, Nauka, Moscow (1968).
[48] V. M. Loktev and Yu. G. Pogorelov, Fiz. Nizk. Temp. **26**, 271 (2000) [Low Temp. Phys. **26**, 171 (2000)].
[49] G. M. Éliashberg, Zh. Éksp. Teor. Fiz. **38**, 966 (1960) [Sov. Phys. JETP **11**, 696 (1960); **39**, 1437 (1960); **12**, 1000 (1961)].
[50] W. L. McMillan, Phys. Rev. **167**, 331 (1968).
[51] M. V. Medvedev, É. A. Pashitskiĭ, and Yu. S. Pyatiletov, Zh. Éksp. Teor. Fiz. **65**, 1186 (1973) [Sov. Phys. JETP **38**, 587 (1973)].
[52] A. E. Karakozov, E. G. Maksimov, and S. A. Mashkov, Zh. Éksp. Teor. Fiz. **68**, 1937 (1975) [Sov. Phys. JETP **41**, 971 (1976)].
[53] P. Morel and P. W. Anderson, Phys. Rev. **125**, 1263 (1963).
[54] T. W. Ebbsen, J. S. Tsai, K. Tanigaki, J. Tabuchi, Y. Shimakawa, Y. Kubo, I. Hirosawa, and J. Mizuki, Nature (London) **355**, 620 (1992).
[55] A. A. Zakhidov, K. Imaeda, D. M. Petty, K. Yakushi, H. Inokichi, K. Kikuchi, I. Ikemoto, S. Suzuki, and Y. Achida, Phys. Lett. A **164**, 355 (1992).
[56] P. Auban-Senzier, G. Ouirion, D. Jerome, P. Bernier, S. Della-Negra, C. Fabre, and A. Rassat, Synth. Met. **56**, 3027 (1993).
[57] D. M. Deaven and D. S. Rokhsar, Phys. Rev. B **48**, 4114 (1993).
[58] A. V. Migdal, Zh. Éksp. Teor. Fiz. **34**, 1438 (1958) [Sov. Phys. JETP **7**, 996 (1958)].
[59] L. Pietronero, Europhys. Lett. **17**, 365 (1992).
[60] L. Pietronero and S. Strasslen, Europhys. Lett. **18**, 627 (1992).
[61] C. Grimaldi, L. Pietronero, and S. Strasslen, Phys. Rev. Lett. **75**, 1158 (1995); Phys. Rev. B **52**, 10530 (1995).
[62] L. Cappeluti, C. Grimaldi, L. Pietronero, and S. Strasslen, Phys. Rev. Lett. **85**, 4771 (2000).
[63] O. V. Dolgov, D. A. Kirzhnits, and E. G. Maksimov, Rev. Mod. Phys. **53**, 81 (1981).
[64] A. A. Abrikosov, L. P. Gor'kov, and I. E. Dzyaloshinskiĭ, *Methods of Quantum Field Theory in Statistical Physics*, Fizmatgiz, Moscow (1962).
[65] Y. Nambu, Phys. Rev. **117**, 648 (1960).
[66] J. M. Luttinger and J. C. Ward, Phys. Rev. **118**, 1417 (1960).
[67] Y. Takada, J. Phys. C **54**, 1779 (1993).
[68] A. I. Akhiezer and V. Ya. Berestetskiĭ, *Quantum Electrodynamics*, Nauka, Moscow (1969).
[69] É. A. Pashitskiĭ and V. I. Pentegov, Fiz. Nizk. Temp. **27**, 140 (2001) [Low Temp. Phys. **27**, 103 (2001)].
[70] H. Fröhlich, Proc. Roy. Soc. **C1**, 544 (1968).
[71] É. A. Pashitskiĭ, Zh. Éksp. Teor. Fiz. **55**, 2387 (1968) [Sov. Phys. JETP **28**, 1267 (1969)].
[72] É. A. Pashitskiĭ and V. M. Chernousenko, Zh. Éksp. Teor. Fiz. **60**, 1483 (1971) [Sov. Phys. JETP **33**, 802 (1971)].
[73] É. A. Pashitskiĭ, JETP Lett. **57**, 648 (1993).
[74] É. A. Pashitskiĭ, Fiz. Nizk. Temp. **21**, 995 (1995) [Low Temp. Phys. **21**, 763 (1995)].
[75] J. Nagamatsi, N. Nakagawa, T. Muranaka, Y. Zenitani, and J. Akimutsu, Nature (London) **410**, 63 (2001).

Translated by M. E. Alferieff

Magnetic polarons in Y–Ba–Cu–O chains

V. V. Eremenko, D. V. Lukashev, and B. L. Ponomarchuk*

B. I. Verkin Physicotechnical Institute for Low Temperatures, Ukrainian Academy of Sciences, pr. Lenina, 47, Khar'kov, 61103, Ukraine

(Submitted April 15, 2002)
Fiz. Nizk. Temp. **28**, 1163–1178 (November 2002)

Mössbauer spectroscopy is used to study electron self-localization in the superconducting cuprate paramagnetic compound Y–Ba–Cu–O. It is shown that the electrons in chains with self-localization form a phase with local magnetic ordering and relaxation time greater than 10^{-7} s. Analysis of the magnitude of the accompanying charge redistribution suggests that when an electron undergoes self-localization a pair of exchange-coupled electrons localized predominantly on the oxygen is formed. Such a quasiparticle, consisting of a pair of antiferromagnetically oriented atomic moments and a pair of self-localized electrons, possesses integral spin and can form a Bose condensate. © *2002 American Institute of Physics.*
[DOI: 10.1063/1.1528574]

1. INTRODUCTION

The concept of a polaron, introduced by Pekar,[1] follows from Landau's idea of electron self-localization.[2] A self-localized electron polarizes the ionic lattice. The polarized lattice, in turn, is a source of an additional self-consistent field which acts on the electron. An electron moving through a crystal transports, together with itself, a region of the deformed lattice. In Ref. 3 Nagaev proposed, by analogy, a model of a magnetic polaron. Of all the diverse models of magnetic polarons we shall study the model developed in Nagaev's works.[4,5] This model makes it possible to explain the coexistence of magnetic and superconducting phases in layered cuprates. In this model it is assumed that a self-localized electron in a paramagnetic medium gives rise to local magnetic ordering of a pair of atomic magnetic moments, since an exchange-interaction parameter arises in its region of localization. It is also conjectured that a pair of ferromagnetically oriented spins and an additional electron migrate through the crystal and transport charge. Further elaboration of this idea reduces to the conjecture that the pairs of these quasiparticles can form a Bose condensate, which could result in the appearance of superconductivity.

In Ref. 6 a model of electron self-localization in chain positions was used to explain the anomalous decrease in the area of the Mössbauer spectrum of a $YBa_2(Cu_{0.98}{}^{57}Fe_{0.02})_3O_{6.95}$ sample at temperatures below 80 K. It was conjectured that a paramagnetic impurity with a very long relaxation time of the magnetic moment appears in the normal paramagnetic medium. Here, a long time is a time greater than the lifetime of nuclei in the excited state (10^{-7} s). In this case two systems of lines should be observed in the spectrum. The normal paramagnetic phase is represented by a narrow single line or a doublet, if the quadrupole interaction is not small. A paramagnetic center with a long relaxation time can be described by at least two Zeeman six-component spectra (sextuplets), corresponding to spin projections 5/2 and 3/2.[7] In this case the outermost lines of the sextuplets move beyond the limits of the observable central part of the spectrum; this results in the apparent decrease in the probability of the Mössbauer effect. These sextuplets are difficult to observe experimentally, since the variance of the local fields at the quasimagnetic impurity centers is large, which produces substantial line broadening.

Various research groups have observed the magnetic components in the spectra of superconducting samples. Magnetic phase diagrams are constructed in Ref. 8. According to these diagrams the magnetic splitting in the Cu1 positions is observed at temperatures below 20 K. Three sextuplets can be resolved in the spectrum. The lowest concentration of the doping isotope ^{57}Fe relative to copper was $x=0.05$. Mössbauer spectra of superconducting samples with $x=0.01$, 0.02, 0.04, and 0.08 are presented in Refs. 9 and 10. At $T=1.3$ K a single magnetic sextuplet is observed in the sample with $x=0.01$ and two magnetic sextuplets are observed in the samples with $x=0.02$ and 0.04. At 4.2 K only line broadening is observed in the spectra of samples with the indicated composition. We were not able to identify the magnetic substructure in the spectrum of at $YBa_2(Cu_{0.98}{}^{57}Fe_{0.02})_3O_{6.95}$ at 4.2 K.

A decrease in the area of the observed spectrum at temperatures below 30 K accompanied by line broadening has also been observed in samples of the 1–2–4 system.[11] The area of the spectrum is a factor of 2 smaller, but no new lines are observed. The authors attributed this anomalous behavior to the appearance of a soft mode in the vibrational spectrum of the crystal. Its appearance does indeed decrease the probability of the Mössbauer effect near a phase transition, but as temperature decreases further, the probability should once again follow the Debye–Waller function. In our case, however, as temperature decreased, the areas of the quadrupole doublets decreased and the derivative continued to increase, which favors the phase-separation model. Since there is no long-range order, the magnetic phase is represented by a superposition of Zeeman sextuplets with different magnitudes of the hyperfine interaction parameters, making it difficult to observe the phase.

To determine the parameters of the subsystem experimentally the iron impurity concentration must be increased.

However, this can result in the formation of magnetic clusters and destroy superconductivity. There arises the obvious question of whether or not iron nuclei are probes that induce a change in the parameters of the superconducting phase. A compromise solution must be found.

The temperature changes in the Mössbauer parameters, which are sensitive to a redistribution of the charge density, were investigated at comparatively high temperatures and near the superconducting transition, where the magnetic structure is not observed in a superconducting sample. When electrons in chain positions undergo self-localization the neighboring lattice sites in the normal paramagnetic state should react to the appearance of an additional electron nearby. In this case the temperature changes of the parameters of the isomeric shift and the quadrupole interaction are observed. It is important to note that these parameters are sensitive to the sign of the charge of a self-localized carrier; this makes it possible to distinguish a hole from an electron polaron.

In addition to the investigations performed on a superconducting sample measurements of the parameters of the model sample—magnetically ordered and oxygen depleted—were performed. The removal of one oxygen (for example, by heating in vacuum) frees two electrons. As a result, the electron density at the metal nuclei should change; this should be manifested as a change in the isomeric shift. In addition, an increase of the electron density at oxygen sites results in the appearance of long-range magnetic ordering, since the indirect exchange interaction parameters increase. Charge redistribution also changes the magnitude of the quadrupole interaction.

It is known that irradiation with visible light influences positively the superconducting transition temperature of samples with intermediate oxygen composition. In Ref. 12 we observed a change in the hyperfine interaction parameters in a magnetically ordered sample which was irradiated with a helium–neon laser. As far as we know, oxygen-saturated superconducting samples do not show under illumination any appreciable changes in the controllable parameters. In this connection, in the present work a superconducting sample is subjected to prolonged photoirradiation at low temperatures. The room-temperature Mössbauer spectra of a sample before and after irradiation were compared.

2. EXPERIMENTAL PROCEDURE

A constant-acceleration spectrometer with a reversible accumulation regime was used for the Mössbauer measurements. A digital–to–analog converter, which formed the reference velocity signal of the source, was connected directly to the address register of the multichannel analyzer. The velocity law was triangular and not the conventional saw shape. This saved time, decreased the nonlinear distortions of the system for moving the source, substantially decreased the ''harmful'' dip in the spectrum, making it possible to fit a straight line to the background when processing the results. A detection system with high long-term stability is needed to measure the temperature dependences of the absolute area of an absorption line. To this end a feedback system consisting of two discriminators, a two-channel integrator, and a difference-signal amplifier, which controlled the power supply of the proportional counter, was built.

As the radioactive source decays, the ratio between the intensities of the emission lines—Mössbauer and a side x-ray line—changes. Since the discriminator cannot suppress the harmful radiation completely, the experimental area of the spectrum depends on the time. To eliminate this drawback the spectrum of a standard sample was obtained before and after a series of measurements and the appropriate time correction was introduced.

The temperature measurements were performed in a flow-through cryostat with a temperature stabilization system (the temperature instability did not exceed 0.1 K). The main advantage of such a cryostat for Mössbauer spectra measurements is that during the entire measurement series (several months) it is not necessary to disassemble the cryostat to change the temperature interval and correspondingly there is no danger of the samples being moved. In addition, round-the-clock measurements can be performed in an automatic mode.

The $YBa_2(Cu_{1-x}{}^{57}Fe_x)_3O_{6+\delta}$ samples were fabricated using the standard ceramic technology. The samples were tested by methods of x-ray structural and chemical analyses. The oxygen index was normalized relative to copper. It was assumed that each iron cation encompasses additionally 0.5 oxygen atoms. For the Mössbauer measurements the powder of the sample (grain size $\sim 10\ \mu$m) was inserted into paraffin with rosin and then placed between thin layers of aluminum. Special attention was devoted to the absence of texture. For control purposes the spectra were measured at the magic angle with respect to the plane of the sample using the procedure of Ref. 6. The absence of texture makes it possible to describe the quadrupole doublets by lines of equal area, and the magnetic sextuplets by lines of its relative areas 3:2:1:1:2:3, which makes it possible to use fewer variable parameters when analyzing the spectra. One side of the sample intended for irradiation was covered with a mica plate. The superconducting sample in a pulverized form was also tested for the Meissner effect in liquid nitrogen. An oxygen-depleted sample was annealed in vacuum. For the superconducting sample $x=0.06$ and $\delta=1$. For the depleted sample $x=0.08$ and $\delta=0.3$.

3. EXPERIMENTAL RESULTS

3.1. Superconducting sample

The typical spectra of a superconducting sample are presented in Fig. 1. A model of three quadrupole doublets describes all spectra well. The doublets correspond to three positions of the ^{57}Fe atoms, which replace copper in the Cu1 positions, and differ by the oxygen environment in the chain plane CuO_δ.[6] The doublet $d1$ corresponds to twinning boundaries with two oxygens in the nearest-neighbor environment. The electric-field gradient is negative and directed along the **c** axis. The doublet $d2$ corresponds to a chain position with an extra oxygen. The field gradient is positive and directed along the **a** axis. The doublet $d3$ corresponds to a position where oxygen occupies both nearest vacancies. The field gradient is positive and directed along **b** axis.

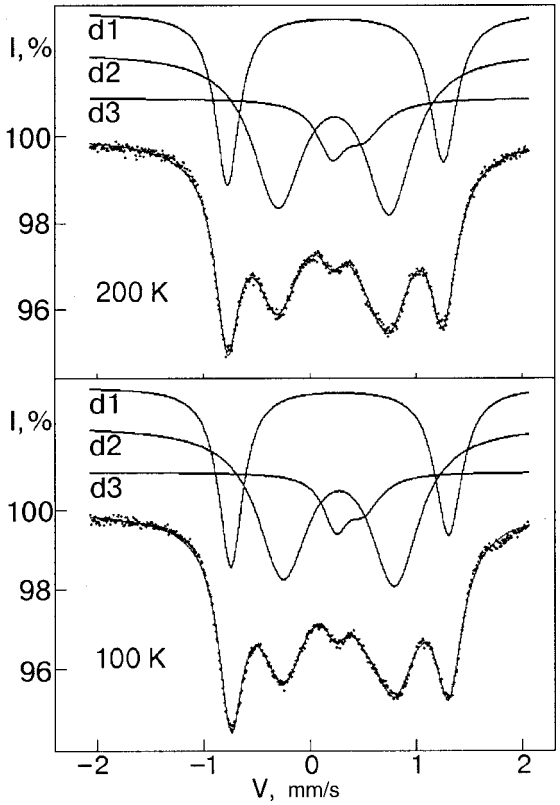

FIG. 1. Mössbauer spectra of the superconducting sample $YBa_2(Cu_{0.94}{}^{57}Fe_{0.06})_3O_7$ at different temperatures. The decomposition of the spectra in a model of three quadrupole doublets is shown.

The temperature dependence of the total area of the spectrum is presented in Fig. 2. The area of the spectrum is normalized to the magnitude of the background. The following function was used to describe the experimental temperature dependence of the total area of the spectrum:

$$S(T)=\{1-W_1L(T_1,T)-W_2L(T_2,T)\}f_D,$$

where $L(T_i,T)$ is the Langevin function, W_i is a weighting factor, and f_D is the Debye–Waller function.

The Langevin function is used to describe the temperature dependence of the magnetization of paramagnets: $L(a)=\coth(a)-1/a$, where $a=\mu H/kT=T_i/T$. We assume that the effective field H due to the self-localization of an additional electron acts on the atomic magnetic moment μ.

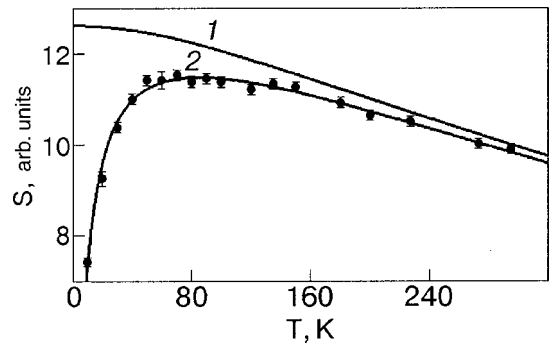

FIG. 2. Temperature dependence of the normalized total area S of the spectrum of a superconducting sample $YBa_2(Cu_{0.94}{}^{57}Fe_{0.06})_3O_7$. The Debye–Waller function *(1)*; a function *(2)* taking account of the existence of a paramagnetic impurity with a long relaxation time is fit to the experimental points.

The iron and copper atoms differ by the magnitudes of their magnetic moments. Therefore the binding energy of a self-localized electron is different for Cu–Cu, Cu–Fe, and Fe–Fe pairs. The Mössbauer method makes it possible to monitor only pairs containing iron. Therefore at least two types of traps must be introduced into the approximating function.

The function

$$P_z(\nu,n)=\frac{z!}{\nu!(z-\nu)!}n^{\nu}(1-n)^{(z-\nu)},$$

where n is the iron concentration relative to copper, gives the probability that a Fe atom has among z closest neighbors υ Fe atoms.[13] For $x<0.1$ the iron atoms replace copper predominantly in the CuO_δ chains. Therefore $n=3x$. Assuming that an interaction is possible not only between neighboring metal atoms along the chain but also between neighboring chains, we set $z=4$. Hence for $x=0.06$ we estimate the relative concentration of Fe–Cu pairs as $W_1=0.45$. We take $W_2=0.55$ for Fe–Fe pairs. The Debye–Waller function is[7]

$$f_D=S_0\exp\left\{-\frac{6E_R}{k\theta_D}\left(\frac{1}{4}+\left(\frac{T}{\theta_D}\right)^2\int_0^{\theta_D/T}\frac{xdx}{\exp(x)-1}\right)\right\},$$

where S_0 is a normalization constant (depends on the thickness of the sample), E_R is the recoil energy of a free nucleus, θ_D is the Debye temperature, and k is Boltzmann's constant.

The least-squares method was used to determine the values of the adjustable parameters. The Debye temperature $\theta_D=356$ K, the thermal activation parameters are $T_1=7.3(5)$ K and $T_2=21.5(6)$ K, and the parameter $S_0=13.88$.[1)] This parameter must also be varied, since it is difficult to determine the thickness of the sample precisely at the location where the γ quanta strike. The Debye–Waller function with these parameters is displayed at the top of Fig. 2; this makes it possible to estimate the scales of the redistribution of the areas. The Debye approximation is valid for a crystal consisting of identical atoms. We neglect the contribution of optical vibrational modes, i.e. a possible change in the probability of the Mössbauer effect as a result of renormalization of the phonon spectrum. It should also be noted that if the area of the spectrum being observed decreases because of the appearance of magnetic sextuplets, then for reasonable values of the magnetic hyperfine field two central lines with relative intensities equal to 1 will remain within the doublet spectrum; this will result in a somewhat high value of the total area of the doublets. Comparing the curves in Fig. 2 shows that even at high temperatures the relative concentration of the magnetic impurities is of the order of 3%, which should be observable in measurements of the magnetic properties. The presence of this impurity could make it possible to texture samples in relatively weak magnetic fields.[6]

Figure 3 shows the temperature dependences of the relative areas of the doublets. The relative probability of the formation of a magnetic phase is highest for the third doublet. The positions corresponding to various doublets differ only by the number of oxygen atoms in the nearest-neighbor environment. The maximum number of oxygen atoms corre-

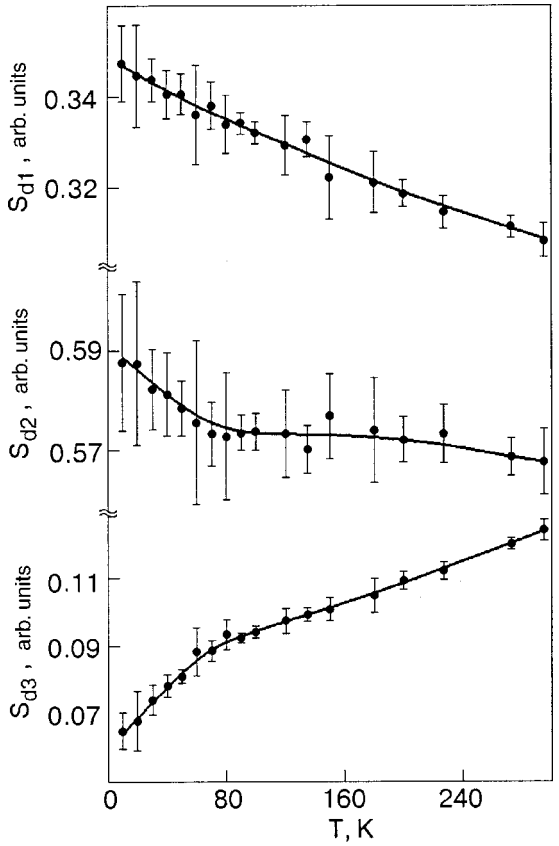

FIG. 3. Temperature dependences of the relative areas S of the quadrupole doublets $d1$, $d2$, and $d3$ in $YBa_2(Cu_{0.94}{}^{57}Fe_{0.06})_3O_7$. The lines are drawn for clarity.

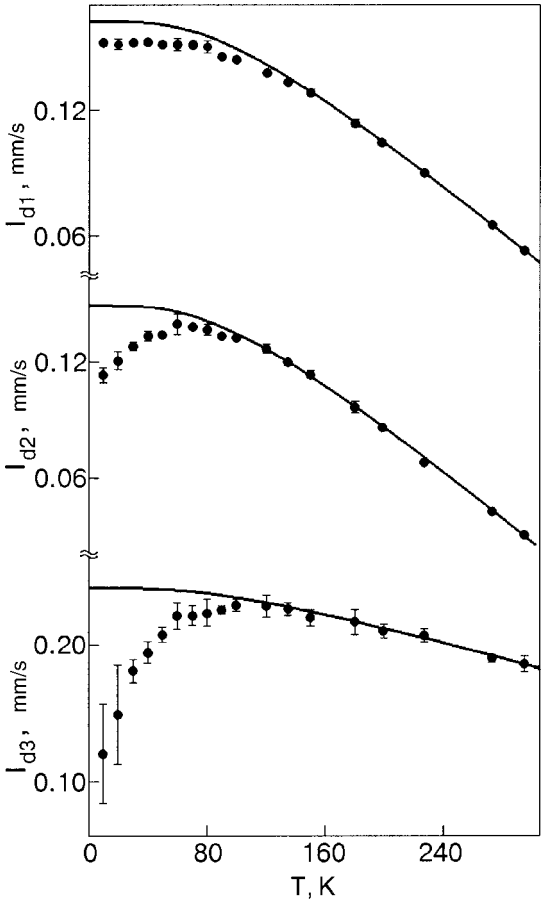

FIG. 4. Temperature dependences of the isomeric shift I of the quadrupole doublets $d1$, $d2$, and $d3$ in spectra of the sample $YBa_2(Cu_{0.94}{}^{57}Fe_{0.06})_3O_7$. The isomeric shift is presented relative to iron. The solid lines show the computed dependences of the temperature shift in the Debye approximation.

sponds to the third doublet. Hence we conjecture that electron self-localization occurs on a triplet of atoms: three paramagnetic metal atoms with an oxygen atom in between. Thus we arrive at an element of an antiferromagnet with an indirect exchange interaction via oxygen.[4]

We shall now consider the temperature variations of the Mössbauer parameters, which depend on the redistribution of the charge density. Electron self-localization in chain positions should be accompanied by a change in the local electric field in some nearest neighbor environment. In addition, according to the Pauli principle the appearance of an extra electron will increase the electron density on neighboring nuclei.

The isomeric shift (position of the center of the spectrum relative to a standard) depends on the magnitude of the electron density on a nucleus (monopolar interaction Δ_i)[7] and on the temperature shift (quadratic Doppler effect, associated with the vibrations of nuclei in a crystal). In the Debye approximation the isomeric shift is given by the formula[14]

$$I_i=\Delta_i-K_i\frac{9k\theta_D}{16mc}\left[1+8\left(\frac{T}{\theta_D}\right)^4\int_0^{\theta_D/T}\frac{x^3dx}{\exp(x)-1}\right],$$

where m is the mass of the nucleus and c is the velocity of light. The dimensionless coefficient K_i (of the order of 1) is introduced to take account of the different bond stiffnesses in crystallographic positions. This parameter makes it possible to describe the temperature dependences of isomeric shifts for various doublets with the same Debye temperature. A thin plate of pure iron with the natural concentration of ^{57}Fe was used as a standard for the zero isomer shift. Using the Debye temperature $\theta_D=356$ K obtained above and adjusting the parameters Δ_i and K_i we fit the theoretical function to the experimental points. The result is presented in Fig. 4. At high temperatures the agreement is satisfactory. The values of the parameters for the doublets at high temperatures are found to be as follows:

$$\Delta_1\approx 0.245 \text{ mm/s}, \quad K_1=0.819;$$

$$\Delta_2\approx 0.235 \text{ mm/s}, \quad K_2=0.885;$$

$$\Delta_3\approx 0.282 \text{ mm/s}, \quad K_3=0.415.$$

The elastic coupling parameter for the third doublet is half the values for the first two doublets. This means that for a given position the rms vibrational rate is less or greater than the characteristic acoustic frequency. We note that in an alternative description, setting $K_3=1$, the Debye temperature for the third doublet will be 1042 K and the isomeric shift will be 0.517 mm/s, which evidently is unacceptable.

At low temperatures the experimental points deviate substantially from the theoretical functions. It is natural to attribute this discrepancy to an increase in the $4s$-electron density. The theoretical dependences of the isomeric shift of ^{57}Fe on the electron charge density were calculated using the Hartree–Fock method (see Ref. 7). For the isomeric shifts obtained above, at high temperatures (the values of Δ_i are

taken relative to iron) it follows from the plot presented in Ref. 7 that for the $3d^5 4s^x$ configuration the $4s$-electron density is $x \simeq 0.03$. For the $3d^6 4s^x$ configuration we obtain x of the order of 0.38 and in the $3d^7 4s^x$ configuration $x \simeq 0.8$. However, it is unlikely that the latter configuration occurs in oxides.

At 10 K the largest deviation from the theoretical function (0.1 mm/sec) is observed for the third doublet (see Fig. 4). If it is assumed that the configuration $3d^5 4s^x$ is realized for this doublet, since all oxygen vacancies in the nearest-neighbor environment are filled, then this deviation means that the increase in charge density is due to the addition of 0.027 electrons. The deviation for the second doublet (0.04 mm/s) is smaller, but if it is assumed that the doublet corresponds to the configuration $3d^6 4s^x$, then the addition of 0.016 electrons compensates this deviation. The first doublet corresponds to a twinning boundary. The probability of electron self-localization could be smallest in this region of the crystal, as a reult of which the deviation of the isomeric shift is smallest. The temperature dependence of the relative area of this doublet suspports this idea (see Fig. 3).

Therefore the experimental dependences of the isomeric shifts attest to an increase in the electron density in chain positions as temperature decreases. The largest observed effect corresponds to the addition of 0.027 s–type electrons at iron nuclei.

The quadrupole interaction, which is sensitive to a change in the charge distribution, is manifested in the splitting of the energy levels of nuclei in a nonuniform electric field. The quadrupole moment of the nucleus and the electric-field gradient influence the magnitude of the splitting. The atomic electrons are polarized in the nonuniform field geberated by external charges and likewise contribute to the field gradient at the nucleus. For trivalent iron the inner electrons and five outer electrons with the configuration of a half–filled d shell, becoming polarized, increase the field gradient at the nucleus by almost an order of magnitude. This circumstance is taken into account by introducing the Sternheimer antiscreening factor $(1-\gamma_{\text{inf}})$, which is a scalar.[7] As a rule, the outer s–type valence electrons make a negative contribution to the gradient. If the field gradient due to external charges is positive, then the f electron shell is elongated in the direction of the gradient and the contribution of this shell to the total gradient will be negative. However, if the gradient is negative, then the electron shell is polarized in the plane perpendicular to the gradient, and the contribution of the shell is positive. In the second case the magnitude of the contribution due to one electron is two times smaller with other conditions remaining the same.[15] It is obviously impossible to take account of the influence of the valence electrons merely by introducing a coefficient; the charge density distribution function must be found.[16]

The electric field gradient tensor was diagonalized by choosing an appropriate coordinate system. The diagonal components of the electric field gradient tensor due to external point charges were calculated using the formula[7]

$$V_{aa} = \sum_i \frac{z_i}{r_i^3}(3\cos^2\theta_i - 1),$$

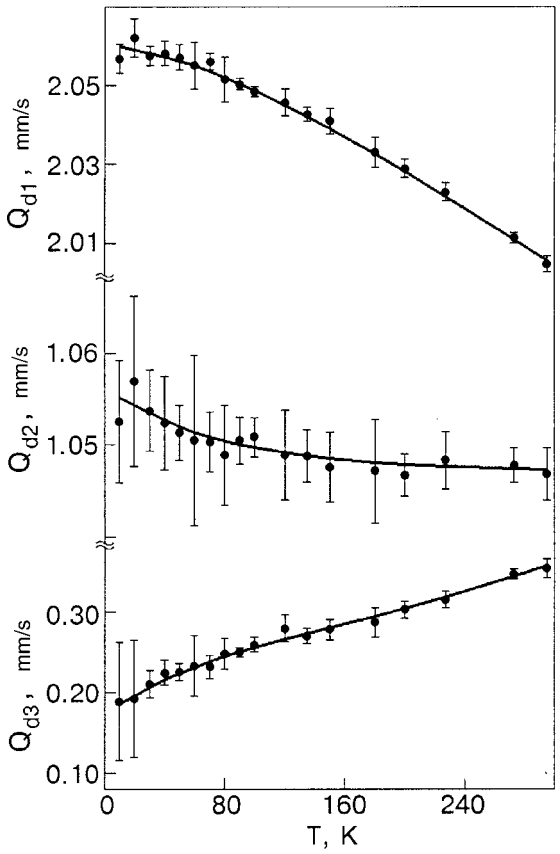

FIG. 5. Temperature dependences of the quadrupole splitting of the doublets of $YBa_2(Cu_{0.94}{}^{57}Fe_{0.06})_3O_7$. The lines are drawn for clarity.

where r_i is the distance from the charge z_i and θ_i is the total angle.

The sum over lattice sites can be conveniently calculated if the charge is expressed in units of the electron charge and the distance in angstroms.[17] Conventionally, a local coordinate system where $|V_{zz}| > |V_{yy}| > |V_{xx}|$ is used. We note that $V_{zz} + V_{yy} + V_{xx} = 0$.[7]

Introducing the asymmetry parameter

$$\eta = (V_{xx} - V_{yy})/V_{zz}$$

and $q = V_{zz}$, the formula for the quadrupole splitting on trivalent iron can be put into the form

$$\Delta E = \frac{1}{2} e^2 q Q (1-\gamma_\infty)\sqrt{1+\eta^2/3},$$

where e is the electron charge and Q is the quadrupole moment of the nucleus.

The quadrupole moment of the nucleus and the antiscreening factor cannot be determined independently. Consequently, we take their values from Ref. 18: $Q = 0.213$ barns and $(1-\gamma_{\text{inf}}) = 10.64$. Then the quadrupole splitting of the doublets of trivalent iron is (in nm/s)

$$Q_d = 3.406 q \sqrt{1+\eta^2/3}.$$

Figure 5 shows the temperature dependences of the quadrupole splitting for three doublets. We note that if the splitting in units mm/s is multiplied by 11.6, then the frequency of the nuclear quadrupole resonance is obtained in megahertz. For the calculations we used the lattice parameters of our sample $a = 3.8231$ Å, $b = 3.8863$ Å, and

TABLE I. Quadrupole interaction parameters for various crystallographic positions for two temperatures.

Position	V_{aa}, Å^{-3}	V_{bb}, Å^{-3}	V_{cc}, Å^{-3}	Q_d, mm/s	Q_d, mm/s	Q_d^*, mm/s
				T		
				300 K	0 K	0 K
1	0.236	0.404	−0.640	−2.204	−2.258	−2.078
2	0.509	−0.141	−0.367	1.788	1.840	1.716
3	−0.064	0.145	−0.081	0.459	0.503	0.413
4	−0.352	−0.256	0.608	2.079	2.081	1.996
5	1.081	−0.428	−0.654	3.709	3.766	3.658

TABLE II. Compensating charges z (in fractions of the electron charge e) and their coordinates for various positions.

Position	z, T = 300 K	z, T = 0 K	Coordinates of the test change
1	−0.376	−0.370	O1(0;0.5;0)
2	−0.804	−0.851	O5(0.5;0;0)
3	−0.153	−0.348	O1(0;0.5;0)
4	−0.377	—	O4(0;0;0.1584)

$c = 11.6809$ Å and the coordinates and rotations for the positions of the ions from Ref. 19: Y (0.5, 0.5, 0.5), Ba (0.5, 0.5, 0.1843), Cu1 (0,0,0), Cu2 (0,0,0.3556), O1 (0,0.5,0), O2 (0.5, 0, 0.3773), O3 (0, 0.5, 0.3789), O4 (0, 0, 0.1584), O5 (0.5,0,0). The O5 position in the $YBa_2Cu_3O_7$ crystal lattice is vacant. The following charges were assigned to the ions: Y^{3+}, Ba^{2+}, Cu^{2+}, and O^{2-}.

Table I gives the results of computer calculations of the components of the electric field gradient tensor and the quadrupole splitting for various positions with different variants of the nearest oxygen environment: 1—first doublet (O1, O5), 2—second doublet (O1, O5, O1), 3—third doublet (O1, O5, O5, O1), 4—fourth doublet, corresponding to the Cu2 position, 5—chain position with two oxygens in the nearest neighbor environment (O1, O1), which, evidently, does not occur for iron. The positions of the nearest neighbors in the (**ab**) plane which are occupied by oxygen are listed in parentheses. The splittings are presented for two temperatures: 300 and 0 K. The lattice parameters for 0 K were determined in a linear approximation using the thermal expansion coefficients obtained in Ref. 20 by x-ray diffractometry. For 0 K we took the following values: $a = 3.8189$ Å, $b = 3.8731$ Å, and $c = 11.6290$ Å. The coordinates of the atoms were the same as the coordinates used previously.

The last column in Table I shows the values of the quadrupole splittings Q_d^* which were obtained assuming that at low temperatures holes are localized in the Cu2 planes. There is one uncompensated positive charge per unit cell. At high temperatures it can be assumed that the effective size of a hole is large and as a result of the rapid movement of the hole the contribution to the field gradient is averaged. However, it is not ruled out that at low temperatures the hole localization time will be longer than the lifetime of a nucleus in the excited state (10^{-7} s). To check this supposition positive charges were arranged in checkerboard fashion in the Cu2 planes. The Cu2 position was chosen as the localization site for this point charge. The fact that in contrast to oxides of univalent oxygen the oxides of trivalent copper exist was taken into account (Ref. 21, Table 70). The quadrupole splitting of the fourth doublet was calculated for the Cu2 position where copper is divalent. Comparing the computational results (Table I) with experiment (Fig. 5) shows that it is difficult to describe the temperature dependence for trivalent iron ions. The contribution of the outer valence electrons must be taken into account.

We used the method of fractional test charges to simulate the valence electron distribution function. A negative fractional charge (in fractions of the electron charge) was placed on the nearest suitable oxygen position; the magnitude of this charge was varied until the computed value of the quadrupole splitting agreed with the experimentally measured value. The contribution of this charge to the electric field gradient was taken into account when calculating the lattice sums. The computational results for the four doublets are presented in Table II. This table also gives the coordinates of these test charges. The parameters of the fourth doublet, the Cu2 position, will be presented below.

It follows from Table II that the temperature dependence of the first doublet (twinning boundary) is completely described by the temperature variation of the lattice parameters; the magnitude of the test charge remains unchanged. For the second doublet the difference of the values of the test charges for 0 and 300 K is 0.047 electrons, and for the third doublet the difference is 0.195. This means that the electron density in chains at the oxygen sites as temperature decreases. We recall that the density at the iron nucleus had to be increased by 0.016 electron charges to describe the temperature dependence of the isomeric shift of the second doublet; for the third doublet the increase was 0.027. Hence follows the idea of a charge distribution function for the additional electron—most of the charge is concentrated on the oxygen and a smaller fraction is concentrated on the metal.

The temperature dependences of the doublet areas, the isomeric shifts, and the quadrupole splitting can be described within a single model, assuming self-localization of an additional electron in chain positions. The localization time must be longer than 10^{-7} s. The quasimagnetic phase arising with self-localization is most likely a pair of antiferromagnetic ordered magnetic moments of metal atoms with indirect exchange interaction via oxygen. An estimate of the s-type electron density at the iron nuclei and the charge density at oxygen for a normal paramagnetic phase shows that with self-localization of an additional electron an exchange pair of electrons with antiparallel spin orientation should form.

In summary, self-localization of an additional electron can result in the appearance of a quasiparticle with integral spin. Therefore a pair of antiferromagnetically oriented atomic moments and an exchange pair of electrons self-localized at oxygen in chain positions which moves along the crystal and carries charge can in principle form a Bose con-

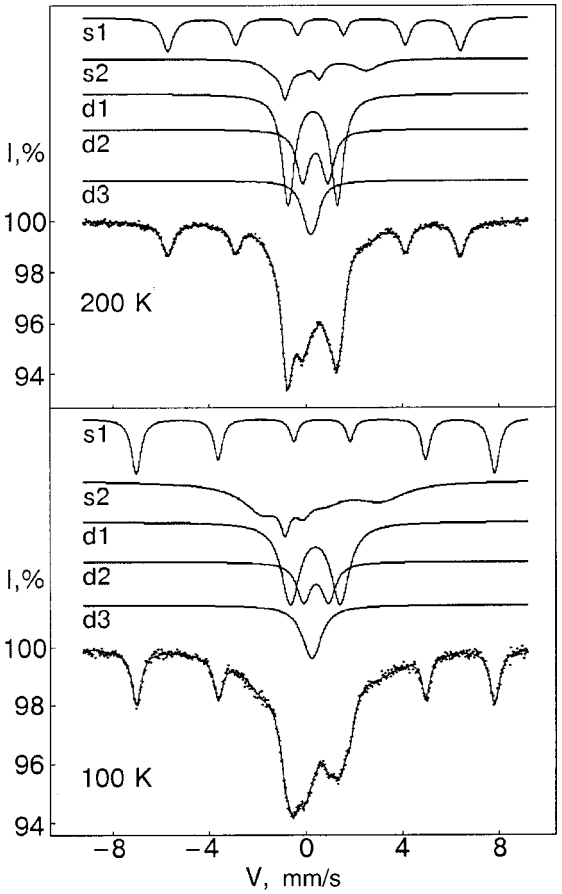

FIG. 6. Mössbauer spectra of the sample $YBa_2(Cu_{0.92}{}^{57}Fe_{0.08})_3O_{6.3}$ at different temperatures. The decomposition of the spectra in a model of two sextuplets and three doublets is shown.

densate. We note that the parameters of the impurity nuclei of iron were monitored only in chain positions. Therefore at this stage it cannot be determined unequivocally whether or not the positions in planes are united by electrons or a nonuniform electron density distribution occurs in chains.

3.2. Magnetically ordered sample

The removal of oxygen increases the density of valence electrons. This is accompanied by the appearance of long-range magnetic order. Then, according to the data Ref. 22, the magnetic order intensifies in Cu2 planes below $T_N = 420$ K and is absent in Cu1 positions in the temperature range which we studied above 100 K with $\delta = 0.3$. The Mössbauer spectra of an oxygen–depleted sample ($x = 0.08$) are presented in Fig. 6. The spectrum is a superposition of two Zeeman sextuplets $s1$ and $s2$ and three quadrupole doublets. The sextuplet $s1$ is characteristic for a tetraphase and is observed in the spectra of oxygen-depleted samples.[8,23] Three quadrupole doublets correspond to three nonequivalent Cu1 positions occupied by iron atoms and are similar to the doublets in the spectra of a superconducting sample. Measurements with textured samples were performed to identify the $s1$ sextuplet. It was determined that the magnetic moments of the atoms are oriented perpendicular to the **c** axis. The electric field gradient is positive and parallel to **c**; this makes it possible to assume that this sextuplet belongs to the Cu2 position.[12] In analyzing the spectra

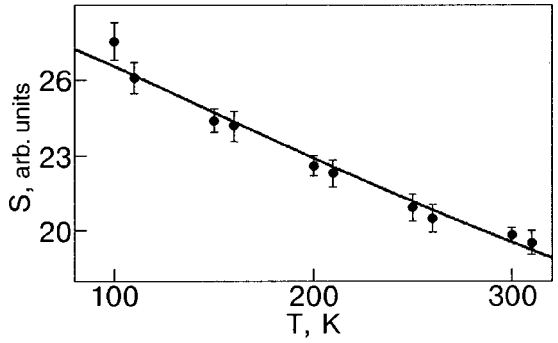

FIG. 7. Temperature dependence of the total area of the spectrum of a sample $YBa_2(Cu_{0.92}{}^{57}Fe_{0.08})_3O_{6.3}$.

the doublets were described by lines with equal areas and the sextuplets were described by lines with area ratios 3:2:1:1:2:3; this decreased the number of variable parameters and made possible to follow the temperature variations of the position parameters. The line widths were varied independently; this is especially noticeable for the second sextuplet. The temperatures of the total area of the spectrum and the relative areas of the components of the spectrum are presented in Figs. 7 and 8. The Debye–Waller function is fitted to the experimental points in Fig. 7. The Debye temperature was found to be $\theta_D = 288(2)$ K. The lower value of the De-

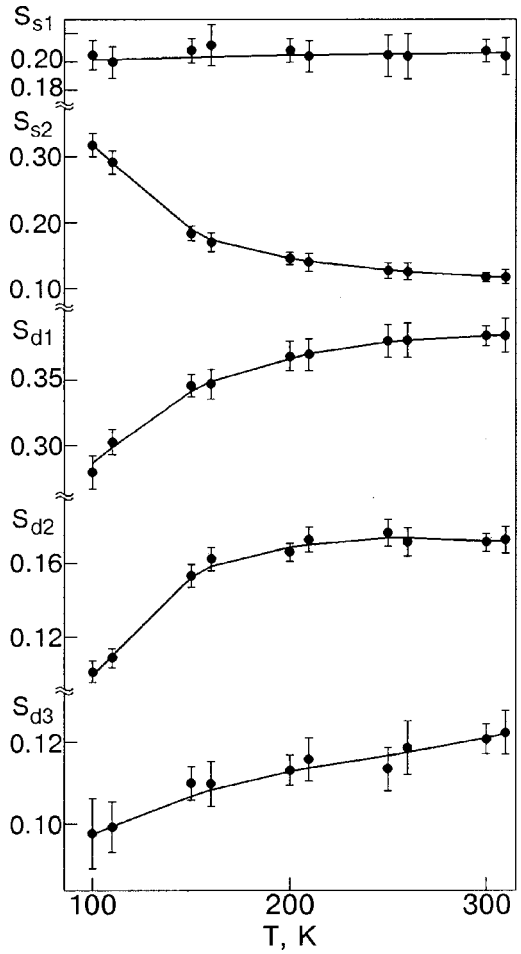

FIG. 8. Temperature dependences of the relative areas S of two sextuplets $s1$ and $s2$ and three doublets $d1$, $d2$, and $d3$ of the sample $YBa_2(Cu_{0.92}{}^{57}Fe_{0.08})_3O_{6.3}$.

bye temperature compared with the temperature of the superconducting sample was evidently due to the loss of oxygen and, correspondingly, loosening of the lattice. According to Fig. 8 the relative area of the first sextuplet is constant in the entire temperature range, and the increase in the relative area of the second sextuplet is accompanied by a decrease in the doublet areas. Therefore the second sextuplet belongs to the magnetic phase in chain positions. The temperature dependences of the magnetic hyperfine splitting for two sextuplets are shown in Fig. 9. The splittings for the ground state of the nucleus are presented; the frequency of the nuclear magnetic resonance can be obtained in MHz by multiplying the values by 11.6.

If a nucleus with spin I and magnetic moment μ is placed in a magnetic field H, then its energy level splits into $2I+1$ components whose energy levels

$$E=-\frac{\mu}{I}mH=-g\mu_n mH,$$

where μ_n is the nuclear magneton, g is the nuclear gyromagnetic ratio, and $m=I,\ I-1,\ \ldots,\ -I$.

In a solid an effective magnetic field whose magnitude is determined primarily by the atomic electrons acts on the nuclear spins. For iron nuclei the spin in an excited state is $I=3/2$ and in the ground state $I=1/2$. In magnetically ordered compounds the Mössbauer experiment gives $\mu^*/\mu=(3g^*/g)=1.72$ for the ratio of the magnetic moments in the excited and ground states. The magnetic moment in the excited state is negative. It should be noted that the magnetic moment of an atom does not determine uniquely the magnitude of the hyperfine magnetic field.[24]

For the sextuplet $s1$ $(3g^*/g)=-1.714$, and the Weiss curve describes the temperature dependence (Fig. 9).[24] This makes it possible to assume that this sextuplet belongs to a magnetically ordered state with long-range magnetic interaction. For the sextuplet $s2$ the temperature dependence of the field at a nucleus clearly shows a tendency to increase as temperature decreases; this could indicated close-range magnetic ordering. Then, as temperature decreases, the exchange interaction parameter increases as a result of an increase in the size of a magnetic cluster. The indirect interaction parameter also should depend strongly on the density of valence electrons forming exchange pairs.

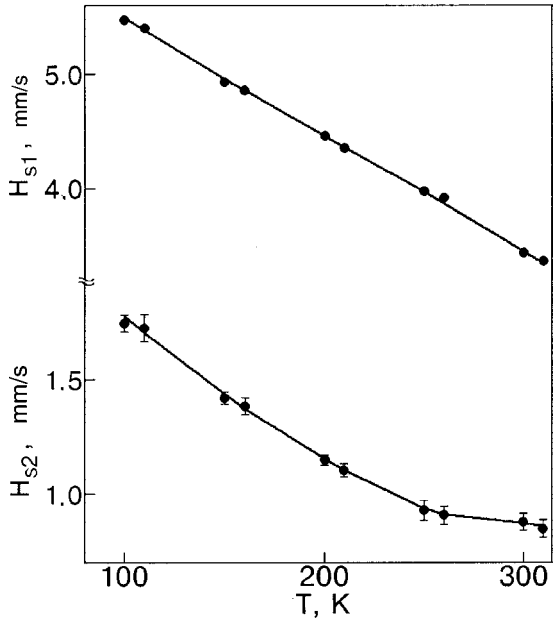

FIG. 9. Temperature dependences of the magnetic hyperfine splitting H of two sextuplets $s1$ and $s2$ of the sample $YBa_2(Cu_{0.92}{}^{57}Fe_{0.08})_3O_{6.3}$. The splittings of the ground state of the nucleus are presented.

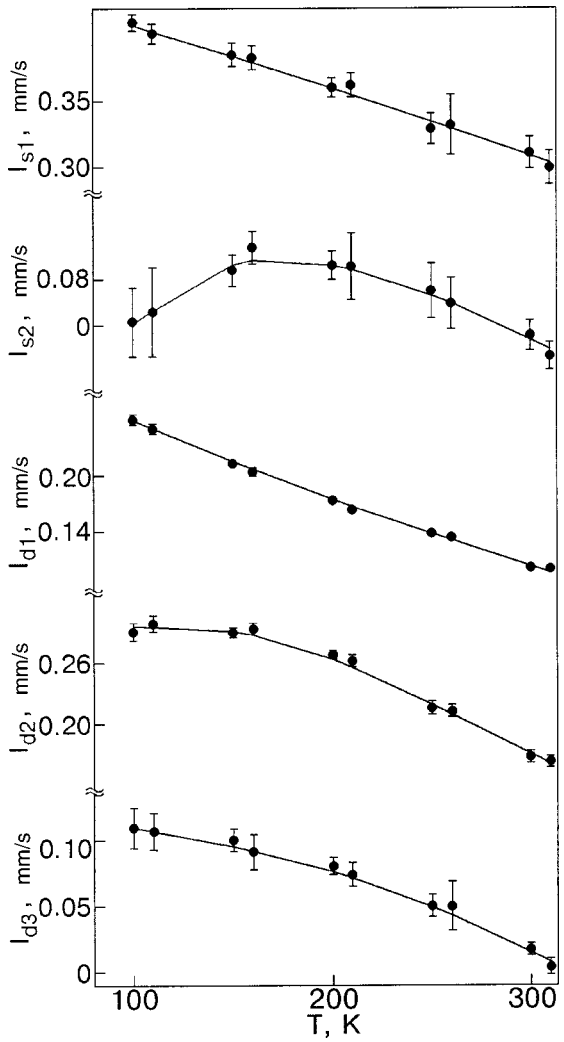

FIG. 10. Temperature dependences of the isomeric shifts I relative to iron of the sextuplets $s1$ and $s2$ and the doublets $d1$, $d2$, and $d3$ of the sample $YBa_2(Cu_{0.92}{}^{57}Fe_{0.08})_3O_{6.3}$.

Let us now consider the changes in the parameters of the spectrum which are sensitive to the charge distribution (see Fig. 6 for the decomposition of the spectrum). Figure 10 shows the dependences of the isomeric shifts of the spectrum components, and Fig. 11 shows the quadrupole splitting. For sextuplets the quadrupole interaction is manifested as line shifts and depends on the angle α between the magnetic moment of an atom and the electric field gradient. For trivalent iron, to a first approximation, the energy levels are given by the expression[7]

$$E=-g\mu_n Hm+(-1)^{|m|+1/2}\frac{1}{4}e^2qQ(1-\gamma_\infty)$$

$$\times\frac{3\cos^2\alpha-1}{2}.$$

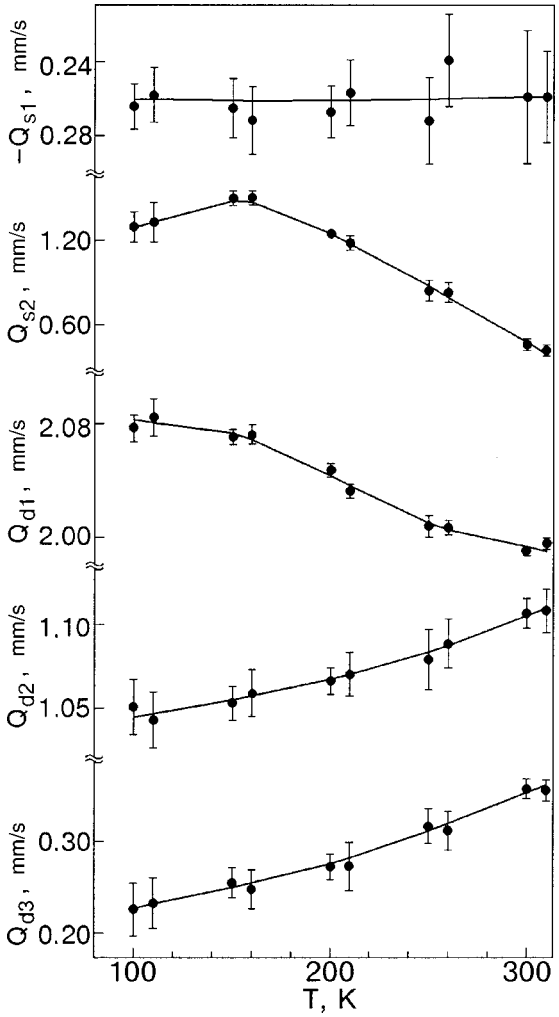

FIG. 11. Temperature dependences of the quadrupole shifts of two sextuplets $s1$ and $s2$ and quadrupole splittings of three doublets $d1$,$d2$, and $d3$ of the sample $YBa_2(Cu_{0.92}{}^{57}Fe_{0.08})_3O_{6.3}$.

Hence it is evident that for the first sextuplet ($\alpha=\pi_2$) the shift for a positive gradient will be negative, and the magnitude of the shift will decrease by a factor of 2 compared with the magnitude of the splitting of the quadrupole moment. For the second sextuplet the quadrupole shift is positive, but (see Fig. 11) the temperature variation is nonmonotonic. The behavior of the isomeric shift of the second sextuplet is the same. Evidently, the second sextuplet is a result of a superposition of at least three sextuplets, originating from three quadrupole doublets. The magnetic fields at the nuclei of these three positions are close in magnitude. In the opposite case a well-resolved magnetic structure should be observed. According to the data presented in Fig. 8 (for 100 K) the first doublet, where the electric field gradient is negative and directed along the **c** axis, makes the largest partial contribution to the area of the second sextuplet. Therefore the positive quadrupole shift of the second sextuplet corresponds to the orientation of the magnetic moment of an atom in the (**ab**) plane for the same position. The second doublet with positive gradient, directed along the **a** axis, makes the second largest contribution. A positive quadrupole shift for this position obtains if the direction of the magnetic moment is along the **a** axis. We note that for this orientation of the magnetic moments the quadrupole shifts for both positions are essentially identical in magnitude, since for the doublets the magnitudes of the quadrupole shifts differ by a factor of 2 (see Fig. 11). The quadrupole splitting of the third doublet is smallest, since the oxygen environment in the first coordination sphere is nearly cubic. In this connection, in an oxygen-depleted sample the direction and sign of the gradient for this position are poorly determined. Thus, the removal of an O1 oxygen in the second coordination sphere changes the sign and direction of the gradient, even though the magnitude of the quadrupole splitting itself remains essentially unchanged. Therefore, within measurement accuracy, one can talk about the direction of the magnetization along the **a** axis only for the first two positions.

The isomeric shifts of the first and second doublets are close (Fig. 10). The difference of the isomeric shifts at 100 K is 0.04 mm/s, which results in broadening of the lines in the superposition sextuplet by the same amount. The isomeric shift of the second sextuplet is less than for the doublets; this indicates that the electronic density increases at the iron nucleus. Thus, for the second doublet with a $3d^64x^x$ configuration the transition to the second sextaplet (change 0.24 mm/s) corresponds to a density increase by 0.096 electrons. For the quadrupole splittings of the first and second doublets the signs of the derivatives of the temperature dependences are different (Fig. 11). For the superposition second sextuplet the magnitude of the measured quadrupole interaction is averaged. For identical partial contributions of the doublets at 100 K the average value is 1.045 mm/s, which is close to the magnitude of the quadrupole shift of the second sextuplet. We took account of the fact that the quadrupole splitting of the first doublet is divided in half. Therefore, to within measurement accuracy it can be concluded that the transition from doublet to sextuplet occurs by electron density transfer between metal nuclei. However, the change in the electron density on the neighboring oxygen is negligible. The temperature dependences of the quadrupole splittings for the doublets (Fig. 11) also demonstrate an increase in charge density in chain positions as temperature decreases similarly to the dependences shown in Fig. 5. Thus, the formation of a magnetic phase occurs in two steps. First, as the temperature decreases, the electron density on the chain sites increases. Then the additional electron self-localizes, and the paramagnetic phase transforms into a magnetic phase.

It is important to note that the quadrupole shift of the first sextuplet (Cu2 position) is temperature independent. Therefore the charge distribution in the nearest-neighbor environment remains unchanged. The quadratic Doppler effect can completely explain the temperature change in the isomeric shift for this position (see Fig. 10). It remains to conjecture that as temperature changes, the redistribution of the charge density occurs only in chain positions. Hence it follows that in the chain sections where iron is present the electron density increases with decreasing temperature and, correspondingly, since the number of charges is conserved, electron-depleted regions are formed, i.e. the charge distribution in the plane of the chains becomes nonuniform.

In summary, an investigation of an oxygen-depleted sample confirms the version that some chain positions transform into a state with local magnetic ordering, which is ac-

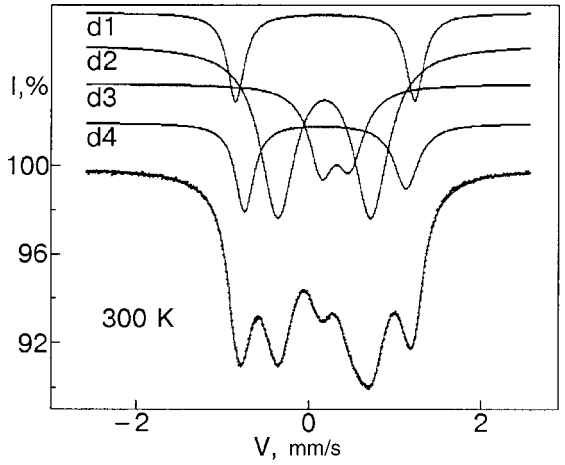

FIG. 12. Spectrum of a briefly oxidized sample. The decomposition of the spectrum in a model of four quadrupole doublets is shown.

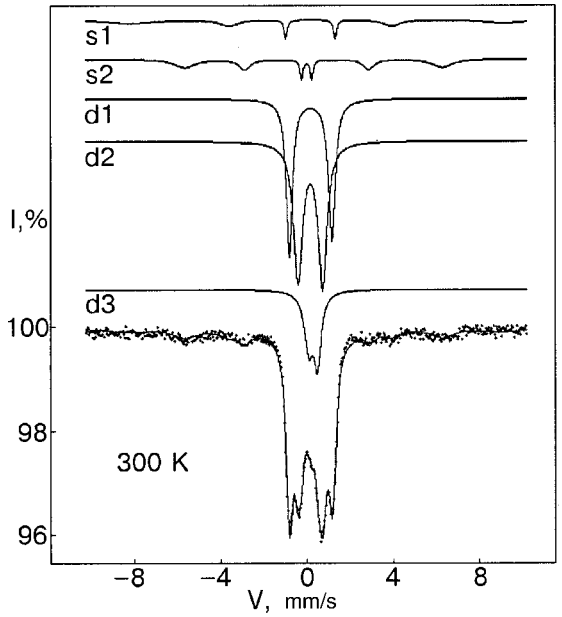

FIG. 13. Spectrum of an irradiated superconducting sample. The decomposition of the spectrum in a model of two sextuplets $s1$ and $s2$ and three doublets $d1$, $d2$, and $d3$ is shown.

companied by an increase in the charge density in these positions. In the process electron-depleted regions arise in the chains.

As a control, the oxygen-depleted part of the sample was held for 1 h at 700 °C in a furnace. Air was pumped through the furnace at a rate 0.5 liters/min. It was assumed that short-time oxidation will produce a structure with a nonuniform oxygen distribution and that it will be possible to observe simultaneously the magnetic and paramagnetic phases of the Cu2 positions. The results were somewhat unexpected (Fig. 12). Even though the statistical accuracy was high, for this spectrum a magnetic phase was not observed. As a control, the spectrum was obtained in an expanded velocity interval, but the same result was obtained. The $d4$ doublet belongs to the Cu2 position, the quadrupole splitting $Q_{d4} = 1.870(1)$ mm/s, and the isomeric shift $I_{d4} = 0.058(1)$ mm/s. Table II gives the additional charge on the O4 oxygen, which gives agreement between the experimental and theoretical $(0.377e)$ values. The quadrupole shift of the first sextuplet is $Q_{s1} = -0.26$ mm/s (Fig. 11). For the fourth doublet an additional 2.845 electron charges must be placed in the O4 position in order to obtain the quadrupole splitting 0.52 mm/s. Therefore as oxygen is removed 2.468 electrons are transferred into the Cu2 plane. We note that the estimate is very approximate, since the changes in the lattice parameters as a result of oxygen removal were neglected. To compensate the difference of the isomeric shifts (0.242 mm/s) the electron density at the nucleus must be increased by 0.097 (a $3d^6 4s^x$ configuration is assumed). It is interesting to note that if the relative area of the first sextuplet is of the order of 0.2 (see Fig. 8), then the relative area of the fourth doublet is 0.1496(4). Therefore, in the oxidation process some iron nuclei migrated from Cu2 positions into Cu1 positions.

3.3. Irradiated sample

In a paramagnetic state the allowed magnetic components in a Mössbauer spectrum are observed only if the lifetime of a ^{57}Fe nucleus in the excited state (10^{-7} s) is less than the lifetime of the frozen state of the atomic magnetic moment. As the relaxation rate increases, the spectrum becomes deformed, shifts toward the center, and ultimately degenerates into a single line or a doublet, if the gradient of the electric field at the nucleus is different from zero. An isolated paramagnetic center of trivalent iron in the limit of an infinitely long relaxation time should give three systems of Mössbauer lines for spin projections 5/2, 3/2, and 1/2.[7] In practice, for finite relaxation times two sextuplets can be observed for the 5/2 and 3/2 states. To a first approximation the magnetic splitting for these sextuplets should corresponds to a 5/3 ratio, and the parameters of the isomeric shift and quadrupole interaction should be the same. In the limit of fast relaxation[25] the existence of ''anomalous'' spectra is possible for a definite set of parameters. In the equations describing the hyperfine structure of the spectra, under conditions of relatively fast fluctuations of the atomic magnetic moment, additional contributions appear and result in renormalization of the nuclear levels. These contributions are equivalent to an additional ''quadrupole'' interaction, in addition to the ''chemical'' shift and the ''quasimagnetic'' hyperfine interaction.[25] Of course, the ratios between the magnitudes of the splittings of the ground and excited states of the nucleus which are typical for magnetically ordered compounds will no longer hold.

Figure 13 shows the spectrum of a superconducting sample, which was irradiated at low temperatures with helium–neon laser radiation (632.8 nm). The light flux density was 13 mW/cm^2. A finely dispersed powder (particle size 10 μm) mixed with paraffin was deposited in a thin layer on aluminum foil and covered with a mica slab. It was assumed that the light reflected from the foil will additionally interact with the powder. The sample thickness was 6 mg/cm^2, the exposure time was 120 h, and the temperature was 100 K. The heating of the sample did not exceed 2 K, which was monitored according to the isomeric shift of the first doublet. After irradiation the sample was allowed to stand for 2 weeks at room temperature in air. It was assumed

that the fast relaxation processes were completed, the free electrons and holes annihilated, and only structural changes remained.

Additional lines which are described by two sextuplets appeared in the spectrum. The variation of the magnetic splittings of the ground and excited states was negligible. The area ratios were taken to be 3:2:1:1:2:3. The line widths varied independently in pairs. The quadrupole doublets were described by lines of equal area. For the first sextuplet the magnetic splitting of the excited state of the nucleus was $\Delta^*(s1)=4.9(3)$ mm/s. For the second sextaplet $\Delta^*(s2)=3.11(4)$ mm/s. Their ratio is 1.581, which is close to 5/3. The splitting of the ground state $\Delta(s1)=2.6(2)$ mm/s and $\Delta(s2)=2.63(3)$ mm/s. The relative areas were $S_{s1}=0.10(1)$ and $S_{s2}=0.11(1)$. The isomeric shifts were $I_{s1}=0.2(4)$ mm/s and $I_{s2}=0.04(9)$ mm/s. The quadrupole shifts were $Q_{s1}=0.3(4)$ mm/s and $Q_{s2}=0.32(8)$ mm/s. We note that the line width for the irradiated sample is smaller than for the initial sample. This is probably why these sextuplets are observable. It is natural to attribute the decrease in the line width to structural ordering and correspondingly a decrease in the variance of the local fields. The quadrupole interaction for the sextuplets is closest to the quadrupole splitting of the third doublet (0.41 mm/s). If both sextuplets are assumed to correspond to the position of the third doublet, then the atomic magnetic moments are oriented along the **b** axis. The difference of the isomeric shifts of the second sextuplet and the third doublet (0.12 mm/s) corresponds to an increase in the electron density at the nucleus by 0.028 electrons ($3d^5 4s^x$ configuration). The quadrupole splitting of the third doublet corresponds to an additional charge of 0.089 electrons on the O1 oxygen, and for the second sextaplet the additional charge is 0.185 electrons. Therefore the formation of a magnetic structure occurs with self-localization of approximately 0.03 electrons at the nucleus and 0.1 electrons at the neighboring oxygen. We also call attention to an interesting feature of the observed sextuplets. In the excited state the ratio of the magnetic splittings shows that a paramagnetic state with a long relaxation time is indeed formed and the sextuplets correspond to spin projections 5/2 and 3/2. In addition, the areas of the sextuplets are close, indicating that these states have the same occupation. However, the magnetic splittings of both sextuplets are essentially identical in the ground state; this is typical for magnetically ordered compounds with long-range spin–spin interaction. The splitting in the ground state is smaller than in the excited state; this can be attributed to the dynamical shift of the nuclear magnetic resonance frequency.[26] The dynamical shift is especially large for antiferromagnets and increases substantially as the frequencies of the electronic antiferromagnetic and nuclear magnetic resonances approach one another.

Irradiating the samples with light produces structural ordering. Evidently, the oxygen atoms migrate from O5 into O1 positions; this decreases the variance of the local fields and results in narrowing of the lines. According to Ref. 27, first, the photoexcited electrons from the CuO_2 planes reconnect at the ends of the chains, creating local instability. At the second stage the oxygen ions located in the neighborhoods of these instabilities move into neighboring oxygen vacancies and thereby increase the length of the chain.

4. CONCLUSIONS

It has been shown in this work that the anomalous decrease in the area of the Mössbauer spectrum of superconducting samples is due to local magnetic ordering of pairs of impurity iron atoms in Cu1 positions; this is due to self-localization of electrons. The accompanying redistribution of the charge density is manifested as a change in the parameters of the quadrupole interaction and the isomeric shift at the nuclei of the neighbors.

Estimates were obtained for the binding energy of a self-localized state. The thermal activation parameters ranged from 7.5 to 21.5 K and depend on the local configuration. The lifetime of a bound state at a lattice site is at least 10^{-7} s. Analysis of the temperature dependence of the charge density for the normal paramagnetic phase suggests that the self-localization of an additional electron results in the formation of an exchange pair with zero effective spin. Therefore a pair of antiferromagnetically oriented atomic moments and an exchange pair of electrons, which is self-localized on oxygen, in principle can form a quasiparticle with integral spin.

Analysis of the temperature dependences of the parameters of a magnetically ordered oxygen-depleted sample showed that the redistribution of the electron density with self-localization of an electron occurs only in chain positions. Therefore phase separation accompanied by the appearance of spatial superstructure is possible in chains.

At low temperatures the effect of photoirradiation of a superconducting sample reduces to ordering of the structure or lengthening of the chains. This decreases the variance of local fields and additional lines which can be described by two sextuplets appear in the spectrum at room temperature. Magnetic sextuplets belong to paramagnetic centers with long relaxation times. The dynamical shift of the nuclear magnetic resonance frequencies for nuclei in the ground state indicates the presence of spin–spin relaxation between these centers. Therefore electron self-localization is accompanied by local magnetic ordering, at least, of a pair of atomic magnetic moments which are oriented perpendicular to the **c** axis of the crystal. Therefore, in an external magnetic field, as a result of the canting of the magnetic moments a ferromagnetic moment can be induced along the **c** axis. This moment is what probably makes it possible to texture powdered samples in comparatively weak magnetic fields.

The conclusions are based on Mössbauer measurements of the parameters of ^{57}Fe nuclei replacing copper predominantly in chain positions. If it is assumed that with electron self-localization magnetic moments of copper are oriented antiferromagnetically in chains and an exchange pair of electrons with integral spin is formed in the process, then superconductivity is possible in chains as a result of Bose condensation of such quasiparticles. The experimental fact that superconducting samples containing no iron impurity become textured in a magnetic field serves an an argument supporting this conjecture.

*E-Mail: ponomarchuk@ilt.kharkov.ua

[1)]Here and below the number in parentheses is the error in the last decimal place.

[1] S. I. Pekar, *Investigations in the Electronic Theory of Crystals*, Gostekhizdat, Moscow (1951).
[2] L. D. Landau, *Collected Works*, Nauka, Moscow 91969), Vol. 1.
[3] É. L. Nagaev, JETP Lett. **6**, 18 (1967).
[4] É. L. Nagaev, Zh. Éksp. Teor. Fiz. **103**, 252 (1993) [Sov. Phys. JETP **76**, 138 (1993)].
[5] É. L. Nagaev, Usp. Fiz. Nauk **165**, 529 (1995) [Phys. Usp. **38**, 497 (1995)].
[6] V. V. Eremneko, D. V. Lukashev, K. M. Matsievskiĭ, and V. L. Pomeranchuk, Fiz. Nizk. Temp. **22**, 1383 (1996) [Low Temp. Phys. **22**, 1048 (1996)].
[7] H. Wertheim, *The Mössbauer Effect*, Mir, Moscow (1966).
[8] I. S. Lyubutin, T. V. Dmitirev, and V. G. Terznev, Zh. Éksp. Teor. Fiz. **102**, 1615 (1992) [Sov. Phys. JETP **75**, 873 (1992)].
[9] S. Suharan, J. Chadwick, D. B. Hannon, D. H. Jones, and M. F. Thomas, Solid State Commun. **70**, 817 (1989).
[10] I. V. Zubov, A. S. Ilyushin, I. A. Nikanorova, A. A. Novakova, I. É. Graboĭ, A. R. Kaul', V. V. Moshchalkov, and I. G. Muttik, SFKHT **2**(3), 51 (1989) [Superconductivity **2**, 69 (1989)].
[11] Y. Wu, S. Pradhan, and P. Boolchand, Phys. Rev. Lett. **67**, 3184 (1991).
[12] V. V. Eremenko, D. V. Lukashev, and V. L. Ponomarchuk, Fiz. Nizk. Temp. **24**, 1207 (1998) [Low Temp. Phys. **24**, 908 (1998)].
[13] S. V. Vonsovskiĭ, *Magnetism*, Nauka, Moscow (1971).
[14] R. N. Kuz'min [Ed.], *The Practice of the Mössbauer Effect*, Izd. Mosk. Universiteta, Moscow (1987).
[15] V. I. Gol'danskiĭ and R. G. Graber [Eds.], *Applications of Mössbauer Spectroscopy in Chemistry* [Russ. trans.], Mir, Moscow (1970).
[16] V. G. Tsirel'son, V. A. Strel'tsov, E. F. Makarov, and R. P. Ozerov, Zh. Éksp. Teor. Fiz. **92**, 1894 (1987) [Sov. Phys. JETP **65**, 1065 (1987)].
[17] V. G. Lyubutin, V. G. Terziev, and V. P. Gor'kov, Zh. Éksp. Teor. Fiz. **95**, 1908 (1989) [Sov. Phys. JETP **68**, 1103 (1989)].
[18] É. I. Yur'eva, V. P. Zhukov, and V. A. Gubanov, SFKHT **4**, 1120 (1991) [Superconductivity **4**, 1027 (1991)].
[19] M. A. Beno, L. Soderholm, D. W. Capone II, D. G. Hinrs, J. D. Jorgensen, Ivan K. Schuller, C. U. Segre, K. Zhang, and J. D. Grace, Appl. Phys. Lett. **51**, 57 (1987).
[20] I. V. Zubov, A. A. Dityat'ev, A. A. Novakova, A. S. Il'yushin, R. N. Kuz'min, and V. V. Moshchalkov, Fiz. Nizk. Temp. **14**, 878 (1988) [Sov. J. Low Temp. Phys. **14**, 483 (1988)].
[21] R. Ripan and I. Chetyan, *Inorganic Chemistry* [Russ. trans.], Mir, Moscow (1972), Vol. 2.
[22] J. M. Tranquada, G. Shirane, B. Keimer, S. Shamoto, and M. Sato, Phys. Rev. B **40**, 4503 (1989).
[23] S. Nasu, H. Kitagawa, M. Yoshida, Y. Oda, K. Ueda, T. Kohara, T. Shindjo, K. Asayama, and F. E. Fujita, Hyperfine Interactions **55**, 1355 (1990).
[24] V. S. Shpinel', *The Mössbauer Effect in Crystals*, Nauka, Moscow (1969).
[25] A. M. Afanas'ev and V. D. Gorobchenko, Zh. Éksp. Teor. Fiz. **66**, 1406 (1974) [Sov. Phys. JETP **39**, 690 (1974)].
[26] M. I. Kurkin and E. A. Turov, *Nuclear Magnetic Resonance in Magnetically Ordered Substances and Its Applications*, Nauka, Moscow (1990).
[27] E. Osquiguil, M. Maenhoudt, B. Wuyts, Y. Bruynseraede, D. Lederman, and I. K. Shuller, Phys. Rev. B **49**, 3675 (1994).

Translated by M. E. Alferieff

LOW-TEMPERATURE MAGNETISM

Guided vortex motion in faceted niobium films

A. K. Soroka*

V. N. Karazin Khar'kov National University, pl. Svobody, 4, Khar'kov, 61077, Ukraine; Institut für Physik, Johannes Gutenberg-Universität, Staudinger Weg 7, 55099 Germany

M. Huth

Institut für Physik, Johannes Gutenberg-Universität, Staudinger Weg 7, 55099 Germany

(Submitted June 6, 2002)
Fiz. Nizk. Temp. **28**, 1179–1182 (November 2002)

Guided vortex motion has been observed in niobium films on a faceted Al_2O_3 substrate. The even and odd components of the longitudinal and transverse magnetoresistances of the samples are measured for various orientations of the transport current relative to the facetting direction. The even and odd components of the magnetoresistance are separated according to a change in the sign of the magnetic field. © *2002 American Institute of Physics.* [DOI: 10.1063/1.1528575]

The efect of pinning anisotropy on vortex dynamics in superconductors is a subject of intense theoretical and experimental investigations.[1–3] Special attention is being focused on the so-called guided vortex motion which arises when parallel pinning planes are present in the sample. This situation can be easily realized experimentally in $YBa_2Cu_3O_{7-\delta}$ single crystals: the existence of unidirectional twins, which have virtually no influence on vortex motion parallel to their plane but are strong pinning centers for motion perpendicular to the direction of a twin, resulting in the appearance of a number of interesting effects.[2,3] In layered high-temperature superconductors the system of parallel ab planes is itself a source of intrinsic pinning for vortices oriented parallel to these planes.[4] In the present article a new experimental model is proposed for studying such phenomena.

Guided vortex motion results in the appearance of ''new'' components of the magnetoresistances of a sample in parallel and perpendicular directions relative to the transport current:[11] the odd longitudinal, with respect to a change in direction of the magnetic field, and even transverse components, respectively,

$$\rho_{\parallel}^{-}=\frac{\rho_{\parallel}(+\mathbf{H})-\rho_{\parallel}(-\mathbf{H})}{2}, \tag{1}$$

$$\rho_{\perp}^{+}=\frac{\rho_{\perp}(+\mathbf{H})+\rho_{\perp}(-\mathbf{H})}{2}, \tag{2}$$

which are absent in the isotropic case. They have been observed experimentally in two $YBa_2Cu_3O_{7-\delta}$ single crystals.[2,3] The theory predicts the following dependence of these components on the angle α between the current direction and planar defects.[1] When the current is directed parallel or perpendicular to the planes the ''new'' components are always zero. This is because the vortices in such a geometry can move, under the action of the Lorentz force, only perpendicular to the transport current and the velocity component parallel to the current is zero. The expected response should be maximum in amplitude in a geometry where $\alpha=45°$.[1]

In the present work the measurements were performed on thin niobium films deposited on a faceted Al_2O_3 substrate. When Al_2O_3 is annealed in air at high temperatures facets form on the substrate surface, as shown in Figs. 1a and 1c.[5] Such a faceted substrate was cut into four parts, and four 390 Å thick niobium films were obtained in a single deposition process by molecular–beam epitaxy.

It was established that the facets in this system act as pinning planes. The nature of these planes is not completely understood: pinning can be due to, for example, grain boundaries or surface effects. The structure making it possible to measure the longitudinal and transverse resistances was deposited by a photolithographic method. Three samples with

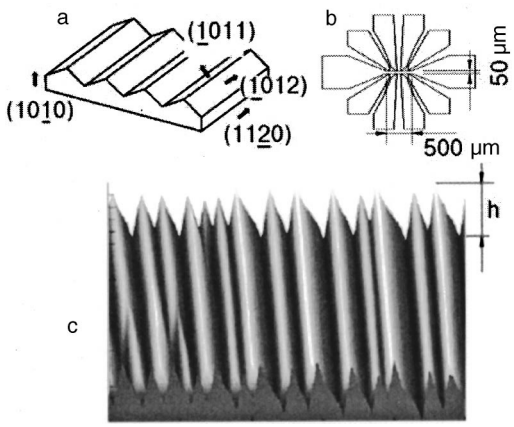

FIG. 1. Surface of a faceted Al_2O_3 substrate (a); measuring bridge (b) and typical image of the surface of a niobium film on a faceted substrate, the image being obtained using a scanning tunneling microscope (a 5×5 μm scanning region is shown; the height of each facet is $h\approx50$ nm) (c).

different orientation of the measuring bridge relative to a facet—parallel, perpendicular, and at an angle $\alpha = 45°$—were prepared for the measurements. Thus, the transverse and longitudinal magnetoresistances with different orientations of the transport current relative to the direction of a facet can be measured for this set of samples. In the course of the experiment the voltage dependences $U_{\parallel}(\mathbf{H})$ and $U_{\perp}(\mathbf{H})$ for two mutually opposite directions of the magnetic field **H**, perpendicular to the sample plane, were measured simultaneously. Then, the components of the longitudinal and transverse magnetoresistances which are even and odd relative to a change in the direction of the magnetic field were calculated from Eqs. (1) and (2). The average transport current density was 5.1 kA/cm^2.

Figure 2a shows for three films $\rho_{\parallel}^{+}$ versus the magnetic field at film temperature 8.5 K. The sample with the current directed at an angle of 45° relative to the direction of a facet has a lower critical field than all other samples. This difference can be attributed to the nonuniform distribution of the temperature in the substrates during film deposition. The transition width is 0.02 T.

The magnetic field dependence of $\rho_{\parallel}^{-}$ in Fig. 2b has a pronounced minimum near the superconducting transition. The curves are virtually identical to one another for all three films: the curve for the sample with the current directed at an angle of 45° is shifted in the direction of low fields relative to curves for the two other samples by an amount equal to the difference of the critical fields of these films (see Fig. 2a). It should be noted that the theory of Ref. 1 predicts zero

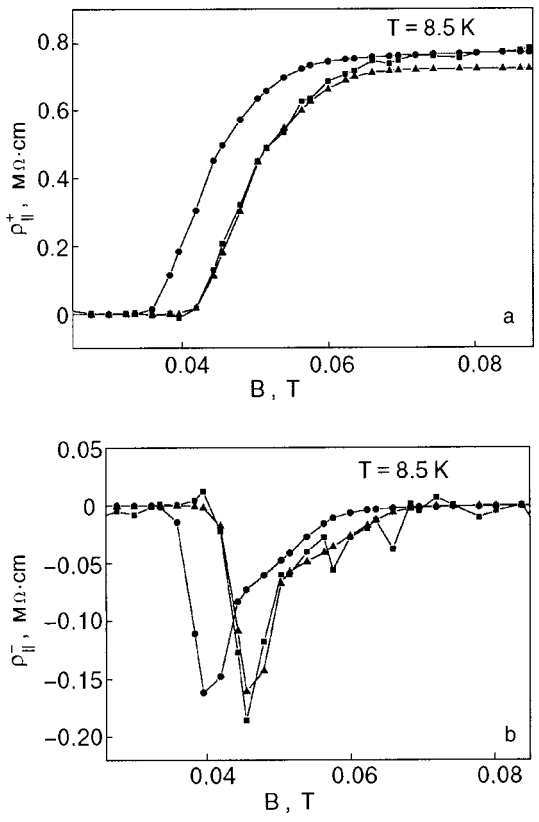

FIG. 2. Even (a) and odd (b) components of the longitudinal magnetoresistivity versus the magnetic field strength for three samples with different orientation of the transport current relative to the facet direction: 0° (■), 45° (●), and 90° (▲).

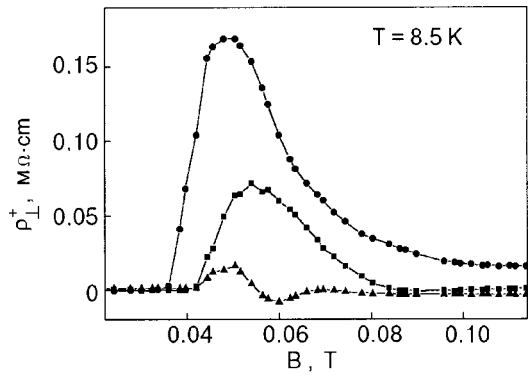

FIG. 3. Even component of the transverse magnetoresistivity versus the magnetic field strength for three samples with different orientation of the transport current relative to the facet direction: 0° (■), 45° (●), and 90° (▲).

magnetic resistance for $\alpha = 0$ and 90°. A dependence similar to that presented for $\alpha = 45°$ has been observed on twinned YBCO single crystals.[2] In the present work the results of measurements of the even and odd parts of the longitudinal and transverse magnetoresistances of a YBCO single crystal with unidirectional twins are presented for two samples with different directions of the transport current: parallel and at an angle of $\alpha = 45°$ with respect to the twin planes. However, the signal amplitude in a sample with current parallel to the twins was an order of magnitude smaller than for the case $\alpha = 45°$. The appearance of an odd (as a function of the field) component in the longitudinal magnetoresistance is a characteristic feature of guided vortex motion. This component is due to the presence of an even component of the velocity perpendicular to the current direction with vortices moving along the pinning planes.[1]

Figure 3 shows the magnetic field dependence of the even component of the transverse magnetoresistance of the sample. It is evident that the effect is strongest for the sample with the transport current oriented at an angle of 45° with respect to the facet direction, as theory predicts. The origin of these ''new'' components of the transverse magnetoresistance is due to vortec motion along pinning planes, specifically, the presence of an odd component of the vortex velocity directed perpendicular to the transport current vector.

The experimental results attest to pinning anisotropy in faceted niobium films. The main result of this work is the experimental observation of an odd component in the longitudinal and an even component in the transverse magnetoresistances of the sample; this indicates guided vortex motion in faceted niobium films. Why the behavior of the odd component of the longitudinal resistance is essentially the same in all three samples is not clear. One possible reason for this behavior could be the presence of a small ($\leqslant 5°$) disorientation angle between the current direction and the facet direction in samples with $\alpha = 0$ and 90°. The existence of nonzero values of $\rho_{\perp}^{+}$ for these directions (see Fig. 3) also attests to this.

The theoretical results of Ref. 1 cannot be directly used for quantitative interpretation of the experimental data, because the theory does not assume the existence of pinning for vortex motion in a pinning plane, i.e. a facet. However, the

experiments show that the critical current in a direction parallel and transverse to the facet direction is of the same order of magnitude. Thus, a further elaboration of the theory of vortex motion that is capable of describing such a situation is needed.

In closing, it should be noted that the system studied in this work is a good object for studying guided vortex motion: parameters such as the facet period and film thickness can be easily varied when the films are being prepared.

We thank V. A. Shklovskiĭ for discussing the results obtained and for checking the manuscript and J. Oster for assisting in sample preparation.

*E-Mail: soroka@mail.uni-mainz.de

[1] V. A. Shklovskiĭ, A. A. Soroka, and A. K. Soroka, Zh. Éksp. Teor. Fiz. **116**, 2103 (1999) [JETP **89**, 1138 (1999)].
[2] A. A. Prodan, V. A. Shklovskij, V. V. Chabanenko, A. V. Bondarenko, M. A. Obolenskii, H. Szymczak, and S. Piechota, Physica C **C302**, 271 (1998).
[3] V. V. Chabanenko, A. A. Prodan, V. A. Shklovskij, A. V. Bondarenko, M. A. Obalenskii, H. Szymczak, and S. Peichota, Physica C **C314**, 133 (1999).
[4] G. Blatter, M. V. Fiegelman, V. B. Geshkenbein, A. I. Larkin, and V. M. Vinokur, Rev. Mod. Phys. **66**, 1125 (1994).
[5] M. Huth, K. A. Ritley, J. Oster, H. Sosch, and H. Adrian, Adv. Funct. Mat. **5**, (2002).

Translated by M. E. Alferieff

Exact solution of the problem of an electron in a magnetic field consisting of a uniform field and arbitrarily arranged magnetic strings parallel to the uniform field

I. M. Dubrovskiĭ*

G. V. Kurdyumov Institute of Metal Physics, Ukrainian National Academy of Sciences, bul. Vernadskogo, 36, Kiev, 03680, Ukraine

(Submitted March 4, 2002)
Fiz. Nizk. Temp. **28**, 1183–1194 (November 2002)

It is shown that the requirements of finiteness, single-valuedness, and definiteness of the wave function and probability current density necessarily lead to the fact that as a magnetic string is approached the wave functions of the electron must decrease in modulus more rapidly than the square root of the distance from the string (a magnetic string is an infinitely thin solenoid carrying a finite magnetic flux). The energy spectrum of an electron is obtained. In general the spectrum is identical to the spectrum in the absence of strings. The general form of the eigenfunctions of the ground state and an operator whose powers give the eigenfunctions of the excited states are found. When there is only one string with magnetic flux which is not a multiple of twice the flux quantum another equidistant sequence of eigenvalues appears in the energy spectrum. This sequence is shifted with respect to the main sequence by a fraction equal to the positive fractional part of the quotient obtained by dividing the magnetic flux by twice the flux quantum. This sequence starts from a level whose number equals the number of the remaining magnetic strings. The wave functions for these special states are also obtained. © *2002 American Institute of Physics.* [DOI: 10.1063/1.1528576]

1. INTRODUCTION

A magnetic string is an infinitely thin solenoid carrying a finite flux. Since the magnetic field intensity of a string is everywhere zero except along the line of the string, the interaction of a charged particle with a string is a purely quantum effect with no classical analog (Aharanov–Bohm effect). The problem of such an interaction arises in the effective-Hamiltonian analysis of an electron in a crystal containing a screw dislocation. The effective Schrödinger equation in a plane perpendicular to the dislocation line can be studied separately. Then the terms linear in the deformation describe in the Hamiltonian a magnetic string (coinciding with the dislocation line) with magnetic flux proportional to the component of the quasimomentum along the dislocation line. This problem and its extension to the case where a uniform magnetic field is present and is oriented parallel to the string have been studied many times (see Refs. 1–3). They are interesting because they describe the simplest case of the interaction of an electron with a shear deformation in a crystal where the variables separate. In Sec. 2 of the present paper these investigations will be supplemented by boundary conditions at the point where the string intersects the plane containing the electron. The conditions under which the string can approximately describe the influence of a magnetic-field nonuniformity with a small radius on the state of an electron will also be examined.

Heuristic arguments concerning the influence of a string on the state of a two-dimensional electron gas in a magnetic field and on the interaction in a gas of two-dimensional composite particles, i.e. particles possessing an electric charge and the associated magnetic structure, play a fundamental role in the theory of the quantum Hall effect.[4] In this connection the exact solution obtained in Sec. 4 of the problem of a charged particle in a magnetic field consisting of a uniform field and many arbitrarily arranged strings could be of interest. This model also describes an electron in a crystal with parallel screw dislocations in a magnetic field. As noted in Ref. 1 quantization in such a system cannot be performed according to the Bohr–Sommerfeld rules, even though the corresponding classical problem can be solved exactly. It is interesting that the exact solution was obtained for a disordered system without any spatial symmetry. The solution was made possible by a transformation, described in Sec. 3, of the Hamiltonian. This transformation requires boundary conditions at the point through which the string passes; these boundary conditions are obtained in Sec. 2.

2. ELECTRON IN THE FIELD OF A SINGLE STRING

The Schrödinger equation for a single string with magnetic flux F

$$\hat{\mathcal{H}}\Omega(\mathbf{r})=\frac{1}{2\mu}\left[\left(\hat{p}_x-\frac{eHy}{2c}-\frac{eFy}{2\pi c(x^2+y^2)}\right)^2+\left(\hat{p}_y+\frac{eHx}{2c}+\frac{eFx}{2\pi c(x^2+y^2)}\right)^2+\hat{p}_z^2\right]\Omega(\mathbf{r})=E\Omega(\mathbf{r}) \tag{1}$$

can be easily solved by separating variables in cylindrical coordinates whose axis is also the line of the string.[2,3] Here e is the modulus of the electron charge and the negativity of the charge is taken into account; $\mathbf{H}$ is the intensity of the uniform magnetic field parallel to the $\mathbf{Z}$ axis; F can be positive or negative depending on the direction of the magnetic field of the string relative to the uniform field; μ is the electron mass. We exclude from the analysis motion along the $\mathbf{Z}$

axis and in what follows we shall examine only the two–dimensional problem. In polar coordinates (r,φ) the eigenfunctions are

$$\Omega(\mathbf{r})=\exp(im\varphi)\exp\left(-\frac{r^2}{2l^2}\right)\times r^{|\nu|}\Phi\left(-\frac{E}{\hbar\omega}+\frac{\nu+|\nu|+1}{2},\ |\nu|+1;\ \frac{r^2}{l^2}\right), \quad (2)$$

where $\Phi(a,c;x)$ is the confluent hypergeometric function, m is any integer, here and below the normalization factor is dropped for brevity, and

$$\omega=\frac{eH}{\mu c},\ \ l^2=\frac{2ch}{eH},\ \ \nu=m+\frac{F}{2F_0},\ \ F_0=\frac{\pi\hbar c}{e}. \quad (3)$$

For the wave function to be finite at the origin of the coordinates (at the point where the string is located) and to remain single-valued in a circuit around this point, of the two fundamental solutions of the confluent hypergeometric equation the function $\Phi(a,c;x)$ is chosen and m must be an integer.

An important distinction of the set of functions $\Omega_{E,m}(r,\varphi)$ from the corresponding solutions of the problem with no magnetic strings[5] is that it always includes either the function with $|\nu|$ and $m\neq 0$ if $F/2F_0$ is an integer or two functions with $0<|\nu|<1$. In the first case the function has no limit as $r\to 0$ and consequently cannot be a wave function. In the second case both functions have a singular gradient in the limit $r\to 0$. Different authoritative sources formulate differently the requirements for continuity of the derivatives of the wave function. Thus, the authors of Refs. 6 and 7 consider that the first derivatives of the wave function remain continuous and bounded in all states, and they do not present any physical arguments to substantiate this requirement. In Ref. 7 it is stated that this requirement is sufficient for boundedness and continuity of the probability current density. In Ref. 8 the derivatives are allowed to approach infinity ''not too strongly.'' In Ref. 5 it is indicated that there can be exceptions, determined by the specific problem being studied, to the continuity of the derivatives.

We introduce the notation

$$\frac{F}{2F_0}=a+\alpha,\ \ a-\text{integer},\ \ 0\leqslant\alpha<1. \quad (4)$$

The amplitude component of the current density in the state (2) is

$$j_\varphi=-\frac{e\hbar}{\mu}\exp\left(-\frac{r^2}{l^2}\right)|\Phi|^2 r^{2|\nu|}\left(\frac{\nu}{r}+\frac{eH}{2c\hbar}r\right). \quad (5)$$

It is obvious that for $0<2|\nu|\leqslant 1$ the expression (5) results in a physically meaningless result—an infinite or nonzero azimuthal current at $r=0$. For $1<2|\nu|<2$ Eq. (5) gives physically admissable values of the probability current in all space, even though the gradient of the function has a singularity at $r=0$. Consequently, we shall adopt the following constraints on the possible values of m neglected in Refs. 2 and 3. For $\alpha=0$, $m\neq -a$. If ν is not an integer, i.e. $\alpha\neq 0$, then there always exists a value of m such that $|\nu|\leqslant 1/2$, and a state with this value of m must be eliminated from the solutions of the Schrödinger equation. For $\alpha\leqslant 1$ $m\neq -a$ and for $\alpha\geqslant 1/2$ $m\neq -1-a$. These selection rules for physically admissable states can be united by a boundary condition: at the point containing the magnetic string the wave function is zero and as this point is approached the modulus of the wave function decreases more rapidly than $r^{1/2}$. (We note that there is another reason why the condition that the function vanishes cannot be the only condition: a linear manifold defined by such a condition is not closed. Indeed, the sequence of functions $r^{1/n}$ belongs to this manifold but the limit of the sequence does not.) Such conditions must also hold for many strings; this situation will be studied below. For this reason spin does not interact with magnetic strings, and it is of no interest to take spin into account.

The boundary conditions on the outer boundary of the domain of definition determine the energy spectrum. If the domain is infinite, then in order for the eigenfunctions to be integrable

$$-\frac{E}{\hbar\omega}+\frac{\nu+|\nu|+1}{2}=-N, \quad (6)$$

where N is a nonnegative integer. Then the energy eigenvalues corresponding to the eigenfunctions (2) have the form

$$E_{Nm}=\hbar\omega\left(N+\frac{\nu+|\nu|+1}{2}\right). \quad (7)$$

Then the confluent hypergeometric functions in Eq. (2) reduce to the generalized Laguerre polynomials $L_N^{|\nu|}(r^2/l^2)$.

The quantum numbers N and m cannot be interpreted directly in terms of the classical motion of an electron. For a physical interpretation of the results obtained below and to compare them with the semiclassical description it is convenient in this solution to switch to the quantum numbers n and k, which were introduced in Ref. 1 and determine, respectively, the energy and distance of the center of a classical orbit from the origin of coordinates. From the solution of the classical problem expressions can be derived for the integrals of motion $C_x(\mathbf{p},\mathbf{r})$ and $C_y(\mathbf{p},\mathbf{r})$—the Cartesian coordinates of the center of an orbit in terms of the Cartesian coordinates and momenta of a classical particle, generalized to the case of a magnetic string:

$$C_x=-\frac{1}{\mu\omega}p_y-\frac{F}{2\pi H}\frac{x}{x^2+y^2}+\frac{x}{2},$$
$$C_y=\frac{1}{\mu\omega}p_x-\frac{F}{2\pi H}\frac{y}{x^2+y^2}+\frac{y}{2}. \quad (8)$$

Switching to operators, the operator of the squared distance of the center of a classical orbit from the magnetic string can be written as

$$\hat{R}^2=\hat{C}_x^2+\hat{C}_y^2=l^2\left(\frac{1}{\hbar\omega}\hat{\mathcal{H}}+i\frac{\partial}{\partial\varphi}-\frac{F}{2F_0}\right). \quad (9)$$

Obviously, $\hat{R}^2$ commutes with the Hamiltonian and the function (2) is its eigenfunction with the corresponding eigenvalue

$$R_{jm}^2=l^2\left(N+\frac{|\nu|-\nu}{2}+\frac{1}{2}\right). \quad (10)$$

We introduce the energy n and distance k quantum numbers of the center of an orbit relative to the origin of the coordinates:

$$n=N+\frac{|m+a|+m+a}{2}\geqslant 0,$$

$$k=N+\frac{|m+a|-m-a}{2}\geqslant 0, \tag{11}$$

$$n-k=m+a, \quad N=k+\frac{(n-k)-|n-k|}{2}.$$

These numbers can take on any noninteger values with the exception of the cases allowed by the selection rules derived above. We shall present expressions for the energy, distance of the center of an orbit from the origin of coordinates, and the radius r_0 of a Larmor orbit in terms of the quantum numbers n and k:

$$E_{nk}=\hbar\omega\left[n+\theta(n-k)\alpha+\frac{1}{2}\right],$$

$$r_0^2=l^2\left[n+\theta(n-k)\alpha+\frac{1}{2}\right], \tag{12}$$

$$R_{nk}^2=l^2\left\{k+[\theta(n-k)-1]\alpha+\frac{1}{2}\right\},\ \theta(x)=\begin{cases}1; & x\geqslant 0\\ 0; & x<0\end{cases}.$$

Hence we can obtain a classical interpretation of the selection rules. For $n=k$ the line of the orbit passes through the point containing the string if $\alpha=0$ or near it (encompassing it) if $\alpha\leqslant 1/2$. If $\alpha\geqslant 1/2$, then an orbit with $m+a=n-k=-1$ would pass near the string without encompassing it. Such orbits are forbidden. (''Near'' means that $|r_0^2-R^2|\leqslant l^2/2$.) Orbits with $n<k$ do not encompass the string; the energy levels form the standard Landau spectrum and are degenerate with respect to k. For $n\geqslant k$ the orbits encompass the string, the energy levels are also equidistant but they are shifted with respect to the Landau levels by $\hbar\omega\alpha$ and are degenerate for all $k\leqslant n$. We shall refer to such states as special states. However, there is no complete correspondence between the electron density distribution and a classical orbit. The coordinates of the center of an orbit (8) do not commute with one another, so that if the modulus of the radius vector is determined by the expression (12), then its azimuth is completely undetermined. For on string, the case which we are now discussing, this azimuth is of no significance for calculating the action integral I_r and the angular momentum M of an electron relative to the axis:

$$I_r=\frac{1}{\pi}\oint p_r dr=\begin{cases}\hbar r_0^2/l^2\\ hR^2/l^2,\end{cases}\quad p_r=\frac{xp_x+yp_y}{\sqrt{x^2+y^2}},$$

$$M=xp_y-yp_x=\frac{\hbar r_0^2}{l^2}-\frac{\hbar R^2}{l^2}-\frac{\hbar F}{2F_0}. \tag{13}$$

Here the upper value of I_r corresponds to orbits which do not encompass the magnetic string. Applying to I_r and M the Bohr–Sommerfeld quantization rules

$$I_r=\hbar\left(N+\frac{1}{2}\right), \quad M=\hbar m, \tag{14}$$

and using the fact that the energy is proportional to the squared radius of the orbit, we can derive the formula (7). We note that to obtain the correct result semiclassical quantization must be used for each degree of freedom separately in accordance with the rules. The often used quantization of the total adiabatic invariant

$$\frac{1}{2\pi}\oint p_x dx+p_y dy=I_r+\frac{1}{2\pi}\oint M d\varphi$$

$$=\begin{cases}\hbar r_0^2/l^2\\ \dfrac{\hbar r_0^2}{l^2}-\dfrac{\hbar F}{2F_0}\end{cases}=\left(n+\frac{1}{2}\right)\hbar \tag{15}$$

leads to a physically meaningless result: for $|a+\alpha|>n+1/2$ and $a<0$ it is found that $r_0^2<0$.

If $\alpha=0$, i.e. the magnetic flux of a string equals an integral number of twice the flux quantum, then the energy spectrum differs from the spectrum in the absence of the string only by the fact that states with $n=k$ are excluded. Then the wave functions differ by the fact that in the factors which depend on r the angular momentum quantum number m is replaced by $\nu=m+a$.

For the case of several strings the number of possible variants of the values of the quantizable integrals of motion increases rapidly with the number of strings. The variant that is realized depends on the radius of the Larmor orbit and on both coordinates of the center of the orbit, which cannot be observed simultaneously. Consequently, for several strings it is impossible to obtain the energy spectrum by quantizing the integrals of motion. In Ref. 1 a hypothesis was proposed for determining the spectrum in this case, but as will be shown below the results obtained are incorrect.

In closing this section we shall examine the states of an electron in the field of a solenoid with a finite radius r_1, field intensity H_i inside the solenoid, and a uniform field H_e outside the solenoid. We introduce the dimensionless variable x and the energy ε:

$$x=\frac{r^2eH_e}{2c\hbar}, \quad \varepsilon=\frac{E\mu c}{\hbar eH_e}. \tag{16}$$

The wave functions inside and outside the solenoid have the form

$$\Omega_e=\exp(im\phi)\exp\left(-\frac{x}{2}\right)x^{|\nu|/2}$$

$$\times\Psi\left(-\varepsilon+\frac{\nu+|\nu|+1}{2},\ |\nu|+1;\ x\right), \tag{17}$$

$$\Omega_i=\exp\left(im'\phi\frac{\beta}{|\beta|}\right)\exp\left(-\frac{|\beta|x}{2}\right)x^{|m'|/2}$$

$$\times\Phi\left(-\frac{\varepsilon}{|\beta|}+\frac{m'+|m'|+1}{2},\ |m'|+1;\ |\beta|x\right), \tag{18}$$

where $\beta=H_i/H_e$ taking account of the sign (we assume the direction of H_e to be positive),

$$\nu = m + \frac{F}{2F_0} = m + \frac{e\pi r_1^2}{2\pi c\hbar}(H_i - H_e) = m + x_1\left(\frac{H_i}{H_e} - 1\right)$$
$$= m + x_1(\beta - 1) = m + x_1\eta. \tag{19}$$

Matching the values of the functions (17) and (18) at $x = x_1$ gives the ratio of the coefficients of these functions and, in addition, the requirement

$$m = m'\frac{\beta}{|\beta|} = m' \operatorname{sgn}\beta. \tag{20}$$

The values of the coefficients can be calculated from the normalization condition. Then, as follows from Eq. (20), the continuity condition for the derivative with respect to φ holds automatically. The continuity condition for the derivative with respect to r can be replaced by continuity of the logarithmic derivative with respect to x:

$$-\frac{|\beta|}{2} + \frac{|m|}{2x_1} + |\beta|\frac{\Phi'}{\Phi} = -\frac{1}{2} + \frac{|\nu|}{2x_1} + \frac{\Psi'}{\Psi}. \tag{21}$$

It determines the spectrum of eigenvalues ε. We shall assume the domain of the eigenvalues to be infinite. Since $\Psi(a,c;x) \sim x^{-a}$ as $x \to \infty$, the solution (17) and (18) satisfies the boundary conditions at infinity and zero for all values of the parameters. Using the properties of the confluent hypergeometric functions (see Ref. 5) we can write

$$\frac{\Phi'}{\Phi} = \frac{1}{|\beta|x_1}\left(-\frac{\varepsilon}{|\beta|} + \frac{m+|m|+1}{2}\right)$$
$$\times\left[\frac{\Phi\left(-\frac{\varepsilon}{|\beta|} + \frac{m+|m|+3}{2},\ |m|+1;\ |\beta|x_1\right)}{\Phi\left(-\frac{\varepsilon}{|\beta|} + \frac{m+|m|+1}{2},\ |m|+1;\ |\beta|x_1\right)} - 1\right],$$

$$\frac{\Psi'}{\Psi} = \frac{-\varepsilon + \frac{\nu+|\nu|+1}{2}}{x_1}\left[\left(-\varepsilon + \frac{\nu-|\nu|+1}{2}\right)\right.$$
$$\left.\times\frac{\Psi\left(-\varepsilon + \frac{\nu+|\nu|+3}{2}, |\nu|+1;\ x_1\right)}{\Psi\left(-\varepsilon + \frac{\nu+|\nu|+1}{2}, |\nu|+1;\ x_1\right)} - 1\right]. \tag{22}$$

The equation (21) is a complicated transcendental equation which depends on the solenoid parameters H_i and x_1. It is simpler to study this equation in the limiting case of a small-radius solenoid carrying a finite magnetic flux:

$$x_1 \to 0,\ |\beta| \to \infty,\ \ \zeta = x_1|\beta| = \text{const}. \tag{23}$$

Then instead of Eq. (21) we obtain approximately

$$\Theta_m(\zeta) = \frac{|\nu|}{2} + \left(-\varepsilon + \frac{\nu+|\nu|+1}{2}\right)\left[\left(-\varepsilon + \frac{\nu-|\nu|+1}{2}\right)\right.$$
$$\left.\times\frac{\Psi\left(-\varepsilon + \frac{\nu+|\nu|+3}{2},\ |\nu|+1;\ x_1\right)}{\Psi\left(-\varepsilon + \frac{\nu+|\nu|+1}{2},\ |\nu|+1;\ x_1\right)} - 1\right], \tag{24}$$

where

$$\Theta_m(\zeta) = \frac{|m|-\zeta}{2} + \frac{m+|m|+1}{2}$$
$$\times\left[\frac{\Phi\left(\frac{m+|m|+3}{2},\ |m|+1;\ \zeta\right)}{\Phi\left(\frac{m+|m|+1}{2},\ |m|+1;\ \zeta\right)} - 1\right]. \tag{25}$$

The spectrum of values of ε can be obtained from Eq. (24) by setting

$$-\varepsilon + \frac{\nu+|\nu|+1}{2} = -N - \gamma, \tag{26}$$

where N is an arbitrary nonzero integer or zero, $|\gamma| < 1$. Then (see Ref. 9), if ν is not an integer

$$\Psi(-N-\gamma, |\nu|+1;\ x_1) \approx \frac{\Gamma(-|\nu|)}{\Gamma(-|\nu|-N)} + \frac{\Gamma(|\nu|)}{\Gamma(-N-\gamma)x_1^{|\nu|}};$$

$$\Gamma(-N-\gamma) \approx \frac{(-1)^{N-1}}{\gamma N!}. \tag{27}$$

From Eq. (24) we have

$$\gamma = \frac{(-1)^N x_1^{|\nu|}\Gamma(-|\nu|)(2\Theta_m(\zeta) - |\nu|)}{N!\Gamma(|\nu|)\Gamma(-|\nu|-N)(2\Theta_m(\zeta)+|\nu|)}. \tag{28}$$

On the basis of the asymptotic behavior of $\Phi(a,c;x)$ in the limits $x \to \infty$ and $x \to 0$ it can be shown that $\Theta_m(\zeta) > 0$. Consequently, the numerator in Eq. (28) has no zeros and γ is always small to the extent that $x_1^{|\nu|}$ is small. If ν is an integer and $\nu \neq 0$, then

$$\Psi(-N-\gamma, |\nu|+1; x_1)$$
$$\approx (-1)^N\left[\frac{(N+|\nu|)!}{|\nu|!} - \gamma\frac{N!}{x_1^{|\nu|}}(|\nu|-1)!\right],$$

$$\gamma = \frac{x_1^{|\nu|}(N+|\nu|)!(2\Theta_m(\zeta) - |\nu|)}{N!|\nu|!(|\nu|-1)!(2\Theta_m(\zeta)+|\nu|)}. \tag{29}$$

The relation (29) is the limiting case of the relation (28) when ν approaches an integer, so that the relation (28) is a general formula for all $\nu \neq 0$. It can be shown that for $\nu = 0$ $\gamma \sim -(\ln x_1)^{-1}$, i.e. this case cannot be described as the limit of the relation (28). As the matching point x_1 and therefore also γ approach zero, the matched confluent hypergeometric functions will pass into the corresponding Laguerre polynomials for all m uniformly in x, except the case $\nu = 0$.

Thus, the states in the field of a magnetic string with $|\nu| > 1/2$ in an unbounded plane approximately describe the

corresponding states in the field of a small-radius solenoid. The qualitative difference is that the energy levels in the field of a solenoid are not degenerate, though they do form close groups near the Landau levels and at distances $\hbar\omega\alpha$ from them, while in the field of a string each Landau level is split into two degenerate levels. This occurs because the energy is determined not only by the classical orbit encompassing the solenoid but also by the fact that the wave function in the solenoid is not zero.

3. FACTORIZATION OF THE HAMILTONIAN

The Hamiltonian of an electron in a magnetic field, which is a superposition of a uniform field and I magnetic strings which are parallel to the uniform field, carry fluxes F_i, and are located at the points $\mathbf{z}_i=(\zeta_{ix},\zeta_{iy})$ in a plane perpendicular to the magnetic field ($i=1,2,\ldots,I$), has the form

$$\hat{\mathcal{H}}=\frac{1}{2\mu}\left[\left(\hat{p}_x-\frac{eHy}{2c}-\sum_{i=1}^{I}(a_i+\alpha_i)w_{iy}\right)^2+\left(\hat{p}_y+\frac{eHx}{2c}+\sum_{i=1}^{I}(a_i+\alpha_i)w_{ix}\right)^2\right], \tag{30}$$

where

$$w_{ix}=\frac{x-\zeta_{ix}}{(x-\zeta_{ix})^2+(y-\zeta_{iy})^2},$$

$$w_{iy}=\frac{y-\zeta_{iy}}{(x-\zeta_{ix})^2+(y-\zeta_{iy})^2} \tag{31}$$

are the components of the vector $\mathbf{w}_i$. It is easily verified that $\operatorname{div}\mathbf{w}_i=0$ everywhere where the derivatives of the components of $\mathbf{w}_i$ are defined. At the same time the flux of $\mathbf{w}_i$ through any circle centered at the point z_i containing the string is 2π. Consequently,

$$\operatorname{div}\mathbf{w}_i=\frac{\partial w_{ix}}{\partial x}+\frac{\partial w_{iy}}{\partial y}=2\pi\delta(\mathbf{r}-\mathbf{z}_i). \tag{32}$$

This Hamiltonian can be factorized by introducing operators which are a generalization of the operators introduced in Refs. 10 and 11 to the case where strings are present:

$$\hat{\pi}_\pm=\left(-i\hbar\frac{\partial}{\partial x}\right)\pm i\left(-i\hbar\frac{\partial}{\partial y}\right)\pm\frac{i\hbar}{l^2}(x\pm iy)\pm i\hbar\sum_{i=1}^{N}(a_i+\alpha_i)(w_{ix}\pm iw_{iy}). \tag{33}$$

In contrast to Ref. 10 and 11, the commutator $[\hat{\pi}_+,\hat{\pi}_-]$, strictly speaking, is not everywhere equal to a constant [see Eq. (32)]:

$$[\hat{\pi}_+,\hat{\pi}_-]=-2\hbar\mu\omega-4\pi\hbar^2\times\sum_{i=1}^{N}(a_i+\alpha_i)\delta(x-\zeta_{xi})\delta(y-\zeta_{yi}), \tag{34}$$

but, as shown above, since the wave functions must have zeros at points containing strings, the Hamiltonian (3), just as in Refs. 10 and 11, can be represented in the form

$$\hat{\mathcal{H}}=\frac{1}{2\mu}\hat{\pi}_+\hat{\pi}_-+\frac{1}{2}\hbar\omega. \tag{35}$$

We introduce the variables and notations (see Ref. 11)

$$z_\pm=x\pm iy,\quad \zeta_{i\pm}=\zeta_{ix}\pm i\zeta_{iy},$$

$$w_{i\pm}=w_{ix}\pm w_{iy}=\frac{1}{z_\mp-\zeta_{i\mp}}. \tag{36}$$

We underscore that the complex variables $z_\pm$ are not independent, since they are complex conjugates of one another. Two independent complex variables would introduce four independent real variables instead of x and y. We introduce the operators

$$\frac{\partial}{\partial z_\pm}=\frac{1}{2}\left(\frac{\partial}{\partial x}\mp i\frac{\partial}{\partial y}\right). \tag{37}$$

This is not differentiation with respect to a complex variable but rather a linear combination of operators of differentiation with respect to the coordinates. Specifically, the functions to which these operators will be applied may not satisfy the Cauchy–Riemann conditions. From the definitions (36) and (37) we obtain

$$\left[\frac{\partial}{\partial z_\pm},z_\pm\right]=1,\quad \left[\frac{\partial}{\partial z_\pm},z_\mp\right]=0 \tag{38}$$

so that the action of the operators (37) on a function of the variables $z_\pm$ can be interpreted as differentiation with respect to independent real variables (the derivatives $\partial w_\pm/z_\pm$, which are proportional to δ functions, are an exception; but, as already mentioned, this is of no significance in our space of the functions.) The operators $\hat{\pi}_\pm$ in these variables have the form

$$\hat{\pi}_\pm=-i\hbar\left(2\frac{\partial}{\partial z_\mp}\mp\frac{1}{l^2}z_\pm\mp\sum_{i=1}^{N}\frac{a_i+\alpha_i}{z_\mp-\zeta_{i\mp}}\right). \tag{39}$$

It follows from Eqs. (34) and (35) that we can write for the functions possessing zeros at points containing strings

$$[\hat{\mathcal{H}},\hat{p}_-]=-\hbar\omega\hat{\pi}_-,\quad [\hat{\mathcal{H}},\hat{\pi}_+]=\hbar\omega\hat{\pi}_+. \tag{40}$$

Hence it is easy to show that if the function ϕ is an eigenfunction of the Hamiltonian, corresponding to the eigenvalue E, then the function $\hat{\pi}_\pm\phi$ will also be an eigenfunction corresponding to the value $E\pm\hbar\omega$, provided that it satisfies all conditions imposed on the solution of the Schrödinger equation.

For many strings, in the classical cace the integrals of motion corresponding to the coordinates of the center of a classical orbit for trajectories which do not intersect strings can also be found. They are analogous to Eq. (8) with Fw_x and Fw_y replaced by the corresponding sums $\Sigma F_i w_{ix}$ and $\Sigma F_i w_{iy}$. In quantum mechanics they also correspond to operators which commute with the Hamiltonian in the space of functions which vanish at points containing strings but which do not commute with one another. From them we can construct the operators

$$\hat{C}_\mp=\hat{C}_x\pm i\hat{C}_y=\pm\frac{i}{\mu\omega}\hat{\pi}_\pm+z_\pm \tag{41}$$

and the hermetian operator for the squared distance of the center of an orbit from any point (ξ_x,ξ_y)

$$\hat{R}^2(\xi_x,\xi_y)=(\hat{C}_+-\xi_-)(\hat{C}_--\xi_+)+\frac{1}{2}l^2, \tag{42}$$

which commutes with the Hamiltonian. From the commutation relations

$$[\hat{R}^2,\hat{C}_+]=l^2\hat{C}_+, \quad [\hat{R}^2,\hat{C}_-]=-l^2\hat{C}_- \tag{43}$$

it follows that the operator $\hat{R}^2(\xi_x,\xi_y)$ possesses a discrete spectrum with spacing l^2; the operator which increases the eigenvalue for the set of eigenstates is $\hat{C}_+$ and the decreasing operator is $\hat{C}_-$.

4. SOLUTION OF THE PROBLEM FOR MANY STRINGS

We shall replace the desired wave functions, writing

$$\Omega=\exp\left(-\frac{z_+z_-}{2l^2}\right)\psi, \tag{44}$$

where the origin of coordinates $z_+=z_-=0$ is chosen arbitrarily, and introduce the operators

$$\hat{p}_\pm=-i\hbar\left(2\frac{\partial}{\partial z_\mp}\mp\sum_{i=1}^{N}\frac{a_i+\alpha_i}{z_\mp-\zeta_{i\mp}}\right). \tag{45}$$

Then the equation for the function ψ has the form

$$\frac{1}{2\mu}\left[\hat{P}_+\hat{P}_-\psi+\frac{2i\hbar}{l^2}z_+\hat{P}_-\psi\right]+\frac{1}{2}\hbar\omega\psi=E\psi, \tag{46}$$

or

$$\frac{1}{2\mu}\left[\hat{P}_++\frac{2i\hbar}{l^2}z_+\right]\hat{P}_-\psi=\left(E-\frac{1}{2}\hbar\omega\right)\psi.$$

It is easy to show from the commutation relations (34) and (40) that if the function ϕ is a solution of Eq. (46) with eigenvalue E_0, then the function $(\hat{P}+2i\hbar z_+/l^2)\phi$ is a solution with eigenvalue $E_0+\hbar\omega$, provided that it satisfies the boundary conditions. As one can expect from the preceding sections of this paper, on an unbounded uniform plane the spectrum of the problem should consist of one or several equidistant sequences of degenerate levels. Then the energy of the ground state should be $\hbar\omega/2$.

Let us consider the problem for an unbounded plane with a finite number of strings. If ϕ is the ground state function of the system, i.e. $E_0=\hbar\omega/2$, then the operator $\hat{P}_-$ transforms ϕ into a function identically equal to zero, i.e. ϕ is an eigenfunction of $\hat{P}_-$ with zero eigenvalue. For other values of E_0, if $\hat{P}_-\phi$ vanishes at all points containing strings, then it is an eigenfunction of Eq. (46) with the eigenvalue $E_0-\hbar\omega$. The operator $\hat{P}_-$ can likewise transform the function ϕ into a function which does not satisfy the conditions. Then, if the level E_0 is nondegenerate, then it is the lowest level of the spectrum of special states; if it is degenerate, then the operator $\hat{P}_-$ could transform a linear combination of its eigenfunctions into a function satisfying the conditions with eigenvalue $E_0-\hbar\omega$. Therefore, for a complete solution of the problem it is sufficient to find the complete system of ground state functions in the sequence of Landau eigenvalues and all possible lowest eigenvalues and the corresponding eigenfunctions in the sequences of special states.

The ground state eigenfunction is also an eigenfunction of the operator $\hat{P}_-$ with zero eigenvalue. Solving the corresponding first-order equation we obtain

$$\hat{P}_-\left\{\Phi(z_-)\prod_{i=1}^{N}(z_+-\zeta_{i+})^{-(a_i+\alpha_i)/2}\right\}\equiv 0, \tag{47}$$

where $\Phi(z_-)$ is an arbitrary function of z_-. It should be chosen so that the eigenfunction of the Hamiltonian satisfies all required conditions: a) it should have no poles; b) it should decrease exponentially as $|z_\pm|=r\to\infty$, i.e. the function $\psi(z_+,z_-)$ can grow no more rapidly than a finite power of r; c) as the point containing the string is approached it should approach zero more rapidly than $\rho^{1/2}$ (ρ is the distance from the string); and, d) it should be determined uniquely everywhere to within a constant phase factor. The last two conditions impose definite requirements on the exponents in cofactor pairs of the form $(z_+-\zeta_{i+})^s\times(z_--\zeta_{i-})^t$. Switching to the standard variables and transferring the origin of coordinates to the point (ζ_{ix},ζ_{iy}) we obtain

$$\begin{aligned}(z_+-\zeta_{i+})^s(z_--\zeta_{i-})^t&=(x'+iy')^s(x'-iy')^t\\&=\exp[i(s-t)\varphi']r'^{(s+t)}.\end{aligned} \tag{48}$$

Hence it follows that the difference $s-t$ should be an integer and the sum $s+t>1/2$. If s and t are half-integers, then $s-t$ and $s+t$ are integers and the condition $s+t>0$ should hold. This requirement need not be applied at the first step of the solution. Then if the obtained wave functions belong to a degenerate level, their linear combinations which vanish at the required points can be constructed. But branch points cannot be eliminated by a linear combination of non-single-valued functions.

Then the desired function has the form

$$\begin{aligned}\psi(x,y)=T(z_-)&\prod_{i=1}^{N}\\&\times(z_+-\zeta_{i+})^{-(a_i+\alpha_i)/2}(z_--\zeta_{i-})^{\kappa_i+(a_i-\alpha_i)/2},\end{aligned}$$

$$\text{where}\quad \kappa_i\geqslant\theta\left(\frac{1}{2}-\alpha_i\right), \tag{49}$$

and $T(z_-)$ is an arbitrary entire function that can be represented as a finite or infinite converging sum of powers of z_-. Consequently, the functions ψ_k, which are determined by the formula (49) with $T_k(z_-)=z_-^k$ and the minimal integer κ_i, can be chosen as the complete system of ground state eigenfunctions on an unbounded plane. The powers of z_-, considered as functions of (x,y) or (r,φ), i.e. $z_-^k=\exp(-ik\varphi)r^k$, are orthogonal in a circle of any radius, so that the functions ψ_k for a fixed set of non-negative integers κ_i are orthogonal with a weighting function and hence are linearly independent. The eigenfunctions of the higher levels can be obtained from the ground state functions by applying powers of the operator $[\hat{P}_++2i\hbar z_+/l^2]^s$. The result of operating with $\hat{P}_+$ on a function of the form (49) with $T_k(z_-)=z_-^k$ is multiplication by the polynominal

$$\frac{2k}{z_-}+2\sum_{i=1}^{N}\frac{\kappa_i-\alpha_i}{z_-\zeta_{i-}}. \tag{50}$$

Consequently, in order that the requirements for the eigenfunctions be satisfied here it is necessary to operate on linear combinations of the functions (49) which are obtained by multiplying them by the corresponding power of the polynomial $\Pi_{i=1}^{N}(z_i-\zeta_{i-})$, i.e. the quantities κ_i must be increased by s so that by operating s times with the raising operator will not cause the functions to violate the conditions at the points containing a string.

The eigenfunctions found for the energy operator are not eigenfunctions of the operator $\hat{R}^2$. Consequently, the quantum number k is not directly related with the determination of the distance of an orbit center from any particular point. Since the operator of the squared distance of the orbit center from the coordinate origin or any other point, as in the case with one string, commutes with the Hamiltonian, a system of functions which will be eigenfunctions of both operators can in principle be found. However, in the case at hand this is a difficult problem to solve.

Proceeding to the question of the special states we place the coordinate origin at a point through which a nonintegral string passes. We seek a solution in the form

$$\psi=\left[z_+^{S_+}z_-^{S_-}\prod_{i}^{N-1}(z_+-\zeta_{i+})^{S_{i+}}(z_--\zeta_{i-})^{S_{i-}}\right]$$
$$\times f(z_+,z_-)=V(z_+,z_-)f(u), \tag{51}$$

where it is assumed that the function $u(z_+,z_-)$ is a product of cofactors of the form $(z_\pm-\zeta_{i\pm})$. The action of the operators $\hat{P}_\pm$ on ψ has the form

$$\hat{P}_\pm Vf=-i\left[\nu_\pm(z_\mp)Vf+V\frac{\partial u}{\partial z_\mp}f'\right], \tag{52}$$

where

$$\nu_\pm=\sum_{i}^{N-1}\frac{2S_{i\mp}\mp(a_i+\alpha_i)}{z_\mp-\zeta_{i\mp}}+\frac{2S_\mp\mp(a+\alpha)}{z_\mp}. \tag{53}$$

At the points (ζ_{i+},ζ_{i-}), through which integral strings pass $(\alpha_i=0)$, we set $S_{i\pm}=\mp a_i/2$. Then the terms corresponding to these strings fall out of the sum $\nu_\pm$, and the function ψ will be single-valued in a circuit around these points but will not vanish on the integral strings. A linear combination of degenerate functions satisfies the last condition [see Eq. (48) and below]. A linear combination of nonsingle-valued functions cannot eliminate branch points. Consequently, exponent pairs for points containing nonintegral strings, including for the coordinate origin, can be in one of two variants:

$$\text{A)}\quad S_{i+}=-\frac{a_i+\alpha_i}{2},\quad S_{i-}=\kappa_i+\frac{a_i-\alpha_i}{2};$$

$$\text{B)}\quad S_{i+}=\kappa_i-\frac{a_i-\alpha_i}{2},\quad S_{i-}=\frac{a_i+\alpha_i}{2}, \tag{54}$$

where $\kappa_i=\theta(1/2-\alpha_i)$. Then, to each nonintegral string there corresponds a term of the form $(\kappa_i\pm\alpha_i)/(z_\pm-\zeta_{i\pm})$ in one of these sums.

The energy of the ground state of a sequence of special states should be greater than $\hbar\omega/2$, and the energy-lowering operator $\hat{P}_-$ should transform this function so that it no longer satisfies the requirements. The function (51) possesses this property provided that one pair of exponents is chosen in the form B. Substituting this function into Eq. (46) and canceling V we obtain

$$\nu_+\nu_-f+2\nu_-\frac{\partial u}{\partial z_-}f'+2\nu_+\frac{\partial u}{\partial z_+}f'+4\frac{\partial^2 u}{\partial z_-\partial z_+}f'$$
$$+4\frac{\partial u}{\partial z_+}\frac{\partial u}{\partial z_-}f''-2\frac{z_+}{l^2}v_-f-4\frac{z_+}{l^2}\frac{\partial u}{\partial z_+}f'$$
$$=-\frac{2\mu}{\hbar^2}\left(E-\frac{\hbar\omega}{2}\right)f. \tag{55}$$

This equation possesses a solution only if besides a nonintegral string at the coordinate origin no more than one nonintegral string is present at any other point (ζ_{1+},ζ_{1-}). Then setting

$$\nu_+=2\frac{\kappa_1-\alpha_1}{z_--\zeta_{1-}}=\frac{2\beta}{z_--\zeta_{1-}},$$
$$\nu_-=2\frac{\kappa_0-\alpha_0}{z_+}=\frac{2\gamma}{z_+};\quad u=\frac{z_+(z_--\zeta_{1-})}{l^2}, \tag{56}$$

we obtain

$$\frac{\beta\gamma}{ul^2}f+\frac{\gamma}{l^2}f'+\frac{\beta}{l^2}f'+\frac{1}{l^2}f'+\frac{u}{l^2}f''-\frac{\gamma}{l^2}f-\frac{u}{l^2}f'$$
$$=-\frac{\mu}{2\hbar^2}\left(E-\frac{\hbar\omega}{2}\right)f,$$
$$u^2f''+u(\gamma+\beta+1-u)f'-\left[\left(-\frac{E}{\hbar\omega}+\frac{1}{2}+\gamma\right)u-\beta\gamma\right]f=0. \tag{57}$$

The solutions of this equation can be represented in the form

$$f=u^\nu\sum_{k=0}^{\infty}\chi_k u^k, \tag{58}$$

where ν are the roots of the equation

$$\nu^2+\nu(\gamma+\beta)+\beta\gamma=0. \tag{59}$$

In order for $f(x,y)$ to be a single-valued function at least one root of Eq. (59) must be an integral root. In general, this is possible if $\beta\gamma=0$. Therefore, special are possible only if one string is a nonintegral string, specifically, the string where the coordinate origin is placed. For $\beta=0$ and $\zeta_1=0$ Eq. (57) transforms into the equation for the confluent hypergeometric function, and it follows from boundary conditions that

$$f\left(\frac{z_+z_-}{l^2}\right)=\Phi\left(-n,\gamma+l;\frac{r^2}{l^2}\right)=L_n^\gamma\left(\frac{r^2}{l^2}\right),$$
$$E=\hbar\omega\left(n+\gamma+\frac{1}{2}\right). \tag{60}$$

Here n is any positive integer or zero, so that the spectrum (60) describes an infinite equally spaced sequence. The lowest eigenvalue of this sequence is nondegenerate. To any eigenvalue with $n=N\neq 0$ there correspond another N eigen-

functions which are obtained from each of the states (60) with quantum numbers $n=N-L$ $(0<L\leqslant N)$ by operating on them with the operator $(\hat{P}_+ + 2i\hbar z_+/l^2)^L$. Therefore each level is $(n+1)$-fold degenerate. This can be used to obtain linear combinations of functions belonging to the same level which vanish at all points containing integral strings. If there are M integral strings, then the lowest level for which this can be done is $(M+1)$–fold degenerate (except for cases of a special arrangement of the strings which will become clear below). For this, it is necessary to construct from the $(M+1)$–st function a linear combination that vanishes at M points $z_\pm = \zeta_{i\pm}$. Using the system of M linear equations obtained for the coefficients of the combinations, the M coefficients can be expressed uniquely in terms of one of them, which then is determined from the normalization condition. Thus if aside from one nonintegral string there are M integral strings, then, whatever their arrangement (aside from arrangements which cause the determinant of the corresponding system of equations to vanish), the spectrum of the special states is described by the relation (60) and starts with $n=M$, and the lowest state is nondegenerate and its eigenfunction is a definite linear combination of functions with $n=M$ and different L $(0<L\leqslant M)$.

The exact results obtained refute the hypothesis previously proposed by the author (see Ref. 1, p. 148), and in certain cases they contradict the intuitively expected results. For example, although the lowest special state for one nonintegral string with $\alpha>1/2$ [see Eqs. (2) and (12)] localized near it in a region with radius of the order of $R_{00}+r_0 = l(\sqrt{\alpha+1/2}+\sqrt{1/2})$, the appearance of at least one additional integral string at a large distance from the nonintegral string makes the existence of this state impossible. This is a consequence of the requirement that the wave function must vanish at a point containing an integral string. It is characteristic for all problems where in the absence of this requirement there is a discrete spectrum with a nondegenerate lowest state. For example, in the problem of a charged particle in the field of an attractive Coulomb center the ground state with the standard boundary conditions at large distances decreases exponentially but it is impossible to satisfy the condition that the function vanish at any distant point. The reason is not, as is sometimes believed, that the wave function of the ground state cannot have zeros. The ground state function in the three-dimensional problem with the potential $U = A/r^2 - B/r$ is proportional to r^s, where $s = \sqrt{2mA/\hbar^2+1/4}-1/2$ (see Ref. 5, the problem for Sec. 36). But the requirement that the wave function vanish exactly at a point destroying the symmetry of the unperturbed problem is very strong. As shown in Sec. 1 of the present paper it is due to the nature of a magnetic string. In contrast, it can be easily shown that a δ–like repulsive potential admits a finite value of the wave function at a point where it is different from zero and results in a ground state shift which is all the smaller, the farther it is located from the center. A nonintegral string is an even stronger perturbation. As shown above, including one such string even at a distance much greater than the localization radius of the special states annihilates all special because of the requirement that the wave function be single-valued in a circuit around any closed contour in the domain definition. As a result, for several screw dislocations special states are completely impossible, because the ''magnetic fluxes'' in this case are identical for all strings. Evidently, this effect also remains for solenoids with a finite radius.

5. CONCLUSIONS

1. It was shown that the formulation of the problem of the interaction of an electron with a magnetic string must be supplemented by the boundary condition that as the string is approached the wave functions decrease in modulus more rapidly than the square root of the distance from the string.

2. Using these boundary conditions the Hamiltonian of an electron for many arbitrarily arranged strings can be represented as a sum of the ground state energy and a product of two conjugate operators. The results of operating with these operators on an arbitrary eigenfunction of the Hamiltonian are also eigenfunctions of the Hamiltonian that correspond to the eigenvalues increased or decreased by one quantum, provided that they satisfy the boundary conditions. The Larmor frequency in a uniform field determines the quantum of energy. Hence it follows that the spectrum of the Hamiltonian consists of one or several equidistant sequences.

3. The general form of the ground state functions was obtained. The eigenfunctions corresponding to other eigenvalues of the main (coinciding with the spectrum in the uniform field) sequence can be obtained by applying the corresponding powers of the operator, raising the energy.

4. It was shown that there can be only one additional sequence of eigenvalues. It appears only when one of the strings possesses magnetic flux which is not a multiple of twice the flux quantum. The shift of this sequence relative to the main sequence is a fraction of the energy quantum equal to the positive fractional part of the quotient obtained by dividing the magnetic flux of the string by twice the flux quantum. The lowest level of the sequence of special states is shifted by this amount from the level of the main sequence, whose number equals the number of the remaining strings.

5. It was shown that these results cannot be obtained by a semiclassical quantization method, even though the corresponding classical problem possesses an exact solution.

*E-Mail: Iodub@dildub.kiev.ua

[1] I. M. Dubrovskiĭ, *The Theory of Electronic Phenomena in Deformed Crystals*, RIO IMF, Kiev (1999).
[2] V. K. Tkachenko, Zh. Éksp. Teor. Fiz. **77**, 1032 (1979) [Sov. Phys. JETP **50**, 520 (1979)].
[3] S. V. Iordanskiĭ and A. E. Koshelev, Zh. Éksp. Teor. Fiz. **91**, 326 (1986) [Sov. Phys. JETP **64**, 190 (1986)].
[4] R. B. Laflin, Usp. Fiz. Nauk **170**, 292 (2000).
[5] L. D. Landau and E. M. Lifshitz, *Quantum Mechanics. Nonrelativistic Theory*, Fizmatgiz, Moscow (1963).
[6] A. Messiah, *Quantum Mechanics*, Nauka, Moscow (1978), Vol. 1.
[7] L. Schiff, *Quantum Mechanics*, Izd. Inostr. Lit., Moscow (1959).
[8] D. I. Blokhintsev, *Foundations of Quantum Mechanics*, Vysshaya Shkola, Moscow (1961).
[9] H. Bateman and A. Érdelyi, *Higher Transcendental Functions. The Hypergeometic Function. Legendre Functions*, Nauka, Moscow (1965).
[10] M. H. Johnson and V. A. Lippman, Phys. Rev. **76**, 828 (1949).
[11] A. Feldman and A. H. Kahn, Phys. Rev. B **1**, 4584 (1970).

Translated by M. E. Alferieff

Magnetic properties of a $LaMn_{0.46}Co_{0.54}O_3$ single crystal

S. N. Barilo, V. I. Gatal'skaya,* S. V. Shiryaev, and L. A. Kurochkin

Institute of Solid State Physics and Semiconductors, Belorussian National Academy of Sciences, ul. I. Brovki, 17, Minsk, 220072, Belorus

R. Shimchak and M. Baran**

Institute of Physics, Polish Academy of Sciences, Al. Lotnikow 32/46, 02-668 Warsaw, Poland
(Submitted May 8, 2002)
Fiz. Nizk. Temp. **28**, 1195–1198 (November 2002)

The magnetic properties of a $LaMn_{0.46}Co_{0.54}O_3$ single crystal, grown by electrochemical deposition, are studied in a wide range of fields and temperatures. The two-phase magnetic state model of the crystal is used to analyze the results. © *2002 American Institute of Physics.*
[DOI: 10.1063/1.1528577]

1. INTRODUCTION

It is well known that the ideal perovskite $LaMnO_3$ is an antiferromagnetic (AF) dielectric. For metallic and ferromagnetic (FM) states to appear in this system manganese with the mixed valence Mn^{3+}/Mn^{4+} must be present. There are at least three possibilities for this: 1) the substitution of divalent metals for lanthanum; 2) the presence of nonstoichiometric oxygen; and, 3) the substitution of magnetic and nonmagnetic ions for manganese. The colossal magnetoresistance (CMR) observed in substituted manganites is ordinarily explained by the double-volume model in combination with Jahn–Teller (JT) distortions of the crystal structure. However, many aspects of the spin/charge/orbital ordering in manganites are still not clear.

The structural and magnetic properties of $LaMn_{1-x}Co_xO_3$ have been investigated in Refs. 1–7 to establish the source of the FM in this system. The results of these works are quite contradictory. Thus, the ferromagnetic states are attributed to the following interactions: monovalent $Mn^{3+}-O-Mn^{3+}$ (Co^{3+} is in the low–spin state and does not contribute to FM),[1] positive superexchange $Mn^{4+}-Co^{2+}$,[2–4,7] or mixed superexchange $Mn^{3+}-O-Mn^{4+}$, $Mn^{3+}-O-Mn^{3+}$, and $Mn^{4+}-O-Mn^{2+}$.[5]

Two magnetic phases with rhombohedral (transition temperature $T_c=225$ K) and orthorhombic ($T_c=175$ K) structures are found in the compound $LaMn_{0.5}Co_{0.5}O_3$.[1,4] Varying the conditions of synthesis makes it possible to obtain only the low– or the high–temperature phase.[4,8] We note that all investigations known to us of the system La–Mn–Co–O were performed on polycrystalline samples. This makes it difficult to interpret the results obtained. In the present work the magnetic properties of a $LaMn_{0.46}Co_{0.54}O_3$ (LMCO) single crystal are studied.

2. EXPERIMENTAL PROCEDURE

LMCO single crystals with Co content close to 0.5 were obtained by electrochemical deposition in a platinum crucible from a solution–in–melt of the binary system $Cs_2MoO_4-MoO_3$. Detailed description of the method used to obtain the single crystals and of the method used to determine the cationic composition are given in Ref. 9. The single crystals grown had a shiny black color and were nearly cubic in shape. X-Ray diffraction was used to determine the phase composition, the lattice parameters, and the orientation of the single crystals.

The magnetization of a single crystal was measured using a SQUID magnetometer (Quantum Design, MPMS–5) in magnetic fields up to 50 kOe in the temperature range 4.2–300 K.

3. EXPERIMENTAL RESULTS AND DISCUSSION

X-Ray structural measurements performed on powders of the crystal material showed that LMCO single crystals are single–phase and their structure is close to rhombohedral.[9] The temperature dependences of the susceptibility of a LMCO single crystal, which were measured in a 50 Oe field in FC and ZFC regimes, are displayed in Fig. 1. The transition from the paramagnetic (PM) into the FM state occurs at $T_c=170$ K. The susceptibility $\chi_{FC}=M/H$ increases as temperature decreases and is close to saturation at all temperatures. The behavior of the susceptibility $\chi_{ZFC}(T)$ differs

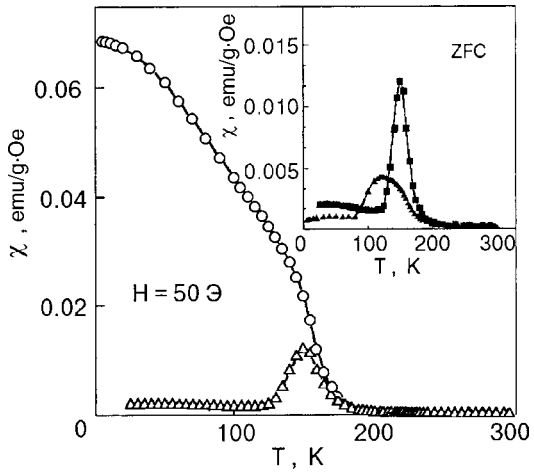

FIG. 1. Temperature dependence of the susceptibility $\chi(T)$ of a LMCO crystal: χ_{FC} (○) and χ_{ZFC} (△). Inset: $\chi_{ZFC}(T)$ in 50 Oe (■) and 1 kOe (▲) fields.

sharply from that of $\chi_{FC}(T)$—so-called thermomagnetic irreversibility is observed. The disparity first appears at temperatures close to T_c, and in contrast to $\chi_{FC}(T)$ a sharp peak is observed on the curve $\chi_{ZFC}(T)$ at $T_m = 150$ K; below T_m χ_{ZFC} decreases. The value of T_m depends on the applied magnetic field and shifts to low temperatures with decreasing magnetic field: for $H = 1$ kOe $T_m = 120$ K (inset in Fig. 1). We note that even in a 50 kOe field irreversibility is observed between χ_{FC} and χ_{ZFC} for temperatures below 50 K ($T_m = 20$ K) (Fig. 2). This behavior attests to the presence of magnetic clusters in the crystal. The PM Curie temperature $\Theta_p = 173$ K was estimated from the temperature dependence of the inverse susceptibility H/M measured in a 50 kOe field under FC conditions. The quantity Θ_p is positive, indicating that the exchange coupling between spins (or magnetic clusters) is of a FM character.

The field dependences of the magnetization $M(H)$ of a LMCO single crystal were measured for temperatures 5–200 K. Figure 3 shows as an example the hysteresis loop for 5 K. The magnetization $M(H)$ saturates at ~ 30 kOe, and the coercive force H_c at low temperatures is large and equals 10 kOe at 5 K. The quantity H_c depends strongly on temperature and decreases to 130 Oe for $T = 140$ K. We note that the typical FM character of the field dependences $M(H)$ confirms that the decrease in M_{ZFC} at low temperatures (Fig. 1) is due not to an FM–AFM transition but rather a gradual freezing of FM clusters. Extrapolating $1/H$ to zero field in the $M-1/H$ plane in high fields we obtain the magnetic saturation moment $\mu_s = 1.75\mu_B$ per formula unit. This value corresponds to the total contributions of Mn^{4+} and Co^{2+}. In Ref. 10 it is shown that as x increases in the system $LaMn_{1-x}Co_xO_3$ ($x \geqslant 0.5$) the total magnetic moment starts to decrease not only because the ratio Mn/Co decreases but also because of hybridization, giving rise to an additional decrease of the magnetic moments of Mn and Co. The value $\mu_s = 175\mu_B$ which we obtained for a LMCO crystal is identical to the theoretical value of the magnetic moment for $x = 0.54$,[10] associated with the $Mn^{4+}-Co^{2+}$ interaction[7] giving rise to FM in a LMCO crystal.

The results obtained can be explained using the model of a magnetically two–phase state which presupposes that at sufficiently low temperatures the system separates into an AF matrix and FM clusters in this matrix. The character of the temperature dependences $M_{ZFC}(T)$ and $M_{FC}(T)$ will depend on the ratio of the contributions of the matrix and the FM clusters. For the FC case, as temperature decreases ($T < T_c$), the spins of the clusters become oriented in the direction of the field and the contribution to M_{FC} will be maximum. For the ZFC case, when the sample is cooled in zero field, there is no preferred orientation of the spins in the FM clusters and the contribution of the FM phase to M_{ZFC} for the lowest temperatures will be minimum (Fig. 1). If a weak magnetic field is applied to the crystal, then the magnetization will strongly depend on the magnetic anisotropy of the system. For strong anisotropy a weak magnetic field will not be able to turn the spins in the required direction and M_{ZFC} will be small. Since the coercive force H_c is due to the magnetic anisotropy of the AF phase, for $H < H_c$ the thermomagnetic irreversibility between M_{FC} and M_{ZFC} at low temperatures will be large. As the magnetic field increases, the difference between M_{FC} and M_{ZFC} decreases (Figs. 1 and 2); this is characteristic when FM clusters are present in the matrix.[11]

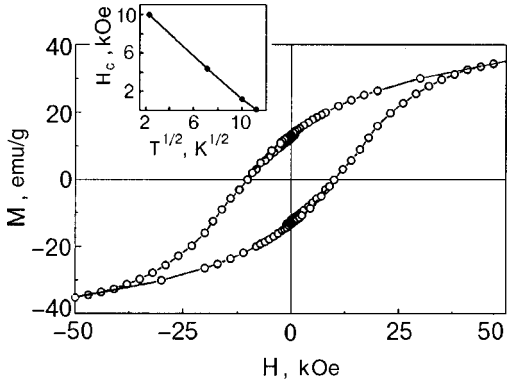

FIG. 3. Hysteresis loop $M(H)$ of a LMCO single crystal at 5 K. Inset: coercive force H_c versus $T^{1/2}$; solid line—fit of the relation (2).

A Langevin function fits well the temperature dependence of the magnetization $M(T)$ measured in a 50 kOe field (Fig. 2). The effective magnetic moment of a cluster is $\mu/\mu_B = 15$, which corresponds to the total moment of several Mn unit cells. Our estimates agree with the results of Ref. 12 concerning the existence of magnetic clusters in a crystal.

The temperature derivative $d(M_{ZFC}-M_{FC})/dT$ of the difference between M_{ZFC} and M_{FC} characterizes the distribution of the temperatures T_B at which as temperature decreases the clusters gradually become blocked according to their magnetic anisotropy energy. According to Fig. 4, this

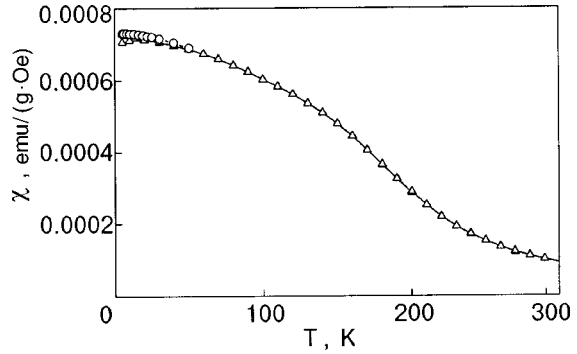

FIG. 2. Temperature dependence of χ of a LMCO single crystal in a 50 kO field: χ_{FC} (○), χ_{ZFC} (△); solid line—fit of a Langevin function.

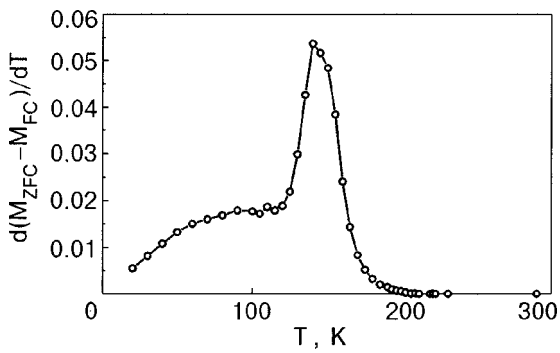

FIG. 4. $d(M_{ZFC}-M_{FC})dT$ versus temperature for a LMCO single crystal ($H = 50$ Oe).

distribution is nonuniform and contains two peaks—a large sharp peak at $T_B = 150$ K and a smaller flat peak at $T_B = 100$ K.

Thus, at least two types of magnetic clusters exist in LMCO at sufficiently low temperatures. The volumes (diameters) of these clusters can be estimated from the value of T_B of a cluster and the curves $M-H$ measured in strong fields. The coercive force H_c depends on the effective magnetic anisotropy constant K and the cluster volume V as

$$H_c = 2K/M_s[1-(25kT/kV)^{1/2}], \quad (1)$$

where M_s the saturation magnetization. In the limit $T \to 0$ $H_{c0} = 2K/M_s$. From Eq. (1) and the relation[13] $25kT_B = KV$ we obtain the following expression for H_c:

$$H_c = H_{c0}(1-T/T_B)^{1/2}. \quad (2)$$

Clusters in LMCO satisfy this relation: the experimental values of H_c lie on the straight line $H_c = f(T^{1/2})$ and $H_{c0} = 1.24$ kOe (see inset in Fig. 3). An estimate of the anisotropy constant K gives 1.5×10^6 ergs/cm^3; the cluster volumes are 3.5×10^{-19} cm^3 ($T_B = 150$ K) and 2.3×10^{-19} cm^3 ($T_B = 100$ K) and the corresponding cluster diameters are 87 and 76 Å.

4. CONCLUSIONS

The magnetic behavior of a $LaMn_{0.46}Co_{0.54}O_3$ single crystal grown by electrochemical deposition was studied in the temperature range 4.2–300 K in fields up to 50 kOe. The results can be explained on the basis of a two–phase model of the magnetic state of the crystal—FM clusters in an AF matrix. The volume (diameter) and blocking temperature of the clusters were estimated.

We thank D. D. Khalyavin for performing the x-ray measurements and P. Aleshkevich for providing the computer program for calculating the Langevin functions.

The work in Warsaw was supported in part by the Committee of Scientific Research (KBN) as part of grant No. 5P03B0162.

*E-mail: v_gatal@ifttp.bas-net.by
**E-mail: baran@ifpan.edu.pl

[1] J. B. Goodenough, A. Wold, R. J. Arnott, and N. Menyuk, Phys. Rev. **124**, 373 (1961).
[2] J. H. Jonker, J. Appl. Phys. **37**, 1424 (1966).
[3] G. Blasse, J. Phys. Chem. Solids **26**, 1969 (1965).
[4] P. A. Joy, Y. B. Khollam, and S. K. Date, Phys. Rev. B **62**, 8608 (2000).
[5] I. O. Troyanchuk, L. S. Lobanovsky, D. D. Khalyavin, S. N. Pastushonok, and H. Szymczak, J. Magn. Magn. Mater. **210**, 63 (2000).
[6] V. L. J. Joly, P. A. Joy, and S. K. Date, J. Phys.: Condens. Matter **13**, L841 (2001).
[7] J.-H. Park, S.-W. Cheong, and T. C. Chen, Phys. Rev. B **B55**, 11072 (1977).
[8] V. L. J. Joly, P. A. Joy, S. K. Date, and C. S. Gopinath, J. Phys.: Condens. Matter **13**, 649 (2001).
[9] D. D. Khalyavin, S. V. Shiryaev, G. L. Bychkov, S. N. Barilo, S. N. Ustinovich, L. A. Kurochkin, and H. Szymczak, in *Proceedings of the 4th International Conference on SCG and HMT, Obninsk (2001)*, Vol. 2, p. 372.
[10] Zh. Yang, L. Ye, and X. Xie, Phys. Rev. B **59**, 7051 (1999).
[11] L. Chivelder, L. A. Castillo, M. A. Gusmao, J. A. Alonso, and L. F. Coen, Phys. Rev. B **60**, 12184 (1999).
[12] J. Z. Sun, L. Krusin-Elbaum, A. Gupta, G. Xiao, and S. S. P. Parkin, Appl. Phys. Lett. **69**, 1002 (1996).
[13] C. P. Bean and J. D. Livingstone, J. Appl. Phys. **30**, 120 (1959).

Translated by M. E. Alferieff

LOW-DIMENSIONAL AND DISORDERED SYSTEMS

Giant resistance switching effect in nano-scale twinned $La_{0.65}Ca_{0.35}MnO_3$ film

V. G. Prokhorov,* G. G. Kaminsky,* and V. A. Komashko*

Institute of Metal Physics, National Academy of Sciences of Ukraine, 36 Vernadsky Str., Kiev, 03142, Ukraine

Y. P. Lee

Department of Physics, Hanyang University, Seoul, 133-791 Korea

A. I. Tovstolytkin and A. N. Pogorily

Institute of Magnetism, National Academy of Sciences of Ukraine, Kiev, 03142, Ukraine

(Received 11 March, 2002; revised 31 May, 2002)
Fiz. Nizk. Temp. **28**, 1199–1202 (November 2002)

The magnetic and transport properties of a 20 nm-scale twinned $La_{0.65}Ca_{0.35}MnO_3$ film are investigated in a temperature range of 77–300 K. The coexistence of ferromagnetic metallic and charge-ordered insulating phases is suggested by analyzing the temperature and current dependences of the resistance at low temperatures. It is shown that thermocycling leads to the formation of a nonequilibrium state in the ensemble of charge-ordered domains and to the appearance of a giant switching in resistance of up to 100%. The experimental results are discussed on the basis of phase separation. © *2002 American Institute of Physics.*
[DOI: 10.1063/1.1528578]

The hole-doped perovskite manganites are of great current interest not only for fundamental science in connection with the discovery of colossal magnetoresistance (CMR), but also for their potential applications to new devices such as magnetic reading heads, field sensors, and memories. Recently evidence was presented for the coexistence of ferromagnetic metallic (FM) and charge-ordered insulating (COI) phases in $La_{0.67}Ca_{0.33}MnO_3$ films at low temperatures governed by the lattice strains accumulated during the deposition.[1,2] This defies the common knowledge that the phenomenon of charge ordering (CO) is observed only in compounds with a small average A-site cation radius, $\langle r_A \rangle \leqslant 0.118$ nm. However, in view of the very similar energies of the COI and FM states in these compounds[3] one might expect the appearance of the COI region in the compound with a larger $\langle r_A \rangle$ induced by a structural distortion away from the ideal cubic perovskite lattice.[2] Charge ordering controlled by lattice strains was observed previously in $Pr_{0.65}Ca_{0.35}MnO_3$ films.[4]

In this paper we report experimental results for the magnetic and transport properties of a $La_{0.65}Ca_{0.35}MnO_3$ film prepared by rf magnetron sputtering using a so-called ''soft'' (or powder) target.[5] The substrate was a $LaAlO_3$ (001) twinned crystal with a lattice parameter a of 0.379 nm for the pseudocubic symmetry. The substrate temperature during deposition was 750 °C. The thickness d of the film was about 50 nm. In contrast to the two-step cooling of the chamber with a hold at 400 °C for 1 h, which is usual for the preparation of films with perfect crystal structure, here one-step cooling was employed to enhance the lattice strains. The θ–2θ x-ray diffraction (XRD) patterns were obtained using a Rigaku diffractometer with CuK_{α_1} radiation. The lattice parameters evaluated directly from the XRD data were plotted against $\cos^2\theta/\sin\theta$. With straight-line extrapolation to $\cos^2\theta/\sin\theta = 0$, a more precise determination of the lattice parameter is obtained. The resistance measurements were carried out by using the four-point-probe method in a temperature range of 77–300 K and a magnetic field up to 1.5 T. The magnetization curves in a field up to 100 Oe were taken with a Quantum Design SQUID magnetometer in a temperature range of 50–300 K.

Figure 1a presents the θ–2θ XRD scan of the $La_{0.65}Ca_{0.35}MnO_3$ film. Only the $(00l)$ peaks of both the substrate and the film are significantly manifested, indicating that the deposition results in a highly oriented film. The out-of-plane lattice parameter was estimated as $c \approx 0.3882$ nm. On the other hand, the splitting of the (003) peak into two separated subpeaks (Fig. 1b) similar to that in the substrate (Fig. 1c) testifies the formation of twinned microstructure in the film. The size of the twinned crystallites, estimated from the XRD data, is ≈20 nm. Analogous results were obtained for $La_{0.67}Ca_{0.33}MnO_3$ films prepared by rf magnetron sputtering using a solid target.[6] Moreover, Rao *et al.*[7] suggested that the full width at half maximum (FWHM) for $La_{1-x}Ca_xMnO_3$ films on $LaAlO_3$ substrates would be limited to between 0.25° and 0.30° due to the twinned structure of $LaAlO_3$. In our case the FWHM for the (002) reflection is 0.25°, which falls within the suggested range of values. Therefore, one can conclude that we are dealing with a nano-scale twinned $La_{0.65}Ca_{0.35}MnO_3$ film. It is reasonable to expect the existence of the nonuniform (with nano-scale spatial modulation) lattice strain distribution that can lead to the formation of a mixed FM and COI state in this film.[1,2]

Figure 2 displays the temperature dependence of the re-

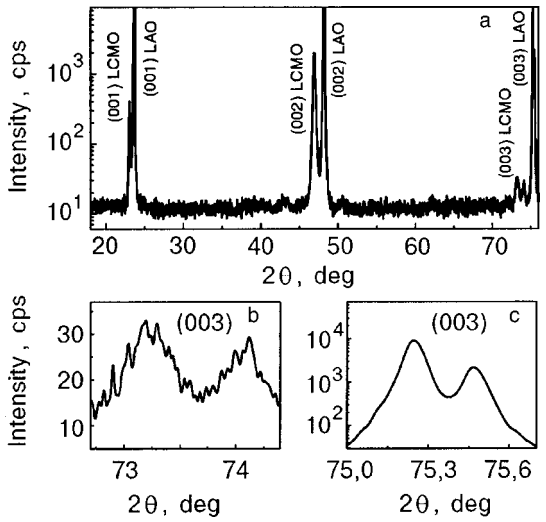

FIG. 1. θ–2θ XRD pattern for a $La_{0.65}Ca_{0.35}MnO_3$ film (a). The (003) diffraction peaks of the film (b) and substrate (c) for the cubic symmetry.

sistance $R(T)$ at different applied magnetic fields. The magnetic field was directed at right angles to both the film surface and the transport current. The first peak at $T_{p1} \approx 250$ K is connected with the usual metal-insulator (MI) transition that is accompanied by the paramagnetic→ferromagnetic transition with decreasing temperature. The inset of Fig. 2 shows zero-field-cooled (ZFC) and field-cooled (FC) temperature-dependent magnetization curves, $M(T)$. It is seen that the Curie temperature for the film is $T_C \approx 250$ K and coincides with T_{p1} of $R(T)$. The position of the second peak is located in the low-temperature range, $T_{p2} \approx 125$ K, and the physical nature needs more discussion, as below. The absence of additional structure on the $M(T)$ curves indicates that the investigated $La_{0.65}Ca_{0.35}MnO_3$ film is chemically homogeneous and undergoes only one magnetic transition. An-

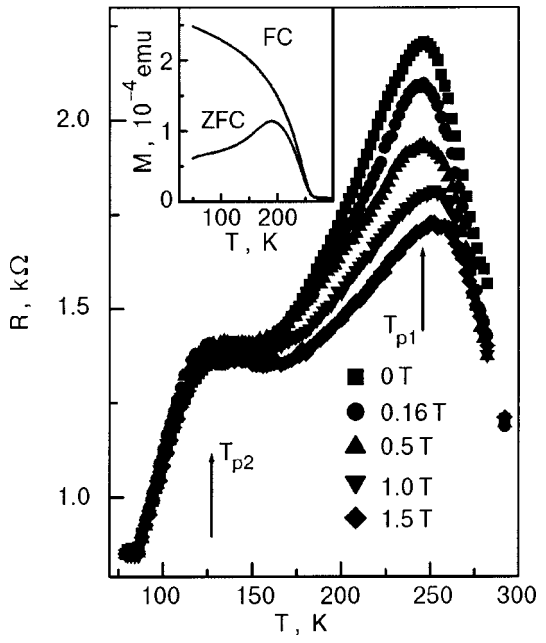

FIG. 2. Temperature dependence of the resistance of a $La_{0.65}Ca_{0.35}MnO_3$ film at different applied magnetic fields. The inset displays the temperature dependence of the field-cooled (FC) and zero-field-cooled (ZFC) magnetization.

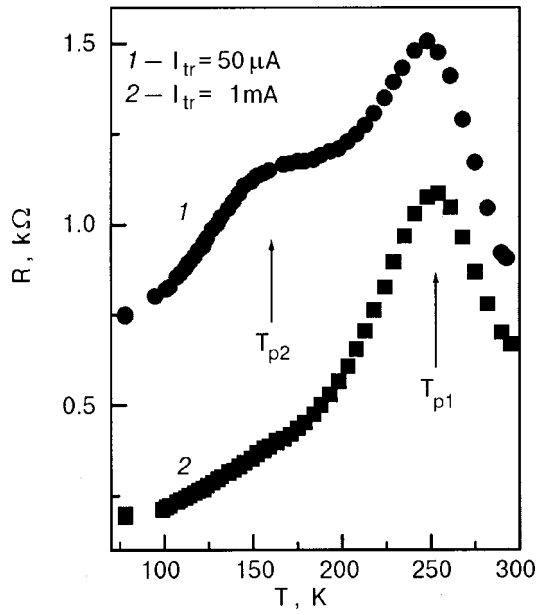

FIG. 3. Temperature dependence of the resistance of a $La_{0.65}Ca_{0.35}MnO_3$ film measured at different transport currents: 50 μA (*1*) and 1 mA (*2*).

other source for the two-peak behavior of $R(T)$ can be grain boundaries (GB) that play the role of magnetic tunnel junctions.[8–11] The spin-polarized tunneling of carriers between ferromagnetic grains through an insulating grain boundary leads to the formation of a peak on the $R(T)$ curve at a low temperature, which must be very sensitive to a low applied magnetic field.[8] However, in our case the resistance has a weak dependence on magnetic field near T_{p2}, and the magnitude of the negative magnetoresistance in this temperature range is much smaller than that observed for manganites films with artificially grown GB.[11,12] Our results are coincident with the $T-H$ phase diagram for a nonuniformly strained $La_{0.67}Ca_{0.33}MnO_3$ thin film, which predicts this type of behavior of the resistance in the COI state.[2] On the other hand, Fig. 3 shows that the second peak disappears at a low electric field. A similar effect was observed recently in epitaxial films of charge-ordered rare-earth manganites and it was shown that the COI state is destroyed by applying a small electrical current.[13,14] Therefore, we might conclude that the nano-scale twinned $La_{0.65}Ca_{0.35}MnO_3$ film becomes phase-separated below the Curie temperature and includes both FM and COI regions simultaneously. There are reasons for a nonuniform distribution of magnetic moments in the film and the unusual behavior of $M(T)$. The absence of saturation on the FC $M(T)$ curve at low temperatures and the very large difference between the ZFC and FC values of the magnetization attest to a spin-glass-like (or cluster-glass-like) magnetic state in the film below T_C. In this case the FM clusters are randomly distributed in the antiferromagnetic insulating matrix, and the long-range exchange interaction between them is essentially suppressed.

Figure 4 displays the influence of thermocycling on the shape of the $R(T)$ curve for the prepared $La_{0.65}Ca_{0.35}MnO_3$ film. In the first cycle (*1*) the film was cooled down to 77 K and the $R(T)$ curve was recorded with increasing temperature. The third cycle (*2*) means that the film was heated to 300 K twice before the measurement. It is seen that the third

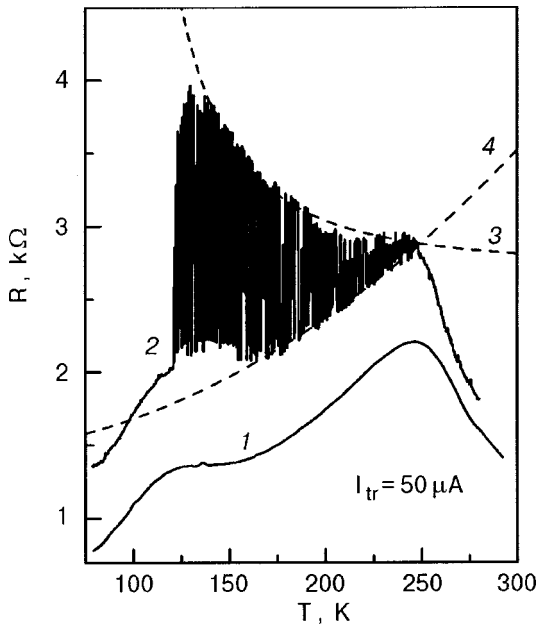

FIG. 4. Temperature dependence of the resistance switching after the first. (*1*) and third (*2*) thermocycles of a $La_{0.65}Ca_{0.35}MnO_3$ film. Theoretical curves (*3*) and (*4*) describe thermally activated and metal-like $R(T)$ behavior, respectively.

cycle invokes a large oscillation in the resistance (or voltage). The resistance switching appears strictly between the two peaks on the $R(T)$ curve and vanishes at both high ($T \geqslant T_{p1}$) and low ($T \leqslant T_{p2}$) temperatures. Further repetition of thermocycling does not change the $R(T)$ shape obtained after the third cycle (Fig. 4, curve *2*). The measurements of the resistance at fixed temperature as a function of time did not manifest voltage oscillations of such giant amplitude. Moreover, the stopping in thermocycling and relaxation of the film during half an hour at 77 K or room temperature leads to disappearance of the resistance switching effect and the $R(T)$ behavior becomes similar to that after the first thermocycle (Fig. 4, curve *1*). Consequently, the observed oscillations of the resistance cannot be explained by telegraph noise or dynamic fluctuation of the resistivity.[15,16]

Figure 4 (curve *2*) shows that the resistance switching takes place between two limited high- and low-resistance states. The temperature dependence of the maximum resistance values in Fig. 4 (curve *3*) can be described by expression of $R(T)=R_0+\alpha T\exp(T_0/T)$ with the following fitting parameters: $R_0=2.6\ \mathrm{k\Omega}$, $\alpha=0.11\ \mathrm{k\Omega/K}$ and $T_0=620\ \mathrm{K}$. Such thermally activated behavior of the conductivity is typical for the $La_{0.65}Ca_{0.35}MnO_3$ compound in the insulating state above the Curie point. The $R(T)$ curve enveloping the minimum resistance values in Fig. 4 (curve *4*) displays metal-like behavior and can be described by $R(T)=R_0+\beta T^2$ with the following fitting parameters: $R_0=1.4\ \mathrm{k\Omega}$, $\beta=0.023\ \mathrm{k\Omega/K^2}$. Therefore, one can conclude that the nano-scale twinned $La_{0.65}Ca_{0.35}MnO_3$ film really consists of COI (high-resistance) and FM (low-resistance) regions with a different behavior of $R(T)$. The thermocycling, owing to the structural transformations in the ensemble of COI domains,[17,18] results in nonequilibrium phase separation of the film and the appearance of resistance switching between the COI and FM states. The disappearance of the switching below T_{p2} can be attributed to freezing of the COI domains, as indicated by Mori *et al.*[19]

In summary, we present evidence for the coexistence of FM and COI phases in a nano-scale twinned $La_{0.65}Ca_{0.35}MnO_3$ film, which has been confirmed by magnetic and transport measurements. Thermocycling leads to a giant switching in resistance, up to 100%, between the COI and FM states. This is explained by the structural perturbation of the COI domains.

This work was supported by a Korea Research Foundation Grant (KRF-2001-015-DS0015) and by the Science and Technology Center of Ukraine through Project No. 1086.

*E-mail: pvg@imp.kiev.ua

[1] A. Biswas, M. Rajeswari, R. C. Srivastava, Y. H. Li, T. Venkatesan, R. L. Green, and A. J. Millis, Phys. Rev. B **61**, 9665 (2000).
[2] A. Biswas, M. Rajeswari, R. C. Srivastava, T. Venkatesan, R. L. Green, Q. Lu, A. L. de Lozanne, and A. J. Millis, *cond-mat/0102321* (2001).
[3] M. Uehara, S. Mori, C. H. Chen, and S.-W. Cheong, Nature (London) **399**, 560 (1999).
[4] Y. P. Lee, V. G. Prokhorov, J. Y. Rhee, K. W. Kim, G. G. Kaminsky, and V. S. Flis, J. Phys.: Condens. Matter **12**, L133 (2000).
[5] V. G. Prokhorov, G. G. Kaminsky, V. A. Komashko, J. S. Park, and Y. P. Lee, J. Appl. Phys. **90**, 1055 (2001).
[6] J.-H. Song, K. K. Kim, Y. J. Oh, H.-J. Jung, J. H. Song, D.-K. Choi, and W. K. Choi, J. Cryst. Growth **223**, 129 (2001).
[7] R. Rao, D. Lavric, T. K. Nath, C. B. Eom, L. Wu, and F. Tsui, Appl. Phys. Lett. **73**, 3294 (1998).
[8] H. Hwang, S.-W. Cheong, N. P. Ong, and B. Batlog, Phys. Rev. Lett. **77**, 2041 (1996).
[9] A. Gupta, G. Q. Gong, G. Xiao, P. R. Duncombe, P. Lecoeur, P. Trouilloud, Y. Y. Wang, V. P. Dravid, and J. Z. Sun, Phys. Rev. B **54**, R15, 629 (1996).
[10] N. D. Mathur, G. Burnell, S. P. Isaac, T. J. Jackson, B.-S. Teo, J. L. MacManus-Driscoll, L. F. Cohen, J. E. Evetts, and M. G. Blamier, Nature (London) **387**, 266 (1997).
[11] R. Gross *et al.*, J. Magn. Magn. Mater. **211**, 150 (2000).
[12] K. Steenbeck, T. Eick, K. Kirscn, H.-G. Schmidt, and E. Steinbeiss, Appl. Phys. Lett. **73**, 2506 (1998).
[13] V. Pannambalam, S. Parashar, A. R. Raju, and C. N. R. Rao, Appl. Phys. Lett. **74**, 206 (1999).
[14] S. Parashar, E. E. Ebenso, A. R. Raju, and C. N. R. Rao, Solid State Commun. **114**, 295 (2000).
[15] R. D. Merithew, M. B. Weissman, F. M. Hess, P. Spradling, E. R. Nowak, J. O'Donnell, J. N. Eckstein, Y. Tokura, and Y. Tomioka, Phys. Rev. Lett. **84**, 3442 (2000).
[16] S. Raquet, A. Anane, S. Wirth, P. Xiong, and S. von Moln'ar, Phys. Rev. Lett. **84**, 4485 (2000).
[17] V. Podzorov, C. H. Chen, M. E. Gershenson, and S.-W. Cheong, cond-mat/0105411 (2001).
[18] V. Podzorov, B. G. Kim, V. Kiryuhin, M. E. Gershenson, and S.-W. Cheong, cond-mat/0107609 (2001).
[19] S. Mori, C. H. Chen, and S.-W. Cheong, Nature (London) **392**, 473 (1998).

This article was published in English in the original Russian journal. Reproduced here with stylistic changes by AIP.

Magnetotransport in a quasi-one-dimensional electron system on superfluid helium

B. A. Nikolaenko,* Yu. Z. Kovdrya, and S. P. Gladchenko

B. P. Verkin Physicotechnical Institute for Low Temperatures, Ukrainian National Academy of Sciences, pr. Lenina, 47, Khar'kov, 61103, Ukraine

(Submitted April 10, 2002; resubmitted June 5, 2002)
Fiz. Nizk. Temp. **28**, 1203–1210 (November 2002)

Magnetotransport in a nondegenerate quasi-one-dimensional electron system on superfluid helium is investigated experimentally. The measurements are performed in perpendicular magnetic fields $B \leqslant 2.6$ T in the temperature range 0.48–2.05 K with 100–400 nm wide conducting channels. In the region where the carriers are scattered by the helium atoms in the vapor ($T > 0.9$ K) and in the region where the electrons are scattered by ripplons ($T < 0.9$ K) the longitudinal component ρ_{xx} of the magnetoresistance of the conducting channels predominantly increases with B. The experimental data in the region of carrier scattering by helium atoms in the vapor agree with the classical Drude law, and in the quantum transport regime with $\omega_c \tau > 1$ (ω_c is the cyclotron frequency and τ is the relaxation time of the electron system) the self-consistent Born approximation for a $2D$ electron system above helium gives a qualitative explanation of the data. It is conjectured that the quantitative differences between the experimental data and the theoretical calculations are due to the difference of the specific features between the experimentally studied and theoretically analyzed systems. The experimental values of the electron mobilities at low temperatures and in weak magnetic fields agree with theoretical calculations for a quasi-one-dimensional system. Weak carrier localization in the experimental electron system explains the negative magnetoresistance of the conducting channels, which was observed in the gas and ripplon carrier scattering regions. © *2002 American Institute of Physics.* [DOI: 10.1063/1.1528579]

1. INTRODUCTION

Surface electrons (SEs) on superfluid helium are a unique classical low-dimensional system because of the extreme purity of the substrate, the high uniformity of the electron layer, and the weak interaction of the carriers with the surface of liquid helium. The electron mobility in such a system can reach record high values. At temperatures $T > 0.1$ K (gas scattering region) the interactions between the carriers and the helium atoms in the vapor and at temperatures $T < 0.9$ K (ripplon region of scattering) surface oscillations of the liquid helium—ripplons—limit the electron mibility. Since the maximum admissable electron density, determined by the development of electrohydrodynamic instability of the charged surface, on liquid helium is relatively low, the SEs form a gas of particles which are separated by distances much larger than the de Broglie wavelength.

Magnetic transport in a two-dimensional electron system ($2D$) on superfluid helium has been investigated quite well both theoretically and experimentally[1–4] in the gas and ripplon carrier scattering regions. It is well known that charge transport in a perpendicular magnetic field B differs substantially from that in a zero magnetic field because of the appearance of discrete energy levels (Landau levels). It has been established that for $\omega_c \tau < 1$ ($\omega_c = eB/m$ is the cyclotron frequency, e and m are the free electron charge and mass, respectively, and τ is the relaxation time of electrons on elastic scatterers) magnetotransport follows the classical Drude law and in the opposite limit, $\omega_c \tau > 1$, a transition occurs into the quantum transport regime with a more complicated magnetic field dependence of the transport characteristics. Under these conditions the magnetoresistance ρ_{xx} (correspondingly, the magnetoconductivity σ_{xx} also) of a $2D$ electron system is due to the interaction of carriers in Landau levels whose width is determined by electron scattering by various nonuniformities. It has been shown that the longitudinal magnetoresistance behaves anomalously in the ripplon scattering region—as temperature decreases, ρ_{xx} at first increases and then decreases. This behavior can be described on the basis of a theoretical model[5] that takes account of the predominant scattering of electrons by ripplons with characteristic wavelengths equal to the magnetic length.

In addition to the well-known quasi-one-dimensional ($Q1D$) and one-dimensional ($1D$) systems based on thin metal wires, semiconductor heterostructures, organic conductors, and so on, analogous systems based on surface electrons on superfluid helium are of substantial interest. A $Q1D$ electron system on helium can be obtained by linear modulation of the properties of the substrate in one direction along its surface. Since the interaction of the SEs with various scatterers in the two-dimensional system on liquid helium has been well studied, effects due to a decrease in dimension, specifically, a transition from a two- to a one-dimensional system, can be observed in the present electron system.

A variant of a quasi-one-dimensional electron system using surface electrons on liquid helium has been proposed in Ref. 6 and realized in Ref. 7. The quasi-one-dimensional electron system was obtained by electron localization in the ''troughs'' of the curved surface of liquid helium flowing under capillary forces in small channels of a shaped dielectric substrate. The transverse size of the electron conducting

channels on helium can be easily varied over wide limits by varying the height of the substrate surface above the helium surface or the intensity of the confining electric field $E_\perp$ directed perpendicular to the substrate.

A special feature of one-dimensional conducting systems is that processes associated with carrier localization, specifically, weak localization processes which influence charge transport, are strong in such systems Weak localization is due to the interaction of surface electrons with nonuniformities, resulting in interference processes between electron wave packets. Weak localization is characterized by the condition $k_T l_0 > 1$ (here k_T is the electron wave number, l_0 is the mean free path length of carriers between elastic scatterers) and can be destroyed by inelastic scattering of electrons by various scatterers or a magnetic field as a result of a decrease in the size of the localization region of the electron wave function and a decrease of l_0. $Q1D$ systems based on a nondegenerate electron gas, such as SEs on liquid helium, have the advantages that the thermal velocity V_T and the mean–free path length of the electrons can be varied over wide limits by varying the temperature or scatterer density and therefore the quantity $k_T l_0$. It is of great interest to investigate localization processes in a $Q1D$ system based on surface electrons on liquid helium.

Preliminary measurements of the magnetoresistance in a $Q1D$ electronic system on superfluid helium were performed in Refs. 8 and 9. The present work is a continuation of a series of experimental investigations of magnetotransport in a quasi-one-dimensional electron system on superfluid helium. The investigations were performed in magnetic fields up to 2.6 T in the gas and ripplon scattering regions at temperatures $T = 0.48–2.05$ K. The conducting channels were 100–400 nm wide, depending on the conditions and the problems of the experiment.

2. EXPERIMENTAL DATA AND DISCUSSION

A quasi-one-dimensional electron system on liquid helium was obtained using a shaped substrate with a small dielectric constant. The structure of the substrate and the method for measuring the magnetoresistance are similar to those described in Ref. 10. The substrate consisted of 150 nylon filaments, each 100 μm in diameter, arranged in a row on a $24.5 \times 19.1 \times 1.2$ mm glass plate and placed on a system of rectangular measuring electrodes.

The quality of the conducting channels of the quasi-one-dimensional electron system based on SEs on helium depends directly on the quality of the substrate and the process used to prepare the electronic conducting system. A miniature 5 μm in diameter tungsten heating filament, whose heating power was negligible, served as the electron source. To eliminate random charging of the substrate or sections of the substrate covered with a thin helium film, the filament was briefly heated at $T \simeq 1.3$ K. The electric field was weak ($\simeq 0.1$ V/cm), which prevented electrons from penetrating directly into the substrate. Next, the electric field was increased to higher values. It was found that the quality of the substrate decreased from one experiment to another. The maximum mobility μ in the $Q1D$ channels at low temperatures in a zero magnetic field is 210 $m^2/(V \cdot s)$.[8,10] However, in the present work we used a substrate of a somewhat lower quality, for which the maximum mobility in a zero magnetic field was $\simeq 160$ $m^2/(V \cdot s)$. A series of experiments was performed on a substrate with low–temperature mobility 90 $m^2/(V \cdot s)$. The difference between the experimental and theoretical values of the mobility is due to some random modulation of the potential along the channels because of surface nonuniformities of the nylon filaments comprising the substrate.

The experiments were performed in a system of rectangular measuring electrodes at 100 kHz. Changes in the amplitude of the 0° and 90° components of the electric signal transmitted through the cell when it was charged by the electrons were measured. The guiding electric field was directed along the conducting channels. The data obtained made it possible to determine the real and imaginary parts of the conductivity of the cell with the electrons and, from these data, the values of ρ_{xx} and the effective mobility of the electrons (the computational procedure is similar to that described in Ref. 10). The error in the determination of the values of ρ_{xx} and μ was about 30%. The results of the experimental investigations are displayed in Figs. 1–4. Figures 1 and 4 show the experimental data obtained on a substrate where μ_0 reached the values 160 $m^2/(V \cdot s)$. Figures 2 and 3 show data obtained with a substrate with maximum mobility in zero magnetic field $\simeq 90$ $m^2/(V \cdot s)$.

Figure 1 shows the temperature dependences of $(ne\rho_{xx})^{-1}$ in magnetic fields 0, 0.68, 1.36, and 2.05 T. These dependences were obtained for the confining electric field $E_\perp = 460$ V/cm. It is evident that at temperatures $T > 0.9$ K the dependence of $(ne\rho_{xx})^{-1}$ on T is essentially exponential, indicating that helium atoms in the vapor predominantly in-

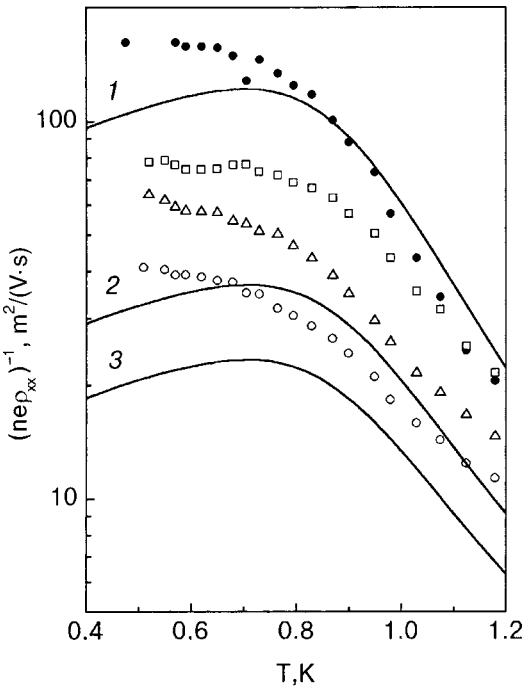

FIG. 1. Temperature dependence of $(ne\rho_{xx})^{-1}$ for a quasi-one-dimensional electron system on helium in magnetic fields B, T: 0 (●); 0.68 (□); 1.36 (△); 2.05 (○). The distance between the electrons in a channel is $5 \cdot 10^{-4}$ cm. The lines denote the theoretical calculation of this quantity for a $2D$ system performed in accordance with Ref. 12 for B, T: 0.8 (*1*), 1.5 (*2*), and 1.9 (*3*).

fluence the carrier scattering. For $T \leqslant 0.9$ K the dependence of $(ne\rho_{xx})^{-1}$ on T is flatter. Electron–ripplon interaction predominates in this temperature range.

The average electron localization length in the first energy level in a direction perpendicular to the channel is $y_0 = (\hbar/m\omega_0)^{1/2}$.[6] The effective width of the conducting channels is $y_n = y_0(kT/\hbar\omega_0)^{1/2}$ (k is Boltzmann's constant and $\hbar\omega_0 = \hbar(eE_\perp/mR)$ is the splitting between neighboring levels in the energy spectrum of the electronic system). In the experimental temperature range this quantity is 200–400 nm a confining electric field $E_\perp = 460$ V/cm and substrate height above the helium level 8 mm. In a zero magnetic field $\hbar\omega_0 = 0.13$ K. The lineal electron density in the channel was $\sim 10^5$ m^{-1}. Correspondingly, the Coulomb interelectron interaction energy is several Kelvins. For the present experimental conditions the minimum carrier mean free path length in the gas region at 2 K is $l_0 < 10^{-7}$ m, which is less than the width of a conducting strip. As T increases, l_0 increases and in the ripplon scattering region $l_0 > y_n$. In the presence of a magnetic field the magnetic length $l_m < y_n$ starting with fields $\sim 10^{-2}$ T.

Thus, the experimental electron system at sufficiently low temperatures and in weak magnetic fields is nearly quasi-one-dimensional in the ripplon-scattering region, and in the gas carrier-scattering region its properties are probably close to a $2D$ system, the only difference being that the electrons in a conducting channel are in the narrow parabolic potential well which forms the channel. Variations of the potential resulting in lower mobility in a zero magnetic field occur along the conducting channels.

Figure 1 shows (solid lines) the results of a theoretical calculation of $(ne\rho_{xx})^{-1}$ for a two-dimensional electron system in magnetic fields close to those used in the experiments performed in Ref. 12.[1)] In this theory only the scattering of electrons by helium atoms in the vapor and by ripplons as well as many electron effects, which result in additional broadening of the Landau levels, were taken into account. It should be noted that the decrease of $(ne\rho_{xx})^{-1}$ in the ripplon region with decreasing temperature which according to the theory should occur in two-dimensional systems was not observed in the experiments. Quantitative differences are also observed between the theoretically calculated and experimentally measured quantities. For $B = 0.8$ T the theoretical values of $(ne\rho_{xx})^{-1}$ are greater than and for $B = 1.5$ and 1.9 T less than the experimental values. Thus, the experimentally obtained dependence of ρ_{xx} on B is weaker than theory predicts. The difference in the behavior of the values of $(ne\rho_{xx})^{-1}$ measured experimentally and computed theoretically for a $2D$ system could be due to the fact that in the quasi-one-dimensional conducting channels studied the electrons are localized in a direction perpendicular to the channels and variations of the potential along the channels are observed.

In the classical limit the Drude model describes well the electron transport in a magnetic field in a $2D$ electronic system on liquid helium. The components of the resistivity and conductivity tensors can be represented in the forms

$$\sigma_{xx} = \frac{\sigma_0}{1+(\mu B)^2}, \quad \sigma_{xy} = \mu B \sigma_{xx}, \tag{1}$$

$$\rho_{xx} = \rho_0, \quad \rho_{xy} = \frac{B}{n_e e}, \tag{2}$$

where $\sigma_0 = I/\rho_0 = ne\mu$.

The experimentally measured values of ρ_{xx} made it possible to determine σ_{xx} from the expression

$$\sigma_{xx} = \frac{\rho_{xx}}{\rho_{xx}^2 + \rho_{xx}^2}. \tag{3}$$

Such calculations can be performed if the Lorentz force $IB/n_2 y_n$ (I is the electric current along the conducting channels and n_2 is the effective two-dimensional electron density) is weaker than the effective force due to the presence of the potential energy of a particle in a channel. Estimates show that these conditions hold in magnetic fields exceeding 0.2 T.

Figure 2 shows the values of σ_{xx}^{-1} computed using Eq. (3) versus the magnetic field B in the gas region of carrier scattering for different temperatures.

The properties of electron transport in the quantum limit for short-range scatterers, which, specifically, helium atoms in a vapor are, are determined by carrier scattering in Landau levels, which, in turn, gives rise to broadening of the levels. The magnetoconductivity σ_{xx} in a two-dimensional electron system under quantum transport conditions has been studied in the self-consistent Born approximation.[13] A theory of quantum magnetotransport in the gas region of electron scattering has been developed in Ref. 14. This theory is applicable in a wide range of magnetic fields. According to this theory the expression for σ_{xx} is

$$\sigma_{xx} = \frac{e^2 n}{m} \frac{\nu_{\text{eff}}}{\omega_c^2 + \nu_{\text{eff}}^2},$$

$$\nu_{\text{eff}} = \frac{2\cosh(\hbar\omega_c/2kT)}{\pi I_1(\Gamma/kT)} \left[\cosh\left(\frac{\Gamma}{kT}\right) - \frac{kT}{\Gamma} \sinh\left(\frac{\Gamma}{kT}\right) \right]. \tag{4}$$

Here ν_{eff} is the effective collision frequency between electrons and helium atoms in the vapor in a magnetic field as-

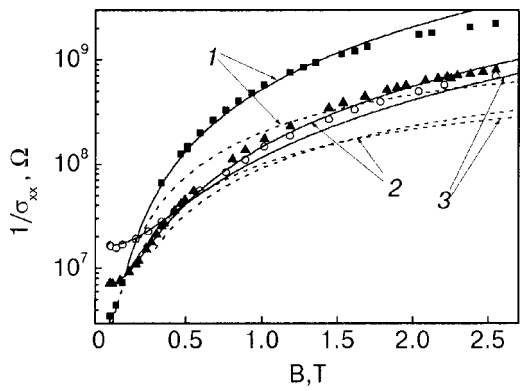

FIG. 2. $1/\sigma_{xx}$ of conducting channels versus B in the gas region of electron scattering at T, K: 1.3 (■); 1.63 (▲); and 2.05 (○). The numbers denote the theoretical dependences referring to the corresponding values of T, K: 1.3 (*1*), 1.63 (*2*), and 2.05 (*3*). The solid lines represent Drude model calculations, the dashed lines represent calculations performed using the expression (4). The experimental electron mobilities in zero magnetic field are 11, 4.0, and 2.0 m^2/(V·s) for temperatures 1.3, 1.63, and 2.05 K, respectively. The electron density in the channels is $2.2 \cdot 10^{11}$ m^{-2}.

suming a semielliptic density of states for the Landau levels, Γ is the effective half-width of a Landau level, and I_1 is a modified Bessel function.

Figure 2 shows for comparison the theoretical calculations performed using the Drude model and the expression (4). In these calculations it was assumed that the effective half-width of the Landau levels is $\Gamma=\sqrt{\Gamma_0^2+\Gamma_s^2}$, where Γ_0 is the Landau-level half-width due to carrier interaction with helium atoms in the vapor and Γ_s is the broadening of a Landau level as a result of substrate nonuniformities. The mobilities in zero magnetic field, which at temperatures 1.3, 1.63, and 2.05 K are, respectively, 11, 4.1, and 2.0 $m^2/(V\cdot s)$ were used to calculate Γ. It was assumed that the values of τ determining the electron mobility have the form $1/\tau=1/\tau_g+1/\tau_s$, where τ_g and τ_s are the relaxation times due to, respectively, the interaction with helium atoms in the vapor and the random potential due to substrate nonuniformities. It is evident that the experimental values of σ_{xx}^{-1} agree well with the Drude calculations [see Eqs. (1)–(3)]. This shows that the expressions (1)–(3) are applicable under the present conditions. It is also evident that the experimental values of σ_{xx}^{-1} disagree quantitatively with the data obtained on the basis of Ref. 14; in addition, the discrepancy increases as temperature decreases. This difference is probably due to the specific nature of the present experimental system, where the carriers are in a parabolic potential well with narrow conducting channels, and possible to the effect of the random variations of the potential along the channels on magnetotransport.

Figure 3 shows the resistivity ρ_{xx} of the conducting channels in a magnetic field versus the magnetic field at $T=0.6$ K. In the ripplon carrier scattering region $\rho_{xx}\propto B$ predominantly for magnetic fields 0–2.6 T.

Carrier transport in a quasi-one-dimensional electron system on liquid helium in a magnetic field parallel to the confining field was studied theoretically in Ref. 15 on the basis of the Boltzmann kinetic equation, taking account of the electron distribution over the energy levels of the one-dimensional-system. The electron–electron interaction was also taken into account in the calculation. The inset in Fig. 3 shows the magnetic field B dependence of the ratio of the electron mobility μ in a magnetic field to the mobility μ_0 in the absence of a field. It is evident that in the weak magnetic field limit, in the region where the theory is applicable ($B\leqslant 0.03$ T), the experimental data agree with the theoretical calculation.

The effect of a magnetic field on the ratio ρ_{xxx}/ρ_0 in the gas carrier–scattering region at 1.2 K and in the ripplon region at $T=0.6$ K is shown in Fig. 4. The data were obtained for a relatively clean substrate ($\mu=160$ $m^2/V\cdot s$) at ($T=0.5$ K). At $T=1.2$ K, as B increases to $\simeq 0.6$ T the ratio ρ_{xx}/ρ_0 decreases to $\simeq 0.9$, after which $\rho_{xx}/\rho_0\propto B^2$. In relatively strong fields $\rho_{xx}/\rho_0\propto B$. The negative magnetoresistance at this temperature is due to weak electron localization on helium atoms in the vapor. As stated above, the weak localization is due to the interference of the electronic wave function in the presence of randomly distributed elastic scattering centers. Weak localization introduces corrections in the kinetic coefficients, specifically, it decreases the conductivity.[16] The suppression of weak localization by a magnetic field increases conductivity. Thus, negative magnetoresistance can serve as an indicator of the influence of weak carrier localization. The further experimentally observed increase in the ratio ρ_{xx}/ρ_0 with increasing magnetic field $B>0.6$ T is due to a transition from the classical to the quantum charge transport regime. Weak localization for a $Q1D$ electronic system on liquid helium at temperatures ranging from 1.3 K and higher has been studied experimentally in Ref. 17. It should be noted that weak localization can also increase the differences between the experimental data and the theoretical calculations (see Figs. 1 and 2).[14]

The quantum transport regime predominates in the ripplon scattering region at $T=0.6$ K. In relatively strong fields a monotonic increase of ρ_{xx}/ρ_0 with increasing B is observed in the experiments, and as noted above this dependence is less steep than for a $2D$ electronic system. In the present work detailed investigations of ρ_{xx} versus the magnetic field were performed in magnetic fields up to 0.2 T with relatively strong confining electric fields (up to $\simeq 2$ kV/cm) to intensify the interaction of the electrons with the ripplon system. The corresponding mobility was $\simeq 60$ $m^2/(V\cdot s)$. The width of the channels for this value of E is 100 nm. The results obtained are displayed in the inset in Fig. 4, which

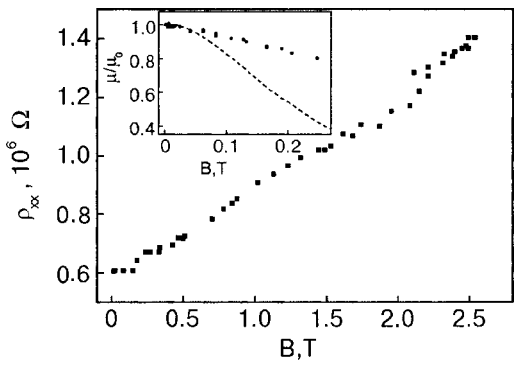

FIG. 3. Longitudinal magnetoresistance for a quasi-one-dimensional electron system ρ_{xx} versus B in the ripplon scattering region at $T=0.6$ K ($\mu_0=90$ $m^2/(V\cdot s)$). Inset: Field dependence of μ/μ_0—the ratio of the electron mobility in a magnetic field to the mobility in the absence of a field—detemined experimentally (●); the broken line was calculated theoretically following Ref. 15.

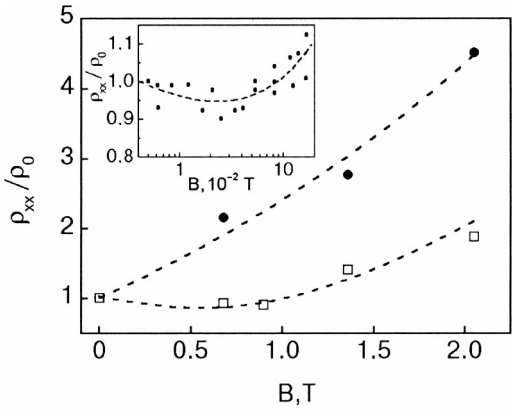

FIG. 4. Reduced magnetoresistance ρ_{xx}/ρ_0 in a quasi-one-dimensional electron system versus the magnetic field at T, K: 1.2 (□) and 0.6 (●). The data were obtained on a freshly prepared substrate. Inset: ρ_{xx}/ρ_0 versus B for weak magnetic fields at $T=0.6$ K; broken lines—least-squares computer fit to the experimental data.

shows ρ_{xx}/ρ_0 versus B. The measurements were performed at the limit of sensitivity of the measurement system, so that a variance was observed in the obtained values. The broken line is a least-squares computer fit to the experimental data. It is evident that a weakly expressed negative magnetoresistance, whose minimum value is about $0.95\rho_0$ at $B \simeq 0.02$ T, is observed in ρ_{xx}/ρ_0 versus B in relatively weak magnetic fields. This effect is also probably due to weak carrier localization at low temperatures and could be due to ripplons or substrate nonuniformities. The experimental investigations of this effect will be continued.

3. CONCLUSIONS

In this work carrier transport in a quasi-one-dimensional electron system on superfluid helium in magnetic fields up to 2.6 K was studied experimentally in the gas and ripplon carrier scattering regions. The width of the conducting channels was 100–400 nm. It was shown that the longitudinal component of the magnetoresistance increases predominantly with increasing magnetic field intensity, and the effect of the field is all the stronger the higher its value and the lower the temperature. The experimental data on the magnetoresistance in the ripplon region, where under the experimental conditions the electron system is nearly quasi-one-dimensional, agree well with the theory for weak magnetic fields.[15] In the gas region the Drude model of a $2D$ system describes well for the classical charge transport regime the experimental values of the resistivity ρ_{xx} in a magnetic field and up to quite large values of the magnetic field (the higher the temperature, the higher the fields). In the ultraquantum regime the theory of magnetotransport for a $2D$ system[14] describes the experimental data only qualitatively. The quantitative difference between the experimental values of the resistivity in a magnetic field and the theoretically computed analogous quantity for a $2D$ system is probably due to the presence of a potential well perpendicular to the channel in which the carriers move and to random variations of the potential along the channels.

The negative magnetoresistance in the gas scattering region at $T=1.2$ K is due to a weak electron localization on helium atoms in the vapor. A weakly expressed negative magnetoresistance was found in the ripplon region. It is conjectured that it is also due to weak electron localization at low temperatures as a result of electron scattering by ripplons or nonuniformities of the solid substrate.

We thank Yu. P. Monarkha for showing interest in this work. This work was supported in part by an INTAS Network grant, program 99–1643.

*E-Mail: nikolaenko@ilt.karkov.ua

[1)]We thank Yu. M. Monarkh for providing the data from the theoretical calculations.

[1] V. N. Grigor'ev, O. I. Kirichek, Yu. Z. Kovdrya, and Yu. P. Monarkha, Fiz. Nizk. Temp. **16**, 394 (1990) [Sov. J. Low Temp. Phys. **16**, 219 (1990)].
[2] R. W. van der Heijden, H. M. Gijsman, and F. M. Peeters, J. Phys. C **21**, L1165 (1988).
[3] A. O. Stone, P. Fozooni, M. J. Lea, and M. Abdul-Gader, J. Phys. Condens. Matter **1**, 2743 (1989).
[4] Yu. Z. Kovdrya, V. A. Nikolaenko, O. I. Kirichek, S. S. Sokolov, and V. I. Grigor'ev, Fiz. Nizk. Temp. **19**, 458 (1993) [Sov. J. Low Temp. Phys. **19**, 323 (1993)].
[5] Yu. P. Monarkha, Fiz. Nizk. Temp. **17**, 146 (1991) [Sov. J. Low Temp. Phys. **17**, 76 (1991)].
[6] Yu. Z. Kovdrya and Yu. P. Monarkha, Fiz. Nizk. Temp. **12**, 1011 (1986). [Sov. J. Low Temp. Phys. **12**, 571 (1986)].
[7] Yu. Z. Kovdrya and V. A. Nikolaenko, Fiz. Nizk. Temp. **18**, 1278 (1992). [Sov. J. Low Temp. Phys. **18**, 894 (1992)].
[8] Yu. Z. Kovdrya, V. A. Nikolaenko, S. P. Gladchenko, and S. S. Sokolov, J. Low Temp. Phys. **113**, 1109 (1999).
[9] V. A. Nikolaenko and Yu. Z. Kovdrya, Physica B **284–288**, 170 (2000).
[10] S. P. Gladchenko, V. A. Nikolaenko, Yu. Z. Kovdrya, and S. S. Sokolov, Fiz. Nizk. Temp. **27**, 3 (2001) [Low Temp. Phys. **27**, 1 (2001)].
[11] S. S. Sokolov, Guo-Qiang Hai, and N. Studart, Phys. Rev. B **51**, 5977 (1995).
[12] Yu. P. Monarkha, Shin-Ichiro Ito, K. Shirahama, and K. Kono, Phys. Rev. Lett. **75**, 2445 (1997).
[13] T. Ando, Y. Matsumoto, and Y. Uemura, J. Phys. Soc. Jpn. **39**, 279 (1975).
[14] P. J. M. Peters, P. Scheuzger, M. J. Lea, Yu. P. Monarkha, P. K. H. Sommerfeld, and R. W. van der Heijden, Phys. Rev. B **16**, 570 (1994).
[15] S. S. Sokolov, Guo-Qiang Hai, and N. Studart, Fiz. Nizk. Temp. **23**, 649 (1997) [Low Temp. Phys. **23**, 487 (1997)].
[16] B. L. Altshuler, D. E. Khmelnitskii, A. J. Larkin, and P. A. Lee, Phys. Rev. B **22**, 5142 (1980).
[17] Yu. Z. Kovdrya, V. A. Nikolaenko, and S. P. Gladchenko, JETP Lett. **73**, 465 (2001).

Translated by M. E. Alferieff

LOW-TEMPERATURE PHYSICS OF PLASTICITY AND STRENGTH

Low-temperature deformation and fracture of bulk nanostructural titanium obtained by intense plastic deformation using equal channel angular pressing

V. Z. Bengus,* E. D. Tabachnikova, and V. D. Natsik

B. I. Verkin Physicotechnical Institute for Low Temperatures, Ukrainian Academy of Sciences, pr. Lenina, 47, Khar'kov, 61103, Ukraine

Ľ. Mishkuf and K. Chakh

Institute of Experimental Physics, Slovakian Academy of Sciences, ul. Vatsonova, 47, Koshitse, 04353, Slovakia

V. V. Stolyarov and R. Z. Valiev

Institute of the Physics of New Materials, Ufim State Aviation Technology University, ul. K. Marksa, 12, Ufa, 450000, Russia

(Submitted June 21, 2002)
Fiz. Nizk. Temp. **28**, 1211–1226 (November 2002)

The low-temperature plasticity and fracture of polycrystals of coarse-grained (CG) and nanostructural (NS) technical-grade titanium of two structural modifications with grain size 0.3 and 0.1 μm, which were prepared by equal channel angular pressing (ECAP) with additional thermomechanical treatment are studied. The measurements are performed at temperatures 300, 77, and 4.2 K with uniaxial compression at deformation rate 4×10^{-4} s^{-1}. The ''stress-plastic deformation'' hardening curves are obtained, the macroscopic yield stress, and the ultimate plasticity are measured for samples with compression axis orientations parallel and transverse to the ECAP axis. It is found that the yield stress for NS titanium is 1.5–2 times higher than for CG titanium and the yield stress on cooling from 300 to 4.2 K. Plasticity anisotropy is also observed in NS titanium—the yield stress is 1.2–1.5 times greater when the compression axis is oriented perpendicular to the ESAP axis than for parallel orientation. The ultimate plasticity with such changes in the structure of samples and under the experimental conditions systematically decreases, but the deformation to fracture remains above 4%. Nanostructural titanium does not show cold-brittleness right down to liquid-helium temperatures, but at 4.2 K plastic flow becomes jumplike, just as in CG titanium. It is established that for low-temperature uniaxial compression NS titanium fractures as a result of unstable plastic shear accompanied by local adiabatic heating of the material. This phenomenon is not characteristic of CG titanium. A study of the morphology of the shear-fracture surfaces using a scanning electron microsope shows a characteristic ''vein'' pattern, attesting to local heating at temperatures $\geqslant 800$ °C. It is established that plastic deformation in NS titanium is thermally activated at low temperatures. It is shown that microstructural internal stresses due to thermal anisotropy and possible microtwinning affect the yield stress. © *2002 American Institute of Physics.* [DOI: 10.1063/1.1528580]

1. INTRODUCTION

Bulk polycrystals of metals and alloys with ultrasmall grain size of the order of 100 nm, which are called nanostructural (NS) materials, are finding increasing applications as structural materials in modern technology.[1] For applications, a very important property of these materials is the optimal combination of high strength and high plasticity. Equal channel angular pressing (ECAP) is an effective technological method which gives a combination of these properties.[1]

Nanostructural titanium is of special interest among the many NS materials obtained up to now. The room-temperature yield stress in samples of NS titanium obtained by the ECAP method is more than two times higher than that in coarse-grained (CG) titanium[2,3] and approaches the value of the theoretical shear strength of titanium single crystals. It was established a long time ago that CG titanium possesses high plasticity at room temperature and this property remains (and even increases) on cooling to 77 K,[4,5] so that it is regarded as a promising structural material in cryogenic technology.[4] In this connection there arises an obvious interest in studying the mechanical properties of NS titanium at low temperatures and the possibilities of using this material in cryogenic technology.

There are several other factors stimulating interest in the plasticity and fracture of NS titanium at low temperatures.

In the first place it has been found that titanium single

crystals with substantially different grain sizes possess different tendencies toward twinning: for CG samples the twinning intensity increases on cooling,[5,6] and for NS samples obtained by ECAP twinning is impeded,[3] though the possibility of twinning at the microlevel cannot be ruled out.. Since the parallel flow and interaction of slipping and twinning play a primary role in the formation of the plastic and strength properties of crystalline materials, the differences noted cast doubt on the possibility of predicting the properties of NS titanium on the basis of results obtained by studying CG samples.

In the second place there now exists experimental evidence of unstable plastic shear in NS titanium. This evidence was obtained by studying the fracture of NS titanium under quasistatic uniaxial compression at 77 K[2] and highspeed impact compression at room temperature:[3] localized shear, resulting in fracture of the samples by slipping of part of the sample along the plane of maximum tangential stresses, was observed in both cases. Such shear fracture of the samples has been interpreted[2] on the basis of considerations formulated in Ref. 7 as being due to thermal and mechanical instability as a result of local adiabatic heating in a catastrophic shear band propagating along integrain boundaries. In this connection it is of interest to study the characteristic features of the fracture of NS titanium under uniaxial compression at liquid helium temperature 4.2 K, for which the specific heat and thermal conductivity of the material are much lower than at 77 K, which is favorable for the appearance of localized heating.[7]

The ECAP method for obtaining NS titanium results in strongly expressed anisotropy of the substructure and mechanical properties of the samples.[2] Consequently, one interesting problem is to study the characteristics of the plasticity and fracture of NS titanium with the samples undergoing deformation parallel and perpendicular to the ECAP axis.

Finally, of special interest is a question which has essentially remained unstudied: the role of grain-boundary dislocations and internal stresses in plastic flow and fracture of NS titanium at low temperatures.

In the present work a systematic experimental study and comparison of the mechanisms of deformation and fracture of NS and CG titanium are performed in a wide range of low temperatures. We pursued two goals in discussing the results obtained: expanding and deepening the understanding of the mechanisms of deformation of NS materials and showing the prospects for using NS titanium in cryogenic technology.

2. MATERIALS AND METHODS

The investigation was performed on samples cut from $14\times14\times160$ mm bars of technical-grade (VT-1-0) polycrystalline titanium. The deformation and fracture of titanium were studied in three structural states:

initial state 1—average grain size $d=15$ μm, obtained by hot pressing;

state 2—average grain size $d=0.3$ μm, obtained by intense plastic deformation of the initial titanium by means of eight ECAP passes at 450 °C;

state 3—average grain size $d=0.1$ μm, obtained by intense plastic deformation of the initial titanium by eight ECAP passes followed by cold rolling to 75% deformation, followed by annealing at 300 °C for 1 h.

The mechanical characteristics were studied under uniaxial compression with a relative deformation rate of about 4×10^{-4} s^{-1} (quasistatic deformation) on a deformation machine with stiffness 13 kN/mm at temperatures 300, 77 (liquid nitrogen), and 4.2 K (liquid helium). The samples used for compression consisted of $2\times2\times7$ mm rectangular prisms. The stress was measured to within ±3 MPa and the deformation to within $\pm0.1\%$.

Samples cut from rods both parallel ($\parallel$) and perpendicular ($\perp$) to the ECAP axis were studied. The following characteristics of the samples were determined:

the deformation diagrams $P(t)$, where P is the deforming load and t is the deformation time, were recorded;

the strain hardening curves $\sigma(\varepsilon)$, where σ is the deforming stress and ε is the plastic strain, were found from the deformation diagrams (in the uniform deformation approximation);

the conventional macroscopic yield stress σ_y was found by the method of intersection of tangents to the deformation diagram $P(t)$ on its initial and stationary sections;

the maximum plastic deformation up to fracture (ultimate plasticity) ε_{ul};

the form of the fracture was determined and the morphology of the fracture surfaces was investigated using a TESLA BS-300 scanning electron microscope.

The quantitative characteristics of the deformation and fracture were found by averaging the data for five or more samples.

3. EXPERIMENTAL RESULTS AND DISCUSSION

3.1. Special features of strain hardening of NS titanium at low temperatures

The mechanisms of strain hardening of coarse-grained polycrystalline titanium under tension were studied previously for strain rates $10^{-3}-8\times10^{3}$ s^{-1} and experimental temperatures 77–1000 K.[6] In a number of samples, for a definite combination of strain rate and testing temperature, the curves $\sigma(\varepsilon)$ showed the standard three-stage character. However, in other cases, for relatively low strain rates $10^{-3}-10^{-1}$ s^{-1} and temperature 77 K the curves $\sigma(\varepsilon)$ were parabolic. Parabolic hardening was also observed with high strain rates 2×10^{3}-8×10^{3} s^{-1} and temperatures 77, 298, and 398 K.[3] The hardening curves obtained in the present work with compression of CG titanium (structural state 1) agree with the results of Refs. 3 and 6 with comparable deformation rates and temperatures.

The study of NS titanium (structural states 2 and 3) with strain rate 4×10^{-4} s^{-1} which we chose revealed a substantially different character of hardening and its response to a temperature change. In the entire temperature range 300–4.2 K a single stable stage of linear hardening was observed on the hardening curves after a narrow transitional stage near the yield stress (Fig. 1). The expression

$$\sigma(\varepsilon)=\sigma_y+\theta\varepsilon, \tag{1}$$

where θ is the strain hardening coefficient, fit the dependences $\sigma(\varepsilon)$ quite well. This expression describes the hardening curves of all experimental samples of NS titanium, but

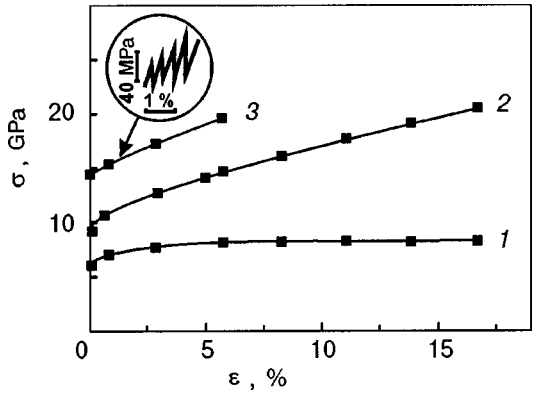

FIG. 1. Curves of the deformation of NS titanium (state 2, ‖. orientation) at temperatures 300 (1), 77 (2), and 4.2 (3) K. The jump-like character of the curve (σ,ε) at 6.2 K is shown in the inset.

its parameters—the conventional yield stress and the strain hardening coefficient—depend strongly on the temperature T and the average grain size d, and they show anisotropy with respect to the ECAP axis. Figure 1 shows that for NS titanium at room temperature there is virtually no hardening θ $(300\ \mathrm{K}) \simeq 0$; a similar phenomenon was observed with NS titanium under tension[8] and nanostructural iron under compression.[9] However, the hardening coefficient increases as temperature decreases: $\theta\,(77\ \mathrm{K}) = 5.7$ GPa and $\theta\,(4.2\ \mathrm{K}) = 8.8$ GPa.

An interesting feature of the low-temperature plasticity of single crystals and polycrystals of VT-1-0 titanium under uniaxial stretching and compression is the unstable (jumplike) character of the plastic flow at liquid-helium temperature.[5,10–12] At 4.2 K the plastic deformation of NS titanium is also jumplike, starting at the yield stress. Figure 2 shows typical examples of uniaxial compression diagrams $P(t)$ at 4.2 K for titanium samples with various grain sizes (in different structural states) and various orientations of the compression axis relative to the ECAP axis. Note that the characteristic amplitudes and frequency of the jumps depend appreciably on the grain size and compression axis orientation.

The above-described features of the deformation diagrams and hardening curves for NS titanium corresponds qualitatively to a source model of plastic deformation and strain hardening, as previously proposed by one of us.[13] According to this model the ''parabolic'' hardening curves $\sigma(\varepsilon)$ were observed when slip bands, arising from discrete sources at a certain threshold value of the deforming stress, subsequently undergo gradual development, increasing their contribution to the deformation as the deformation stress increases. When the slip bands give only a one-time (''discrete'') contribution to deformation on nucleation with no further development and the nucleation sources are distributed throughout the volume of the sample statistically homogeneously and act independently, a ''stagewise'' (in the particular case—linear) curve $\sigma(\varepsilon)$ should be observed.[13]

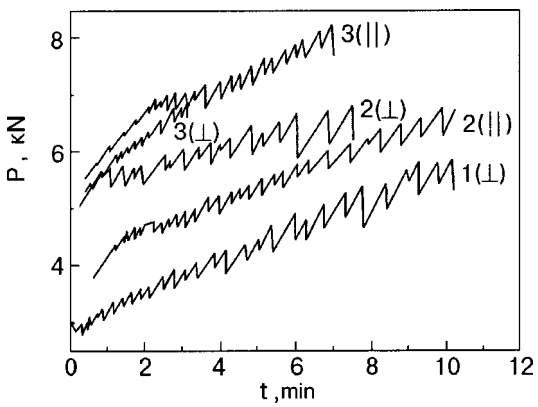

FIG. 2. Sections of diagrams of jump-like deformation $P(t)$ during uniaxial compression at 4.2 K of titanium samples in different structural states and with different orientation of the compression axis relative to the ECAP axis (see text).

This ''discrete'' nature of deformation development is probably inherent to NS materials. The observation of acoustic emission, which was accompanied by plastic deformation of NS copper, can serve as additional experimental confirmation of the discrete character of plastic deformation in NS materials.[14] It is natural to conjecture that the source regions in NS titanium are individual, favorably oriented grains where plastic shear starts and then develops along the boundaries of many grains. The propagation of such shear can be judged by observing the amplitudes of the deformation jumps at 4.2 K.

The curves in Fig. 2 make it possible to compare the character of the jump-like deformation for titanium samples with different structural states and different orientations. For example, for the structural state 2 in samples with ''perpendicular'' (⊥) orientation the number of load jumps per unit plastic deformation is almost 1.5 times smaller than for ''parallel'' (‖) samples. For the same ⊥-orientation a transition from state 1 to state 2 is accompanied by a decrease in the frequency of jumps by almost a factor of 2. This shows that the number of sources responsible for the initiation of an individual act of plastic deformation and the corresponding load jump is smaller in ''perpendicular'' samples; correspondingly, for these samples the average amplitudes of the jumps are almost twice as large. The measured amplitudes of the first jumps are of the order of 60 N, which corresponds to a $\sim 0.1\%$ contribution to the plastic deformation of a sample, and prior to fracture the jump amplitudes increase approximately by a factor of 10. It is obvious that such a substantial plastic deformation in an individual jump should be of a cooperative character and encompass many grains (grain boundaries) in the deformed sample. However, the available information is still inadequate for identifying unequivocally the sources of grain-boundary shears which propagate along many grain boundaries and transform into a localized shear band, resulting in jumps.

The ultimate plasticity ε_{ul} to fracture under compression of NS titanium is quite high and comparable to the plasticity of coarsegrained rod titanium under uniaxial tension (18–20%[5]). The plasticity resource systematically decreases with decreasing grain size; this is evident in Fig. 2. However, even in the least plastic structural state 3 at 4.2 K ε_{ul} is 12% for ‖ and 4% for ⊥ orientations. This shows that bulk nanostructural titanium obtained by equal channel angular pressing does not tend toward cold-brittleness.

In summary, the ECAP method makes it possible to obtain bulk nanostructural titanium, which can be regarded as a

TABLE I. Yield stress σ_y of titanium versus temperature, grain size, and orientation of the compression axis.

Structural state of the sample	Orientation of the compression axis relative to the ECAP axis	σ_y, GPa		
		300 K	77 K	4.2 K
1	∥	0.44	0.78 (0.98)	0.97 (1.22)
	⊥	0.50	0.90 (1.10)	1.03 (1.28)
2	∥	0.65	0.87 (0.85)	1.24 (1.22)
	⊥	0.87	1.33 (1.39)	1.47 (1.54)
3	∥	1.00	1.32 (1.52)	1.67 (1.92)
	⊥	1.14	1.55 (1.75)	1.79 (2.04)

Note: For temperatures 77 and 4.2 K the values of $\sigma_y^0 = \sigma_y - \sigma_{ii}^{th}$ are presented in parentheses. Here σ_{ii}^{th} are the characteristic values of the microstructural thermoelastic stresses due to thermal expansion anisotropy of titanium grains (see Sec. 3.3.3).

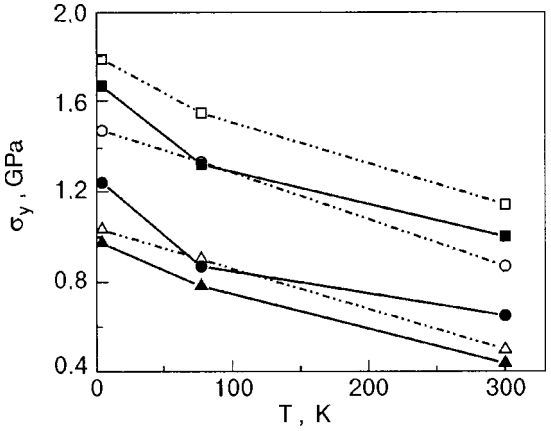

FIG. 3. Temperature dependences of the yield stresses of titanium in different structural states: 1 (∥) (▲); 1 (⊥) (△); 2 (⊥) (●); 2 (⊥) (○); 3 (∥) (■); 3 (⊥) (□).

potential structural material for applications in cryogenic technology.

3.2. Conventional yield stress in NS titanium at 300–4.2 K

The conventioanl yield stress σ_y was found by the method of intersection of tangents to the computer deformation diagram $P(t)$ on its initial and stationary sections. The conventioanl yield stresses at 300, 77, and 4.2 K for the three experimental structural states (with different average grain size d) under uniaxial compression parallel and perpendicular to the axis of the rods are presented in Table I.

The yield stress in the initial CG titanium is in good agreement with published data,[16] and the yield stresses in NS titanium are substantially higher than for the initial state 1. Substantial anisotropy of the yield stress is also observed: σ_y is substantially higher for the perpendicular orientation than for the parallel orientation of the compression axis relative to the ECAP axis. In the entire low-temperature range σ_y in the structural state 3 is approximately 1.7–2 times higher than in the initial state 1.

We note that σ_y in the state 3 is comparable to the yield stress in strongly alloyed VT-6 CG alloy ($\sim$0.9 GPa at 300 K, 1.4 GPa at 77 K, and 1.6 GPa at 4.2 K[16]). This observation makes it possible to draw another conclusion which is of interest for the technology of producing titanium materials with a high yield stress: the effectiveness of ECAP technology is in certain respects comparable to that of alloying.

To illustrate more clearly the differences in the yield points of NS and CG titanium the curves $\sigma_y(T)$ constructed on the basis of the data in Table I are presented in Fig. 3.

According to Fig. 3, the character of the temperature dependence $\sigma_y(T)$ remains the same as the grain size varies: for samples of all types the yield stress increases monotonically with decreasing temperature. This dependence shows that the elementary acts of plastic shear in NS titanium are thermally activated. The same mechanism is also characteristic for CG titanium[17] and single-crystal titanium.[18]

At the same time the temperature dependences of the yield stresses of NS and CG titanium have definite differences. In the first place, at a fixed deformation temperature σ_y systematic increases with decreasing d and when the orientation is switched from parallel to perpendicular. Another noticeable feature is the large increase (several-fold) in the derivative $\partial\sigma_y/\partial T$ in the temperature range 77–4.2 K when the structural state changes from CG to NS.

It is natural to attribute these differences to a difference in the micromechanisms of plastic deformation of CG and NS titanium. In CG titanium grains mechanical twinning intensifies as temperature decreases;[5,6] in NS titanium obtained by ECAP this is difficult to achieve because of the small grain size.[3] This behavior is similar to the previously observed cessation of twinning in polycrystalline titanium in the process of developed plastic deformation (for deformations exceeding 0.4)[19] and to the development of slipping along twinning boundaries.[20] This slipping is a manifestation of integrain deformation due to the motion of grain-boundary dislocations[21,22] in the twinning direction. The appearance of microscopic twins (which do not develop with increasing deformation of the material) also cannot be ruled out in nanostructural titanium, but final judgment requires electron-microscopic observations of the deformed material. Therefore the quantitative differences in the absolute values of $\sigma_y(T)$ and the derivative $\partial\sigma_y/\partial T$ in the temperature range 77–4.2 K are probably due to a difference in the activation energies and activation volumes for intragrain and intergrain (grain boundary) slipping in CG and NS titanium and probably for thermally activated processes of nucleation of twinning dislocations.

We also note that the comparatively large value of the derivative $\partial\sigma_y/\partial T$ for NS titanium below 77 K strongly influences the appearance of unstable plastic shear, which determines the low-temperature fracture of this material (see Sec. 3.6).

TABLE II. Anisotropy coefficient ψ for the yield stress of titanium polycrystals and ψ^0 of titanium for a hypothetical state of the material with no internal thermal-anisotropy stresses (see Sec. 3.3.3).

State	ψ			ψ^0	
	300 K	77 K	4.2 K	77 K	4.2 K
1	0.14	0.15	0.06	0.12	0.05
2	0.34	0.53	0.18	0.63	0.27
3	0.14	0.17	0.07	0.15	0.06

3.3. Anisotropy of the yield stress in NS titanium

3.3.1. Quantitative characteristics and temperature dependence of the anisotropy effect

The measurements presented in Figs. 2 and 3 and in Table I indicate the presence of more or less substantial anisotropy of plasticity and the yield stress in CG and NS titanium. This anisotropy is manifested as a dependence of the mechanical characteristics of the experimental samples on the orientation of the compression axis with respect to the axis of the rods from which the samples were cut (the latter was the same as the ECAP direction and the rolling direction in the process of preparing the rods). At 4.2 K the yield stress, the hardening coefficient, and the parameters of jumplike deformation are anisotropic. The anisotropy coefficient ψ for the yield point

$$\psi = \frac{\sigma_{y\perp} - \sigma_{y\parallel}}{\sigma_{y\parallel}} \tag{2}$$

can serve as a quantitative measure of this anisotropy. The values of ψ for all types of experimental samples and deformation temperatures are presented in Table II.

To illustrate the anisotropy effect more clearly we present plots of the temperature dependences of ψ for each structural state. These dependences were constructed using the data in Table II (Fig. 4).

It is interesting that for the initial state 1, which was obtained without ECAP, the anisotropy is small and the anisotropy coefficient ψ_1 varies little with temperature and is only 6% at 4.2 K. The yield stress anisotropy is much larger for structural state 2, for which the grains are characteristically elongated along the ECAP axis.[23] The temperature dependence of ψ_2 is nonmonotonic: at 77 K ψ_2 reaches 53%, substantially exceeding the anisotropy at 300 and 4.2 K. For the structural state 3, which was obtained from the state 2 by rolling and short-time annealing, the ECAP-induced anisotropy is virtually eliminated as a result of the fragmentation of the elongated grains by rolling. Consequently, the anisotropy coefficient ψ_3 is comparatively small and close in magnitude to ψ_1 for all experimental temperatures.

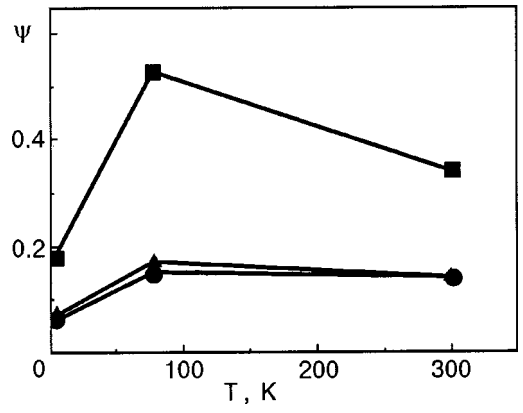

FIG. 4. Temperature dependences of the anisotropy coefficient ψ for different structural states of Ti: 1 (●), 2 (■), 3 (▲).

The anisotropy effects reflected in Tables 1 and 2 and in Figs. 2–4 can occur for diverse physical reasons:

a) shape anisotropy of grains elongated along the ECAP axis;[23]

b) crystallographic texture in the grain volume after ECAP[24] and associated anisotropy of intragrain plastic shears, due to the high plastic anisotropy of the crystal lattice of titanium;[25]

c) complicated system of internal stresses due to ECAP and the large anisotropy of the thermal expansion coefficient of grains at low temperatures;[15]

d) polarity of mechanical twinning, which can contribute to deformation and accommodation of internal stresses; and,

e) polarity of the motion of grain boundary dislocations.[22]

3.3.2. Internal stresses arising in grains on cooling as a result of the thermal expansion anisotropy of titanium

Analysis of the nonmonotonic temperature dependence, described in Sec. 3.3.1, of the anisotropy coefficient $\psi_2(T)$ of NS titanium in the structural state 2 shows that the combined effect of two factors could be an important reason for the anisotropy:

crystallographic texture, which is greatest in the state 2;

appearance of internal microstresses, which are due to the thermal expansion anisotropy of titanium at low temperatures, in grains during cooling below 300 K.[15]

Such stresses were called thermal anisotropy stresses. Ordinarily, they arise in polycrystalline materials with noncubic symmetry because when temperature changes, the sizes of grains change differently in different crystallographic directions.[26] The method proposed by Likhachev in Ref. 27 can be used to estimate the magnitude and sign of these microstructural internal stresses.

The principal components of the tensor $\sigma_{ik}^{\text{th}}(T)$ of internal thermal-anisotropy stresses, which appear in individual grains of polycrystalline titanium when the titanium is cooled from room temperature 300 K to liquid-nitrogen temperature 77 K and liquid-helium temperature 4.2 K, are calculated in the Appendix using the most reliable data[15] on the thermal expansion coefficient of titanium single crystals at temperatures 300–4.2 K and the anisotropy of this coefficient. They are presented in Table III (see Appendix). The calculations were performed using Likhachev's method[27] for an hcp structure, which titanium possesses. The cooling is accompanied by the appearance of compressive stress $\sigma_{33}^{\text{th}}(T) < 0$ in grains along the crystallographic direction [0001] (six-fold axis) and tensile stresses, equal in magnitude, $\sigma_{11}^{\text{th}}(T) = \sigma_{22}^{\text{th}}(T) > 0$ in perpendicular directions $[\bar{1}, 2, \bar{1}, 0]$ and $[1, 0, \bar{1}, 0]$.

It is known that crystallographic texture appears in titanium rods subjected to ECAP (structural state 2). In this

TABLE III. Elastic constants c_{ik} of titanium, the integral $I(T)$, and the computed principal thermal anisotropy stresses σ_{11}^{th} and σ_{33}^{th} at 77 and 4.2 K.

T, K	c_{11}, GPa	c_{12}, GPa	c_{13}, GPa	c_{33}, GPa	$c_{11}^{(0)}-c_{12}^{(0)}$, GPa	I	σ_{33}^{th}, MPa	$\sigma_{11}^{\text{th}}=\sigma_{22}^{\text{th}}$, MPa
300	162.4	91.3	65.3	180.7	81	0	0	0
77	174.7	86.6	67.9	189.3	100.6	$3.3\cdot10^{-3}$	−200	52
4.2	176.1	86.9	68.3	190.5	102.6	$4.0\cdot10^{-3}$	−250	64

texture the six-fold axis in the grains is predominantly oriented perpendicular to the ECAP axis.[24] Consequently, our computed values of the internal thermal-anisotropy stresses must unavoidably enter into the experimentally measured values of $\sigma_{y\perp}$ and $\sigma_{y\parallel}$ for state 2 at any temperature:

$$\sigma_{y\parallel}=\sigma_{y\parallel}^{0}+\eta\sigma_{11}^{\text{th}},\quad \sigma_{y\perp}=\sigma_{y\perp}^{0}+\eta\sigma_{33}^{\text{th}}. \tag{3}$$

In these expressions $\sigma_{y\parallel}^{0}$ and $\sigma_{y\perp}^{0}$ are the yield stresses for parallel and perpendicular orientations of the sample in the absence of internal thermal-anisotropy stresses; the coefficient η takes account of the decrease in σ_{ik}^{th} as a result of the presence of texture. Following the recommendation made in Ref. 27, in analyzing our experimental data we shall set $\eta=1$ for weakly textured structural states 1 and 3 and $\eta=0.3$ for the textured structural state 2.

The quantities $\sigma_{y\parallel}^{0}$ and $\sigma_{y\perp}^{0}$ characterizing the yield stesses in titanium in the absence of internal thermal-anisotropy stresses were calculated from the relations (3) using the data in Tables 1 and 3 and are presented in Table I (in parentheses). Table II gives the corresponding values of the renormalized anisotropy coefficient ψ_0 for a hypothetical state of the material with no internal thermal-anisotropy stresses:

$$\psi^{0}=\frac{\sigma_{y\perp}^{0}-\sigma_{y\parallel}^{0}}{\sigma_{y\parallel}^{0}}. \tag{4}$$

Taking account of microstructural thermal anisotropy stresses did not eliminate the peak in ψ_2 at 77 K but rather increased the peak (see Table II). Thus the thermal-anisotropy stresses cannot be responsible for the nonmonotonic temperature of the anisotropy coefficient ψ_2 of titanium in the structural state 2, and the temperature dependence $\psi^{0}(T)$ has is qualitatively the same for all three structural states. The higher value of ψ for state 2 is also observed at 300 K, i.e. in the absence of cooling. This could be due to the following:

internal stresses induced by ECAP (the magnitude and sign of these stresses could be measured by x-ray diffraction);

microtwinning and grain-boundary shears in the twinning direction with compression of the ''parallel'' orientation samples in state 2 (perpendicular to the six-fold axis;[28] this also explains the small number of jumps, i.e. the difficulty of the appearance of grain-boundary shears in ''perpendicular'' orientation samples in state 2.

The weak anisotropy of the yield stress σ_y in the states 1 and 3 (see Table II and Fig. 4) could indicate the absence of appreciable texture. In this case it is natural to conjecture that of the randomly oriented grains it is primarily the grains with a favorable orientation (along the compression axis) of the compressive principal stresses σ_{33} that deform at the yield stress. Here $\sigma_y=\sigma_y^{0}+\sigma_{33}^{\text{th}}$ for all orientations of the compression aixs. In this case the thermal anisotropy stresses (see Table II) have virtually no effect on the anisotropy coefficient: $\psi\simeq\psi^{0}$.

In summary, the maximum anisotropy of the conventional yield stress in titanium at 77 K, observed for the structural state 2, is not associated with internal thermal-anisotropy stresses. It is probably due to microtwinning, which is possible in ''parallel'' orientation samples but is forbidden in ''perpendicular'' orientation samples.

3.4. Dependence of the yield stress in NS titanium on grain size

It is well-known that for polycrystals the Hall-Patch relation

$$\sigma_y=\sigma_0+k_y d^{1/2} \tag{5}$$

describes the dependence of the yield stress σ_y on the grain size d well in many cases. This relation holds for annealed CG polycrystals in a wide range of grain sizes but breaks down for d 100 nm.[29] In Refs. 29–31 it was noted that this could be due to the specific structure of the boundaries of such small grains and to internal stresses in materials obtained by ECAP.

For the structural states of titanium which were studied in the present work, the internal stresses arising as a result of ECAP, the possible appearance of microtwins in axially textured state 2 in ''parallel'' orientation samples, and the fact that their formation is forbidden in ''perpendicular'' orientation samples could complicate the form of the function $\sigma_y(d)$.

The plots $\sigma_y(d)$ constructed on the basis of the data in Table I in $\sigma_y-d^{1/2}$ coordinates are displayed in Fig. 5. It is evident that the relation (5) holds satisfactorily only at 300 and 4.2 K for ''perpendicular'' titanium samples (the curves $\sigma_y-d^{1/2}$ are rectilinear). In all other cases appreciable deviations are observed from the Hall-Patch relation. This is due to the values of σ_y for samples with the structural state 2 ($d=0.3$ μm).

Thus we observe a substantial deviation from the Hall-Patch law for ''parallel'' samples, where $\sigma_{y\parallel}$ is low in the structural state 2. This could be due to the possibility of twinning under compression of axially textured titanium perpendicular to the six-fold axis.[28] Twinning is impossible in ''perpendicular'' titanium samples (compression parallel to the six-fold axis in the state 2).[28]

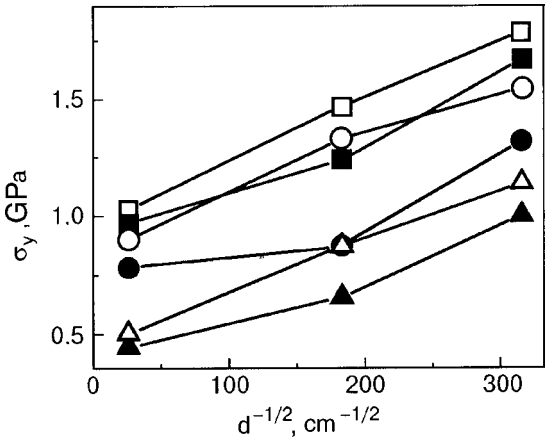

FIG. 5. Low-temperature yield stress σ_y of titanium versus the average grain size d under compression parallel ∥. and perpendicular ⊥ to the ECAP axis: 300 K (∥) (▲); 300 K (⊥) (△); 77 K (∥); 77 K (⊥) (○); 4.2 K (∥) (■); 4.2 K (⊥) (□).

The observed increase in $\sigma_{y\|}$ with decreasing grain size can be taken as indirect evidence of intragrain slipping making the predominant contribution to the deformation of nanostructural titanium at the yield stress.

3.5. Low-temperature shear fracture of NS titanium as a consequence of unstable plastic shear

We first reported on shear fracture by catastrophic slipping of one part of a sample relative to another under low-temperature quasistatic compression of nanostructural titanium samples in Refs. 2 and 32. This phenomenon was observed not only at 77 and 4.2 K: under compression of NS titanium samples in structural state 2 perpendicular to the ECAP axis catastrophic shear could also be observed at 300 K. At the same time unstable plastic shear can never be observed with quasistatic compression of coarse-grained titanium (structural state 1). Consequently, it is natural to treat the observed unstable plastic shear as a phenomenon inherent to NS titanium.

Unstable plastic shear was previously observed with low-temperature quasistatic compression of rods of bulk metallic glasses[33–35] and with tension on thin ribbons of metallic glasses.[36] Shear instability was explained by the specific nature of its propagation along intercluster boundaries as a characteristic component of the structure of metallic glasses. Stable propagation of shear over large distances can be disrupted by an unfavorably oriented triple joint of boundaries, where the presence of such a joint is due to the random orientation of polyclusters.[37] The high stress (of the order of $G/10$,[38] where G is the shear modulus) necessary to overcome such a triple joint determines the subsequent high-velocity propagation of macroscopic shear. This explains the distinct dynamical character of low-temperature plastic shear in metallic glasses: even under conditions of quasistatic deformation macroscopic shear propagates with near-solid velocity[36] and is accompanied by the emission of a strong acoustic pulse.

We have observed shear fracture of NS titanium under compression for compressive stresses ranging from 1.4 to 2.4 GPa. The shear fracture surfaces, along which slipping of one part of a sample relative to another occurred, were oriented at a angle of about 45° to the compression axis (Fig. 6a), similarly to what was observed under compression of rods of bulk metallic glasses (Fig. 6b).[34,35] A study of the morphology of fracture surfaces, using a scanning electron microscope, revealed a characteristic ''vein'' pattern on all surfaces of the shear fracture.

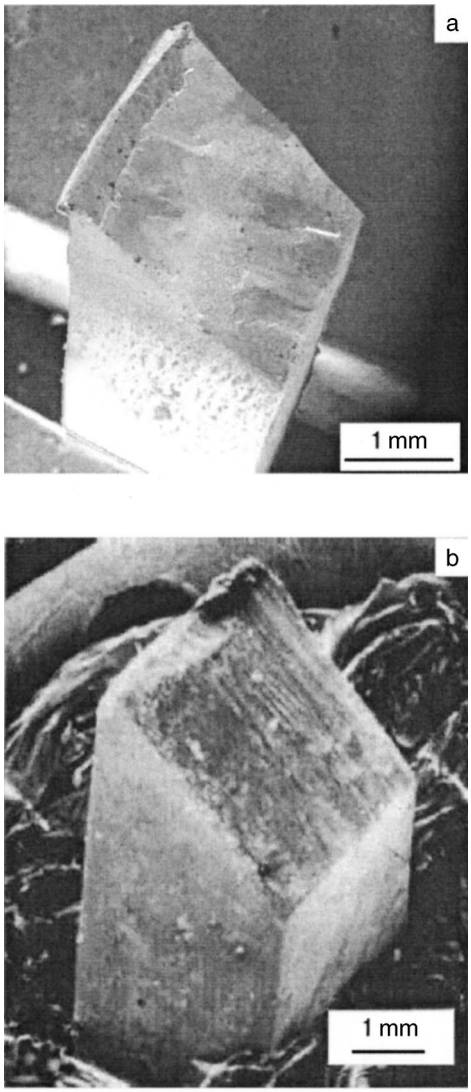

FIG. 6. Overall view of a sample after shear fracture under quasistatic uniaxial compression: NS titanium in state 3, deformation perpendicular to the ECAP axis at 4.2 K (a); bulk metallic glass $Zr_{41.2}Ti_{13.8}Ni_{10}Cu_{12.5}Be_{22.5}$,[34,35] deformation at 300 K (b).

In metallic glasses the ''vein'' pattern is a consequence of the meniscus instability accompanying rupture of material locally heated up to the quasiliquid[39] (superplastic[40]) state in the catastrophic shear band preceding fracture. Local adiabatic heating up to premelting temperatures in this band is due to the specific nature of the process in which the work of plastic shear is dissipated: local heat release is large as a result of the near-sonic shear velocity, the high fracture stress, and the low thermal conductivity of the material.[33–36] Similar physical conditions in the shear band are also realized in NS titanium: high fracture stress, near-sonic velocity of plastic shear, and low thermal conductivity of the material. Consequently, the observed ''vein'' pattern on the surface of

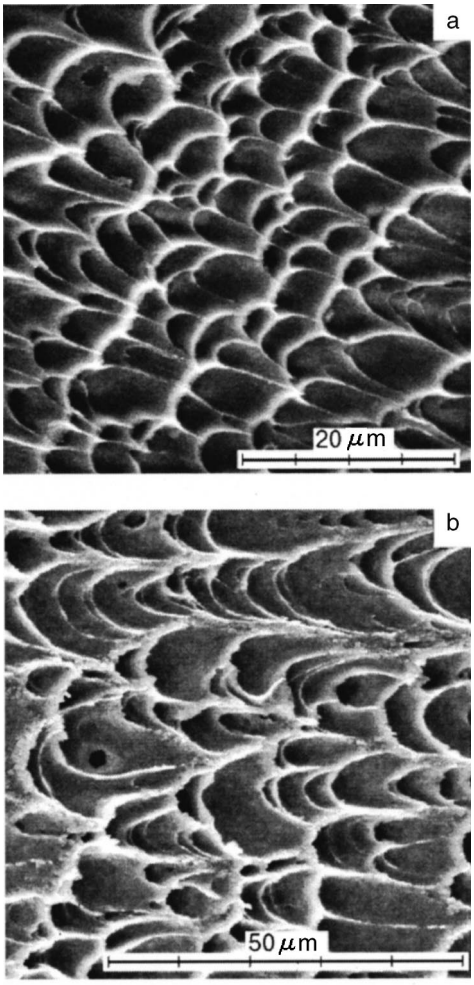

FIG. 7. Morphology of the ''vein'' pattern on shear fracture surfaces of NS titanium in state 3 at 4.2 K: smooth ''veins'' (a); ''veins'' with roughness due to separation on grain boundaries (b).

shear fracture of NS titanium can be regarded as indirect evidence of strong local heating.

The observed ''vein'' pattern on the fracture surfaces of NS titanium samples possesses characteristic features. It is useful to discuss this in greater detail. First, it should be noted that the observed ''vein'' pattern is nonuniform: in individual regions of the fracture surface the ''veins'' are smooth and they are similar to those observed on the fracture surface of metallic glasses (Fig. 7a); in other regions the veins have a rough surface (Fig. 7b).

The spatial distribution of ''veins'' is different in samples oriented parallel and perpendicular to the ECAP axis. In Ref. 2 it was demonstrated that in the structural state 3 the distribution of the ''veins'' after shear fracture at 77 K is more uniform in samples oriented parallel rather than perpendicular to the ECAP axis. This result could be a consequence of more uniform adiabatic heating and more uniform propagation of catastrophic shear in the first case ($\parallel$) as compared with the second case ($\perp$). A similar pattern is also observed at 300 K, but in this case the spatial nonuniformities have several different scales: from 0.3–0.1 mm (see Figs. 8a and 8b) up to 0.01–0.005 mm (Fig. 8c). The observed nonuniformities could be a consequence of the nonuniform distribution of internal microstructural stresses and,

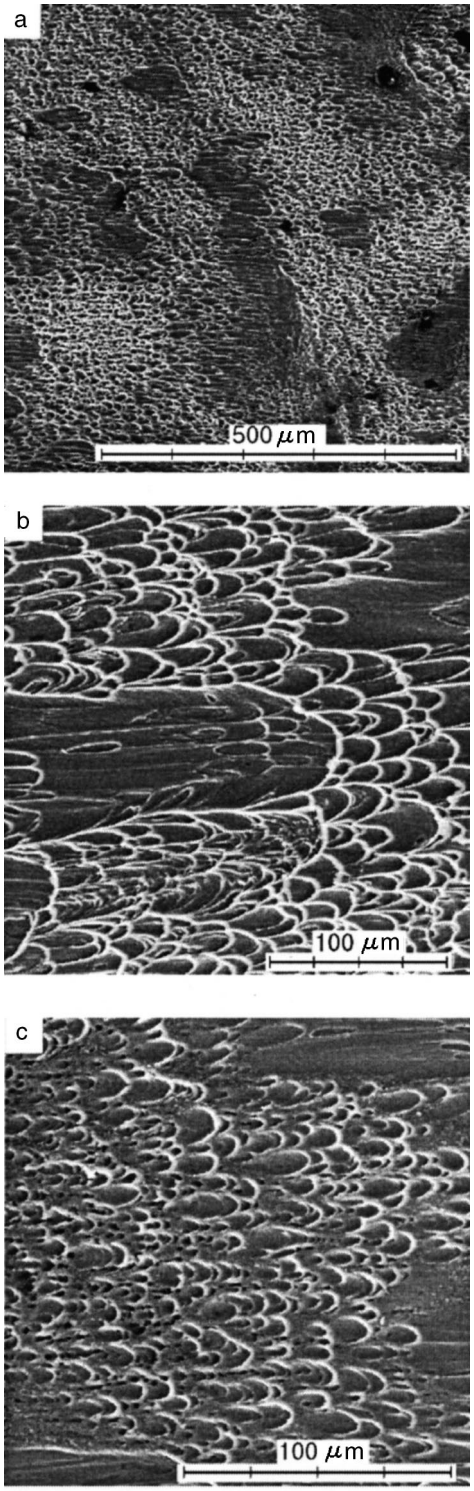

FIG. 8. Difference scale of nonuniformities of the ''vein'' pattern which are observed on a shear fracture surface of NS titanium in state 3 under compression perpendicular to the ECAP axis at 4.2 K: 0.3–0.1 mm (a, b); 0.01–0.005 mm (c).

owing to this nonuniformity, the variance of the local shear velocities and magnitude of local heating.

In contrast to bulk metallic glasses, the surface of shear fracture in NS titanium shows no evidence of local melting, specifically, there are no solidified drops of melt. This is because the melting temperature of titanium (1668 °C) is much higher than the melting temperature of metallic

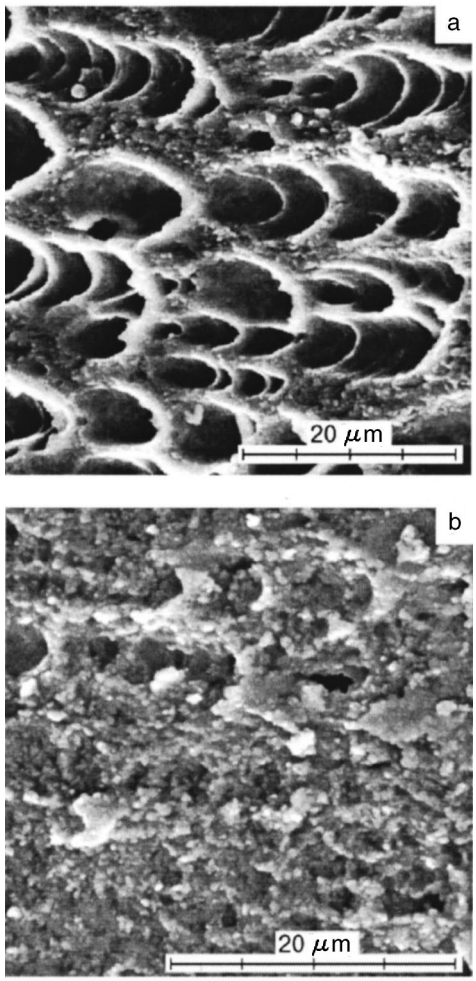

FIG. 9. Roughness of the ''vein'' pattern of NS titanium due to individual grains (a). Individual grains on the shear fracture surface of NS titanium manifested (tentatively) as a result of shear fracture under local heating in the temperature range of the α-β phase transition (b).

glasses. Consequently, melting does not occur on a shear-fracture surface in NS titanium.

For large magnifications individual grains can be observed near a surface shear fracture where veins have a rough surface (Fig. 7b): such separation of NS titanium into individual grains is shown in Figs. 9a and 9b. This effect could be due to high-temperature grain-boundary slipping (which develops at 800–940 °C[41] and results in micrograin superplasticity of titanium) or it could be a consequence of local heating up to the temperature of an α-β phase transition (882.5 °C), when a decrease in the specific volume of titanium[25] and localized shear in this temperature range accompany a transition from an hcp to an fcc lattice. Loosening of the material should accompany plastic deformation at the temperature of this polymorphic transformation. This phenomenon explains the separation of grains along their boundaries in the catastrophic shear band. However, this hypothesis requires additional checking in the future.

A qualitative theoretical analysis of the propagation of unstable plastic shear in NS titanium[32] suggests that for large plastic deformations unstable macroscopic propagation of localized grain boundary shear is possible by means of high-velocity motion of grain-boundary dislocations. This process should result in viscous shear fracture in NS titanium. A subsequent analysis of the dynamical behavior of dislocation ensembles in NS titanium should make it possible to attribute the observed instability of plastic shear to the characteristic features of grain-boundary slipping.

Unstable plastic shear, resulting in shear fracture, is observed under quasistatic uniaxial compression of NS titanium only and has not been observed under compression of CG titanium. A phenomenological criterion for the appearance of catastrophic adiabatic heating under deformation[7] and the difference, detected in our experiments, of the values of the derivatives $\partial\sigma_y/\partial T$ for CG and NS titanium at low temperatures (see Sec. 3.2) give a qualitative explanation of this difference. According to Ref. 7, under tension catastrophic shear arises as a result of increasing local heating if

$$\varepsilon > \varepsilon_c = -\left.\frac{C\theta}{\partial\sigma_y/\partial T}\right|_{\varepsilon\dot{\varepsilon}}, \tag{6}$$

where C is the specific heat per unit volume and $\theta = \partial\sigma/\partial\varepsilon|_{\varepsilon\dot{\varepsilon}}$ is the coefficient of hardening in Eq. (1). Applying the phenomenological criterion (6) to the compression case it follows that the tendency toward unstable plastic shear is higher in NS than in CG titanium as a result of the increase in the absolute value of $\partial\sigma_y/\partial T|_{\varepsilon\dot{\varepsilon}}$.

4. CONCLUSIONS

In the present work the low-temperature plasticity and fracture of an ultrafine-grained structural modification of polycrystalline titanium—so-called nanostructural titanium prepared by the equal channel angular pressing method—was studied systematically. The initial material for obtaining NS titanium was a coarse-grained polycrystal. The problems of this investigation were to compare the high-temperature values of the mechanical parameters of the CG and NS modifications of titanium and to establish the unity and differences of the micromechanisms of deformation and fracture of these structural states at low temperatures. The measurements were performed by the quasistatic uniaxial compression method at temperatures 300, 77, and 4.2 K. The following basic conclusions can be drawn from the results obtained and their analysis:

the smaller (than in CG titanium) grains in NS titanium substantially increases the yield stress (by a factor of 1.5–2) and decreases the ultimate plasticity in the entire experimental temperature range (300–4.2 K);

the strain hardening curve of NS titanium at low temperatures has a single linear stage and differs substantially from the parabolic or multistage hardening curve of the CG titanium;

the observed features of plastic flow in NS titanium at low temperatures correspond to the source model of deformation and hardening, according to which primary microscopic slip bands appear in the volume of the materials statistically independently and give a one-time (''discrete'') contribution to deformation;

NS titanium samples obtained by ECAP possess a definite texture, which is manifested in the dependence of the yield stress on the orientation of the compression axis with respect to the ECAP axis;

the curves of the yield stress of NS titanium versus the grain size show that intragrain slip makes the main contribu-

tion to deformation at the yield stress and the observed features are due to the possibility of microtwinning under certain conditions;

plastic deformation of NS titanium at low temperatures is thermally activated, which is also observed for CG titanium but the quantitative differences of the yield stresses and the temperature dependences of the deforming stress show that the intragrain and intergrain slipping and also twinning make different contributions to the deformation of the structural modifications of titanium;

at low temperatures the fracture of NS titanium under uniaxial compression is due to propagation of unstable plastic shear, which is accompanied by local adiabatic heating of the material;

examination of the morphology of the surface of shear fracture of NS titanium under an electron microscope shows a specific ''vein'' pattern, analysis of which yields an estimate for the temperature of local heating of the order of or greater than 800 °C;

cold-brittleness for NS titanium was not observed down to liquid-helium temperatures, and the ratio of the yield stress and the ultimate plasticity shows that NS titanium is a promising structural material for cryogenic technology.

In conclusion, we note that in the present work we were able to measure the low-temperature mechanical characteristics of NS titanium at only three temperatures. This made it impossible to perform a detailed thermal-activation analysis of plasticity and to establish unequivocally the microscopic mechanisms determining the plastic flow of this material: type of dislocations, mechanism of dislocation nucleation, nature and parameters of the barriers which stop slipping, and so on. This will be done in the future. The experiments should include detailed measurements of the temperature dependences of the yield stress, the rate sensitivity of the deforming stress, and thermal-activation analysis of these dependences using the scheme previously implemented for CG titanium.[17] Examination of deformed NS titanium under an electron microscope is also proposed to determine the possible appearance of microtwins.

We thank V. Otselik, V. N. Kovaleva, V. A. Moskalenko, and S. N. Smirnov for collaborating on this work and for fruitful discussions of the results obtained and O. I. Yuzefovich and S. V. Bengus for assisting in the preparation of the computer versions of the figures.

This work was partially supported as part of the projects INTAS-99-01741, INTAS-2001-nano-320, and VEGA 2101.

5. APPENDIX

5.1. Microstructural internal stresses due to the thermal expansion anisotropy of grains

In polycrystals of materials with noncubic symmetry, as temperature changes, microstructural thermoelastic stresses appear due to the thermal expansion anisotropy of individual grains.[26] Likhachev was the first to perform a detailed quantitative analysis of this effect.[27] He called such stresses internal stresses due to thermal anisotropy. To estimate the components σ_{ik}^{th} of the tensor of the thermal anisotropy stresses Likhachev examined the problem of thermoelastic stresses in an anisotropic grain embedded in an effective isotropic medium which simulates the polycrystalline matrix surrounding a grain.[27] In Ref. 27 the question of the stresses σ_{ik}^{th} arising when polycrystals are heated above room temperature was studied, but Likhachev's results can also be used, with slight modifications, to estimate the microstructural stresses σ_{ik}^{th} arising when titanium polycrystals are cooled from room temperature to liquid-nitrogen and liquid-helium temperatures.

A rectangular (orthohexagonal[42]) coordinate system with x_1 and x_2 axes oriented in the directions $[\bar{1},2,\bar{1},0]$ and $[1,0,\bar{1}\bar{0}]$ and the x_3 axis oriented along the crystallographic direction $[0,0,0,1]$ (six-fold axis) was used to calculate the components of the thermal-anisotropy stress tensor for crystals in the hexagonal system. In these coordinates the increments to the diagonal components σ_{ii}^{th}, due to small increments to the temperature ΔT, have the form

$$\Delta\sigma_{11}^{\text{th}}=\Delta\sigma_{22}^{\text{th}}=\frac{(c_{11}+c_{12}-2c_{13})(\alpha_3-\alpha_1)}{3\left[1+\frac{1}{2}(c_{11}+c_{12}+c_{13})/(c_{11}^{(0)}-c_{12}^{(0)})\right]}\Delta T, \quad \text{(A1)}$$

$$\Delta\sigma_{33}^{\text{th}}=\frac{4(c_{13}-c_{33})(\alpha_3-\alpha_1)}{3\left[1+\frac{1}{2}(c_{11}+c_{12}+c_{13})/(c_{11}^{(0)}-c_{12}^{(0)})\right]}\Delta T. \quad \text{(A2)}$$

Here c_{11}, c_{12}, c_{13}, and c_{33} are elastic constants of an hcp single crystal; $c_{11}^{(0)}$ and $c_{12}^{(0)}$ are the average elastic constants of the polycrystalline medium surrounding a grain; and, α_3 and α_1 are the thermal expansion coefficients parallel and perpendicular to the six-fold axis.

At temperatures above room temperature, α_3 and α_1, as a rule, vary little[43] and the difference $\alpha_3-\alpha_1$ can be assumed to be constant, but below 300 K α_3 and α_1 are strongly temperature-dependent. Consequently, when the expressions (A1) and (A2) are used to calculate $\sigma_{ii}^{\text{th}}(T)$ for the case of cooling from 300 K to some temperature T the increment $(\alpha_3-\alpha_1)\Delta T$ must be replaced by the integral

$$I(T)=\int_{300}^{T}[\alpha_3(\xi)-\alpha_1(\xi)]d\xi. \quad \text{(A3)}$$

We calculated the integral $I(T)$ numerically using data on the temperature dependence $\alpha(T)$ from Ref. 15. The value of the integral changes most in the temperature range 300–400 K and then changes little with further cooling. The values of I for 77 and 4.2 K are presented in Table III, which also shows the values of the elastic constants of titanium (found by extrapolating the data in Ref. 44 from 73 and 4 K) and $c_{11}^{(0)}-c_{12}^{(0)25}$ for the effective isotropic medium. The values of $c_{11}^{(0)}-c_{12}^{(0)25}$ were obtained by extrapolating from 300 K using the temperature dependence of the quantity $c_{11}-c_{12}$.[44]

The principal thermal anisotropic stresses $\sigma_{11}^{\text{th}}=\sigma_{22}^{\text{th}}$ and σ_{33}^{th} calculated at 77 and 4.2 K using the scheme described above are presented in the last two columns in Table III. Evidently, $\sigma_{33}<0$ whereas σ_{11} and $\sigma_{12}>0$, i.e. on cooling from room temperature each titanium grain is subjected to compressive stresses along the six-fold axis and tensile stresses in a perpendicular direction. It should be noted that the stresses σ_{11}^{th} and σ_{33}^{th} in Table III were calculated assum-

ing that there is no crystallographic texture in the polycrystal. If texture is present, these values are 2–3 times smaller.[27]

*E-Mail: bengus@ilt.kharkov.ua

[1] *Investigations and Applications of Severe Plastic Deformation*, edited by T. C. Lowe and R. Z. Valiev, NATO Science Ser. 3. High Technology **80**, Kluwer Academic Publishers, Dordrecht (2000), p. 394.
[2] E. D. Tabachnikova, V. Z. Bengus, V. V. Stolyarov, G. I. Raab, R. Z. Valiev, K. Csach, and J. Miskuf, Mater. Sci. Eng., A **309-310**, 524 (2001).
[3] D. Jia, Y. M Wang, K. T. Ramesh, E. Ma, Y. T. Zhu, and R. Z. Valiev, Appl. Phys. Lett. **79**, 611 (2001).
[4] E. W. Collings, *The Physical Metallurgy of Titanium Alloys*, American Society for Metals, Metals Park (1984), p. 223.
[5] R. A. Ul'yanov and V. A. Moskalenko, *Metallovedenie Termicheskaya Obrabotka Metallov*, No. 10, 48 (1966).
[6] S. Nemat-Nasser, W. G. Guo, and J. Y. Cheng, Acta Mater. **47**, 3705 (1999).
[7] M. R. Staker, Acta Metall. **29**, 683 (1981).
[8] Yu. R. Kolobov, R. Z. Valiev, G. P. Grabovetskaya, A. P. Zhilyaev, E. F. Dudarev, K. V. Ivanov, M. B. Ivanov, O. A. Kashin, and E. V. Naĭdenkin, *Grain-Boundary Diffusion and the Properties of Nanostructural Materials*, Nauka, Novosibirsk (2001).
[9] D. Jia, K. T. Ramesh, and E. Ma, Scr. Mater. **42**, 73 (2000).
[10] V. A. Moskalenko, V. I. Startsev, and V. N. Kovaleva, Cryogenics **20**, 503 (1980).
[11] V. N. Kovaleva, V. A. Moskalenko, and V. I. Startsev, Fiz. Met. Metalloved. **52**, 391 (1981).
[12] V. I. Eremin, V. N. Kovaleva, and V. A. Moskalenko, in *Cryogenic Materials and Their Welding*, edited by K. A. Yushenko and D. A. Vigli, Naukova dumka, Kiev (1986), p. 74.
[13] V. Z. Bengus, J. Phys. IV **11**, Pr5-237 (2001).
[14] A. Vinogradov, Scr. Mater. **39**, 797 (1998).
[15] V. I. Nizhankovskiĭ, M. I. Katsnel'son, G. V. Peschanskikh, and A. V. Trefilov, JETP Lett. **59**, 733 (1994).
[16] V. N. Kovaleva and V. A. Moskalenko, Cryogenics **29**, 1002 (1989).
[17] V. N. Kovaleva, V. A. Moskalenko, and V. D. Natsik, Philos. Mag. A **70**, 423 (1994).
[18] E. D. Levine, *Transactions of the Metallurgical Society AIME* **234**, 1558 (1966).
[19] M. Blicharski, S. Nonrbakhs, and J. Nutting, Metal Sci. **13**, 516 (1979).
[20] V. V. Rybin, *Large Plastic Deformations and Fracture of Metals*, Metallurgiya, Moscow (1986).
[21] J. Schiotz, T. Vegge, F. D. Di Tolla, and K. W. Jacobsen, Phys. Rev. B **60**, 11971 (1999).
[22] A. N. Orlov, V. N. Perevezentsev, and V. V. Rybin, *Grain Boundaries in Metals*, Metallurgiya, Moscow (1980).
[23] I. Kim, W.-S. Jeong, J. Kim, K.-T. Park, and D. H. Shin, Scripta Mater. **45**, 575 (2001).
[24] A. R. Kil'mametov, V. V. Smolyarov, L. O. Shestakova, and I. V. Aleksandrov, in *Structure and Properties of Nanocrystalline Materials*, edited by P. G. Taluts and N. I. Noskov, Uro RAN, Ekaterinburg (1999), p. 185.
[25] U. Zwicker, *Titan und Titanlegierungen*, Springer-Verlag, New York (1974).
[26] W. Boas and R. W. K. Honeycombe, Proc. R. Soc. London **188**, 427 (1947).
[27] V. A. Likhachev, Fiz. Tverd. Tela **3**, 1827 (1961) [Sov. Phys. Solid State **3**, 1330 (1961)].
[28] M. V. Klassen-Neklyudova, *Mechanical Twinning of Crystals*, Izd. AN SSSR, Moscow (1960).
[29] M. Furukawa, Z. Horita, M. Nemoto, and T. G. Landon, in *Ultra Fine-Grained Materials Prepared by Severe Plastic Deformation*, edited by R. Z. Valiev, Ann. Chim. **21**, 493 (1996).
[30] R. Z. Valiev, in *Investigations and Applications of Severe Plastic Deformations*, edited by T. C. Love and R. Z. Valiev, NATO Science Ser. 3. High Technology **80**, Kluwer Academic Publishers, Dordrecht (2000), p. 221.
[31] G. T. Gray III, T. C. Lowe, C. M. Cady, R. Z. Valiev, and I. V. Alexandrov, Nanostruct. Mater. **9**, 477 (1997).
[32] V. Z. Bengus, E. D. Tabachnikova, K. Csach, J. Miskuf, V. V. Stolyarov, R. Z. Valiev, V. Ocelik, and J. Th. M. De Hosson, in *Science of Metastable and Nanocrystalline Alloys. Structure, Properties, and Modelling*, edited by A. R. Dinesen and M. Eldrup, Riso National Laboratory, Roskilde, Denmark (2001), p. 217.
[33] E. D. Tabachnikova, V. Z. Bengus, V. V. Molokanov, and T. N. Mikhaĭlova, Fiz. Tver. Tela (St. Petersburg) **36**, 2335 (1994) [Phys. Solid State **36**, 1280 (1994)].
[34] E. Tabachnikova, V. Bengus, J. Miskuf, K. Csach, V. Ocelik, W. Johnson, and V. Molokanov, *Material Science Forum* 343-346, Proc. ISMA-NAM-99, Trans. Tech. Publications, Switzerland (2000), p. 197.
[35] V. Z. Bengus, E. D. Tabachnikova, J. Miskuf, K. Csach, V. Ocelik, W. L. Johnson, and V. V. Molokanov, J. Mater. Sci. **35**, 4449 (2000).
[36] V. Z. Bengus, E. D. Tabachnikova, S. E. Shumilin, Y. I. Golovin, M. V. Makarov, J. Miskuf, K. Csach, and V. Ocelik, Int. J. Rapid Solidif. **8**, 21 (1993).
[37] A. S. Bakai, *Topics in Applied Physics* **72**, *Glassy Metals III*, edited by H. Beck and H.-J. Gunterodt, Springer, Berlin (1994), p. 209.
[38] A. S. Bakaĭ, *Polycrystalline Amorphous Bodies*, Énergoatomizdat, Moscow (1987).
[39] A. Argon, Glass Science and Technology **5**, 79 (1980).
[40] V. Bengus, E. Tabachnikova, K. Csach, J. Miskuf, and V. Ocelik, Scripta Metallugica et Materialia **35**, 781 (1996).
[41] B. A. Kolachev, V. A. Livanov, and A. A. Bukhanova, *Mechanical Properties of Titanium and Its Alloys*, Metallurgiya, Moscow (1974).
[42] Ch. S. Barrett, *The Structure of Metals*, Metallurgizdat, Moscow (1948).
[43] S. I. Novikova, *Thermal Expansion of Solids*, Nauka, Moscow (1974).
[44] E. S. Fisher and C. J. Renken, Phys. Rev. A **135**, 482 (1964)

Translated by M. E. Alferieff

SHORT NOTES

Magnetoelastic waves in multisublattice systems

I. R. Kyzyrgulov* and M. Kh. Kharrasov

Bashkir State University, ul. Frunze, 32, Ufa, 450074, Russia
(Submitted March 25, 2002; resubmitted May 27, 2002)
Fiz. Nizk. Temp. **28**, 1227–1229 (November 2002)

Coupled magnetoelastic waves in antiferromagnetic crystals with a 2^n sublattice magnetic subsystem ($n=0,1,2,\ldots$) are studied. An explicit relation is found between the interaction parameters of the subsystems and the phenomenological constants. A dispersion equation for the characteristic frequencies of the coupled magnetoelastic waves is obtained. © *2002 American Institute of Physics.* [DOI: 10.1063/1.1528581]

Virtually all magnetically ordered crystals contain several atoms per unit cell, i.e. they are multisublattice crystals. Examples are rare–earth orthoferrites with eight magnetic sublattices, rare–earth iron garnets with 32 sublattices, the popular antiferromagnet $CuCl_2\cdot 2H_2O$ with four sublattices, and many others.[1,2] The microscopic theory of a magnet containing more than two magnetic atoms per unit cell is technically extremely complex. It is even very difficult to determine the elementary excitation spectrum of such a magnet, to say nothing of analyzing the nonlinear processes. This situation make it urgent to develop methods for finding the spin–wave spectrum for multisublattice systems.

There exists a developed theory of the spin–phonon interaction in magnetically ordered crystals.[3–5] However, the maximum number of spin lattices studied did not exceed four.[6–8] In the present paper we study coupled magnetoelastic waves in antiferromagnetic crystals with a 2^n-sublattice magnetic subsystem ($n=0,1,2,\ldots$).

We start with a Hamiltonian that takes account of the energy of the magnetic and elastic parts of the multisublattice system and their interaction energy:

$$\mathcal{H}=\mathcal{H}_M+\mathcal{H}_U+\mathcal{H}_{MU}, \tag{1}$$

$$\mathcal{H}_M=\frac{1}{2}\int d\mathbf{x}\left[\chi_{jm}^{\alpha\beta}M_j^{\alpha}M_m^{\beta}+\alpha_{ijmn}^{\alpha\beta}\frac{\partial M_i^a}{\partial x_j}\frac{\partial M_m^{\beta}}{\partial x_n}-2\sum_{\alpha}(\mathbf{H}_0,\mathbf{M}^{\alpha})\right], \tag{2}$$

$$\mathcal{H}_U=\frac{1}{2}\int d\mathbf{x}(\rho\dot{u}^2+\Lambda_{ijmn}u_{ij}u_{mn}), \tag{3}$$

$$\mathcal{H}_{MU}=\int d\mathbf{x}\lambda_{ijmn}^{\alpha\beta}M_i^{\alpha}M_j^{\beta}u_{mn}, \tag{4}$$

where $\chi_{jm}^{\alpha\beta}=I_{jm}^{\alpha\beta}+\beta_{jm}^{\alpha\beta}$; $I_{jm}^{\alpha\beta}$ is the uniform exchange interaction tensor; $\beta_{jm}^{\alpha\beta}$ is the anisotropy tensor; $\alpha_{ijmn}^{\alpha\beta}$ is the nonuniform exchange interaction tensor; Λ_{ijmn} is the elastic constants tensor; $\lambda_{ijmn}^{\alpha\beta}$ is the magnetostriction tensor; u_{mn} is the deformation tensor; $\mathbf{M}^{\alpha}$ is the magnetization of the sublattices; $\alpha,\beta=1,\ldots,2^n$; $i,j,m,n=x,y,z$.

We shall write the Hamiltonian (1) in an approximate second-quantization representation.[9] The magnetizations $\mathbf{M}^{\alpha}$ of the sublattices can be expressed in terms of the Holstein–Primakoff operators.[10] Then the energy of the magnetic subsystem will have the form

$$\mathcal{H}_M=\sum_{k\gamma}\varepsilon_{k\gamma}^{M}c_{k\gamma}^{+}c_{k\gamma}, \tag{5}$$

where $\varepsilon_{k\gamma}^{M}=[C_{\gamma}^2-D_{\gamma}^2]^{1/2}$ is the spin–wave energy;

$$C_{\gamma}=\sum_{\beta=1}^{2^n}a[\gamma,\beta]A_k^{1\beta},\quad D_{\gamma}=\sum_{\beta=1}^{2^n}a[\gamma,\beta]B_k^{1\beta}, \tag{6}$$

$$A_k^{\alpha\beta}=\mu M_0\left[(x_{jm}^{\alpha\beta}e_{\perp j}^{\alpha *}+\alpha_{ijmn}^{\alpha\beta}k_jk_ne_{\perp i}^{\alpha *})e_{\perp m}^{\beta}-\delta^{\alpha\beta}\left(\sum_{\beta jm}\chi_{jm}^{\alpha\beta}e_{3j}^{\alpha}e_{3m}^{\beta}+\frac{1}{\mathbf{M}_0}(\mathbf{H}_0,\mathbf{e}_3^{\alpha})\right)\right],$$

$$B_k^{\alpha\beta}=\mu M_0[\chi_{jm}^{\alpha\beta}e_{\perp j}^{\alpha *}+\alpha_{ijmn}^{\alpha\beta}k_jk_ne_{\perp i}^{\alpha *}]e_{\perp m}^{\beta *}.$$

The quantity $a[\gamma,\beta]$, which depends on γ and β, determines the signs of $A_k^{1\beta}$ and $B_k^{1\beta}$, i.e. it takes on the values 1 or -1. Table I must be used to determine $a[\gamma,\beta]$.

We shall now study the elastic subsystem (3). Quantizing the elastic deformations we find the spectrum of elastic waves

$$\mathcal{H}_U=\sum_{ks}\varepsilon_{ks}^{U}b_{ks}^{+}b_{ks}. \tag{7}$$

Switching to the second–quantization operators $c_{k\gamma}$ and b_{ks} the interaction energy of the magnetic and elastic subsystems (4) becomes

$$\mathcal{H}_{MU}=\sum_{ks\gamma}\Psi_{k\gamma s}^{MU}c_{k\gamma}[b_{-ks}-b_{ks}^{+}]+\text{h.c.} \tag{8}$$

$$\Psi_{k\gamma s}^{MU}=i\sum_{\beta\alpha}\sqrt{\frac{8\mu M_0^3}{\rho\varepsilon_{ks}^{U}}}\lambda_{ijnm}^{\alpha\beta}e_{3i}^{\alpha}Q_{jk}^{\beta\gamma}e_{km}^{s}k_n; \tag{9}$$

$$Q_{jk}^{\beta\gamma}=e_{\perp j}^{\beta}u_{k\beta\gamma}+e_{\perp j}^{\beta *}v_{k\beta\gamma}.$$

TABLE I. Scheme for calculatng $a[\gamma,\beta]$ as a function of the number of lattices.

1 sublattice $n=0;\ \gamma,\beta=1$	2 sublattices $n=1;\ \gamma,\beta=1,2$	4 sublattices $n=2;\ \gamma,\beta=1,2,3,4$	8 sublattices $n=3;\ \gamma,\beta=1,\ldots,8$	…	2^n sublattices $\gamma,\beta=1,\ldots,2^n$
$A:=1$	$B:=\begin{pmatrix} A & A \\ A & -A \end{pmatrix}$	$C:=\begin{pmatrix} B & B \\ B & -B \end{pmatrix}$	$D:=\begin{pmatrix} C & C \\ C & -C \end{pmatrix}$	…	$\{N+1\}:=\begin{pmatrix} \{N\} & \{N\} \\ \{N\} & -\{N\} \end{pmatrix}$
$a[\gamma,\beta]:\quad A$	$a[\gamma,\beta]:\quad B$	$a[\gamma,\beta]:\quad C$	$a[\gamma,\beta]:\quad D$		$a[\gamma,\beta]:\quad \{N+1\}$

The transformations have shown that in the present approximation only spin waves on the first and second branches, corresponding to the operators c_{k1} and c_{k2}, interact with sound waves.

Then the antiferromagnetic Hamiltonian (1) assumes the form

$$\mathcal{H}=\sum_{k\gamma}\varepsilon^{\mathbf{M}}_{k\gamma}c^{+}_{k\gamma}c_{k\gamma}+\sum_{ks}\varepsilon^{U}_{ks}b^{+}_{ks}b_{ks}+\left[\sum_{\substack{ks,\gamma'\\ \gamma'=1,2}}\Psi_{k\gamma' s}c_{k\gamma'}(b_{-ks}-b^{+}_{ks})+\text{h.c.}\right]. \tag{10}$$

The antiferromagnetic Hamiltonian (10) which is quadratic in the operators $c_{k\gamma}$ and b_{ks} can be diagonalized by switching to operators which are superpositions of the operators $c_{k\gamma}$ and b_{ks} and applying the Bogolyubov canonical transformation. Then we obtain the following dispersion equation for the frequencies of the coupled magnetoelastic waves:

$$\prod_{\gamma,s}(\varepsilon^{M^2}_{k\gamma}-\omega^2)(\varepsilon^{U^2}_{ks}-\omega^2)-4\sum_{s}\varepsilon^{M}_{k1}\varepsilon^{U}_{ks}|\Psi^{MU}_{k1s}|^2$$
$$\times(\varepsilon^{M^2}_{k2}-\omega^2)\prod_{s'\neq s}(\varepsilon^{U^2}_{ks'}-\omega^2)-4\sum_{s}\varepsilon^{M}_{k2}\varepsilon^{U}_{ks}|\Psi^{MU}_{k2s}|^2$$
$$\times(\varepsilon^{M^2}_{k1}-\omega^2)\prod_{s'\neq s}(\varepsilon^{U^2}_{ks'}-\omega^2)=0. \tag{11}$$

In summary, in this work we have found the spin-wave spectrum for a multisublattice antiferromagnet, determined the coupling parameter between the spin and elastic waves, and obtained in general form a dispersion equation for the spectrum of coupled magnetoelastic waves.

*E-mail: kizirgulovir@ic.bashedu.ru

[1] E. A. Turov, *The Physical Properties of Magnetically Crystals*, Nauka, Moscow (1963).
[2] J. Smart, *The Effective Field in the Theory of Magnetism*, Nauka, Moscow (1968).
[3] A. I. Akhiezer and V. G. Bar'yakhtar, *Spin Waves*, Nauka, Moscow (1967).
[4] E. A. Turov and V. G. Shavrov, Usp. Fiz. Nauk **140**, 429 (1983) [Sov. Phys. Usp. **26**, 593 (1983)].
[5] M. A. Savchenko, Fiz. Tverd. Tela (Leningrad) **6**, 864 (1964) [Sov. Phys. Solid State **6**, 666 (1964)].
[6] Yu. G. Pashkevich, V. G. Sobolev, and V. V. Shakhov, Fiz. Nizk. Temp. **12**, 962 (1986) [Sov. J. Low Temp. Phys. **12**, 545 (1986)].
[7] V. N. Krivoruchko, A. A. Stepanov, and D. A. Yablonskii, Fiz. Nizk. Temp. **12**, 962 (1986) [Sov. J. Low Temp. Phys. **12**, 411 (1986)].
[8] A. U. Abdullin, M. A. Savchenko, and M. Kh. Kharrasov, Dokl. Akad. Nauk **342**, 753 (1995) [Phys. Dokl. **40**, 285 (1995)].
[9] A. S. Tyablikov, *Methods of the Quantum Theory of Magnetism*, Nauka, Moscow (1965).
[10] T. Holstein and H. Primakoff, Phys. Rev. **58**, 1098 (1940).

Translated by M. E. Alferieff